Micro-welding of Engineering Materials by High Brightness Lasers

March 2012

Mohd Idris Shah Ismail

Graduate School of
Natural Science and Technology
(Doctoral Course)

OKAYAMA UNIVERSITY

Abstract

Recently, many parts and components of electronic devices are being made smaller to meet the requirements of lighter, thinner and compacter in the electrical and electronic industries. Therefore, there exists a demand for high quality joining method of thin, difficult-to-weld and high performance materials. Lasers are considered to be the best choice among a variety of micro-scale material joining methods due to its non-contact nature and high intensity resulting from the ability to focus it to a small diameter. In order to comprehensively understand the characteristics of laser welding in thin, difficult-to-weld and high performance materials, it is necessary to do further fundamental researches by means of both experiment and numerical simulation. As the laser micro-welding is pushed to its limits in new and unique applications, this research work investigates into the anatomy of micro-welding on engineering materials by high brightness lasers.

In the micro-welding of thin material, a three-dimensional finite element model has been developed to simulate the temperature, stress, strain and deformation fields during CW laser micro-welding of thin stainless steel sheet. The numerical model using a combination of surface heat source and adaptive volumetric heat source could be well represented the real welding as the heat source penetrates into the material. Application of developed thermal model demonstrated that the laser parameters, such as laser power, scanning velocity and spot diameter have a significant effect on temperature field and the resulting weld pool. In the case of welding deformation, numerical simulation was carried out by an uncoupled thermo-mechanical model. The welding stress and deformation are generated by plastic deformation during the heating and cooling periods. In addition, the residual stress is higher than yield strength and has strongest effect upon the welding deformation. It was confirmed that the stress field and final deformation also vary with various laser parameters. The numerical simulated results have proved that the developed finite element model is effective to predict thermal histories, thermally induced stresses and welding deformations in the thin material. Moreover, it helped to understand the process mechanism in the laser micro-welding of thin material.

In the micro-welding of difficult-to-weld material, the overlap welding between a FPC, which consist of a thin copper circuit on a polyimide film, and a thick brass electrode by a pulsed Nd:YAG laser were experimentally and numerically investigated. By an approach of pulse waveform in laser pulse, the temperature could be controlled in the weld region and avoided the problem of an unstable process. The pre-heating effect on the pulse waveform was essential to increase the surface temperature of copper and induced higher absorption of laser energy at the beginning of laser pulse. While, the post-heating effect on the pulse waveform performed a positive result to remove the bump defect. Furthermore, a better weld joint without weld defects could be achieved by adding a rest time in the post-heating phase. It was proved that the higher shear strength could be obtained by the control of pulse waveform to perform the good joining without weld defects.

In the micro-welding of high performance material, the micro-welding of a super thermal conductive (STC) aluminum-graphite composite was experimentally and numerically investigated by pulsed Nd:YAG laser. Porosity and bump were observed as remarkable weld defects without a control of laser pulse. Moreover, the graphite was not mixed with aluminum during welding process to prevent from the formation of aluminum carbide, which could degrade the weld joint. The controlled pulse waveform with slow cooling at the end of laser pulse was essential to relieve internal stress during solidification, since the lack of fusion was observed on the joining zone due to the rapid cooling. It was proved that free weld defects and higher strength could be performed by using an appropriate controlled pulse waveform.

要旨

近年，電気電子業界で用いられる多くの電子機器の部品は軽量化，薄型化，小型化などに対応して設計，製作されている．そのため，薄くて溶接が困難な高性能材料の高品質な接合方法に対する要望が高まっている．レーザ加工は非接触の性質と小径に集光する能力から，様々な材料を微細で高強度に接合する最良の方法であると考えられる．したがって，薄くて溶接が困難な高性能材料のレーザ溶接特性を総合的に理解するために，実験と数値解析の両面から基礎研究を行うことが重要である．また，レーザ微細溶接は新しく，新たなアプリケーション展開が進んでいることから，本研究では高輝度レーザを用いた高機能性工業材料の微細溶接に関しても詳細な検討を行った．

第2章と3章では，薄板料の微細溶接を対象としており，薄いステンレス鋼板のCWレーザ微細溶接時の温度，応力，ひずみおよび変形場を理解するために三次元有限要素モデルを検討した．キーホール効果により，熱源が材料内部からも生じるにように表面の熱源と適応体積熱源の組み合わせたモデルを，実際の溶接に沿って表現した．この熱源モデルによって，レーザ出力，走査速度，スポット径のパラメータが温度場と溶接ビードに対して大きな影響を及ぼすことが示された．溶接変形の検討に対しては，熱・構造モデルと2階段で行った．溶接時から冷却するまでの間に塑性変形が生じることから，熱応力とそれにともう変形が生じた．さらに，残留応力が降伏応力よりも大きくなり，溶接変形に大きな影響を与えたと考えられる．以上のように，応力場と最終的な変形の関係性を明らかにできた．本研究で開発した要素モデルは，薄板料における時間的な熱変化，およびそれにともう熱応力と溶接変形を予測するために有要であることを考えられる．

第4章では溶接が困難な材料の微細溶接として，パルス Nd:YAG レーザを用いたポリイミドのフィルムと薄い銅の回路で構成される FPC と厚い真鍮の配線間におけるオーバーラップ溶接を実験と数値解析の両面から検討した．レーザパルス波形のアプローチの仕方によって，溶接領域の温度が制御でき，不安定なプロセスの問題を回避することができた．パルス波形による予熱の効果は，レーザパルスの開始時に銅の表面温度を高め，レーザエネルギー吸収率を大きくするために不可欠であった．一方，パルス波形でのポストヒーティングの効果は，バンプの欠陥を除去するために有効であった．さらに，休止時間を有するポストヒーティングを用いることで溶接欠陥の無い精密な接合継手をつくりだすことができた．そして，溶接欠陥のない接合継手を可能とするパルス波形制御を用いて接合することで高いせん断強度が得られた．

第5章では高性能材料であるの超熱伝導性（STC）アルミニウム-グラファイト複合材に対するパルスNd:YAGレーザを用いた微細溶接を検討した．レーザパルスを制御しない場合，ポロシティとバンプが顕著な溶接欠陥として観察された．溶接継手を成分分析したところ，溶接プロセス中においてグラファイトとアルミニウムとの混合物は生成されなかったことから，炭化アルミニウム形成による継手の劣化はないと判断できた．また，急速な冷却では溶融域に融合不良が観察されたことから，凝固時の内部応力を緩和させるために終了前のパルス波形を緩やかな冷却制御にすることが不可欠であることが明らかなとなった．そして適切なパルス波形に制御することで，溶接欠陥が無く，高い接合を示すことが明らかとなった．

Table of contents

Abstract i
Abstract (in Japanese) ii
Table of contents iii
List of figures vi
List of tables xi
Nomenclatures xii
Acronyms and abbreviations xv

Chapter 1 Introduction 1
1.1 Background and motivation 1
1.2 Laser welding 3
1.2.1 Laser-material interaction 4
1.2.2 Mechanism of laser welding 5
1.2.3 Applications 7
1.3 Research objective 8
1.4 Overview and research scope 10
References 11

Chapter 2 Temperature Field Induced by Laser Micro-welding 13
2.1 Introduction 13
2.2 Brief review of literature 13
2.3 Transient heat transfer analysis 14
2.3.1 Three-dimensional transient heat conduction equation 15
2.3.2 Boundary and initial conditions 17
2.3.3 Finite element formulation 17
2.4 Finite element modeling 20
2.4.1 Geometry, mesh and element models 21
2.4.2 Heat input model 22
2.4.3 Material model 24
2.4.4 Boundary conditions model 25
2.4.5 Solution scheme 25
2.5 Equipments 27
2.5.1 Single-mode CW fiber laser 27

2.5.2 Galvano scanner 28
2.6 Experimental work 29
2.7 Results and discussion 31
2.8 Conclusions 39
References 40

Chapter 3 Thermal Deformation in Laser Micro-welding 43
3.1 Introduction 43
3.2 Brief review of literature 44
3.3 Welding stresses and deformations 45
3.3.1 Thermal stresses in welding 45
3.3.2 Welding induced residual stresses and deformations 46
3.4 Non-linear structural analysis 48
3.4.1 Basic equations of elasticity 49
3.4.2 Theory of plasticity 54
3.4.3 Finite element formulation 58
3.5 Finite element modeling 62
3.5.1 Geometry, mesh and element models 63
3.5.2 Material model 63
3.5.3 Boundary conditions model 65
3.5.4 Solution scheme 65
3.6 Equipments 67
3.7 Experimental work 68
3.8 Results and discussion 68
3.8.1 Temperature fields 68
3.8.2 Welding stress fields 71
3.8.3 Plastic strain fields 84
3.8.4 Welding deformations 88
3.9 Conclusions 101
References 102

Chapter 4 Direct Micro-joining of Brass and Copper of FPC by Pulsed Nd:YAG Laser 105
4.1 Introduction 105
4.2 Overview of approach 106

4.3 Equipments 108
4.3.1 Pulsed Nd:YAG laser 108
4.3.2 Field emission scanning electron microscope 111
4.3.3 Universal testing machine 111
4.4 Experimental procedures 112
4.5 Numerical analysis 115
4.6 Results and discussion 116
4.6.1 Rectangular pulse waveform 116
4.6.2 Pulse waveform with pre-heating effect 119
4.6.3 Pulse waveform with pre- and post-heating effects 123
4.6.4 Evaluation of weld strength 126
4.7 Conclusions 128
References 129

Chapter 5 Micro-welding of Super Thermal Conductive Composite by Pulsed Nd:YAG Laser 131
5.1 Introduction 131
5.2 Background and overview 132
5.3 Equipments 136
5.4 Experimental procedures 136
5.5 Numerical analysis 138
5.6 Results and discussion 140
5.6.1 Bead-on-plate welding 140
5.6.2 Overlap welding 145
5.6.3 Evaluation of weld strength 154
5.7 Conclusions 157
References 158

Chapter 6 Conclusions 160

Acknowledgements 163
List of publications 164

List of figures

Figure 1.1	Power densities and interaction times for various laser processes	2
Figure 1.2	Variations of reflectivity with wavelength for several metallic materials	5
Figure 1.3	Schematic illustration of conduction mode welding	6
Figure 1.4	Schematic illustration of keyhole mode welding	7
Figure 1.5	Output characteristics of laser beam under different oscillation conditions	8
Figure 2.1	Element with transient conduction	16
Figure 2.2	Various heat transfer modes in a three-dimensional solid V bounded by a surface A	18
Figure 2.3	FEM procedures of thermal analysis	20
Figure 2.4	Geometries used in finite element analysis	21
Figure 2.5	Meshes generated in finite element analysis	22
Figure 2.6	Heat input model in finite element analysis	23
Figure 2.7	Thermophysical properties of austenitic stainless steel SUS304	24
Figure 2.8	Thermal boundary condition in finite element analysis	25
Figure 2.9	Movement of laser irradiation	26
Figure 2.10	Photographs of (a) single-mode fiber laser and (b) intensity distribution of formed laser beam	28
Figure 2.11	Schematic diagram of optical components in galvano scanner	29
Figure 2.12	Schematic diagram of experimental setup	30
Figure 2.13	Temperature field at the top surface along the weld direction (y-axis) at t: 0.3 ms (d: 17.5 μm, P: 40 W, v: 2.0 m/s)	31
Figure 2.14	Temperature histories of the three evaluated points transverse to the weld direction (d: 17.5 μm, P: 30 W, v: 1.5 m/s)	32
Figure 2.15	Temperature histories of the two evaluated points on the top and bottom surfaces (d: 17.5 μm, P: 30 W, v: 1.5 m/s)	33
Figure 2.16	Temperature fields during laser irradiation (a-c) and cooling (d-f) (d: 17.5 μm, P: 30 W, v: 1.5 m/s)	34
Figure 2.17	Temperature field contours for six welding conditions under a constant energy density	35
Figure 2.18	Temperature history of a reference plane (d: 17.5 μm, P: 30 W, v: 1.5 m/s)	36
Figure 2.19	Comparison between experimental and simulated weld bead geometry	37
Figure 2.20	Comparison between experimental solidification pattern and simulated melting isotherm at the center of weld top surface	38
Figure 3.1	Schematic representation of temperature and thermal stress change during bead-on-plate welding	46

Figure 3.2	Schematic representation of typical residual stresses in welded rectangular plate	47
Figure 3.3	Various types of welding deformation	48
Figure 3.4	Stress at a point: (a) normal and shear stresses and (b) components of stress	50
Figure 3.5	Equilibrium of forces on a cubic element in *x*-direction	51
Figure 3.6	Deformation of a cubic element	52
Figure 3.7	Graphical illustrations of (a) isotropic hardening rule, (b) kinematic hardening rule and (c) stress-strain relationship of hardening rule	57
Figure 3.8	Graphical illustrations of incremental Newton-Raphson procedure	61
Figure 3.9	FEM procedure of uncoupled thermo-mechanical simulation	62
Figure 3.10	Mechanical properties of austenitic stainless steel SUS304	64
Figure 3.11	Multi-linear isotropic stress-strain model of austenitic stainless steel SUS304	65
Figure 3.12	Boundary condition in structural analysis	66
Figure 3.13	Schematic diagram of deformation measurement	69
Figure 3.14	Temperature field contour at the top of weld surface and comparison of cross-sectional view between experimental and simulated weld bead geometry	70
Figure 3.15	Equivalent stress distribution for different vertical layer of the specimen (*d*: 35.0 μm, *P*: 50 W, *v*: 1.0 m/s)	71
Figure 3.16	Distributions of temperature and equivalent stress at the top surface along the welding line (*d*: 35.0 μm, *P*: 50 W, *v*: 1.0 m/s)	72
Figure 3.17	Equivalent stress distribution during laser irradiation and cooling along the width of specimen (*d*: 35.0 μm, *P*: 50 W, *v*: 1.0 m/s)	73
Figure 3.18	Distributions of normal stresses (a-c) and shear stresses (d-f) during laser irradiation (*d*: 35.0 μm, *P*: 50 W, *v*: 1.0 m/s)	74
Figure 3.19	Distributions of temperature and normal stresses at the top surface along the welding line (*d*: 35.0 μm, *P*: 50 W, *v*: 1.0 m/s)	75
Figure 3.20	Distributions of longitudinal stress during (a) laser irradiation and (b-d) cooling (*d*: 35.0 μm, *P*: 50 W, *v*: 1.0 m/s)	76
Figure 3.21	Temperature and longitudinal stress distributions of two evaluated points on the top and bottom surfaces (*d*: 35.0 μm, *P*: 50 W, *v*: 1.0 m/s)	77
Figure 3.22	Longitudinal and transverse residual stress distributions along (a) *x*-axis and (b) *y*-axis under different spot diameter (*P*: 30 W, *v*: 1.0 m/s)	79
Figure 3.23	Longitudinal and transverse residual stress distributions along (a) *x*-axis and (b) *y*-axis under different laser power (*d*: 35.0 μm, *v*: 1.0 m/s)	80
Figure 3.24	Longitudinal and transverse residual stress distributions along (a) *x*-axis and (b) *y*-axis under different scanning velocity (*d*: 17.5 μm, *P*: 30 W)	81

Figure 3.25	Equivalent stress distribution on the top surface of specimen during intermediate of laser irradiation and end of cooling period for four welding conditions	83
Figure 3.26	Equivalent strain distribution during (a) laser irradiation and (b-d) cooling (*d*: 35.0 µm, *P*: 50 W, *v*: 1.0 m/s)	84
Figure 3.27	Longitudinal strain histories of two evaluated points on the top and bottom surfaces (*d*: 35.0 µm, *P*: 50 W, *v*: 1.0 m/s)	85
Figure 3.28	Distribution of (a) temperature, (b) stress and (c) plastic strain during laser irradiation and cooling periods (*d*: 35.0 µm, *P*: 50 W, *v*: 1.0 m/s)	87
Figure 3.29	Temporal distribution of plastic strain for four welding conditions	88
Figure 3.30	Schematic diagram of deformation angle calculation	89
Figure 3.31	Temporal distributions of deformation angle at the top and bottom surface of specimen (*d*: 35.0 µm, *P*: 50 W, *v*: 1.0 m/s)	90
Figure 3.32	Relationship of deformation with (a) temperature, (b) stress and (c) plastic strain during laser irradiation and cooling periods (*d*: 35.0 µm, *P*: 50 W, *v*: 1.0 m/s)	92
Figure 3.33	Displacement along the width direction during (a) laser irradiation and (b-d) cooling (*d*: 35.0 µm, *P*: 50 W, *v*: 1.0 m/s)	93
Figure 3.34	Displacement along the welding direction during (a) laser irradiation and (b-d) cooling (*d*: 35.0 µm, *P*: 50 W, *v*: 1.0 m/s)	94
Figure 3.35	Temporal distributions of deformation angle for four welding conditions	95
Figure 3.36	Final displacement along the width direction for four welding conditions	96
Figure 3.37	Final displacement along the welding direction for four welding conditions	96
Figure 3.38	Measured displacement for four welding conditions	98
Figure 3.39	Comparison between experimental and simulated deformation angle	99
Figure 4.1	Thermophysical properties and absorptivity of copper for 1064 nm wavelength	106
Figure 4.2	Setting shape and actual signal of pulse waveform (*P*: 300 W, τ: 3 ms)	108
Figure 4.3	Schematic illustration of pulsed Nd:YAG laser	109
Figure 4.4	Schematic illustration of pulsed output	110
Figure 4.5	Setting of pulse waveform in PC-Terminal 2 software	111
Figure 4.6	Photograph of flexible printed circuit	112
Figure 4.7	Photograph of brass electrode	112
Figure 4.8	Schematic diagram of experimental setup	113
Figure 4.9	Schematic illustration of (a) shearing test setup and (b) observation of fracture point	114
Figure 4.10	Finite element model for the heat conduction analysis	115
Figure 4.11	Cross-section view of welding results with rectangular pulse waveform	117

Figure 4.12	Spatial temperature distribution at 500 W – 3 ms with rectangular pulse waveform	118
Figure 4.13	Temporal temperature distribution at 500 W – 3 ms with rectangular pulse waveform	118
Figure 4.14	Schematic illustration of welding mechanism with pre-heating	119
Figure 4.15	Spatial temperature distribution with pre-heating effect on pulse waveform	120
Figure 4.16	Temporal temperature distribution with pre-heating effect on pulse waveform	121
Figure 4.17	Removal part of adhesive and polyimide films in phase 1 of controlled pulse waveform (P_1: 50 – 300 W, τ_1: 1.5 ms)	121
Figure 4.18	Bottom view of FPC in phase 2 of pulse waveform with pre-heating effect (P_2: 300 W)	122
Figure 4.19	Welding result of pulse waveform with pre-heating effect (P: 400 W, τ: 3.5 ms)	122
Figure 4.20	Welding result of pulse waveform with pre- and post-heating effects (P: 400 W, τ: 6.5 ms)	123
Figure 4.21	Welding result of two pulse waveforms with pre- and post-heatings including rest time (P: 400 W, τ: 4.7 ms)	124
Figure 4.22	SEM images, EDS spot and mapping analysis of pulse waveform with pre- and post-heatings including rest time	125
Figure 4.23	Pulse waveforms used for shearing test	126
Figure 4.24	Fracture on the top of brass electrode	127
Figure 4.25	Shear strength of the welding with and without the control of pulse waveform	127
Figure 5.1	Thermal conductivity and thermal expansion coefficient of STC composite and other materials	132
Figure 5.2	Al-C phase diagram	133
Figure 5.3	Schematic illustration and optical micrographs of STC Al-Gr composite	135
Figure 5.4	Schematic diagram of experimental setup	137
Figure 5.5	Configurations of shearing test specimen	138
Figure 5.6	Finite element models for investigation of temperature distributions	139
Figure 5.7	Thermophysical properties of pure aluminum	140
Figure 5.8	Influence of laser power on the top surface of weld bead	141
Figure 5.9	SEM photographs and element mapping of Al and C	142
Figure 5.10	Influence of pulse width on the top surface of weld bead	143
Figure 5.11	Influence of scanning velocity on the top surface of weld bead	143
Figure 5.12	Spatial temperature distributions in bead-on-plate welding	144
Figure 5.13	Temperature histories in bead-on-plate welding	145
Figure 5.14	Welding results with rectangular pulse waveform	146

Figure 5.15	Schematic illustration of welding process with spike pulse waveform	147
Figure 5.16	Influence of laser power (P_2) in phase 2 of spike pulse waveform	148
Figure 5.17	Influence of pulse width (t_2) in phase 2 of spike pulse waveform	149
Figure 5.18	SEM images and EDS mappings with spike pulse waveform	150
Figure 5.19	Setting shape and actual signal of controlled pulse waveform	151
Figure 5.20	Temperature histories by three controlled pulse waveforms	151
Figure 5.21	Spatial temperature distributions by three controlled pulse waveforms	152
Figure 5.22	SEM images and EDS mappings of cross-section with (a) annealing and (b) trailing pulse waveforms	153
Figure 5.23	Shear strength of the welding with and without the control of pulse waveform (R: Rectangular, S: Spike, A: Annealing, T: Trailing)	154
Figure 5.24	SEM photographs of fracture on the top of STC Al-Gr composite	155
Figure 5.25	SEM photographs and EDS mappings of fracture with trailing pulse waveform on the (a) bottom surface of aluminum and (b) top surface of STC Al-Gr composite	156

List of tables

Table 2.1	Laser parameters in FEM thermal analysis	27
Table 2.2	Specifications of single-mode fiber laser	28
Table 2.3	Chemical compositions of austenitic stainless steel SUS304	30
Table 3.1	Laser parameters in FEM structural analysis	67
Table 3.2	Specifications of laser displacement sensor	67
Table 3.3	Reversed deformation for four welding conditions	97
Table 4.1	Specifications of pulsed Nd:YAG laser	109
Table 4.2	FEM analysis conditions	116
Table 4.3	Thermal properties for adhesive, polyimide, tin and brass	116
Table 5.1	Material properties of STC Al-Gr composite	134
Table 5.2	FEM analysis conditions	140
Table 5.3	Element composition of points 1-10 in Figure 5.25	156

Nomenclature

Symbol	**Description**	**Unit**
A	Surface area	m^2
I	Intensity distribution	W/m^2
I_0	Intensity of the incident laser beam	W/m^2
J_i	Stress invariants (i = 1, 2, 3)	Pa
E_p	Pulse energy	J/pulse
F	Pressure	Pa or bar
F_i	Force per unit volume ($i = x, y, z$)	N/m^3
F_j	External force (j = 1, 2, 3, 4)	N
F_{load}	Force or load	N
F_{melt}	Pressure for melting	Pa or bar
G_e	Elastic modulus or Young modulus	Pa
G_s	Shear modulus or modulus of rigidity	Pa
M_{ii}	Bending strength in direction ($i = x, z$)	Pa
OL	Overlapping ratio	%
P	Laser power	W
P_a	Average power	W
P_p	Peak power	W
P_s	Heat power absorbed on the surface	W
P_v	Heat power absorbed by the keyhole wall	W
Q_e	Effective output laser power	W
Q_s	Surface heat flux	W/m^2
Q_v	Volumetric heat flux	W/m^3
R	Electrical resistivity	Ω·m
R_p	Pulse repetition rate	Hz
R_r	Reflectivity	-
T_i	Surface tractions per unit area ($i = x, y, z$)	N/m^2
V	Solid volume	m^3
c	Specific heat capacity	J/(kg·K)
d	Spot diameter or beam diameter	m
h	Thickness	m
h_c	Convective heat transfer coefficient	$W/(m^2 \cdot K)$
h_d	Depth	m

k	Thermal conductivity	W/(m·K)
k_{ii}	Thermal conductivity in direction ($i = x, y, z$)	W/(m·K)
l	Length	m
q''	Heat flux	W/m^2
q'''	Internal heat generation per unit volume	W/m^3
q_c	Convective heat flux	W/m^2
r	Radial distance from the laser beam center	m
r_c	Current radius	m
r_d	Characteristic radius	m
r_0	Initial radius	m
t	Time	s
t_p	Retention time	s
t_0	Initial time	s
$t_{\delta_{final}}$	Time of final deformation angle	s
$t_{\delta_{max}}$	Time of maximum deformation angle	s
v	Welding speed or scanning velocity	m/s
w	Width	m
x	First Cartesian coordinate	m
y	Second Cartesian coordinate	m
z	Third Cartesian coordinate	m
z_i	Current depth	m
σ	Normal stress	Pa
$\bar{\sigma}$	Equivalent stress or von Mises stress	Pa
σ_0	Yield strength in uniaxial tension	Pa
σ_m	Hydrostatic stress	Pa
$\sigma_{tensile}$	Tensile strength	Pa
σ_{yield}	Yield stress	Pa
σ_{shear}	Shear strength	Pa
σ_{xx}	Longitudinal normal stress	Pa
σ_{yy}	Transverse normal stress	Pa
σ_{zz}	Through thickness normal stress	Pa
α	Thermal expansion coefficient	1/K
α_{ii}	Thermal expansion coefficient in direction ($i = x, y, z$)	1/K
δ	Deformation angle	°
δ_{final}	Final deformation angle	°

δ_{max}	Maximum deformation angle	°
δ_{rev}	Reversed deformation angle	°
ε	Normal strain	-
$\bar{\varepsilon}$	Equivalent strain	-
ε_{xx}	Longitudinal strain	-
ε_{yy}	Transverse strain	-
ε_{zz}	Through thickness strain	-
ε_{θ}	Thermal strain	-
$\Delta\varepsilon$	Strain gradient	-
γ_{ij}	Shear strain (i or j = x, y, z)	-
ρ	Density	kg/m³
τ	Pulse width	s
τ_{ij}	Shear stress (i or j = x, y, z)	Pa
υ	Poisson's ratio	-
λ	Wavelength	m
η	Absorption rate or absorptivity	%
η_{a}	Absorption coefficient	1/m
θ	Temperature	K
θ_0	Initial temperature	K
θ_{∞}	Ambient or room temperature	K
θ_{melt}	Melting temperature	K
θ_{evap}	Evaporation temperature	K
$\Delta\theta$	Temperature gradient	K
$[\ ]$	Matrix	-
$\{\ \}$	Vector	-
∇	Gradient	-

Acronyms and abbreviations

APDL	ANSYS Parametric Design Language
CCC	Carbon-Carbon Composite
CCD	Charge Coupled Device
CTE	Coefficient of Thermal Expansion
CMC	Ceramic Matrix Composite
CW	Continuous Wave
EDS	Energy Dispersive Spectroscopy
FD	Finite Difference
FEM	Finite Element Method
FE-SEM	Field Emission Scanning Electron Microscope
FPC	Flexible Printed Circuit
HAZ	Heat-affected Zone
ISM	Iterative Substructure Method
LDS	Laser Displacement Sensor
LED	Laser Emitting Diode
MMC	Metal Matrix Composite
PC	Personal Computer
PMC	Polymer Matrix Composite
RoHS	Restriction of Hazardous Substances Directive
RTPS	Real-Time Power Supply
SEM	Scanning Electron Microscope
STC	Super Thermal Conductive
TEM	Transverse Electromagnetic Modes
WDS	Wavelength Dispersive Spectroscopy
WEEE	Waste Electrical and Electronic Equipment Directive

Chapter 1: Introduction

1.1 Background and motivation

Laser is one of the greatest innovations of 20th century. In 1917, Albert Einstein introduced the theory of stimulated emission, which became the basic of Light Amplification by Stimulated Emission of Radiation, and it is known by the acronym laser. The first laser was realized by Maiman using a ruby crystal.[1.1] Almost of today's lasers were invented in the mid-1960s, but they remained in research laboratories and military establishments. Companies only started to manufacture lasers for commercial use towards the end of that decade.[1.2] Laser has capability to generate high energy concentration because of their monochromatic, coherent, highly collimated and low divergence properties with wavelength ranging from ultra-violet to infrared.[1.3)–1.5] Laser can delivers very low (~mW) to extremely high (1–100 kW) focused power with a precise beam size and interaction time (10^{-3}–10^{-15} s) on to any kinds of substrate through any medium.[1.6] The range of possible processes with the laser mapped against power density and interaction time is illustrated in **Figure 1.1**.

The laser technologies became important or even dominant in industrial applications. Further possibilities of processing, innovation and advancement on laser materials processing are still in progress and very challenging. The increasing demand of laser in material processing can be attributed to several unique advantages of laser such as non-contact processing, elimination of processing operation, improvement of product quality, cost reduction, high productivity and flexibility, and ease of automation. One of the earliest and most widely practiced applications of laser material processing was the welding of metallic sheets.[1.7] The first laser welds were carried out around 1963, and involved the joining in stainless steel by a pulsed ruby laser. Two years later, the first industrial application of laser welding appeared using a pulsed Nd:YAG laser in the electronic industry.[1.2] Continued laser development has made laser welding economically competitive with other welding methods. Over the last three decades, the laser welding became a chosen for many industrial fields such as aerospace, aviation, biomedical, electronic and automobile production.

In general, the laser welding is based on high power density welding technologies, which have the possibility of focusing the laser power to a very small spot diameter. As a result, the laser welding process offers a number of advantages over the conventional arc welding processes, leading to the narrower heat-affected zones (HAZ), the lower distortions, residual stresses and strains.[1.7)–1.10] In addition, the advantage of laser welding with deep penetration capability, makes it successfully applied for thin sheet metal welding even under the conduction welding mode.[1.11] The laser welding

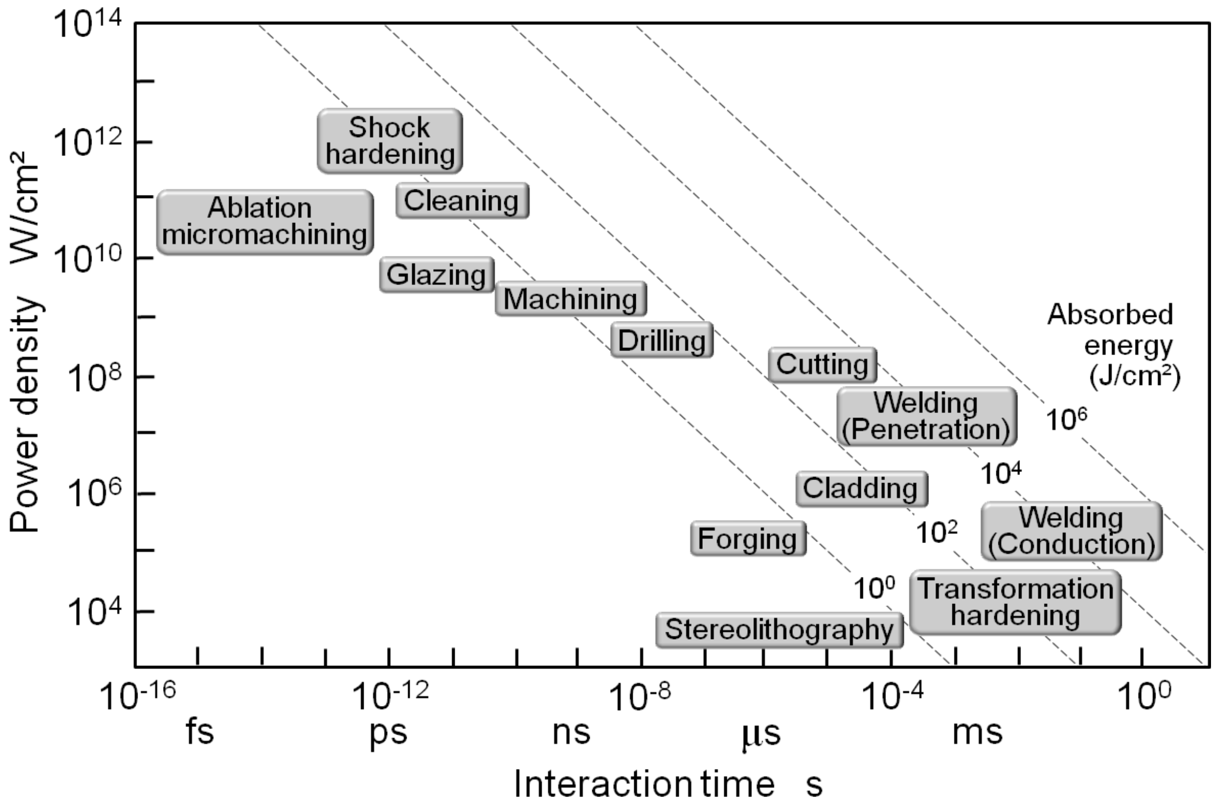

Figure 1.1 Power densities and interaction times for various laser processes[1.3), 1.4)]

also offers a great potential in the joining of difficult materials such as copper, aluminum and magnesium alloys.[1.12)–1.14)] From these viewpoints, it is expected that laser welding will be used more widely to join a variety of materials and wide range of sizes in industries.

Recently, many parts and components of electronic devices are being made smaller to meet the requirements of lighter, thinner and compacter in the electrical and electronic industries. Therefore, there exists a demand for high quality and faster joining method of thin metal sheets. Thin metal sheets show very sensitive response to heat input in weld bead, and the weld bead geometry is important for joining strength. It is very difficult to weld thin metal sheet using conventional methods, because excessive heat input leads to blow holes in the weld bead. The small thickness of thin metal sheets also accompanies the risk of distortion problem in micro-welding. Thus, the minimum heat input to thin metal sheet is effective in both technical and economical points. Technically, less heat input leads to smaller HAZ, less distortion and little loss of materials due to evaporation. Economically, less heat input requires lower laser power that relates to less equipment investment and low running cost.

Subsequently, as the best material selection for connecting conductive parts in electronic devices, copper and its alloys are typically used because of its superior ability to efficiently conduct electrical energy and transmit signals. However, the very high thermal conductivity that makes copper rapidly diffuses heat away from the weld joint, making it difficult to maintain heat balance and weld reliability. High power is required to overcome the reflectivity and to ensure the sufficient absorption of energy to the copper, and raises its temperature and decreases the material reflection. As the absorption of laser power occurs less than a 10^{-9} seconds,[1.15)] there is a rapid change in absorbed power. The high power that was initially required, now far exceeds from the required power to generate the weld. As a result, the material rapidly overheats and vaporizes, leaving a large porosity or a hole. Therefore, the challenge of copper welding is the control of the heat balance in these small and highly conductive parts to enable the welding by ensuring no over- or under-heating.

Advanced materials are recently gaining importance as replacements for conventional materials. The development of advanced materials with the material combination of various metals and non-metals has led to new metal matrix composites (MMCs) as a great attractive material in the electronic industries. MMCs exhibit higher strength-density ratios, stiffness, wear resistance, and low thermal expansion. Despite their potential applications, limited joining and machining processes have hindered their wide industry usage. Mechanical joining of these materials results in excessive tool wear and is relatively expensive cost. Fusion joining provides a better alternative for MMCs welding. However, it has been found the difficulties on the fusion joining of MMCs because of the different properties of the base matrix and the particulate reinforcements. Novelty and relative complexity of MMCs adds unwanted complications to an already challenging field. All these provide hindrances in effective and reliable weld joints in MMCs.

From the above demands and difficulties on the present industrial applications, the electronic industry has been increasingly interested in the laser welding technology to joint electronic components. Furthermore, the production technologies with high reproducibility, high accuracy, and short processing time are required. Laser micro-welding with high beam quality offers the potential to become a promising technology within this application field. In order to comprehensively understand the characteristics of laser welding in thin, difficult-to-weld and high performance materials, and it is necessary to do further fundamental researches by means of both experiment and numerical simulation.

1.2 Laser welding

Laser welding is an advanced fusion joining process that applies the high energy conversion from a very concentrated laser irradiation to melt the materials, and consecutively continued with the materials joint after solidification. It involves several complex phenomena such as formation of keyhole, weld pool geometry and plasma formation. In the following sections, the laser-material interaction, mechanisms and applications of laser welding are described.

1.2.1 Laser-material interaction

In materials processing with laser, the optical energy is absorbed by the interaction of the electric field of the electromagnetic radiation with electrons.[1.16)] If the electron is bound within the phonon structure of a solid, this force will be transferred to the structure. If there is a sufficient flux of photons, the force becomes enough to cause the structure vibrate, which generates the heat. With greater photon fluxes, the vibration becomes sufficient to break the solid structure and it firstly melts, then evaporates. The vapors is ionized forming a plasma and finally the solid is ionized introducing Coulomb forces to remove the material. This last effect is only achieved with the immense power that is currently available with femto-second pulses. Beyond this power range, lasers are being used for atomic fusion.

When a laser beam is irradiated on the surface of a material, the absorbed energy causes the heating, melting, and or/and evaporation of the material, which are depending on the absorbed laser power density as shown in **Figure 1.1**. The efficiency of absorbed energy is defined as the ratio of energy absorbed by the irradiated materials to the laser output energy. The absorption of laser irradiation in the material is generally expressed as equation (1.1), and it is known as the Beer-Lambert law.[1.3), 1.5)]

$$I(z) = I_0 \exp(-\eta_a z) \tag{1.1}$$

where I_0 (W/m^2) is the intensity of the incident laser beam, $I(z)$ (W/m^2) is the intensity at depth z (m), and η_a (1/m) is the absorption coefficient. The laser beam intensity required for the welding is 10^5–10^7 W/cm^2.[1.17)] One of the important parameters influencing the effects of laser-material interactions is absorptivity of the material for laser irradiation. It can be defined as the fraction of incident radiation that is absorbed at normal incidence. For opaque materials, the absorptivity η, can be expressed as equation (1.2).[1.1)]

$$\eta = 1 - R_r \tag{1.2}$$

where R_r is the reflectivity of the material. The variation of reflectivity with the wavelength of some common metallic materials is shown in **Figure 1.2**. The effects due to the absorption of laser beam can occur very rapidly, and the irradiated surface rises to its melting temperature.

Melting without vaporization is produced within a low range of laser power density. At the high level of laser power density, the surface begins to evaporate before a depth of molten material is produced. Melting of a material by laser irradiation depends on the heat flow in the material.[1.18)] Heat flow depends on the thermal conductivity k (W/(m·K)), while it is not the only factor that influences the

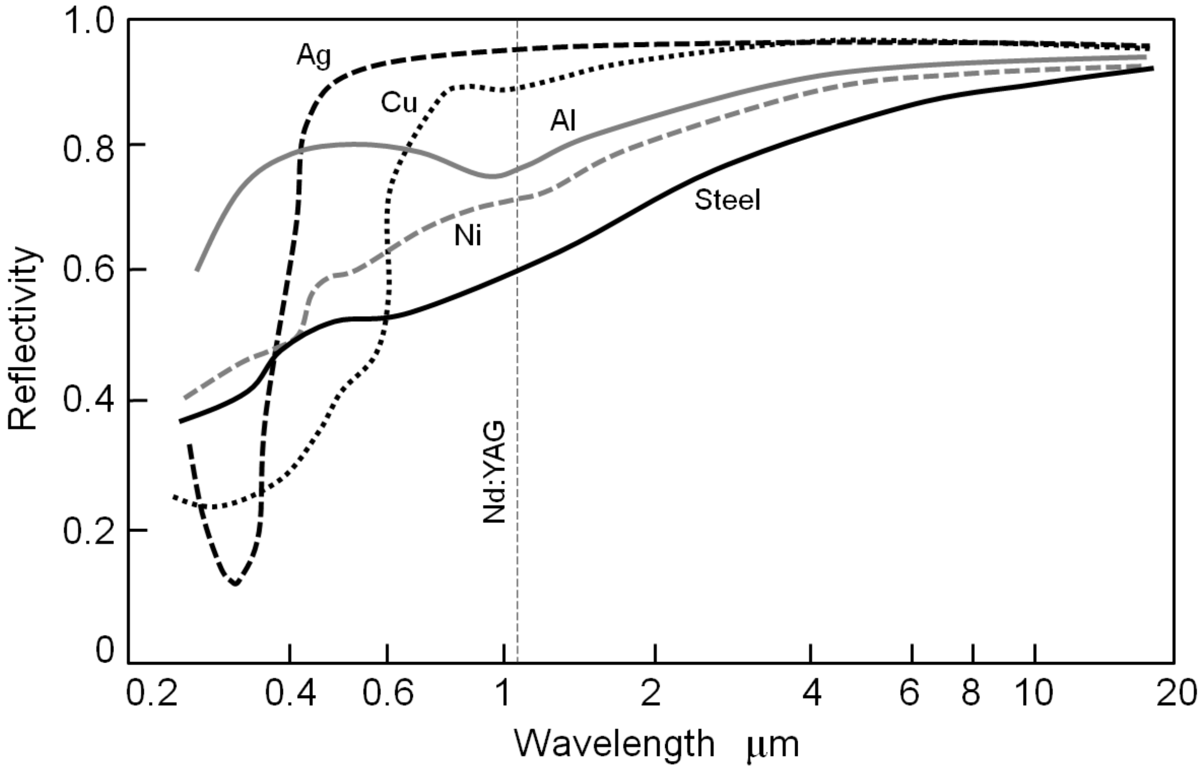

Figure 1.2 Variations of reflectivity with wavelength for several metallic materials[1.1)]

heat flow. The change rate of temperature also depends on the specific heat c (J/(kg·K)) of the material. In fact, the heating rate is inversely proportional to the specific heat per unit volume, which is equal to ρc, where ρ (kg/m^3) is the material density. The important factor for heat flow is $k/\rho c$ (m^2/s). It is known by the descriptive term of thermal diffusivity and recognized as the diffusion coefficient for heat. The significance of this material property determines how fast a material will hold and conduct the thermal energy. In general, it can be noticed that the high thermal diffusivity allows faster conduction of the heat energy through the material and it permits greater welding depth. However, the high surface reflectivity can reduce the energy absorption on surface.

1.2.2 Mechanisms of laser welding

The mechanisms of laser-material interaction are influenced by many parameters such as the laser power, the intensity distribution of laser power at the surface, the irradiation time and the material properties. In general, there are two fundamental modes of laser welding: (a) conduction model welding and (b) keyhole mode welding.

(a) Conduction mode welding

Conduction mode welding is usually used at relatively lower power densities ($<10^6$ W/cm^2).[1.4)] The material is melted at the surface to the melting point and the heat is transferred into material by

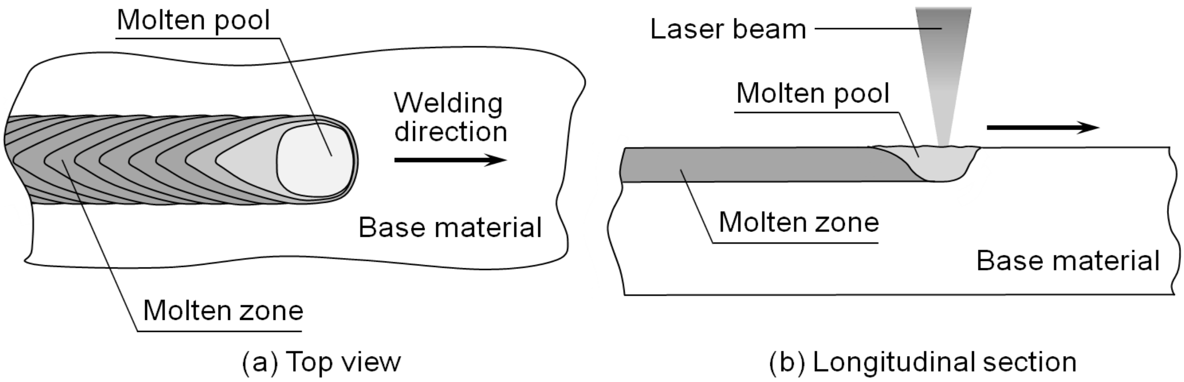

Figure 1.3 Schematic illustration of conduction mode welding

heat conduction. Convection phenomenon also plays a role once a weld pool is formed.[1.4)] The conduction mode welding does not penetrate into the material with the minimal evaporation. Since the heat conduction takes place not only in vertical direction, but also in horizontal direction along the surface of the material, the isotherms are semi-circles around the beam irradiation, which means the cross-section of weld bead shows a semi-circular shape. The weld bead geometry in conduction mode welding is shallow and wide as shown in **Figure 1.3**. In general, the transition from conduction mode to the keyhole mode occurs with the increase in laser intensity and irradiation time applied to the material.

(b) Keyhole mode welding

In contrast to conduction mode welding, the keyhole mode welding occurs once the sufficient energy of laser irradiation heats up the material to over its evaporation temperature at the focal area of the laser beam. The keyhole mode welding at the power density beyond 10^6 W/cm^2 generates a keyhole, which leads to the deep penetration welds with the high aspect ratio and the temperature inside the keyhole can reach up to 20000 K.[1.4), 1.6), 1.19)] The basic mechanism of keyhole formation is schematically shown in **Figure 1.4**. The keyhole is filled with metal plasma and can extend over the full thickness of the material. The plasma goes out from the keyhole and forms a plasma plume above the material. The weld seam is usually protected from oxidation by means of a shielding gas. The vapor channel which is surrounded by a region of liquid material, and the combination of the plasma pressure that in the keyhole and the vapor pressure of the evaporating material maintains the equilibrium and prevents keyhole collapsing.[1.20)] Keyhole mode welding is better energy coupling and higher penetration than conduction mode welding. However, keyhole welding can be unstable, as the keyhole oscillates and closes intermittently. This intermittent closure causes porosity due to gas entrapment. On the other hand, conduction mode welding is more stable, since vaporization is minimal and there is no further absorption below the surface of the material.

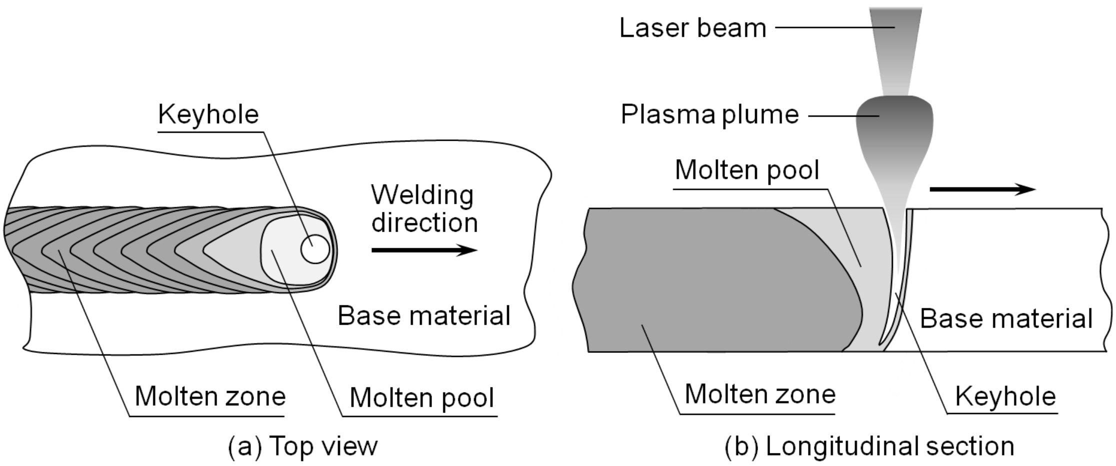

Figure 1.4 Schematic illustration of keyhole mode welding

1.2.3 Applications

Laser has greatly contributed to major fields of science and technology since the first success in laser oscillation in 1960. Manufacturing technologies have become more reliant upon laser, and it will continue to play an important role and become more valuable. In addition, the development of latest electronic devices, measuring instruments, automobiles and aircraft might have been vastly limited without the laser materials processsing.[1.21)]

Laser welding constitutes the second largest segment of laser materials processing market with a share of about 40 %.[1.11)] Laser welding is finding an increasing number of applications in the industry and research, because it can lead to an increase in productivity, reduction in distortion and consistent weld integrity. It is also ideal for applications in the field of micro-joining and dissimilar materials where conventional welding methods are impossible to be implemented. Moreover, laser welding equipments are in continuous growth and competition which laser will gain more importance. In the modern laser welding system, the ability of computer control allows laser power to be varied for different welding conditions. The use of optical feedback and monitoring systems further optimizes the laser welding process to better suit different industrial applications and needs.[1.7)]

The output of laser beam can be continuous, pulsed or Q-switched operations. In the welding applications, the continuous wave (CW) lasers deliver a constant or an average power during a seam welding. It also can be modulated on and off to deliver a marginally higher peak power for a spot welding. On the other hand, the pulsed lasers could achieve a high peak power with millisecond pulses to create a molten zone, and the seam welding could be created by its overlapping of pulses. Q-switched lasers deliver very high peak power with nanosecond pulses of low energy compared with pulsed lasers. **Figure 1.5** shows the comparison of the output characteristics for various Nd:YAG laser under different oscillation conditions. In this research work, CW and pulsed laser welding are considered.

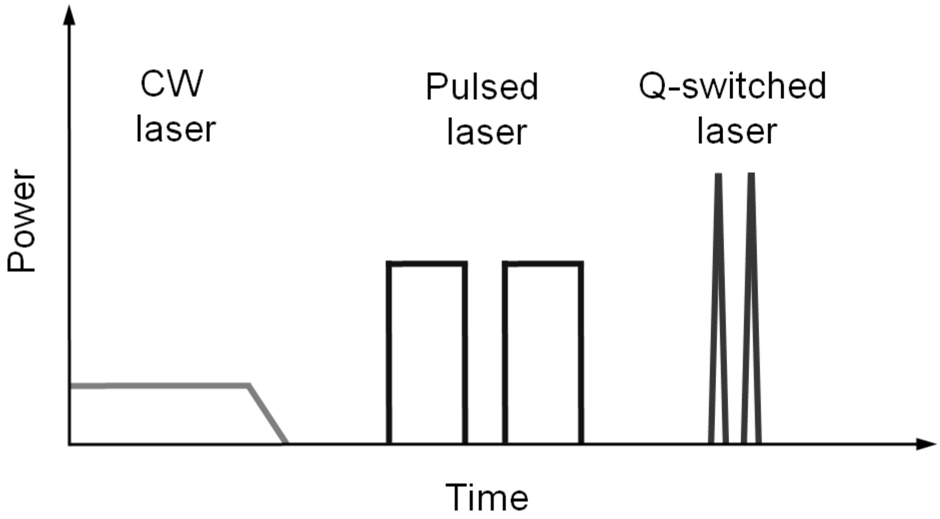

Figure 1.5 Output characteristics of laser beam under different oscillation conditions

1.3 Research objective

The present approach is to investigate the fundamental aspects on a laser micro-welding. Without a comprehensive understanding on the physical phenomena associated with the micro-welding process, the potential of lasers can not be completely realized. As the laser micro-welding is pushed to its limits in new and unique applications, this research work investigates into the anatomy of micro-welding on engineering materials by high brightness lasers.

Laser welding is most efficient for thin sheet applications. The small spot diameter enables welding of ultra-thin metal sheets. At the high welding speed up to 833 mm/s, a very smooth and homogeneous welding seam can be generated.[1.22] However, it is very difficult to provide an accurate measurement of temperature distribution of weld pool because of the short heating time and rapid cooling time. Therefore, finite element analysis seems to be more comprehensive and high efficiency to simulate and analyze the thermal process of laser micro-welding. Knowledge of temperature field in the weld pool and in the adjacent solid region can provide insight about the heat during welding. These complex calculations can produce reliable predictions of temperature field and weld bead geometry that are great importance for in-depth analysis and eventual improvement of process.

One of the major problems with welded materials is represented by the residual stress and distortion resulted because of local heating during welding.[1.23] While effects associated with welding deformation are already understood well in laser welding in the macro range, the detailed characteristics of laser micro-welding at the high-speed scanning have not yet been clarified sufficiently. Therefore, the evolution of mechanical fields in terms of stress and strain distributions is important to evaluate the welding deformation. However, the destructive and non-destructive techniques to measure the stress and strain distributions, in practice is usually limited by either cost or accuracy. As the present work employed finite element method (FEM) to evaluate the thermal fields, this method offers a comprehensive solution for the prediction of residual stress and strain as well as welding deformation in welded materials. The knowledge on these problems may lead to the better control over the undesirable aspects of the process.

Most of the micro-joining requires welding dissimilar, high reflective and high performance materials. It is more critical in dissimilar welding process, because it can be more difficult to meet and to match different properties of different materials in order to obtain the high-quality weld bead. In the welding high performance materials such as MMCs, the major difficulty is that prolonged contact between a molten metal matrix and particulate reinforcement can lead to undesirable chemical reactions, which lead to further embrittlement of the weld joint. In addition, it was difficult and almost impossible to weld the reflective or difficult-to-weld materials with CW laser.[1.24)] Pulsed laser has a capability to deliver the high peak power and the very short pulse width during the laser pulse and the solidification time is shorter than CW laser. By an approach of pulse waveform in laser pulse, the temperature would be controlled in the weld region and would avoid the problem of an unstable process. It also might be possible to produce the free defect of welds by changing the laser pulse shape. Furthermore, the temperature field is fundamental to understand and analyze heat effects of welding and weld defects. Therefore, the FEM is the efficient method to help quantify the reasonable welding parameters and to further recognize the mechanism involved in micro-welding.

The aims of this research work are to represent a phenomenon, originalities and advantages of laser micro-welding in the fields of industries. This work consisted of experimental and numerical investigations with qualitative and quantitative descriptions of laser micro-welding. Development of simplified engineering approaches based on numerical simulation and correlations with experimental data could be very beneficial to industrial applications. Findings from the investigation would provide a better understanding into the characteristics and performances of laser micro-welding in thin, difficult-to-weld and high performance materials.

The specific objectives for the research can be summarized as follows:

- Development of a numerical model to represent the real laser micro-welding using a combination of surface and adaptive volumetric heat source as the heat source penetrates into the material.
- Investigation of the thermal and mechanical fields in laser micro-welding to determine and predict the weld bead geometry and welding deformation in laser micro-welding.
- Investigation of the fundamental characteristics in dissimilar laser micro-welding on the difficult-to-weld and high performance materials.
- Investigation of welding phenomenon by controlling the pulse waveform to determine the optimum welding conditions with minimum weld defects.

1.4 Overview and research scope

This doctoral thesis presents the research work carried out within a period of three years. It consists of six chapters, and the contents of each chapter are briefly described as follows:

Chapter 1 introduces the research background and motivation. The laser-material interaction, mechanisms and applications of laser welding are described. This chapter also outlines the objective and scope of research work.

Chapter 2 demonstrates the temperature field induced by laser micro-welding in thin stainless steel sheet using numerical simulation. A three-dimensional finite element model is developed to simulate dynamically the laser micro-welding process, which gives considerable insight into the thermal profile in the weld pool. The numerical model can calculate the temperature distribution and predict the weld bead geometry. In order to validate the numerical model, the micro-welding of a thin stainless steel sheet is experimentally investigated using a single-mode CW fiber laser with the high-speed scanning system in the bead-on-plate welding condition.

As an extension of numerical simulation, Chapter 3 demonstrates the thermal deformation of thin stainless steel sheet in the laser micro-welding. The investigations are made to advance the fundamental insight into the complex thermo-mechanical phenomena in laser micro-welding. A thermo-mechanical modeling is developed to simulate the stress-strain distributions and deformation in laser micro-welding. The experimental work is parts to measure the welding deformation and characterizing the influence of specific welding conditions on the deformation. The discussion of the computational modeling results includes the comparison with the experimental results.

Chapter 4 demonstrates the investigation of dissimilar micro-welding in copper of flexible printed circuit (FPC) and brass by pulsed Nd:YAG laser. The weld behaviors for both materials are studied experimentally and numerically using the control of pulse waveform, which can provide a well-directed controlling of the heat input with the high energy density. In addition, the shearing strength is evaluated with and without the control of pulse waveforms. The potential benefits of pulse waveform are discussed and provides insight into the direct laser micro-welding process.

Chapter 5 demonstrates the investigation of micro-welding in super thermal conductive (STC) composite by pulsed Nd:YAG laser. The experimental work is carried out in two sections, namely the bead-on-plate welding and the overlap welding. This chapter also discusses the proper heat input by numerical model, which is used to simulate the temperature distribution in the weld zone. These investigations lead to an optimum welding condition proposed for a pulsed laser welding with minimum weld defects. The weld strength is also evaluated by a shearing test for the overlap welding with and without the control of pulse waveform.

Chapter 6 completes this thesis with the conclusion derived from this study.

References

1.1) N.B. Dahottre and S.P. Harimkar : Laser Fabrication and Machining of Materials, Springer Science, (2008), 3, 36-37.

1.2) J.C. Ion : Laser Processing of Engineering Materials – Principles, Procedures and Industrial Application, Elsevier Butterworth-Heinemann, (2005), 1, 20.

1.3) W.M. Steen : Laser Material Processing (Third Edition), Springer, (2003), 3, 70, 79, 85-86, 228.

1.4) E. Kannatey-Asibu : Principles of Laser Materials Processing, John Wiley & Sons, Inc., (2009), 118-128, 410, 515-516.

1.5) J.F. Ready and D.F. Farson : LIA Handbook of Laser Material Processing, Laser Institute of America, Magnolia Publishing Inc., (2001), 5, 91-94.

1.6) J.D. Majumdar and I. Manna : Laser Processing of Materials, Sadhana, (2003), Vol. 28, No. 3&4, 495-562.

1.7) W.W. Duley : Laser Welding, John Wiley & Sons, Inc., (1999), 1, 7, 201-225.

1.8) J. Xie and A. Kar : Laser Welding of Thin Sheet Steel with Surface Oxidation, Welding Journal, (1999), Vol. 78, No. 10, 343s-348s.

1.9) K. Inose, J.Y. Lee, Y. Nakanishi and Y.-C. Kim : Characteristics of Welding Distortion/Residual Stress Generated by Filler Welding with Laser Beam and Verification of Generality of Its Highly Accurate Prediction, Welding International, (2009), Vol. 23, No. 8, 581-588.

1.10) A. Belhadj, J. Bessrour, J.-E. Masse, M. Bouhafs and L. Barrallier : Finite Element Simulation of Magnesium Alloys Laser Beam Welding, Journal of Materials Processing Technology, (2010), Vol. 210, 1131-1137.

1.11) W. Chen, P. Ackerson and P. Molian : CO_2 Laser Welding of Galvanized Steel Sheets Using Vent Holes, Materials and Design, (2009), Vol. 30, 245-251.

1.12) A. Blom, P. Dunias, P. Engen, W. Hoving and J. Kramer : Process Spread Reduction of Laser Micro-spot Welding of Thin Copper Parts Using Real-time Control, Proceedings of SPIE, (2003), Vol. 4977, 493-507.

1.13) W. Chen and P. Molian : Dual-beam Laser Welding of Ultra-thin AA 5052-H19 Aluminum, International Journal of Advanced Manufacturing Technology, (2008), Vol. 39, 889-897.

1.14) L.K. Pan, C.C. Wang, Y.C. Hsiao and K.C. Ho : Optimization of Nd:YAG Laser Welding onto Magnesium Alloy via Taguchi Analysis, Optics and Laser Technology, (2004), Vol. 37, 33-42.

1.15) G. Shannon and P. Severloh : Microwelding Conductive Materials, Practical Welding Today, (2011), September 2011.

1.16) W. M. Steen : Laser Material Processing – An Overview, Journal of Optics A: Pure and Applied Optics, (2003), Vol. 5, S3-S7.

1.17) V.A. Katulin : Laser Technology in Industry, Hyperfine Interactions, (1987), Vol. 37, 423-432.

1.18) J.F. Ready : Industrial Applications of Lasers (Second Edition), Academic Press, (1997), 316.

1.19) C. Carmignani, R. Mares and G. Toselli : Transient Finite Element Analysis of Deep Penetration Laser Welding Process in a Singlepass Butt-welded Thick Steel Plate, Computer Methods in Applied Mechanics and Engineering, (1999), Vol. 179, 197-214.

1.20) J. Dowden, M. Davis and P. Kapadia : The Flow of Heat and the Motion of the Weld Pool in Penetration Welding with a Laser, Journal of Applied Physics, (1985), Vol. 57, No. 9, 4474-4479.

1.21) I. Miyamoto : Challenge to Advanced Laser Materials Processing in Japanese Industry, RIKEN Review, (2003), Vol. 50, 20-28.

1.22) Y. Okamoto, A. Gillner, A. Olowinsky, J. Gedicke and Y. Uno : Fine Micro-welding of Thin Stainless Steel Sheet by High Speed Laser Scanning, Journal of Laser Micro/Nanoengineering, (2008), Vol. 3, No. 2, 95-99.

1.23) K. Masubuchi : Prediction and Control of Residual Stresses and Distortion in Welded Structures, Transactions of JWRI, (1996), Vol. 25, No. 2, 53-67.

1.24) M. Naeem : Microwelding Performance Comparison Between a Lower Power (125 W) Pulsed Nd:YAG Laser and a Low Power (100–200 W) Single Mode Fiber Laser, Proceedings of PICALO 2008 – The 3rd Pacific International Conference on Application of Lasers and Optics, (2008).

Chapter 2:
Temperature Field Induced by Laser Micro-welding

2.1 Introduction

Laser micro-welding technology has been increasingly applied in industrial manufacturing. This technology offers a great potential for a new product design and manufacturing. Compared with the conventional welding processes, it has significant advantage in welding of heat sensitive components with precision control of heat input, minimal thermal distortion, small heat-affected zone (HAZ) and excellent repeatability.[2.1), 2.2)]

Generally, the laser micro-welding involves many variables: laser power, scanning velocity, spot diameter and shielding gas. Every of these parameters may have an important effect on temperature field and the resulting weld pool. However, it is difficult to measure the temperature field of micro-welding process, especially in the laser micro-welding with high-speed scanning. The finite element based numerical techniques has proven to be very useful and efficient for research, design development and production engineering, and capability in the prediction of temperature field and weld bead geometry.[2.3), 2.4)] In addition, the simulation of laser welding process enables to estimate the transient stresses, residual stresses and distortion. Therefore, a thermal model that describes the thermal field as a function of process parameters is extremely required.

In this chapter, the laser micro-welding process was investigated through numerical simulation. A three-dimensional finite element model has been developed to simulate the laser micro-welding process. In order to validate the numerical model, the weld bead geometry of a thin stainless steel sheet is experimentally investigated using a single-mode CW fiber laser with high-speed scanning system on the bead-on-plate welding condition. The weld bead geometry is measured at different laser power, scanning velocity and spot diameter. The computational results are compared with the experimental measurements, analyzing the temperature field that is essential to predict the weld bead geometry.

2.2 Brief review of literature

The initial attempt to simulate laser welding was primarily based on the Rosenthal's work.[2.5)] However, this analytical model does not consider the temperature-dependent material properties and distributed heat flux corresponding to the laser beam. Steen et al.[2.6)] combined the point and line sources to model effectively a keyhole welding. As this model assumes an infinitely thick specimen, it is inappropriate for thin specimens. Instead of using two sources, Binda et al.[2.7] proposed a semi-empirical model of the temperature field in laser welding, based on a modification of the Rosenthal solution. As the main disadvantage of the analytical model, it does not consider the variation of the thermal properties with temperature, which has very little practical or theoretical relevance to describe the real laser welding.

The first numerical solution of heat transfer for laser materials processing was made by Mazumder and Steen.[2.8] The authors developed a three-dimensional model using finite difference (FD) numerical techniques in solving the heat conduction equation. There are many research papers,[2.3), 2.9)–2.12] which deal with the temperature field and weld bead geometry of laser welding by using numerical models. Furthermore, the modeling of laser welding is challenging since many complicated factors are involved. Especially those associated with weld pool dynamics, metal evaporation, plasma formation, absorption mechanism in the keyhole, and the interaction between laser and plasma plume.[2.13)–2.17]

Although a critical review of the previous work indicates that the models have provided significant insight into the welding process and welded materials, they are not widely used in designing and manufacturing today.[2.18] Therefore, a simple model is required to describe the temperature fields. Particularly, if the primary goal is to compute the thermal stress during the welding process. Kazemi and Goldak[2.3] developed a simple three-dimensional numerical simulation for laser welding, which capable to calculate the weld bead geometry with the combination of two heat sources. The authors are reported that the complicated fluid flow in liquid metal and in the plasma was neglected.

In the laser micro-welding, the influencing factors on the prediction of weld bead geometry have not been extensively studied. The present work is required in terms of conducting finite element simulation for understanding the combined effect of laser parameters on temperature fields and weld bead geometry in thin metal sheet.

2.3 Transient heat transfer analysis

One objective with heat transfer analysis in welding applications is to determine the temperature fields in a specimen resulting from conditions imposed on its boundaries.[2.19] Heat transfer involved in the laser welding process is due to the heating by the laser beam on the surface of a specimen. The heat transfer modes are characterized by conduction, convection and radiation. Part of the heat is transferred inside the specimen by conduction, and part of the heat is transferred to the surroundings by convection and radiation effects. However, in many applications of practical importance only one or two of these mechanisms may actually intervene.[2.20] The temperature fields in the specimen can be calculated using the finite element method (FEM). In this section, the finite element formulations of the heat transfer analysis are derived from the law of conservation of thermal energy, which applied in the sheet metal material.

2.3.1 Three-dimensional transient heat conduction equation

The fundamental behavior of heat conduction is that a heat flux q'' (W/m^2) of energy flows from a hot region to cold regions is linearly dependent on the temperature gradient $\nabla\theta$ as in equation (2.1).

$$q'' = -k\left(\frac{\partial\theta}{\partial x} + \frac{\partial\theta}{\partial y} + \frac{\partial\theta}{\partial z}\right) = -k\nabla\theta \tag{2.1}$$

where k (W/(m·K)) is the thermal conductivity of the material and θ (K) is temperature. It should be noted that the minus sign is necessary in order to make q'' positive, because heat is always transferred in the direction of decreasing temperature. The equation (2.1) is called the Fourier's law of heat conduction.

The temperatures as stated above were considered independently from the time. Under such conditions, the heat transfer through the surface does not vary over time and there is no storage of heat in the surface itself. Refer to the cubic element shown in **Figure 2.1** and assume that the element is crossed by heat only in the direction x. If conditions are unsteady, heat dQ_{in} enters the cubic element and heat dQ_{out} exits the elements. The heat dQ is stored in the cubic element and is equal to as equation (2.2).

$$dQ = dQ_{\mathrm{in}} - dQ_{\mathrm{out}} \tag{2.2}$$

If the A surface of the element registers the thermal gradient $\partial\theta/\partial x$, based on Fourier's law, the heat dQ_{in} crossing the surface $dydz$ within the time dt can be written as equation (2.3).

$$dQ_{\mathrm{in}} = -k\frac{\partial\theta}{\partial x}dydzdt \tag{2.3}$$

On the other side, B surface of the cubic element at distance dx from the A surface, the thermal gradient is given by equation (2.4).

$$\frac{\partial\theta}{\partial x} + \frac{\partial}{\partial x}\frac{\partial\theta}{\partial x}dx = \frac{\partial\theta}{\partial x} + \frac{\partial^2\theta}{\partial x^2}dx \tag{2.4}$$

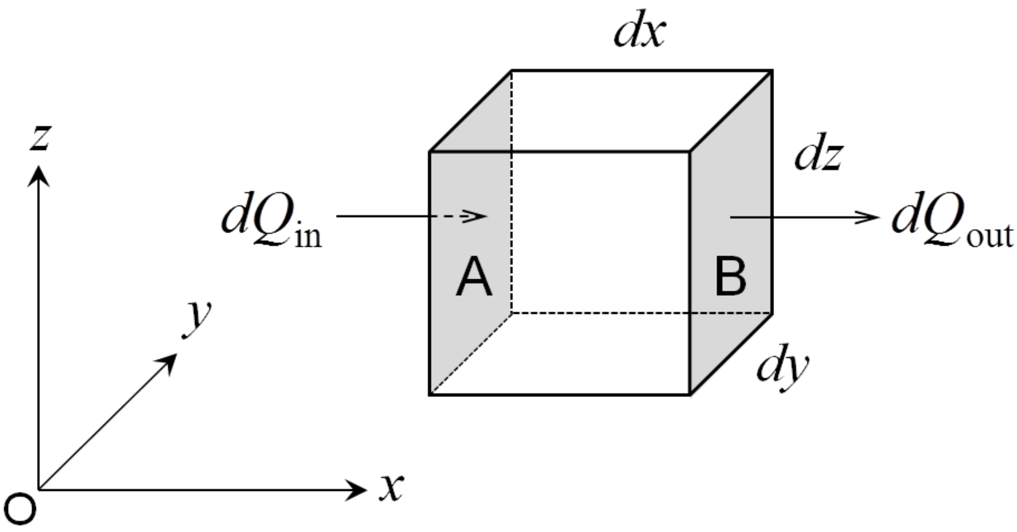

Figure 2.1 Element with transient conduction

Therefore, the dQ_{out} can be expressed as equation (2.5).

$$dQ_{\text{out}} = -k\left(\frac{\partial\theta}{\partial x} + \frac{\partial^2\theta}{\partial x^2}dx\right)dydzdt \tag{2.5}$$

Then, equation (2.2) can be described as equation (2.6).

$$dQ = k\frac{\partial^2\theta}{\partial x^2}dxdydzdt \tag{2.6}$$

This heat increases the temperature of the cube within the time dt and this increase is equal to $(\partial\theta/\partial t)dt$. The heat dQ is equal to the volumetric specific heat of the material multiplied by the volume of cubic element and by the noted increase in the temperature. Therefore, it can be expressed as equation (2.7).

$$dQ = \rho c\, dxdydz\frac{\partial\theta}{\partial t}dt \tag{2.7}$$

where c (J/(kg·K)) is the specific heat capacity and ρ (kg/m^3) is the density of material. Then, a comparison between equations (2.6) and (2.7) leads to equation (2.8).

$$\rho c\frac{\partial\theta}{\partial t} = k\frac{\partial^2\theta}{\partial x^2} \tag{2.8}$$

Writing an energy balance for a three-dimensional material and utilizing Fourier’s law of heat conduction yields, an expression for the transient diffusion within a material is in equation (2.9).

$$\rho c \frac{\partial \theta}{\partial t} = k\left(\frac{\partial^2 \theta}{\partial x^2} + \frac{\partial^2 \theta}{\partial y^2} + \frac{\partial^2 \theta}{\partial z^2}\right) + q''' = -\nabla \cdot q'' + q''' \tag{2.9}$$

where q''' (W/m^3) is the internal heat generation per unit volume. The equation (2.9) referred to as the heat diffusion equation or the heat equation, which provides a basis for most types heat conduction analyses.

2.3.2 Boundary and initial conditions

The heat conduction equation only determines the temperature inside the material. To completely establish the temperature field, it is necessary to solve the differential heat equation (2.9) for prescribed the boundary and initial conditions. During welding, a significant amount of heat is lost through the surfaces by means of natural convection or free convection. This phenomenon is known as heat convection, and mathematically it is described by the Newton equation as shown in equation (2.10).

$$q_c = h_c(\theta - \theta_\infty) \tag{2.10}$$

where q_c (W/m^2) is the convective heat flux, h_c (W/(m^2·K)) is the convective heat transfer coefficient, and θ_∞ (K) is the ambient temperature. As θ_∞ is the atmospheric temperature or room temperature, the initial condition (t=0) is written as equation (2.11).

$$\theta(x, y, z, 0) = \theta_\infty \tag{2.11}$$

2.3.3 Finite element formulation

A general formulation of element equations for transient heat transfer in a material can be derived from a three-dimensional solid V bounded by a surface A with various heat transfer modes such as conduction and convection as shown in **Figure 2.2**. The solution domain V is divided into E elements, and each element has m nodes. Within each element, the temperature and temperature gradient are simply expressed in matrix form as equations (2.12) and (2.13), respectively.

$$\theta(x, y, z, t) = [N(x, y, z)]\{\theta(t)\} \tag{2.12}$$

$$\nabla\theta(x, y, z, t) = [B(x, y, z)]\{\theta(t)\} \tag{2.13}$$

where $\{\theta(t)\}$ is the vector of element nodal temperatures. $[N(x, y, z)]$ is the temperature

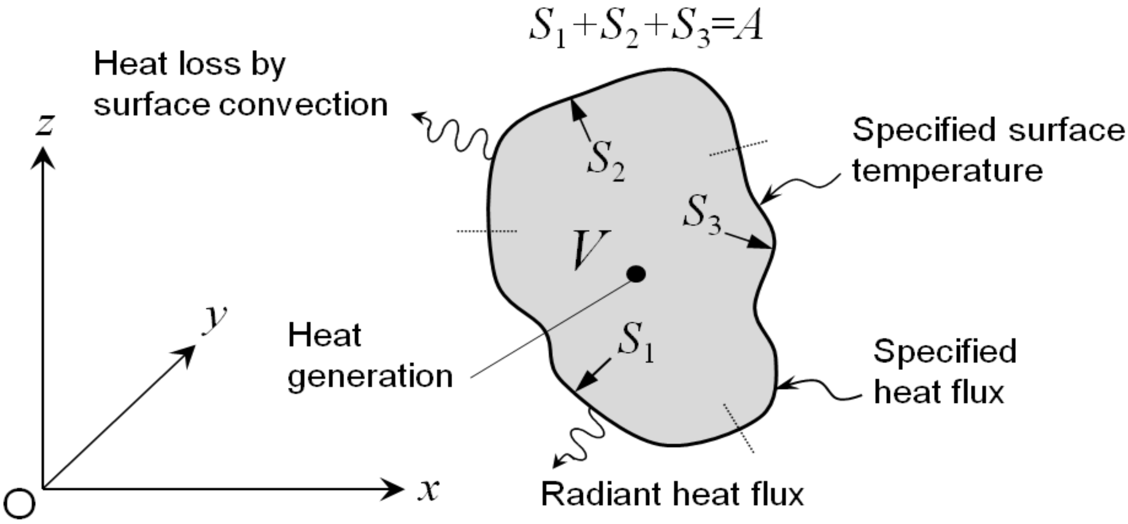

Figure 2.2 Various heat transfer modes in a three-dimensional solid *V* bounded by a surface *A*

interpolation matrix, $[B(x,y,z)]$ is the temperature gradient interpolation matrix, and both matrixes can be written as equations (2.14) and (2.15), respectively.

$$[N\,(x,y,z)] = [N_1 \quad N_2 \quad \cdots \quad N_m] \tag{2.14}$$

$$[B\,(x,y,z)] = \begin{bmatrix} \dfrac{\partial N_1}{\partial x} & \dfrac{\partial N_2}{\partial x} & \cdots & \dfrac{\partial N_m}{\partial x} \\ \dfrac{\partial N_1}{\partial y} & \dfrac{\partial N_2}{\partial y} & \cdots & \dfrac{\partial N_m}{\partial y} \\ \dfrac{\partial N_1}{\partial z} & \dfrac{\partial N_2}{\partial z} & \cdots & \dfrac{\partial N_m}{\partial z} \end{bmatrix} \tag{2.15}$$

For a single element, the Galerkin method is used to derive the element equations starting with the equation (2.9), it can be expressed as equation (2.16).

$$\int_{V(E)} \left(\nabla \cdot q'' - q''' + \rho c \frac{\partial \theta}{\partial t} \right) N_i dV = 0 \tag{2.16}$$

where $V(E)$ is the domain of element and N_i is the temperature interpolation function. By Gauss's theorem, which introduces surface integrals of the heat flow across the element boundary $A(E)$, the term of $\int_{V(E)} (\nabla \cdot q'') N_i dV$ is integrated. Thus, the following re-arranged form is obtained from equation (2.16) as shown in equation (2.17).

$$\int_{V(E)} \rho c \frac{\partial \theta}{\partial t} N_i dV - \int_{V(E)} \nabla \cdot q'' N_i dV = \int_{V(E)} q''' N_i dV - \int_{A(E)} (q'' \cdot \hat{n})\, N_i dA \qquad (i = 1, 2....., m) \tag{2.17}$$

When the surface integral is expressed as the sum of integrals over S_1, S_2, and S_3 $\left(A(E)=S_1+S_2+S_3\right)$, and taking the boundary conditions into account, the equation (2.17) is changed to equation (2.18).

$$\int_{V(E)} \rho c \frac{\partial \theta}{\partial t} N_i dV - \int_{V(E)} \nabla \cdot q'' N_i dV = \int_{V(E)} q''' N_i dV - \int_{S_1} \left(q'' \cdot \hat{n}\right) N_i dA$$
$$+ \int_{S_2} q'' N_i dA - \int_{S_3} h_c \left(\theta_{(x,y,z,t)} - \theta_\infty\right) N_i dA \qquad \left(i = 1, 2....., m\right) \qquad (2.18)$$

The element temperatures for the equation (2.12) and Fourier's law of equation (2.1) are introduced. Fourier's law is expressed with the equation (2.19) as follows.

$$\{q''\} = -[k][B]\{\theta\} \qquad (2.19)$$

With the manipulation on the equation (2.19), the resulting element equations become as equation (2.20).

$$[C]\{\dot{\theta}_E\} + [K]\{\theta_E\} = \{F_E\} \qquad (2.20)$$

where $[C]$ is the specific heat matrix, $[K]$ is the thermal conductivity matrix, and $\{F_E\}$ is the heat flow vector. $\{\theta_E\}$ is the vector of nodal temperature and $\{\dot{\theta}_E\}$ is the vector of time derivative of $\{\theta_E\}$. The matrix $[C]$, matrix $[K]$ and vector $\{F_E\}$ are written as equations (2.21), (2.22) and (2.23), respectively.

$$[C] = \rho \int_{V(E)} c \{N\}[N] dV \qquad (2.21)$$

$$[K] = [K_a] + [K_b] = \int_{V(E)} [B]^T [k][B] dV + \int_{S_3} h_c \{N\}[N] dA \qquad (2.22)$$

$$\{F_E\} = \{F_a\} + \{F_b\} + \{F_c\} + \{F_d\} = \int_V q''' \{N\} dV$$
$$- \int_{S_1} \left(q'' \cdot \hat{n}\right)\{N\} dA + \int_{S_2} q'' \{N\} dA + \int_{S_3} h_c \theta_\infty \{N\} dA \qquad (2.23)$$

where $[K_a]$ is the thermal conductivity matrix related to conduction, $[K_b]$ is the thermal conductivity related to convection, $\{F_a\}$, $\{F_b\}$, $\{F_c\}$ and $\{F_d\}$ are the heat flow vector arising from internal heat generation, the heat flow vector arising from specified temperature, the heat flow vector arising from specified surface heating and the heat flow vector arising from the surface convection, respectively. Equation (2.20) represents a general non-linear formulation of element equations for the transient heat conduction. In order to obtain the system equations, the element equations are assembled by the standard procedure.

2.4 Finite element modeling

Finite element method (FEM) is widely used in engineering analyses. Successful FEM analyses depend on several factors as below.[2.21)]

(1) the proper formulation of physical problems into FEM models

(2) the convergent solutions of FEM models

(3) the appropriate interpretation of FEM results

In other words, the proper procedures of FEM analyses are the key to its success. **Figure 2.3** shows the procedures of thermal analysis for simulating a laser welding process including important process parameters and material properties. A temperature field is obtained by thermal analysis.

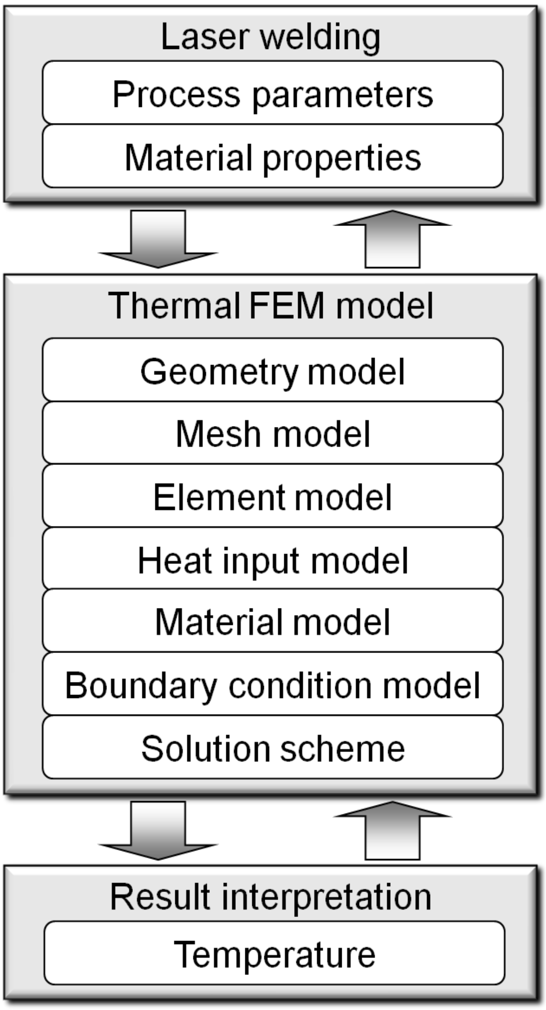

Figure 2.3 FEM procedures of thermal analysis

Temperatures induced in the specimen by laser irradiation was calculated by the non-linear transient thermal finite element equation (Equation (2.20)). In this study, a three-dimensional finite element model was performed using ANSYS finite element software.

2.4.1 Geometry, mesh and element models

The dimension of geometry model is 1 mm in length, 2 mm in width and 50 μm in thickness as illustrated in **Figure 2.4**. As the welding process was performed in the middle of the specimen, the selection of a portion of the specimen in the analysis model is an approach to reduce the computation time. **Figure 2.5** shows the meshes generated for the present simulation. The mesh has been graded such that it is the finest in the region of highest and most rapid temperature gradient near the heat input. In order to limit the total number of elements used in the simulation, a coarse mesh was used outside the heating zone. With this mesh pattern, both accurate results of simulation and the reduction of simulation time can be achieved. The mesh generation is carried out first on the upper or lower surface of the specimen, which generates quadrilateral elements and triangular elements. Then, 3D mesh can be generated by taking offsets across the specimen thickness. In order to capture the characteristics of the laser welding process accurately, the mesh size increases exponentially across the thickness of the specimen, being finer near the heated side of the specimen. The mesh is composed of a total number of 56768 elements. The elements were the thermal analysis element PLANE77 and SOLID70 for 2D eight-node thermal solid and 3D eight-node thermal solid, respectively.

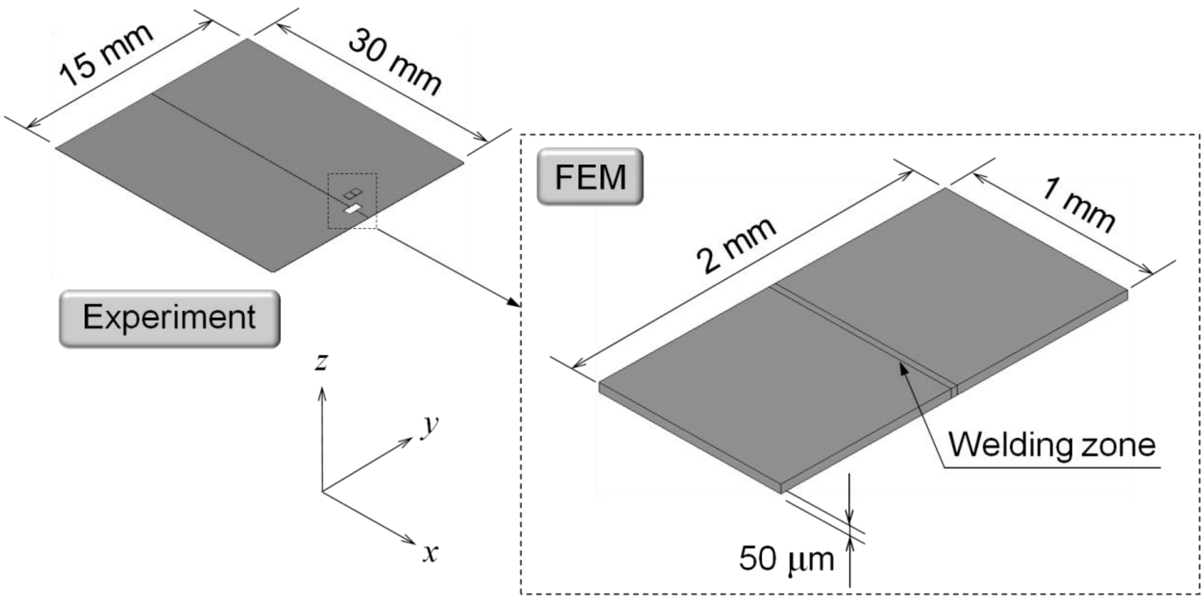

Figure 2.4 Geometries used in finite element analysis

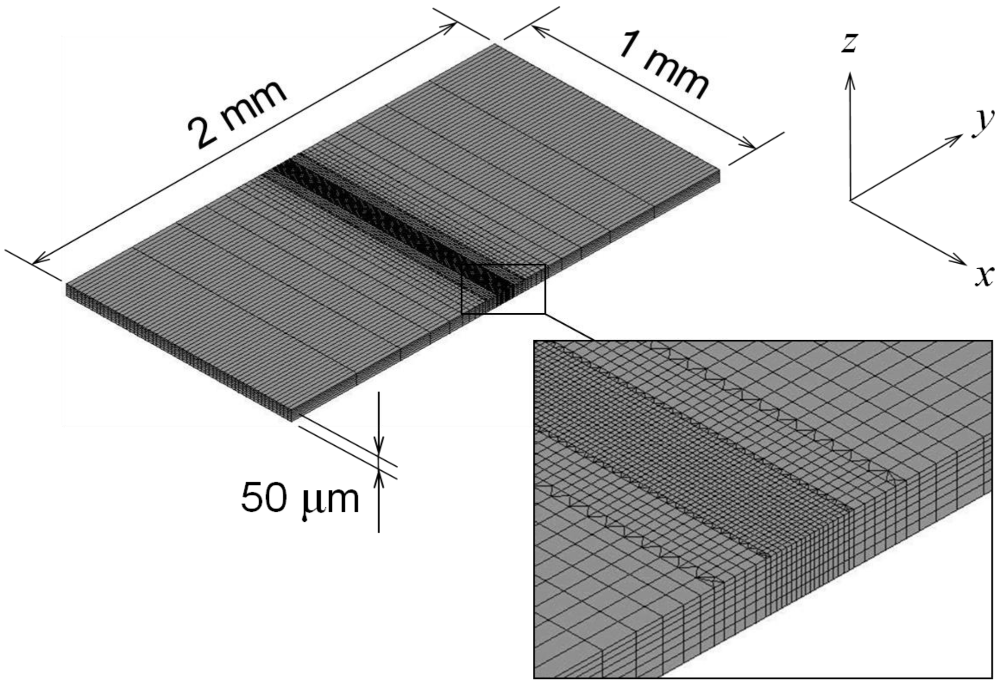

Figure 2.5 Meshes generated in finite element analysis

2.4.2 Heat input model

In order to simulate the weld line during laser seam welding, it was necessary to develop the proper heat input model to describe the weld bead shape. In the case of laser welding, the energy is absorbed by the base material and converted into heat, and it was simulated by the heat flux. For the heat input model, when P (W) is the laser power and η is the absorption rate of the material, then the effective output laser power Q_e (W) can be expressed as equation (2.24).

$$Q_\mathrm{e} = \eta \times P \tag{2.24}$$

The absorption rate has been related to the material resistivity and the wavelength of the laser irradiation, and it was calculated from Bramson's formula as in equation (2.25).[2.3), 2.18)]

$$\eta = 0.365 \cdot \left(\frac{R}{\lambda}\right)^{1/2} - 0.0667 \cdot \left(\frac{R}{\lambda}\right) + 0.006 \cdot \left(\frac{R}{\lambda}\right)^{3/2} \tag{2.25}$$

where λ (nm) is the wavelength, and R (μΩ·cm) is the electrical resistivity of the materials. The average electrical resistivity of stainless steel SUS304 is 80 μΩ·cm,[2.10), 2.22)] and the wavelength of fiber laser is 1090 nm. Substituting these values into equation (2.25), the absorption rate is obtained as 0.27. In addition, the reported value of absorption rate by Katayama[2.23)] indicated the absorption rate of Nd:YAG laser (λ=1064 nm) is 0.25 for the SUS304 without coating. While, the absorption rate increases to 0.60 for SUS304 with carbon coating on the specimen surface.

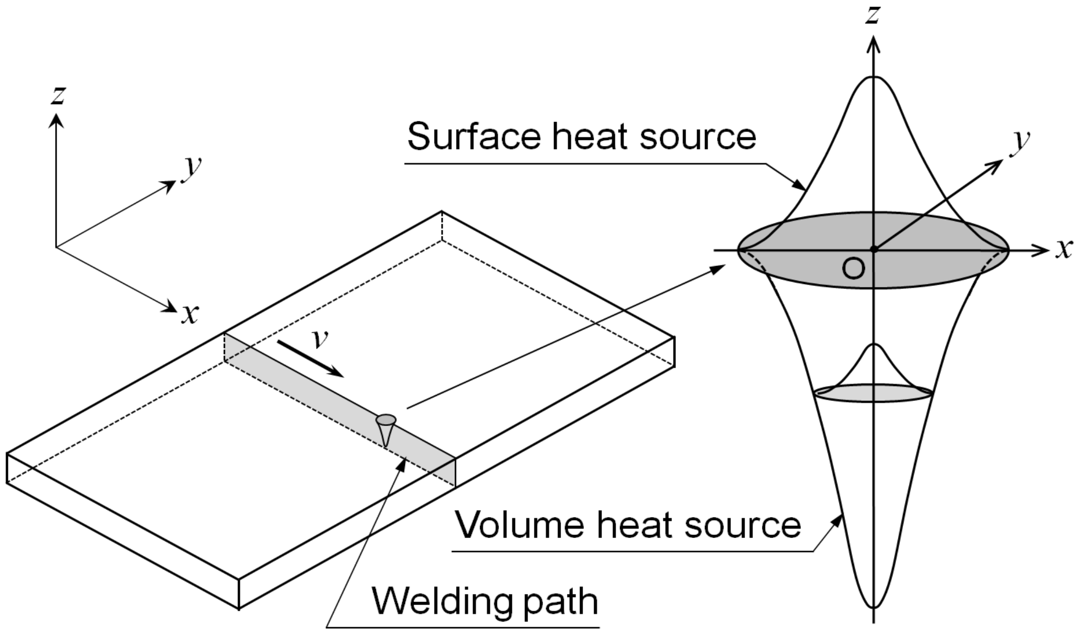

Figure 2.6 Heat input model in finite element analysis

A Gaussian representation of the laser beam by assuming the heat input only on the top surface of the material might not lead to correct results, especially for high power density that rapidly penetrate through some distance into the material thickness and resulting in the high depth-to-width ratio and the small HAZ. It has been reported by experiments that the heat flux distribution need to be conical.[2.9)] In this study, the total heat input is computed from the summation of surface heat source on the top surface and volume heat source along the thickness direction as shown in **Figure 2.6**. The heat power absorbed on the surface of the specimen, P_s (W) is 25 %, and the remaining 75 % is absorbed by the keyhole wall, P_v (W).[2.24), 2.25)] The surface heat flux Q_s (W/m^2) is applied in Gaussian distribution, and it can be expressed as equation (2.26).[2.24), 2.26)]

$$Q_s = \frac{3P_s}{\pi r_d^2} \exp\left(-3\frac{r^2}{r_d^2}\right) \tag{2.26}$$

where r (μm) is the radial distance from the laser beam center and r_d (μm) is the characteristics radius (defined as the radius at which the intensity of the laser beam falls to 5 % of the maximum intensity).

The three-dimensional conical Gaussian heat source model is adopted to calculate volumetric heat flux Q_v (W/m^3) as the heat input around the molten pool, and it can be written as equation (2.27).[2.24), 2.27)]

$$Q_v = \frac{3P_v}{\pi r_0^2 h_d} \exp\left(-3\frac{r_c^2}{r_0^2}\right) \cdot \left(1 - \frac{z_i}{h_d}\right) \tag{2.27}$$

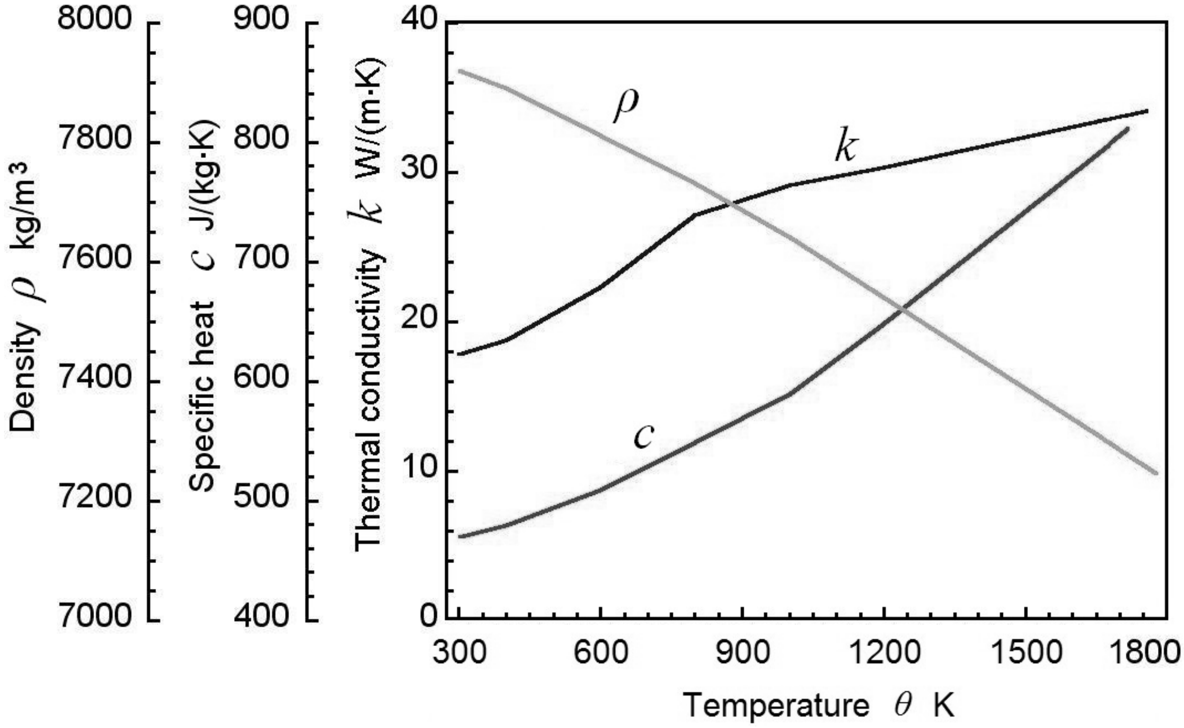

Figure 2.7 Thermophysical properties of austenitic stainless steel SUS304

where r_0 (μm) is the initial radius (at the top of the keyhole), h_d (μm) is the depth, r_c (μm) is the current radius, i.e. the distance from the cone axis, and z_i (μm) is the current depth. The total heat input Q to the analysis model is computed from the summation of surface and volume heat source models, and it can be expressed as equation (2.28).

$$Q = Q_s + Q_v \tag{2.28}$$

2.4.3 Material model

The temperature-dependent material properties are important for the accurate calculation of a temperature field. As can be seen from equation (2.19), the temperature response in a material involved in high heat fluxes is determined by the thermal material properties of thermal conductivity, specific heat and density, which are dependent on temperatures. Therefore, temperature-dependent thermal properties of austenitic stainless steel SUS304 are used in the finite element model. These properties are assumed to be isotropic and homogeneous and are taken according to the Sabbaghzadeh et al.[2.28] The thermal material properties are shown in **Figure 2.7**, which were taken from the literatures.[2.23), 2.29)]

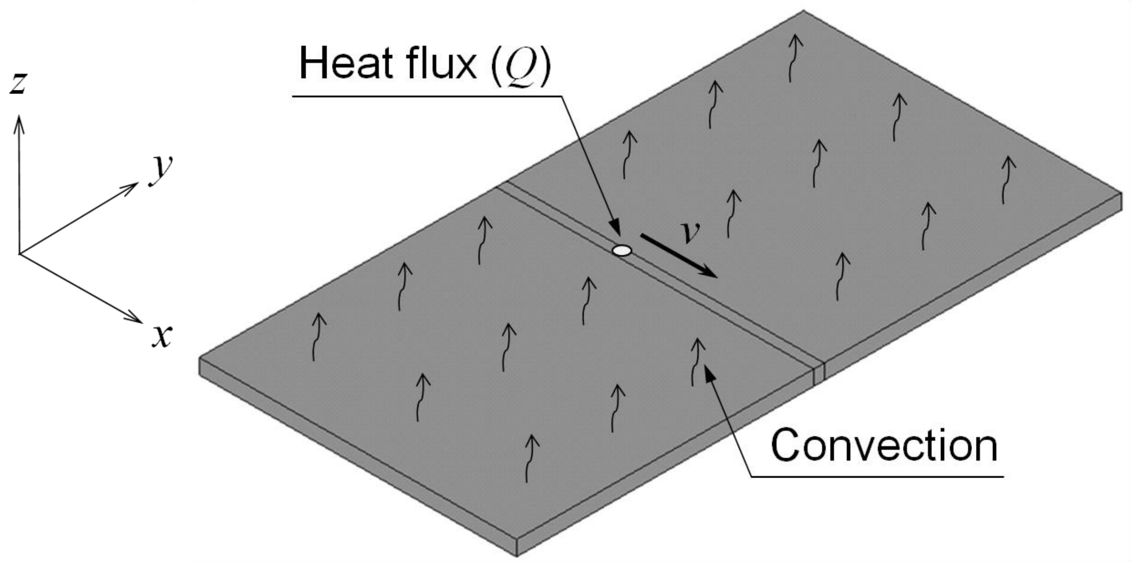

Figure 2.8 Thermal boundary condition in finite element analysis

2.4.4 Boundary conditions model

A specimen is surrounded by air or shielding gas at room temperature. Therefore, the initial condition for the entire region was a room temperature $(\theta_0 = \theta_\infty = 293\,\mathrm{K})$. In laser welding, the heat exchange between the welded specimen and its surroundings during welding and subsequently cooling period takes by the convection as shown in **Figure 2.8**. The boundary conditions of the heat transfer equation (2.9) are assumed as the heat flux generated by the laser beam is only applied on the top surface of the specimen and is defined by equation (2.26). While, on the non-irradiated top surface, the heat flux is assumed to be only the convective heat flux q_c (equation (2.10)), where the convective heat transfer coefficient h_c is 10 W/(m^2·K). Furthermore, since a small portion was selected on the middle of specimen (Section 2.4.1), the boundary condition at x-z and y-z planes of the specimens were considered as adiabatic condition, i.e. $-k\nabla\theta = 0$.

2.4.5 Solution scheme

A three-dimensional finite element model was performed using ANSYS finite element software, which provides a convenient means of numerical modeling in laser welding processes. The solution technique is depending on the type of problem. In the present case, since the thermal history of a weld bead is required, a transient thermal analysis must be performed. This requires an integration of the heat conduction with the respect to the time. In the finite element formulation, this equation can be written for each element as equation (2.20). This equation is simply the vector and matrix equivalent of equation (2.9).[2.30] The difference between any two time points is known as the integration time. If it is necessary, the time step can be varied during the transient. The program's automatic time-stepping feature can be employed to automatically increase or decrease the

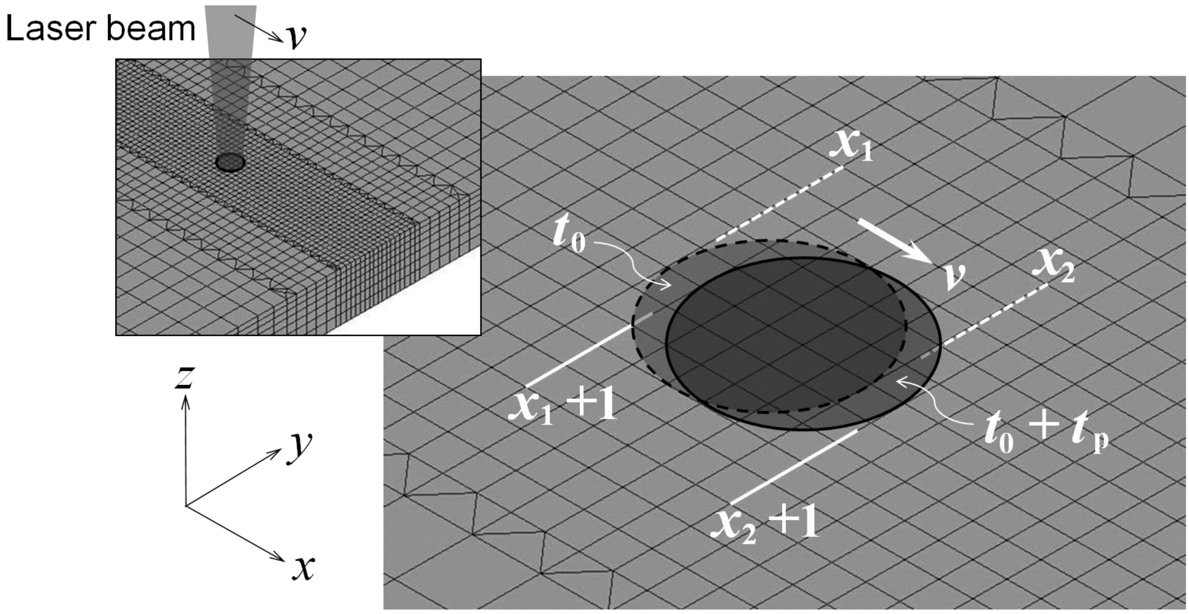

Figure 2.9 Movement of laser irradiation

integration time step based upon response conditions.

The first iteration in the solution procedure solves the system equations at an assumed starting temperature, and subsequent iterations use temperatures from the previous iterations to calculate the thermal conductivity matrix. The iterative process continues until a converged solution is achieved. Convergence checking can be based on the out-of-balance heat flux vector and/or the temperature increment from one iteration to the next. The number of iterations necessary for an accurate solution depends upon the non-linearity of the problem. The solution data are in the form of nodal temperatures and heat flux. These data may be used in the post-processing phase to produce displays of temperature contours (isotherms). Other post-processing options may be used to extract more specific information, such as the thermal gradient and thermal flux at nodes and element centroids. This information can be displayed either graphically or in tabular form.

In the present simulation, the heat fluxes obtained from equations (2.26) and (2.27) are used as a surface heat flux and internal heat flux, respectively. The heat fluxes are imposed on the selected set of element. For calculation of moving heat flux, the position and magnitude of heat flux are confirmed every time firstly. The distributed heat flux moves with the time. When the distributed heat flux moves to the next step, the former distributed heat flux step is deleted. In the present case, a moving laser beam heat source with small steps is adopted in order to simulate its continuous scanning as shown in **Figure 2.9**. When t=t_0, the laser beam converges in the elements between x_1 and x_2, and when t= t_0+t_p, it moves to x_1+1~x_2+1 elements. The retention time t_p (s) at every element can be expressed as equation (2.29).

$$t_{\mathrm{p}} = \frac{\Delta x}{v} = 1\,\mathrm{step} \tag{2.29}$$

where Δx is the size of an element in the x-direction, and v (m/s) is the scanning velocity. Obviously, if Δx is sufficiently small, the moving laser beam will have sufficient precision. An ANSYS Parametric Design Language (APDL) was used to model the moving heat source. In this study, six process conditions with various laser powers, scanning velocities and spot diameters under a constant energy density of 114.29 J/cm^2 are investigated as shown in **Table 2.1**. The model is the validated by comparing the experimental results with established numerical simulation results.

Table 2.1 Laser parameters in FEM thermal analysis

Case			1	2	3	4	5	6
Laser power	P	W	20	30	40	20	40	60
Scanning velocity	v	m/s	1.0	1.5	2.0	0.5	1.0	1.5
Spot diameter	d	μm	17.5	17.5	17.5	35.0	35.0	35.0

2.5 Equipments

2.5.1 Single-mode CW fiber laser

Figure 2.10(a) shows the CW laser source of single-mode Yb (Ytterbium) fiber laser manufactured by SPI Laser (Model: SP-100C) used in this study. The laser source unit comprises semiconductor pump laser diodes, a fiber laser module, electrical component drivers, a thermal management and an optical fiber delivery cable with a collimated output beam. The system status and the output power level can be monitored and controlled by external RS232 and I/O analog interface.

The fiber laser emitting at 1090 nm wavelength and operating in TEM_{00} mode or Gaussian mode as shown in **Figure 2.10(b)**. It has an excellent beam quality ($M^2 \leq 1.1$), which can allows the use of long focal lenses. The capabilities to produce high brightness and high power densities, make it suitable for micro-processing applications and sufficient for the welding thin metals. The laser output power (~100 W) stability also leads to a stable welding process.

The CW fiber laser can be modulated and provide pulsing capabilities with pulse widths ranging from 50 μs to 250 ms. The ability to modulate the pulse frequency and the pulse width provide a significant improvement in the controllability of the weld. In addition, since the fiber laser is not equipped with the flashlamp, it offers a lower maintenance cost. The main specifications of laser source are listed in **Table 2.2**.

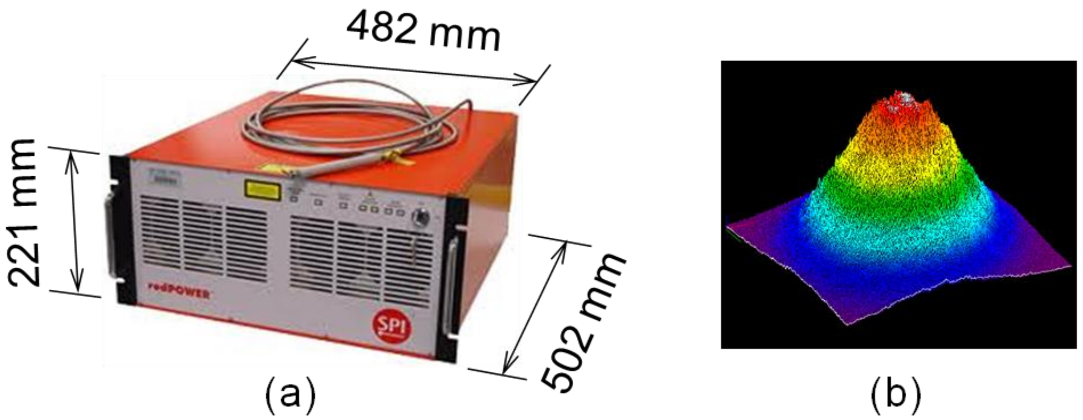

Figure 2.10 Photographs of (a) single-mode fiber laser and (b) intensity distribution of formed laser beam

Table 2.2 Specifications of single-mode fiber laser

Output power	100 W
Central emission wavelength	1090 nm
Emission bandwidth	3.2 nm
Beam diameter	5.4 mm
Beam divergence	0.28 mrad
M^2	1.1
Circularity	99 %
Eccentricity	± 0.3
Concentricity	± 0.1

2.5.2 Galvano scanner

The galvano scanner consists of scanner head with two movable mirrors and controller, which the movement configuration was programmed by the microcomputer. The microcomputer generates the commands and sequentially transferred the digital input data to the controller. The data was converted to an analog signal in the DA converter and fed to the drive control circuit. The circuit generates a drive signal of the scanner on the basis of the analog signal to drive the galvano scanner.

Figure 2.11 shows the optical components in galvano scanner. The laser beam was deflected by two motor-driven mirrors in the x and y directions. Then the laser beam focused on the specimen by a telecentric type $f\theta$ lens of 100 mm in focal length. The telecentric type $f\theta$ lens keeps the laser beam focus in a flat plane and controls the incident laser beam perpendicular to the scan area. The scanner has high scanning speed up to 10 m/s with a high accuracy of position repeatability in the scanning area of 60 x 60 mm^2.

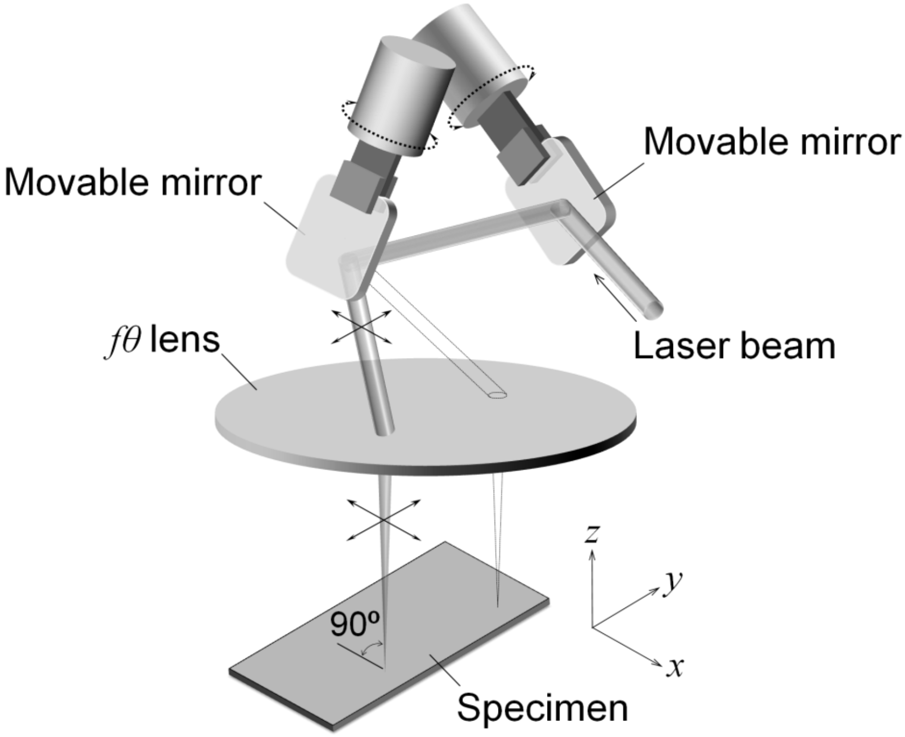

Figure 2.11 Schematic diagram of optical components in galvano scanner

2.6 Experimental work

The austenitic stainless steel SUS304 was used as a specimen. The chemical composition of the specimen material is shown in **Table 2.3**. The sizes of each specimen were 30 mm length, 15 mm width with thickness of 50 μm. A schematic diagram of experimental setup is shown in **Figure 2.12**. In this study, the wavelength of 1090 nm single-mode CW Yb fiber laser was used. The laser was delivered by optical fiber and focused by a telecentric type $f\theta$ lens of 100 mm in focal length. The laser scanning was carried out by a Galvano scanner to achieve the high-speed beam scanning. The expander was installed between the isolator and the bending mirror to change the diameter of laser beam. In addition, the experiments with bead-on-plate welding were carried out in shielding gas of nitrogen under a constant pressure 100 kPa.

The clamping plate with an opening slot of 2 mm was set to ensure the straighten of specimen sheets. The groove was prepared under the specimen to keep the non-contact space between the specimen and the clamping plate. In addition, the alumina-ceramic plates of 1 mm thickness were located between specimen and clamping plate to minimize the heat loss during welding experiments. After the laser welding, the welded specimens were cut perpendicular to the scanning direction for the observation of weld bead by optical microscope. All the specimens were ground and polished. Etching was performed using a solution containing 4 ml HNO_3, 16 ml HCl, 12 ml $C_6H_3N_3O_7$ (5%) and 10 ml distilled water for 3 seconds.

Table 2.3 Chemical compositions of austenitic stainless steel SUS304 (wt. %)

C	Si	Mn	P	S	Ni	Cr	Fe
<0.08	1.0	2.0	<0.045	<0.03	8.0–10.5	18–20	Bal.

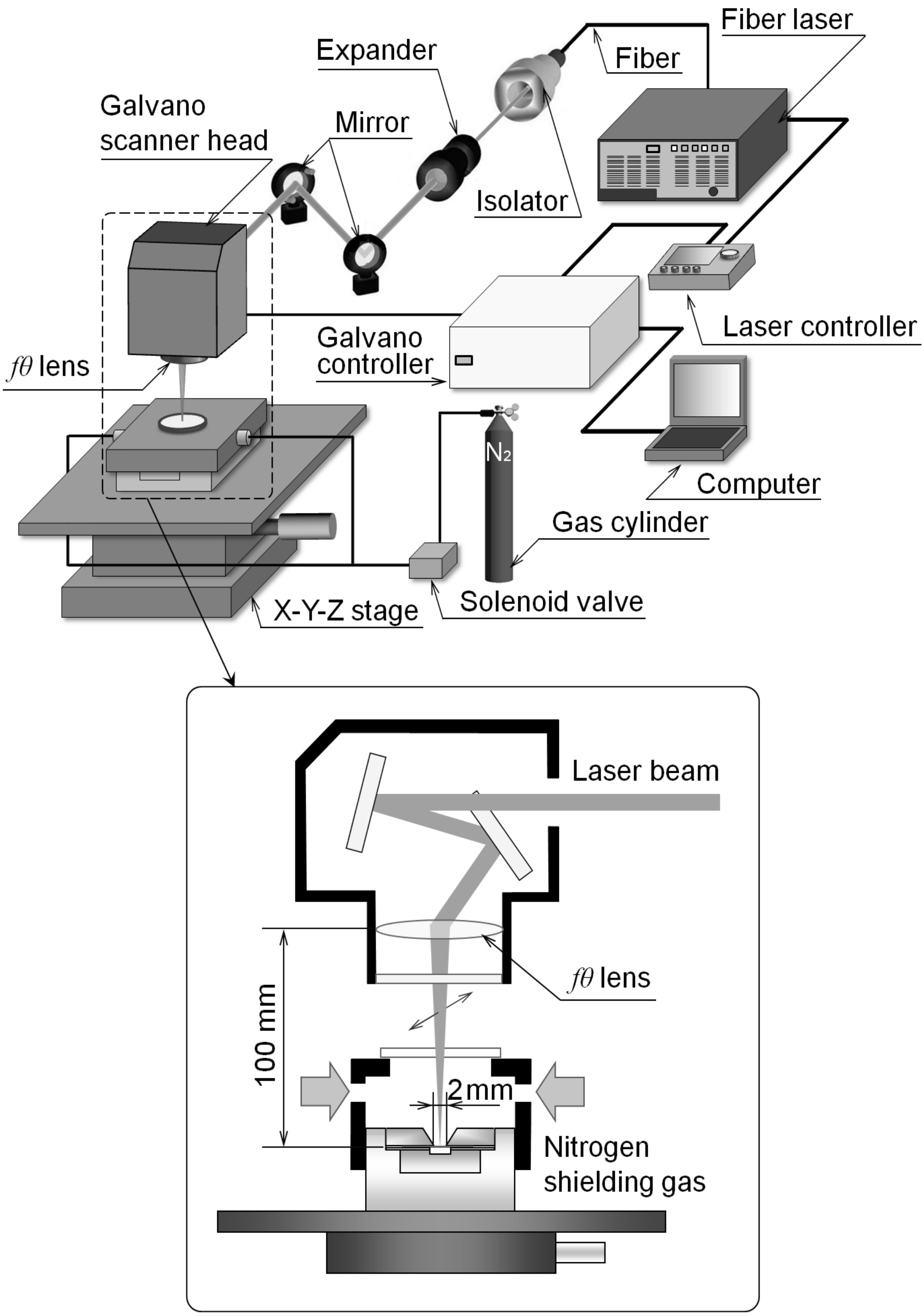

Figure 2.12 Schematic diagram of experimental setup

2.7 Results and discussion

Figure 2.13 shows the temperature field at the top surface of the specimen along the weld direction (x-axis) for the 40 W laser power, 2.0 m/s scanning velocity and 17.5 μm spot diameter. The laser beam location is 550 μm from the specimen edge (x=0) and it is irradiated on the specimen at 0.3 ms after the beginning of laser irradiation. It can be seen that the laser irradiation pre-heats a very small area in the front of the laser beam where the heat source is going to pass with the temperature of approximately 600 K. It is clear that the temperature at the top surface rapidly increases during heating by the laser. The temperature dropped rapidly with the increase of distance to the center of the weld. As the laser beam moves along the weld line, the temperature is around 6700 K at the center of the weld, while the temperature at the adjacent point is 1500 K at the same instance.

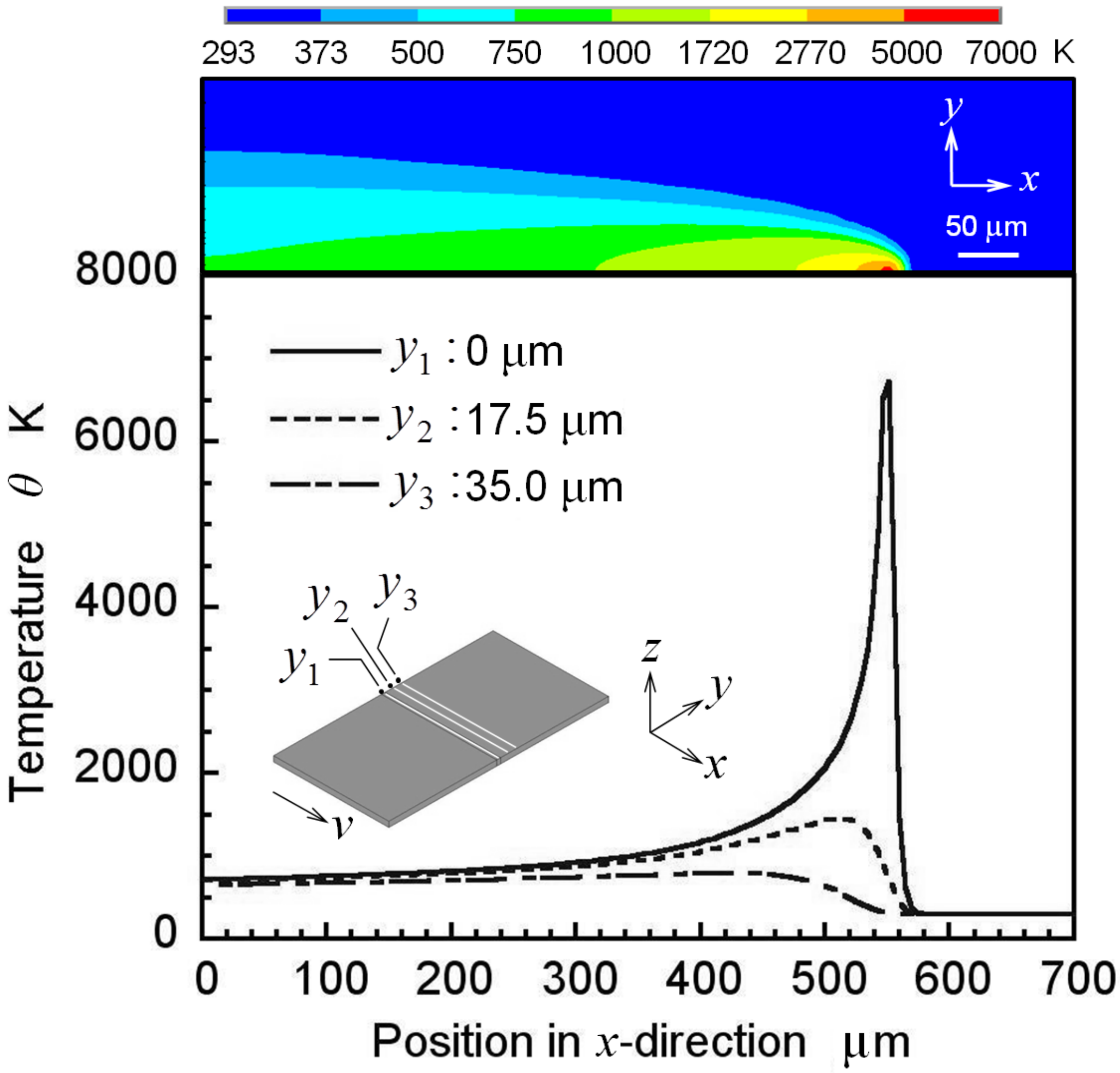

Figure 2.13 Temperature field at the top surface along the weld direction (x-axis) at t: 0.3 ms (d: 17.5 μm, P: 40 W, v: 2.0 m/s)

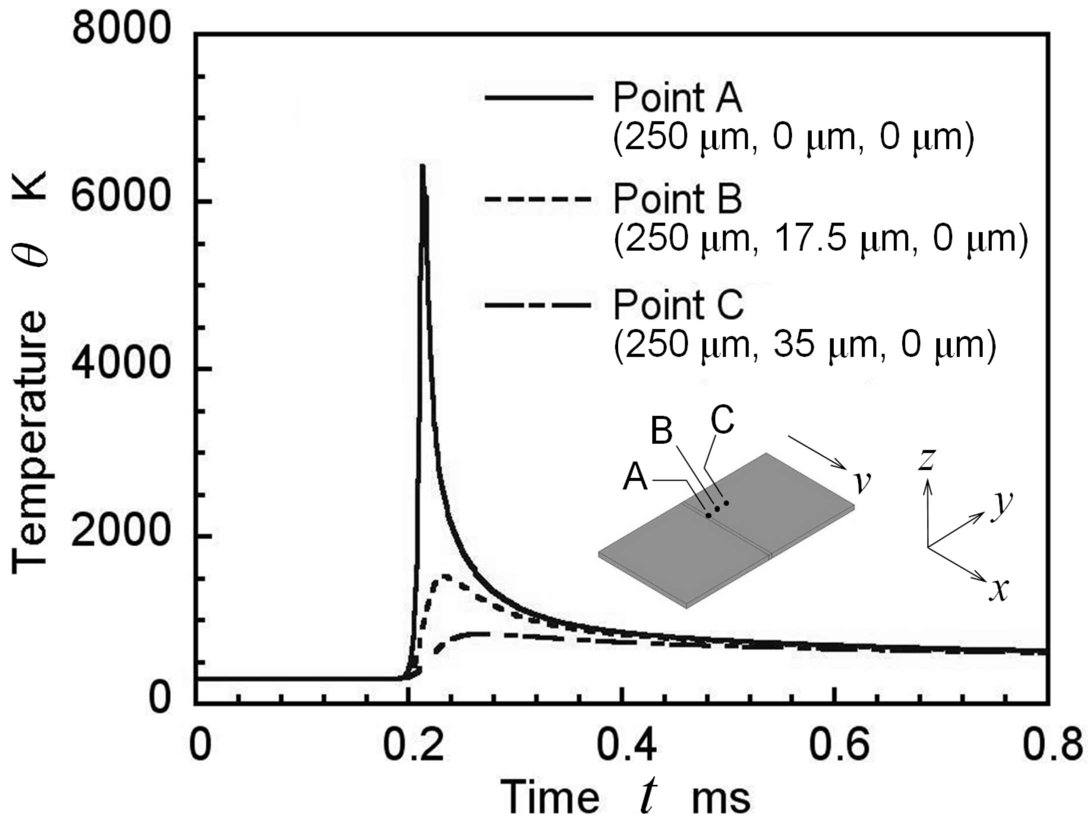

Figure 2.14 Temperature histories of the three evaluated points transverse to the weld direction (d: 17.5 μm, P: 30 W, v: 1.5 m/s)

Because the surface temperature rapidly rises during the laser irradiation, while the cooling process is relatively due to the convection heat transfer. It can be observed a "tail" behind the laser beam due to the heat transfer during the cooling process.

Figure 2.14 shows the temperature histories for three points located transversally to the weld direction. The peak temperatures are at the "heel" of the center of the laser beam. In this period, the peak temperature remains constant and already in the quasi-steady state. For the same period, the velocity of the rising temperature decreases at the bottom surface as shown in **Figure 2.15**. Since the temperature at the top surface is much higher than that at the bottom surface, the larger temperature difference between the top and bottom surface leads to a high temperature gradient. This significant temperature difference through the specimen thickness can also affect the final deformation of the specimen.[2.30), 2.31)].

Figure 2.16 illustrates the temperature fields at six different time periods of 0.183 ms, 0.365 ms, 0.548 ms, 0.730 ms, 1.000 ms and 2.500 ms, respectively. It can be seen that the temperature field changes as the laser beam and the melt pool moves along with the laser beam. It shows that the temperature in the fusion zone is significantly higher when the laser beam just passes the plane and it decreases rapidly with time. In the middle of the specimen, the temperature field goes to balance or

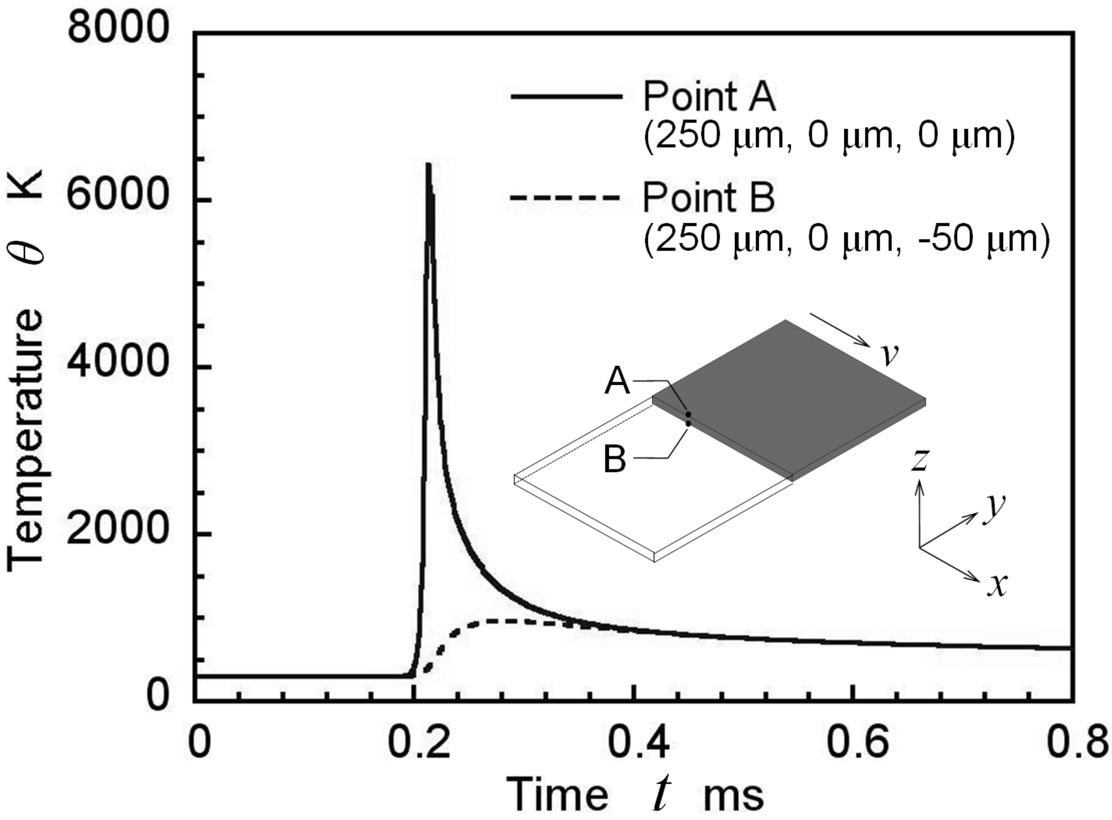

Figure 2.15 Temperature histories of the two evaluated points on the top and bottom surfaces (d: 17.5 μm, P: 30 W, v: 1.5 m/s)

quasi-steady state. It also shows the weld pool shape around the high-energy heat source presents elliptical shape. This elliptical shape of weld pool varies with the process parameters. The cooling phase that occurs after the heating phase as shown in **Figures 2.16(d)**, **2.16(e)** and **2.16(f)**. In this phase, the temperature decreases gradually with the time when the heat in the fusion zone is transferred through the heat conduction.

Figure 2.17 shows the temperature field contours for the melting temperature of SUS304 (1720 K), which defines the weld pool size and shape. It shows the weld pool becomes more elliptical shape for higher laser power and scanning velocity compared to that of lower laser power and scanning velocity. As can be seen from the figure, an increase of the laser power led to the deep penetration. This is because of the high power density distribution of the laser beam. This expansion of power density was also caused by an increase of the peak temperature, the heat input along the thickness and longer "heating tail". In addition, the weld pool shape of lower laser power and scanning velocity with larger spot diameter led to the circular shape of weld pool. The larger of spot diameter covers a wide area on the top surface of the specimen and a shallower weld pool of the laser weld was generated. This condition can be considered that conduction mode welding occurs, while the smaller spot diameter results in the keyhole mode welding. In the keyhole mode welding, the exit

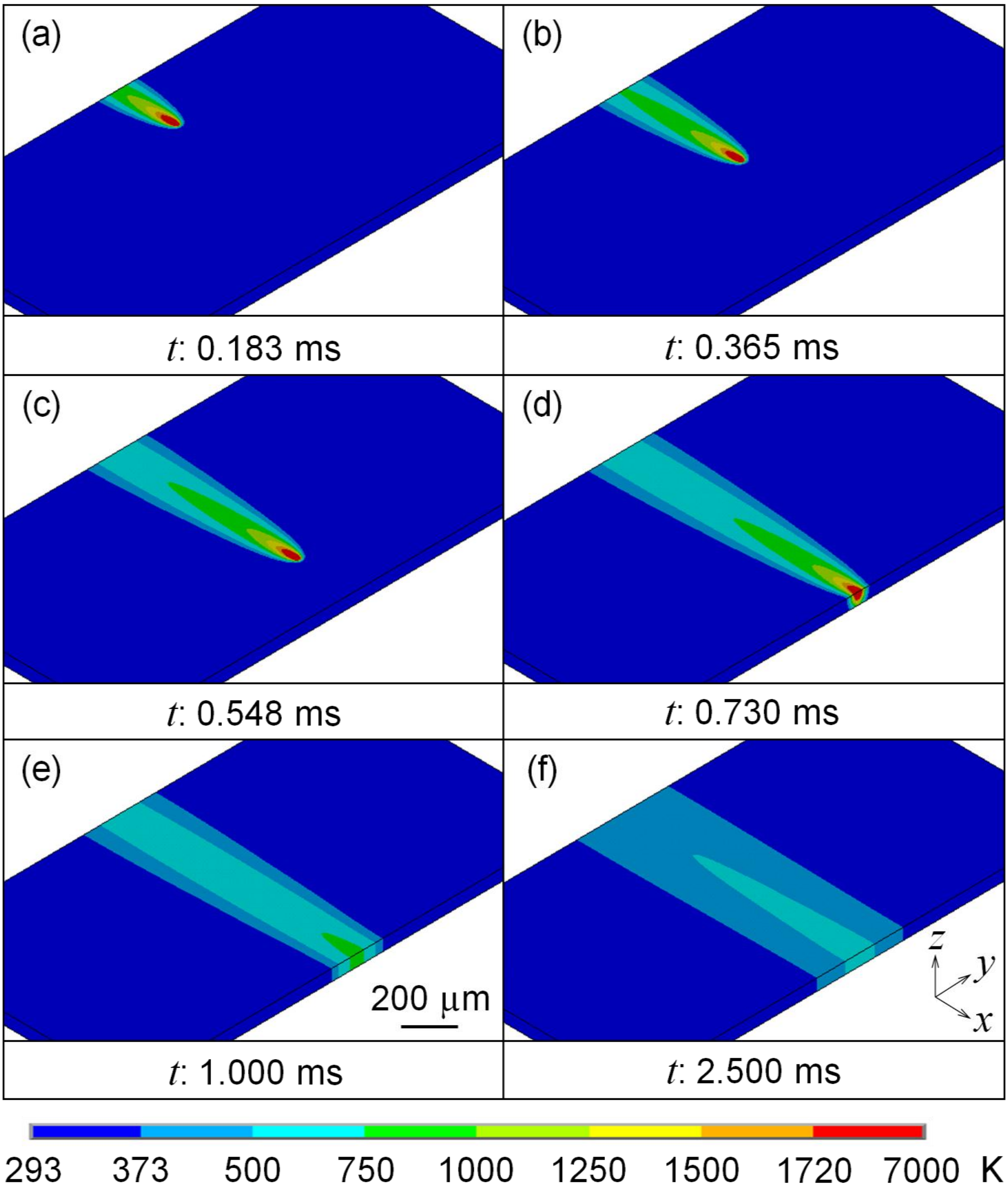

Figure 2.16 Temperature field during laser irradiation (a-c) and cooling (d-f) (*d*: 17.5 μm, *P*: 30 W, *v*: 1.5 m/s)

of keyhole at the top surface is larger than the lower exit, and the inclination angle of the front wall of keyhole is larger than the rear wall.

Figure 2.18 shows the temperature fields when the moving heat source passes the transverse plane at time t_0 and subsequent time steps. The red area represents the melted material in the weld pool, in which the temperature is higher than the melting point. It shows that the effect of the moving heat source on the temperature fields of the specimen with the time and the rapid heat transfer in the

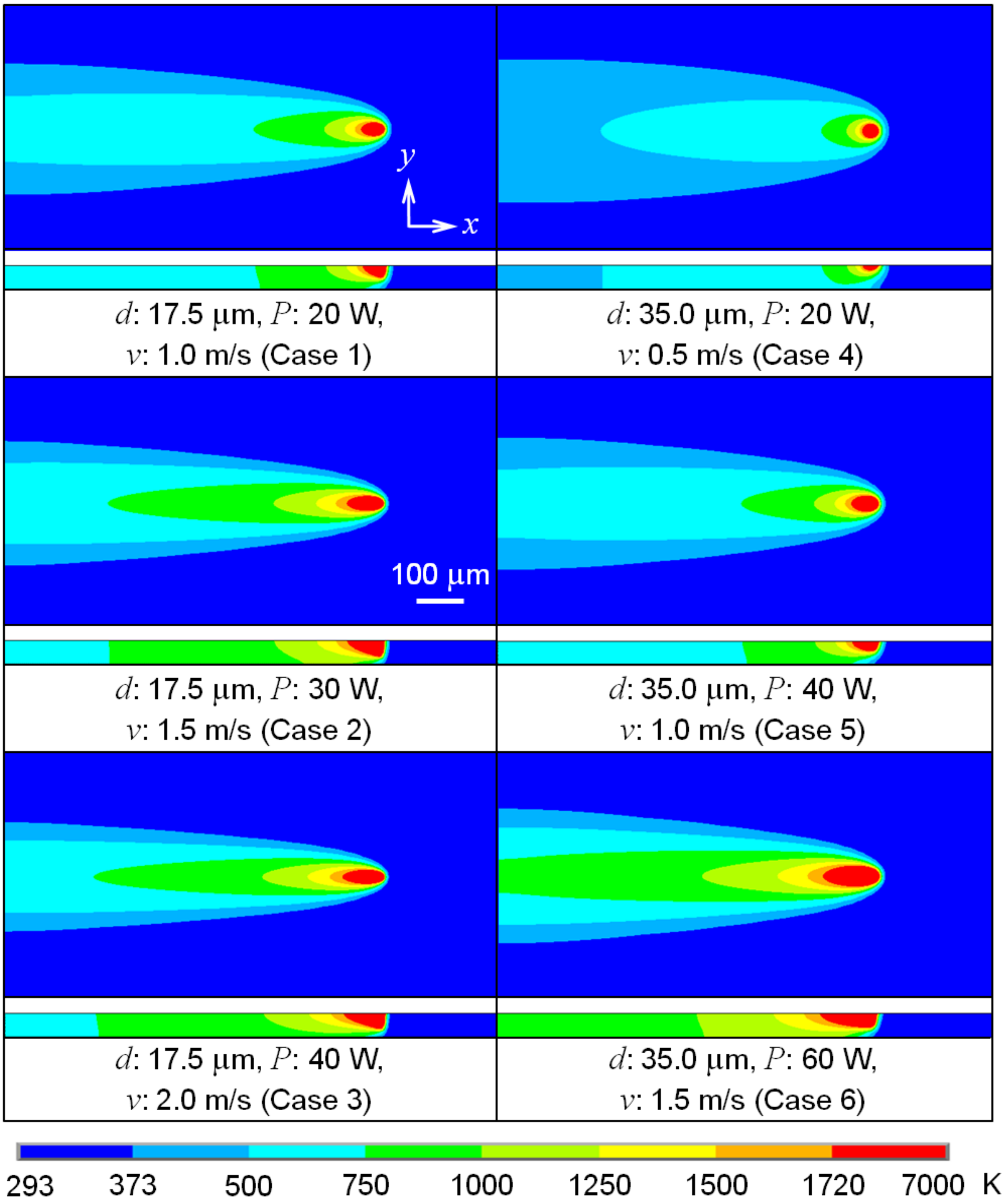

Figure 2.17 Temperature field contours for six welding conditions under a constant energy density

fusion zone. Heat input to the weld pool is transferred quickly in the thickness direction and then in the width direction to reach uniform distribution. Due to the rapid diffusion of the heat into the surrounding materials in the laser irradiation zone, the specimen temperature gradually decreases to the room temperature. It is also clear that the heat conduction plays an important role in the heat flow

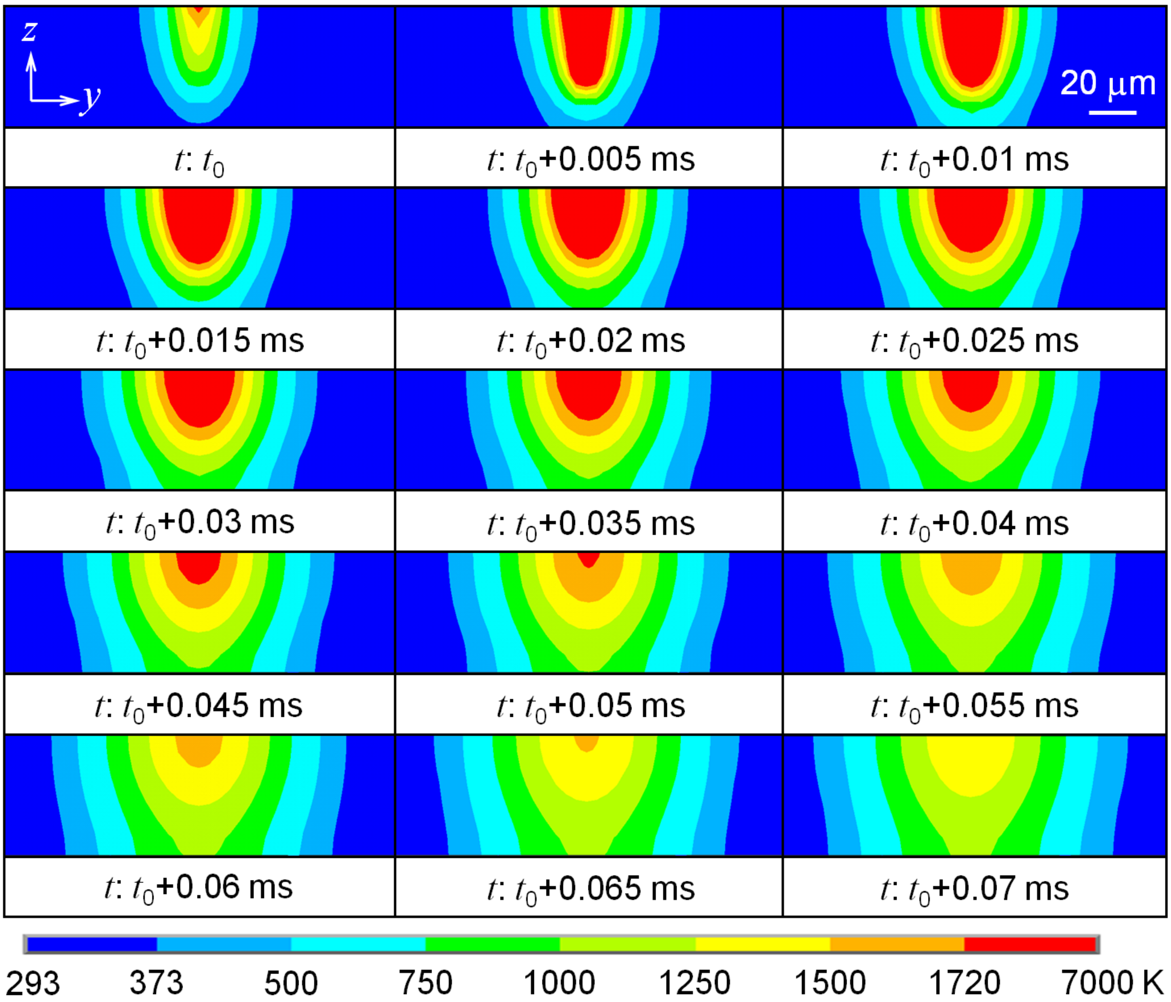

Figure 2.18 Temperature history of a reference plane (d: 17.5 μm, P: 30 W, v: 1.5 m/s)

and the surface convection.

In order to verify the simulation results, the weld bead profiles in the transverse direction obtained from experiments and the 1720 K isothermal contours from simulation were compared under the constant energy density of 114.29 J/cm^2 as shown in **Figure 2.19**. The simulation results give a good estimation of the weld bead cross-section, which gives an average error of 8 % in prediction. The fair agreement indicates validity of the numerical model. As can be seen, the different process parameters show the different weld bead profiles. It is expected that higher laser power leads to greater weld bead geometry with an increase of the power density. Both the experimental and the computed results show that the increase in the spot diameter leads to the wider and shallower weld bead geometry. This observation is consistent with distribution of energy density over a wider area in the spot diameter. Conversely, when the laser beam employs smaller spot diameter, the deeper penetration can be predicted even though in the higher scanning velocity. Since the thermal analysis was conducted under a constant energy density, the scanning velocity shows less

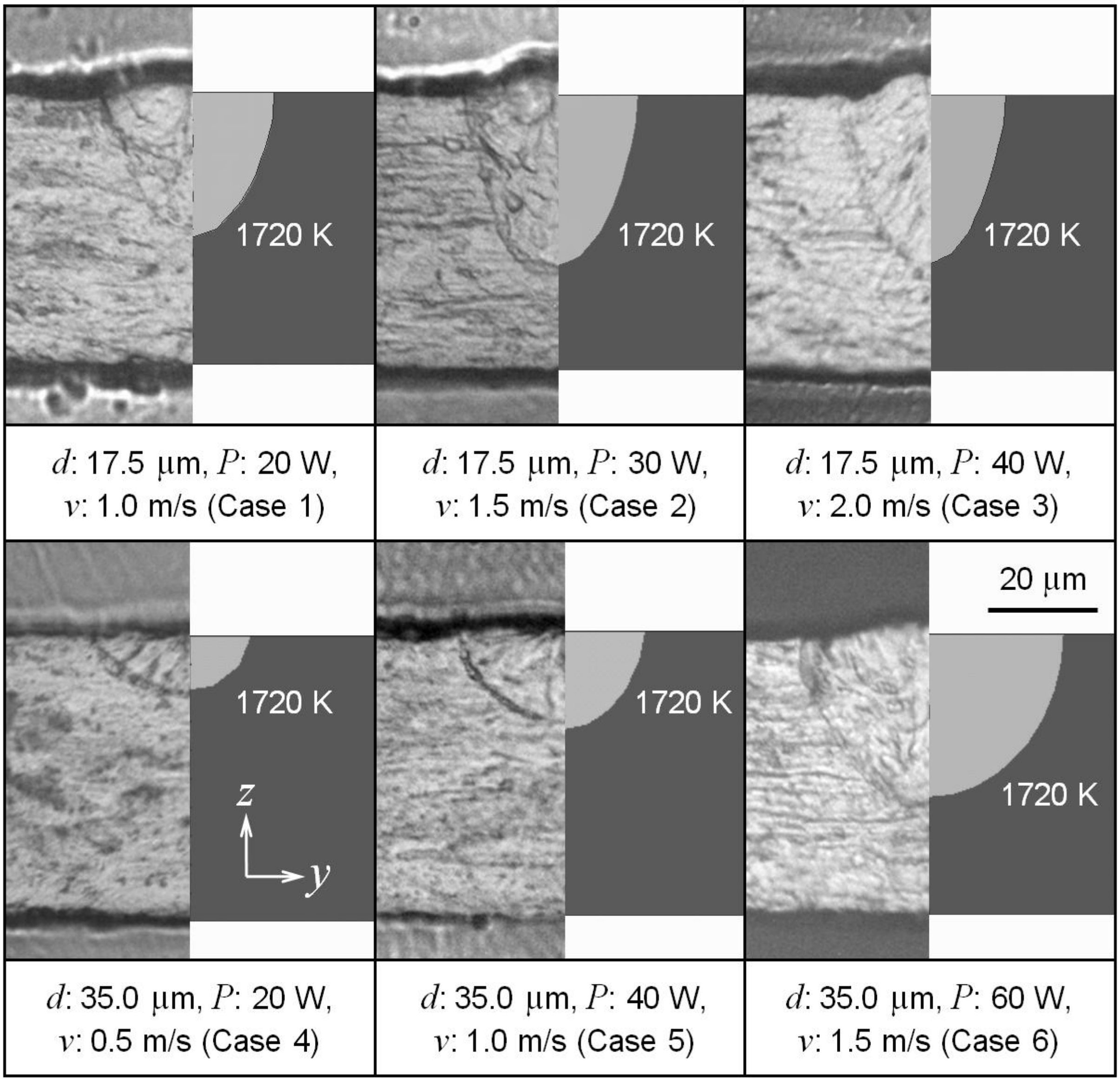

Figure 2.19 Comparison between experimental and simulated weld bead geometry

significant on the weld bead geometry compared to the laser power and spot diameter, which present the major effects on the weld bead geometry. However, it can be noticed that the depth-width ratio increases with increasing scanning velocity.

Solidification patterns of the weld top surface were also compared with the simulated isotherm of the welded zone as shown in **Figure 2.20**. The solidification pattern and melting isotherm are circular shape at lower power density (Case 4 and 5). On the other hand, the solidification pattern and melting isotherm are V-shaped tail and elliptical shape at the higher power, respectively. In addition, the shape of the melting isotherm is slightly curvature than the solidification pattern of actual weld.

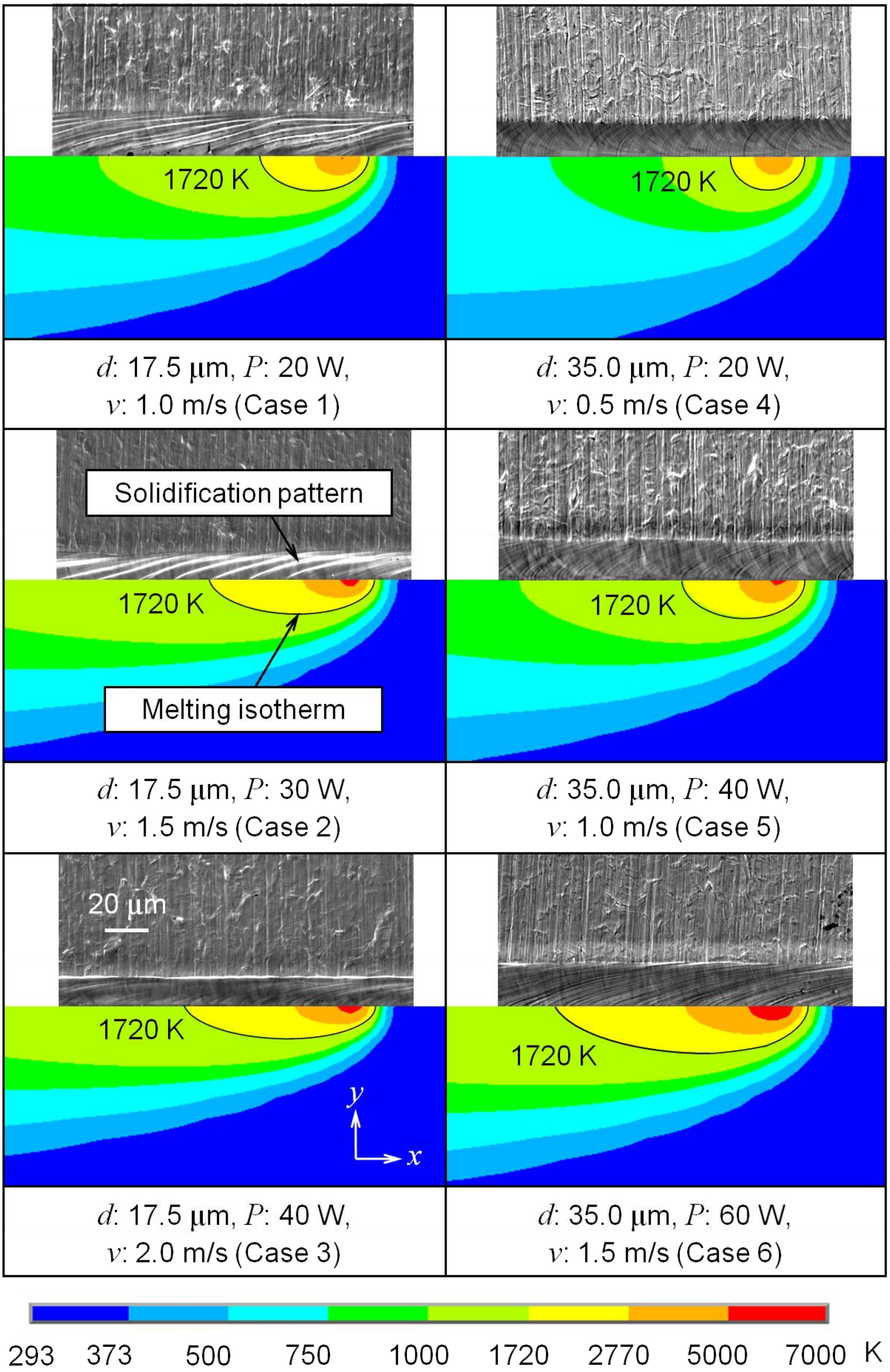

Figure 2.20 Comparison between experimental solidification pattern and simulated melting isotherm at the center of weld top surface

2.8 Conclusions

A three-dimensional finite element model has been developed to simulate the thermal history during laser micro-welding of thin steel sheet. Main conclusions obtained in this chapter are as follows:

(1) The developed numerical model using a combination of surface heat source and adaptive volumetric heat source can well represent the real welding as the heat source penetrates into the material.

(2) Laser power, scanning velocity and spot diameter have a significant effect on the temperature field, weld pool size and shape, and weld bead geometry.

(3) Heat input to the weld pool is transferred rapidly first in the thickness direction of the sheet and then in the width direction to reach uniformed distribution.

(4) The numerical model can well predict the weld bead geometry for various process parameters. The numerical results are in good agreement with the experimental measurements.

(5) Temperature fields obtained from the developed model can be used as inputs for the thermo-mechanical analysis of laser welding of thin steel sheet.

References

2.1) H. Schlueter : Laser Beam Welding – Benefits, Strategies and Applications, Welding Journal, (2007), Vol. 86, No. 5, 37-39.

2.2) S. Tsukamoto : Laser Welding, Welding International, (2003), Vol. 17, No. 10, 767-774.

2.3) K. Kazemi and J.A. Goldak : Numerical Simulation of Laser Full Penetration Welding, Computational Materials Science, (2009), Vol. 44, 841-849.

2.4) K. Abderrazak, S. Bannour, H. Mhiri, G. Lepalec and M. Autric : Numerical and Experimental Study of Molten Pool Formation During Continuous Laser Welding of AZ91 Magnesium Alloy, Computational Materials Science, (2009), Vol. 44, 858-866.

2.5) D. Rosenthal : Mathematical Theory of Heat Distribution During Welding and Cutting, Welding Journal, (1941), Vol. 20, 220-234.

2.6) W.M. Steen, J. Dowden, M. Davis and P. Kapadia : A Point and Line Source Model of Laser Keyhole Welding, Journal of Physics D (Applied Physics), (1998), Vol. 21, 1255-1260.

2.7) B. Binda, E. Capello and B. Previtali : A Semi-empirical Model of the Temperature Field in the AISI 304 Laser Welding, Journal of Materials Processing Technology, (2004), Vol. 155-156, 1235-1241.

2.8) J. Mazumder and W.M. Steen : Heat Transfer Model for CW Laser Material Processing, Journal of Applied Physics, (1980), Vol. 51, 941-947.

2.9) M.R. Frewin and D.A. Scott : Finite Element Model of Pulsed Laser Welding, Welding Journal, (1999), Vol. 78, 15s-22s.

2.10) X. He, P.W. Fuerschbach and T. DebRoy : Heat Transfer and Fluid Flow During Laser Spot Welding of 304 Stainless Steel, Journal of Physics D (Applied Physics), (2003), Vol. 36, 1388-1398.

2.11) S. Bag, A. Trivedi and A. De : Development of a Finite Element Based Heat Transfer Model for Conduction Mode Laser Spot Welding Process Using an Adaptive Volumetric Heat Source, International Journal of Thermal Sciences, (2009), Vol. 48, 1923-1931.

2.12) G. Buvanashekaran, N.S. Shanmugam, K. Sankaranarayanasamy and R. Sabarikanth : A Study of Laser Welding Modes with Varying Beam Energy Levels, Proceedings of the IMechE (Part C: Journal of Mechanical Engineering Science), (2009), Vol. 223, 1141-1156.

2.13) W. Sudnik, D. Radaj, S. Breitschwerdt and W. Erofeew : Numerical Simulation of Weld Pool Geometry in Laser Beam Welding, Journal of Physics D (Applied Physics), (1996), Vol. 33, 662-671.

2.14) X. He, J.T. Norris, P.W. Fuerschbach and T. DebRoy : Liquid Metal Expulsion During Laser Spot Welding of 304 Stainless Steel, Journal of Physics D (Applied Physics), (2006), Vol. 39, 525-534.

2.15) L. Zhang, J. Zhang and H. Murakawa : An Analysis of the Role Side Assisting Gas During CO_2 Laser Welding, Transactions of JWRI, (2006), Vol. 35, No. 1, 89-94.

2.16) M. Medale, C. Xhaard and R. Fabbro : A Thermo-hydraulic Numerical Model to Study Spot Laser Welding, C.R. Mecanique, (2007), Vol.335, 280-286.

2.17) G. Tani, L. Tomesani, G. Campana and A. Fortunato : Evaluation of Molten Pool Geometry with Induced Plasma Plume Absorption in Laser-material Interaction Zone, International Journal of Machine Tools & Manufacture, (2007), Vol. 47, 971-977.

2.18) R. Rai and T. DebRoy : Tailoring Weld Geometry During Keyhole Mode Laser Welding Using A Genetic Algorithm and a Heat Transfer Model, Journal of Physics D (Applied Physics), (2006), Vol. 39, 1257-1266.

2.19) F.P. Incropera and D.P. DeWitt, Fundamentals of Heat and Mass Transfer (Fourth Edition), John Wiley & Sons, (1996), 52-55.

2.20) D.B. Marghitu : Mechanical Engineer’s Handbook, Academic Press, (2001), 451.

2.21) Y.C. Hsiao : Finite Element Analysis of Laser Forming, Master Dissertation, Massachusetts Institute of Technology, (1997), 105-106.

2.22) JSSA : Stainless Steel Databook, The Nikkan Kogyo Shimbun (in Japanese), (2002), 44.

2.23) T. Katayama : Three-dimensional Thermal Elastic-plastic Analysis of Laser Forming Process by Finite Element Method, Master Dissertation, Chubu University (in Japanese), (1998), 29-31, 34.

2.24) H. Du, L. Hu, J. Liu and X. Hu : A Study on the Metal Flow in Full Penetration Laser Beam Welding for Titanium Alloy, Computational Materials Science, (2004), Vol. 29, 419-427.

2.25) N.S. Shanmugam, G. Buvanashekaran, K. Sankaranarayanasamy and K. Manonmani : Some Studies on Temperature Profiles in AISI 304 Stainless Steel Sheet During Laser Beam Welding Using FE Simulation, International Journal of Advanced Manufacturing Technology, (2009), Vol. 43, 78-94.

2.26) T. Mahmood, A. Mian, M.R. Amin, G. Auner, R. Witte, H. Herfurth and G. Newaz : Finite Element Modeling of Transmission Laser Microjoining Process, Journal of Materials Processing Technology, (2007), Vol. 186, 37-44.

2.27) S.A. Tsirkas, P. Papanikos and Th. Kermanidis : Numerical Simulation of the Laser Welding Process in Butt-joint Specimens, Journal of Materials Processing Technology, (2003), Vol. 134, 56-69.

2.28) J. Sabbaghzadeh, M. Azizi and M.J. Torkamany : Numerical and Experimental Investigation of Seam Welding with a Pulsed Laser, Optics & Laser Technology, (2008), Vol. 40, 289-296.

2.29) JSTP : Thermophysical Properties Handbook, Japan Society of Thermophysical Properties (in

Japanese), (2001), 213.

2.30) W.M. Steen : Laser Material Processing (Third Edition), Springer-Verlag, (2003), 302.

2.31) E. Kannatey-Asibu : Principles of Laser Materials Processing, John Wiley & Sons, Inc., (2009), 619-620.

Chapter 3:
Thermal Deformation in Laser Micro-welding

3.1 Introduction

Laser micro-welding has become a significant industrial process because there are many outstanding advantages over the conventional welding process. One of the greatest challenges in laser micro-welding process is to create a reliable and accurate joint. During the process, the rapid cooling and the associated material shrinkage of the weld zone often causes a thermal distortion. For a precision welding, the thermal deformation is very important factor, and it is essential to understand the distortion caused by laser micro-welding process. Correcting unacceptable weld distortion of thin sheet is extremely costly and impossible in some cases.[3.1)]

Welding deformation has negative effects on the accuracy of assembly, external appearance in final product quality and mechanical properties of the weld joint.[3.2), 3.3)] It can not be ignored especially for precision welding in thin sheet, where the accuracy is required. As the welding stresses have a strong influence on weld deformation, the evaluation of welding stresses have become imperative. The knowledge of stress distributions and deformations may lead to better control over undesirable aspects of the machining process, which includes the dimensional inaccuracies and distorted shapes. However, the measurement of thermal stresses associated to a weld joint is complicated and practically limited by either cost or accuracy.[3.2), 3.4), 3.5)] With modern computing technologies, the numerical simulation has proven to be a effective tool and offers a comprehensive solution in predicting the welding induced stresses and deformations. Therefore, numerical simulations based on finite element method (FEM) had been used to solve this problem.

In this chapter, the thermal deformation of thin stainless steel sheet in laser micro-welding was investigated through numerical simulation. The simulation consists of two analyses, which are thermal analysis and structural analysis. To simplify the simulation procedure, uncoupled numerical simulations have been used. The temperature fields were computed during the thermal analysis and subsequently, these temperature fields were used in the structural analysis to calculate the stress and strain fields. In order to validate the numerical model, the welding deformation in laser micro-welding is experimentally investigated using a single-mode CW fiber laser with a high-speed scanning system on the bead-on-plate welding condition. The weld deformation is measured at different laser power, scanning velocity and spot diameter. The computational results are compared with the experimental measurements, and the stress and strain distributions, that is essential to predict the weld deformation were analyzed.

3.2 Brief review of literature

The general understanding in welding is appropriately characterized as a thermo-mechanical process involving complex multi-physics.[3.6)] An extensive review on laser welding and related processes were carried out by Mackwood and Crafer.[3.7)] The main emphasis of this review is on thermal modeling of laser welding, and there a lack of review in thermo-mechanical analysis. A number of analytical models have been used to evaluate stress distribution during the welding process and predict the residual stresses and deformations.[3.8), 3.9)] However, the analytical method is often become complicated and the stochastic processes are not well described by this method.

Numerical simulation on the welding process has been a major topic in welding research. The results of simulations can be used to explain complex phenomenon in the welding process and process optimization. In the past decades, many numerical analyses had been conducted for predicting welding deformation. Liang et al.[3.10)] and Deng and Murakawa[3.11)] have employed a three-dimensional FEM using iterative substructure method (ISM) in a long welded joint. Schenk et al.[3.12)] studied the influence of clamping on welding deformation using FEM. They found that the residual stresses and deformations depend strongly on the clamping conditions. However, these advances are mostly associated with conventional arc welding. Similar numerical models for laser forming have been developed.[3.13)–3.15)] Namba and Katayama[3.13)] carried out to explore the thermal stresses generated during laser forming process using three-dimensional thermal elastic-plastic analysis. They reported that the thermal expansion and contraction occurred during the laser forming.

Prediction of welding stresses and deformations induced by laser welding is extremely difficult. There is very limited numerical data of the welding deformation in laser welding. Many numerical models were developed for laser welding in thick materials,[3.16)–3.18)] and little attention has been made to welding stresses in laser micro-welding. In general, the three-dimensional thermal elastic-plastic analysis could be uncoupled into a thermal transient analysis and a elastic-plastic structural analysis.[3.19)] Spina et al.[3.16)] attempted to predict deformations in 3 mm aluminum alloy plate and suggested that an accurate thermal analysis is required to predict welding deformations in structural analysis. Moraitis and Labeas[3.17), 3.18)] focussed on the thermo-mechanical numerical model , which is based on the keyhole theory to simulate the stress, strain and deformation fields.

In the laser micro-welding, the influencing factors on the prediction of stresses and deformation have not been extensively studied. Prediction welding deformation is great significance at the early stage of product design and process development, and to extend the industrial applications of laser micro-welding. The present work is required in terms of conducting finite element simulation for understanding the combined effect of laser parameters on stress, strain and welding deformation in thin metal sheet.

3.3 Welding stresses and deformations

Laser welding process joins the materials using the local heating and cooling. This process causes a non-uniform temperature distribution, which is a major source of thermal stresses. The deformations are generated by the thermal stresses and continued with the residual stresses. This section discussed the thermal stress during welding and the causes of residual stress and deformation in weldments.

3.3.1 Thermal stresses in welding

The changes in temperatures and stresses during welding process have been reported by Masubuchi.[3.1] **Figure 3.1** shows schematically the changes of temperature and resulting stresses that occur during welding. A bead-on-plate weld is being made along the *x*-axis. The heat source of welding which is moving at a speed *v* (m/s) is presently located at the origin O as shown in **Figure 3.1(a)**. **Figures 3.1(b)** and **3.1(c)** show the temperature distributions along several cross-sections and thermally induced stresses along the *x*-direction, respectively.

Section A–A is ahead of the heat source and it not yet significantly affected by the heat input. The temperature change $\Delta\theta$ (K) due to welding is essentially zero. Since section A–A is not affected by the heat input, the longitudinal stress σ_{xx} (MPa) is zero. Along the section B–B, which passes through the heat source, very high temperatures exist in the immediate vicinity of the weld, and low temperatures away from the weld. Since the molten pool does not have any strength to support any loads, the σ_{xx} in the region underneath the heat source is close to zero. In the regions with a short distance from the heat source, there are compressive stresses (σ_{xx}: negative) because the expansion of these areas is restrained by the surrounding material of lower temperatures. In addition, the yield stress is low at the high temperatures and that makes the stresses low. In the areas farther away from the weld, the tensile stresses are developed that balance the compressive stresses close to the weld.

Behind the heat source of section C–C, the lower temperatures exist in the weld bead, which the temperature gradient becomes less steep and eventually uniform temperature distribution along section D–D further behind the heat source. Along section C–C, the weld metal and base metal regions near the weld have cooled, and have a tendency to contract, consequently generating tensile stresses (σ_{xx}: positive) in regions close to the weld. As the distance from the weld increases, the stresses first change to compressive and then become tensile. Finally, along section D–D, the high tensile stresses are generated in regions near the weld, while compressive stresses are generated in regions away from the weld. Since section D–D is well behind the heat source, the stress distribution doest not change significantly beyond it, and this stress distribution is the residual stresses distribution, which remain after welding process is completed.

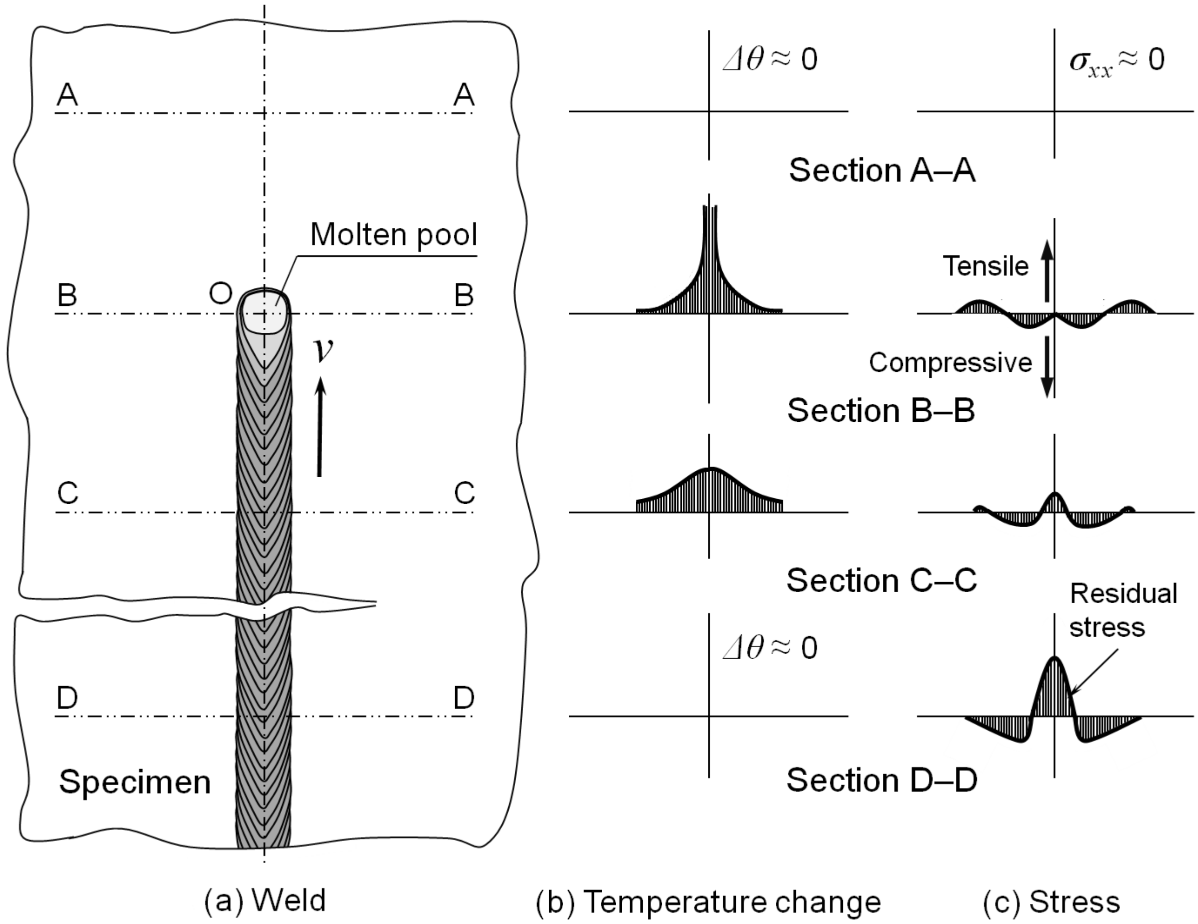

Figure 3.1 Schematic representation of temperature and thermal stress changes during bead-on-plate welding[3.1), 3.20), 3.21)]

3.3.2 Welding induced residual stresses and deformations

The thermal cycle imposed on welded material causes thermal expansions and contractions. It occurs vary with time and location. Since this expansion is not uniform, stresses that appear in hot regions near the weld are restrained by cooler regions further away. Welding residual stresses are generated in a material as a consequence of local plastic deformations introduced by local temperature history consisting of a rapid heating and subsequent cooling phase. Residual stresses or internal stresses[3.20)] are the stresses remaining after all external loads has been removed.

As discussed in section 3.3.1, during the welding process, the weld area is heated up sharply compare to the surrounding area and fused locally. The material expands as a result of being heated. The heat expansion is restrained by the surrounding cooler area, which gives rise to thermal stresses. The thermal stresses partly exceed the yield limit, which is lowered at elevated temperatures. Consequently, the weld area is plastically hot-compressed. After cooling down too short, too narrow or too small comparing to the surrounding area, it develops tensile residual stress, while the surrounding areas are subjected to compressive residual stresses to maintain the self-equilibrium.[3.2)]

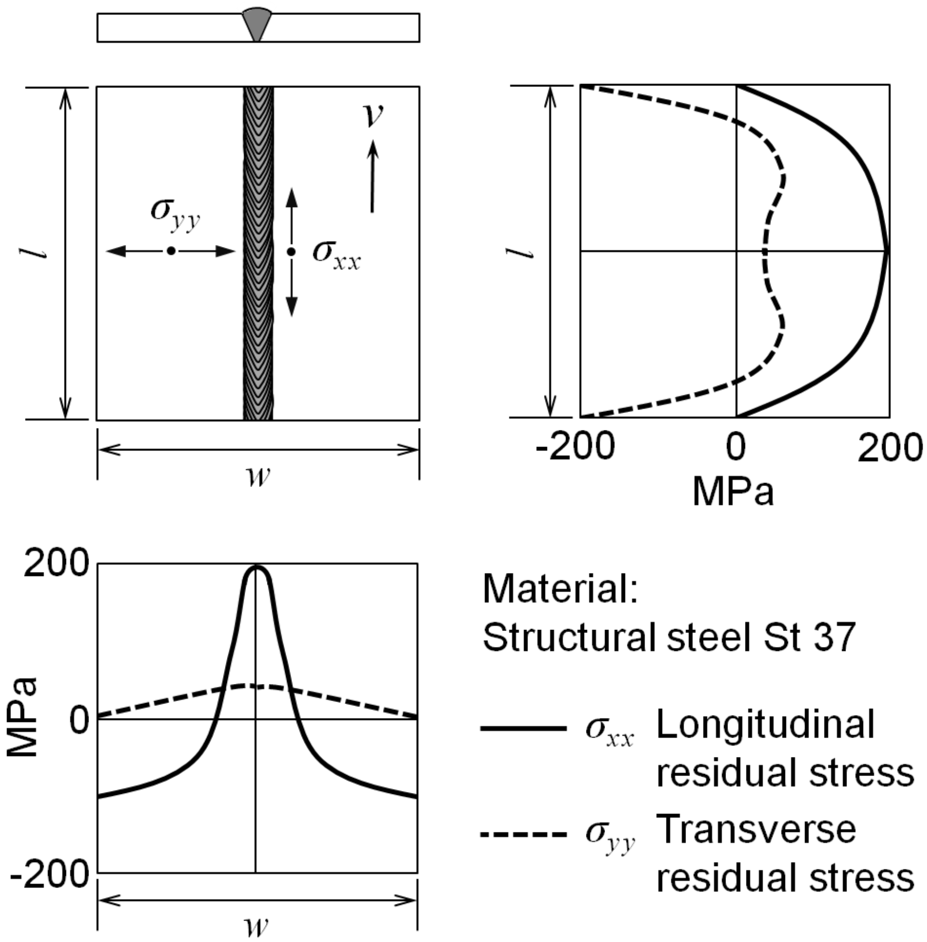

Figure 3.2 Schematic representation of typical residual stresses in welded rectangular plate[3.2)]

Stresses in a welded material are usually divided in two directions, longitudinal and transverse to the weld. In most cases, the through thickness stresses are low and the stress field of the material is described in the *xy*-plane mostly.[3.22)] Longitudinal stresses are defined as the stresses along the welding direction or *x*-direction. While transverse stresses are defined as the stresses perpendicular to the welding direction or *y*-direction. **Figure 3.2** shows the calculated longitudinal and transverse residual stresses in centre cross-sections of rectangular plate. Due to the heating and cooling cycles and constraints from surrounding materials, high longitudinal stress is developed at central section of the plate. As the distance from the weld centre increase, the longitudinal stress gradually decreases. Along the transverse direction, the longitudinal stress changes to compressive, whereas along the longitudinal direction it reduces to zero, as dictated by the equilibrium condition of residual stresses. Similar transverse residual stress with minor differences in distribution from the longitudinal stress and smaller magnitude is observed.

The weld metals are not only accompanied by the stresses but also the deformation. Welding deformations can be defined as the change in shape and dimension of a welded material. It can be temporary or residual.[3.2)] The interaction of solidifying weld metal with the base metal, results in

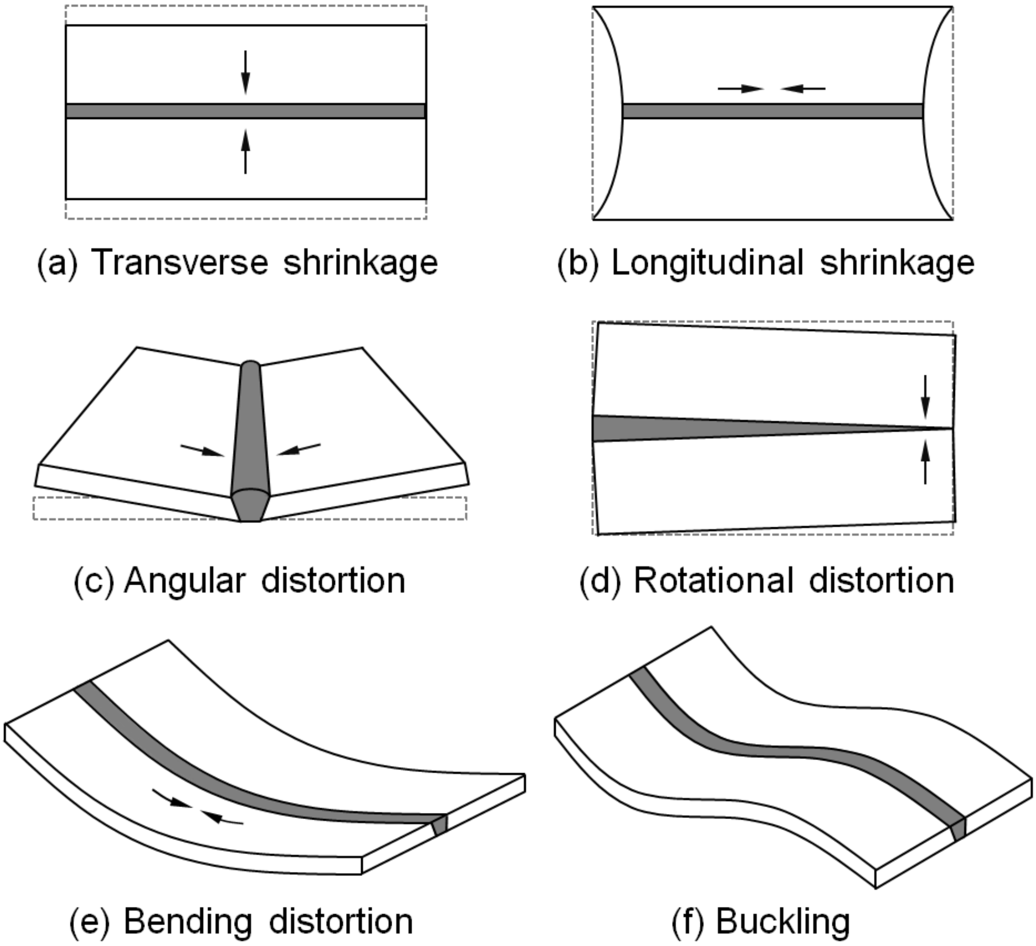

Figure 3.3 Various types of welding deformation[3.1), 3.23)]

change in dimensions and shape of the weldments. Welding typically results in several types of deformations as shown in **Figure 3.3**. Most of these types of deformation are directly by the shrinkage of the weld metal during cooling as depicted by the arrows. Deformation of a welded material is extremely complex. The amount of deformation is affected by many parameters including welding parameters, joint design and restraint.[3.1)] In laser micro-welding, a major problem that makes the analysis and control of deformation very complex is that the thin sheet is welded by micro-beam spot with a high-speed scanning. This subject is discussed in more detail in the section 3.8.

3.4 Non-linear structural analysis

The stress and strain development during welding process is complex to visualize, since it is a three-dimensional, time and temperature dependent problem. To investigate the stress and strain distributions and magnitudes, the numerical analysis based on FEM is the best and less cost if time is not an important factor. Modeling of stress and strain in welding deformations can be predicted by structural analysis. The structural analysis or elastic-plastic analysis of welds is more complex than the thermal analysis because of the geometry changes and the complex stress-strain relationship. As laser welding is a thermo-mechanical process, a thermal analysis uncoupled with structural analysis are conducted to calculate the stress, strain and deformation. In order to incorporate the finite element model in the mechanical problem of the laser welding, the elastic-plastic element formulation needs to be addressed. In this section, the finite element formulations of the structural analysis for calculating spatial and temporal distributions of the stress, strain and deformation are derived.

3.4.1 Basic equations of elasticity

Consider a three-dimensional body in equilibrium under the action of a set of external forces (F_1, F_2, F_3, F_4) as shown in **Figure 3.4(a)**. The application of the external forces will result the development of stresses within the medium. The stress σ, acting on a small area δA can be divided into the normal stress σ_{n} and two shear stress components (τ_x, τ_y). This indicates that stress on an area is fully defined if the three values are known. When a small cubic element is taken into account as shown in **Figure 3.4(b)**, nine values of stress components are necessary for the stresses in the body to be fully calculated, which can be displayed as elements of the square matrix as equation (3.1).

$$\sigma = \begin{bmatrix} \sigma_{11} & \sigma_{12} & \sigma_{13} \\ \sigma_{21} & \sigma_{22} & \sigma_{23} \\ \sigma_{31} & \sigma_{32} & \sigma_{33} \end{bmatrix} = \begin{bmatrix} \sigma_{xx} & \tau_{xy} & \tau_{xz} \\ \tau_{yx} & \sigma_{yy} & \tau_{yz} \\ \tau_{zx} & \tau_{zy} & \sigma_{zz} \end{bmatrix} \tag{3.1}$$

(a) Equilibrium equations

The equilibrium of the surface forces acting on each plane in *x*-direction and the body force acting at the center of the cubic element are shown in **Figure 3.5**. When the derivation of the stress components are taken into account due to small changes, the corresponding components of stress acting on the surface of a small distance *dx*, *dy* and *dz* can be written as equations (3.2), (3.3) and (3.4), respectively.

$$\sigma_{xx} + \frac{\partial \sigma_{xx}}{\partial x} dx \tag{3.2}$$

$$\tau_{yx} + \frac{\partial \tau_{yx}}{\partial y} dy \tag{3.3}$$

$$\tau_{zx} + \frac{\partial \tau_{zx}}{\partial z} dz \tag{3.4}$$

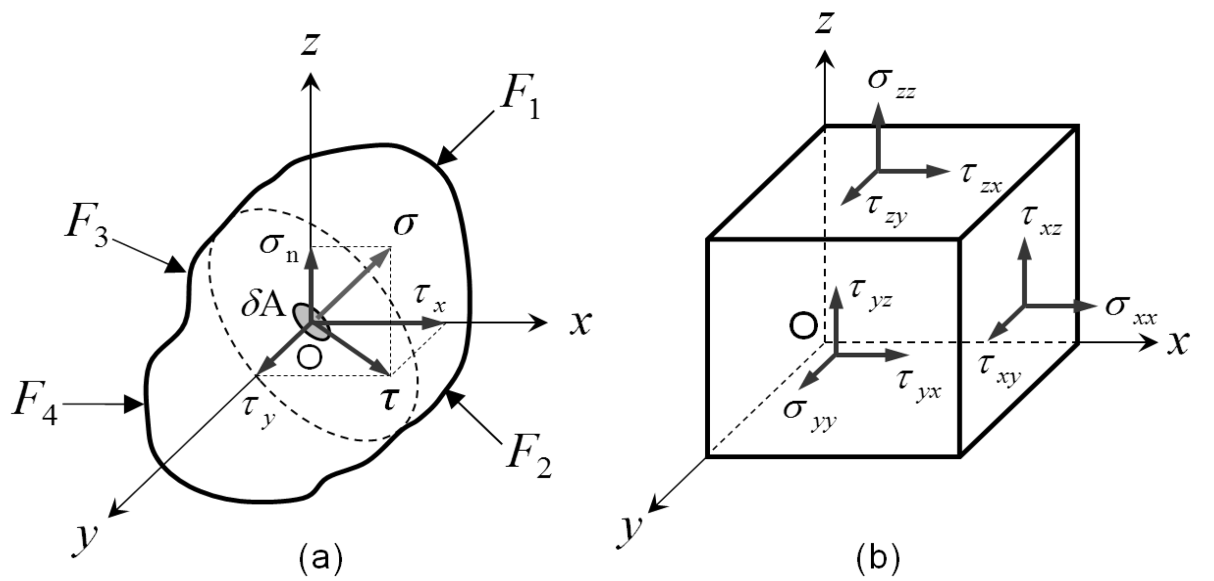

Figure 3.4 Stress at a point: (a) normal and shear stresses and (b) components of stress

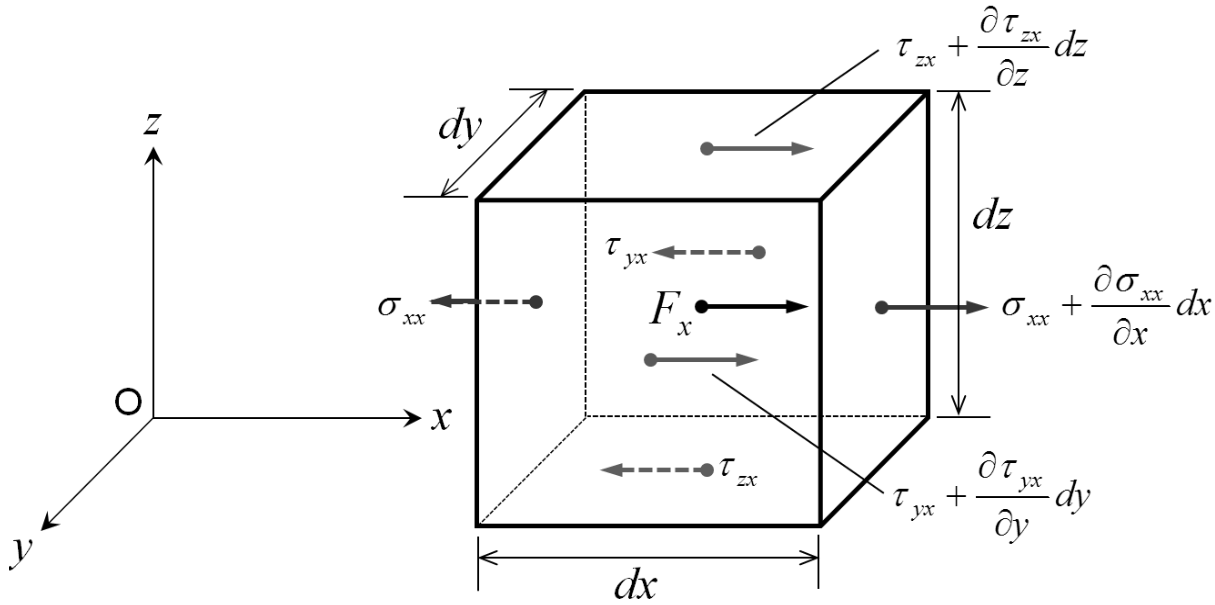

Figure 3.5 Equilibrium of forces on a cubic element in *x*-direction

It denotes the component of body force per unit volume acting at the center of cubic element in *x*-direction by F_x. Then, the equilibrium of the forces in the *x*-direction acting on the element is expressed in equation (3.5).

$$\left(\sigma_{xx} + \frac{\partial \sigma_{xx}}{\partial x} dx\right) dydz - \sigma_{xx}\, dydz + \left(\tau_{yx} + \frac{\partial \tau_{yx}}{\partial y} dy\right) dxdz - \tau_{yx}\, dxdz$$
$$+ \left(\tau_{zx} + \frac{\partial \tau_{zx}}{\partial z} dz\right) dxdy - \tau_{zx}\, dxdy + F_x\, dxdydz = 0 \tag{3.5}$$

After simplification, equation (3.5) can be written as equation (3.6).

$$\frac{\partial \sigma_{xx}}{\partial x}+\frac{\partial \tau_{yx}}{\partial y}+\frac{\partial \tau_{zx}}{\partial z}+F_x=0 \tag{3.6}$$

The two other equations for equilibrium of the forces in the *y*- and *z*-directions can be obtained in the same way as shown in equations (3.7) and (3.8).

$$\frac{\partial \tau_{xy}}{\partial x}+\frac{\partial \sigma_{yy}}{\partial y}+\frac{\partial \tau_{zy}}{\partial z}+F_y=0 \tag{3.7}$$

$$\frac{\partial \tau_{xz}}{\partial x}+\frac{\partial \tau_{yz}}{\partial y}+\frac{\partial \sigma_{zz}}{\partial z}+F_z=0 \tag{3.8}$$

Equations (3.6) to (3.8) are called the differential equations of equilibrium[3.24)] and must be satisfied at all points in the body.

(b) Strain-displacement relations

Consider an elastic body of arbitrary shape subjected to temperature change and external forces. When a point E in the elastic body undergoes a small displacement *u*,*v* and *w* in the *x*-, *y*- and *z*-directions, respectively, the deformation of a cubic element *dxdydz* at the point E in the body shown in **Figure 3.6**. A small element EF parallel to the *x*-axis becomes E"F" after small deformation. The length of the component in the *x*-direction of the element E"F" is expressed as equation (3.9).

$$(\mathrm{E''F''})_x = dx+u_\mathrm{F}-u_\mathrm{E}=dx+\frac{\partial u_\mathrm{E}}{\partial x}dx \tag{3.9}$$

The normal strains at the point E in the *x*-direction is expressed in equation (3.10).

$$\varepsilon_{xx}=\frac{(\mathrm{E''F''})_x-\mathrm{EF}}{\mathrm{EF}}=\frac{\partial u}{\partial x} \tag{3.10}$$

The normal strains at the point E in the *y*- and *z*-directions are given in the same manner as shown in equations (3.11) and (3.12), respectively.

$$\varepsilon_{yy}=\frac{\partial v}{\partial y} \tag{3.11}$$

$$\varepsilon_{zz}=\frac{\partial w}{\partial z} \tag{3.12}$$

Now, let define the shearing strain γ_{xz} as the distortion of the angle between the elements EF

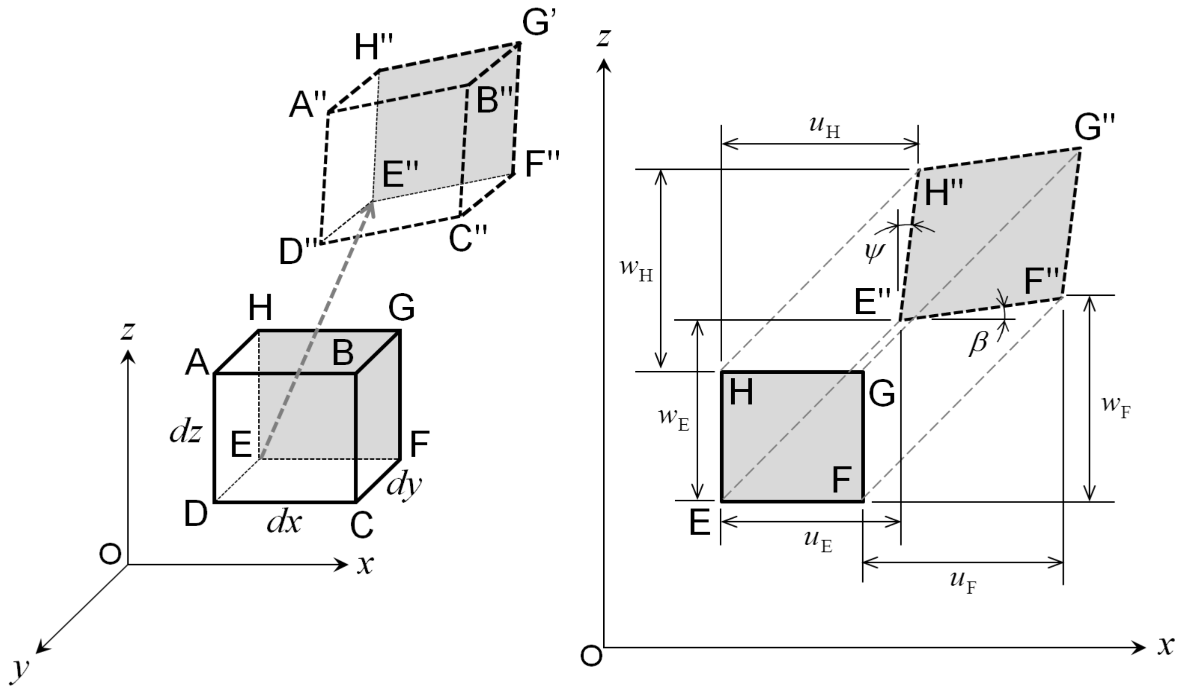

Figure 3.6 Deformation of a cubic element

and EH. Since the shearing strain γ_{xz} is expressed by the sum of the small angle between the element E"F" and the *x*-axis, and the small angle between the element E"H" and the *z*-axis, the shearing strain γ_{xz} is given by equation (3.13).

$$\gamma_{xz} = \beta + \psi \cong \tan\beta + \tan\psi = \frac{w_{\mathrm{F}} - w_{\mathrm{E}}}{(\mathrm{E''F''})_x} + \frac{u_{\mathrm{H}} - u_{\mathrm{E}}}{(\mathrm{E''H''})_z} = \frac{\partial w}{\partial x} + \frac{\partial u}{\partial z} \tag{3.13}$$

The shearing strains γ_{xy} and γ_{yz} at point E are given in the same manner are as shown in equations (3.14) and (3.15), respectively.

$$\gamma_{xy} = \frac{\partial v}{\partial x} + \frac{\partial u}{\partial y} \tag{3.14}$$

$$\gamma_{yz} = \frac{\partial w}{\partial y} + \frac{\partial v}{\partial z} \tag{3.15}$$

Hence, there are six distinct components of strain. Equations (3.10) to (3.15) are called the strain-displacement equations.

(c) Stress-strain relations

In the relationship between stress and strain, two important phenomena are associated with homogeneous and isotropic stated as below.[3.25)]

(i) Hooke's law in one dimension, which states the proportionality between uniaxial stress and strain in the same direction, i.e. $\sigma_{xx} = G_{\mathrm{e}}\varepsilon_{xx}$ (G_{e} (N/m^2) is the Young's modulus or elastic modulus). Hooke's law also holds for shear stress and shear strain in the linearly elastic range as $\tau_{xy} = G_{\mathrm{s}}\gamma_{xy}$ (G_{s} (N/m^2) is the shear modulus or modulus of rigidity).

(ii) The Poisson effect, i.e. the observation that a stress in one direction induces not only strain in that direction but also strains in the other two orthogonal directions, $\varepsilon_{yy} = \varepsilon_{zz} = -\upsilon\varepsilon_{xx}$ (υ is the Poisson's ratio).

Using the two effects, a generalized expression of Hooke's law in three-dimensional directions can be obtained by simple superposition as shown in equations (3.16) to (3.21), and called the constitutive relations.

$$\varepsilon_{xx} = \frac{1}{G_{\mathrm{e}}}\left[\sigma_{xx} - \upsilon\left(\sigma_{yy} + \sigma_{zz}\right)\right] \tag{3.16}$$

$$\varepsilon_{yy} = \frac{1}{G_{\mathrm{e}}}\left[\sigma_{yy} - \upsilon\left(\sigma_{xx} + \sigma_{zz}\right)\right] \tag{3.17}$$

$$\varepsilon_{zz} = \frac{1}{G_{\mathrm{e}}}\left[\sigma_{zz} - \upsilon\left(\sigma_{xx} + \sigma_{yy}\right)\right] \tag{3.18}$$

$$\gamma_{xy} = \frac{1}{G_{\mathrm{s}}}\tau_{xy} \tag{3.19}$$

$$\gamma_{xz} = \frac{1}{G_{\mathrm{s}}}\tau_{xz} \tag{3.20}$$

$$\gamma_{yz} = \frac{1}{G_{\mathrm{s}}}\tau_{yz} \tag{3.21}$$

It can be shown for a linear, isotropic and homogeneous material, the three elastic constants of G_{e}, G_{s} and υ are related to each other as shown in equation (3.22).

$$G_{\mathrm{e}} = 2G_{\mathrm{s}}\left(1 + \upsilon\right) \tag{3.22}$$

A rise in temperature causes materials to expand. The increase in dimension is simply proportional to the temperature rise, via a constant of thermal expansion coefficient α (1/K). Therefore, the thermal strain is the multiplication of temperature change $\Delta\theta$ (K) with the thermal expansion coefficient as shown in equation (3.23).

$$\varepsilon_{\theta} = \alpha \cdot \Delta\theta \tag{3.23}$$

By applying superposition, the thermal strain can be directly added to the stress-strain equations

(3.16) to (3.18), and can be written as equations (3.24) to (3.26).

$$\varepsilon_{xx} = \frac{1}{E}\left[\sigma_{xx} - \upsilon\left(\sigma_{yy} + \sigma_{zz}\right)\right] + \alpha \cdot \Delta\theta \tag{3.24}$$

$$\varepsilon_{yy} = \frac{1}{E}\left[\sigma_{yy} - \upsilon\left(\sigma_{xx} + \sigma_{zz}\right)\right] + \alpha \cdot \Delta\theta \tag{3.25}$$

$$\varepsilon_{zz} = \frac{1}{E}\left[\sigma_{zz} - \upsilon\left(\sigma_{xx} + \sigma_{yy}\right)\right] + \alpha \cdot \Delta\theta \tag{3.26}$$

(d) Boundary conditions

In order to solve the thermoelasticity problems, it is necessary to consider the boundary conditions. There are two kinds of boundary conditions.

[1] First boundary-value problem

When the stress is prescribed over the entire boundary surface, the problem is called the first boundary-value problem. This boundary condition can be expressed as equation (3.27).

$$\begin{aligned} \sigma_{xx}n_x + \tau_{yx}n_y + \tau_{zx}n_z &= T_x \\ \tau_{xy}n_x + \sigma_{yy}n_y + \tau_{zy}n_z &= T_y \\ \tau_{xz}n_x + \tau_{yz}n_y + \sigma_{zz}n_z &= T_z \end{aligned} \tag{3.27}$$

where T_x, T_y, T_z (N/m^2) are the surface tractions per unit area, and n_x, n_y, n_z denote the direction cosines of the outward directed normal to the surface at the point of interest.

[2] Second boundary-value problem

When the displacement is prescribed over the entire boundary surface, the problem is called the second boundary-value problem. This boundary can be expressed as equation (3.28).

$$u = \bar{u}, \quad v = \bar{v}, \quad w = \bar{w} \tag{3.28}$$

where $\bar{u}, \bar{v}, \bar{w}$ are boundary displacements.

3.4.2 Theory of plasticity

Plasticity means deformation that is not recovered when loads are removed. Plastic behavior is involved in the laser welding process, and begins when induced stresses by thermal expansion exceed the yield point of the material. Plasticity is characterized by the non-linear relationship between stress and strain, which is the stress is a non-linear function of the strain. Their relationship is also path dependent. The stress depends on the strain history as well as the strain itself. There are three ingredients in plasticity theory, which are the yield criterion, flow rule and hardening rule.

(a) Yield criterion

The yield criterion is used to predict initial yield. The combination of stress components for transition from elastic to plastic deformation is referred to the yield criterion. In general, the yield function *f* can be expressed as equation (3.29).

$$f(J_1, J_2, J_3) = 0 \tag{3.29}$$

where J_1, J_2, J_3 are the stress invariants, and can written as equation (3.30).

$$\begin{aligned} J_1 &= \sigma_{xx} + \sigma_{yy} + \sigma_{zz} \\ J_2 &= -(\sigma_{xx}\sigma_{yy} + \sigma_{yy}\sigma_{zz} + \sigma_{xx}\sigma_{zz}) + \tau_{xy}{}^2 + \tau_{yz}{}^2 + \tau_{xz}{}^2 \\ J_3 &= \sigma_{xx}\sigma_{yy}\sigma_{zz} - \sigma_{xx}\tau_{yz}{}^2 - \sigma_{yy}\tau_{xz}{}^2 - \sigma_{zz}\tau_{xy}{}^2 + 2\tau_{xy}\tau_{yz}\tau_{xz} \end{aligned} \tag{3.30}$$

In addition, yield surface is the boundary surface between elastic and plastic flow, which geometrical maps in stress space. The yield surface is usually is expressed in terms of a three-dimensional principle stress space, a two- and three-dimensional space panned by stress invariants. In the metallic materials, the hydrostatic pressure on the yielding is neglected. Therefore, the yield function in equation (3.29) can be rewritten as equation (3.31).

$$f(J_2', J_3') = 0, \quad J_1' = 0 \tag{3.31}$$

where J_1', J_2', J_3' are the deviatoric stress invariants, and can be expressed as equation (3.32).

$$\begin{aligned} &\sigma_{xx}' = \sigma_{xx} - \sigma_m \ , \quad \sigma_{xx}' = \sigma_{xx} - \sigma_m \ , \quad \sigma_{xx}' = \sigma_{xx} - \sigma_m \\ &\sigma_m = \tfrac{1}{3}(\sigma_{xx} + \sigma_{yy} + \sigma_{zz}) \\ &\tau_{xy}' = \tau_{xy} \ , \quad \tau_{xy}' = \tau_{xy} \ , \quad \tau_{xy}' = \tau_{xy} \end{aligned} \tag{3.32}$$

where σ_m is hydrostatic stress (a stress invariant).

The von Mises yield criterion is the most commonly used as the yield stress for metal. If the Bauschinger effect is not present, the J_3' can be ignored. Therefore, the von Mises yield surface is only dependent on the J_2' and the yield function can be expressed as equation (3.33).

$$f = \sqrt{3J_2'} - \sigma_0 \tag{3.33}$$

where σ_0 is yield strength in uniaxial tension. Next, the second deviatoric stress invariant J_2' can be expressed as equation (3.34).

$$\begin{aligned}
J_2{}' &= -\left(\sigma'_{xx}\sigma'_{yy} + \sigma'_{yy}\sigma'_{zz} + \sigma'_{xx}\sigma'_{zz}\right) + \tau'_{xy}{}^2 + \tau'_{yz}{}^2 + \tau'_{xz}{}^2 \\
&= \frac{1}{2}\left[\sigma'_{xx}{}^2 + \sigma'_{yy}{}^2 + \sigma'_{zz}{}^2 + 2\left(\tau'_{xy}{}^2 + \tau'_{yz}{}^2 + \tau'_{xz}{}^2\right)\right]^{1/2} \\
&= \frac{1}{6}\left[\left(\sigma_{xx} - \sigma_{yy}\right)^2 + \left(\sigma_{yy} - \sigma_{zz}\right)^2 + \left(\sigma_{zz} - \sigma_{xx}\right)^2 + 6\left(\tau_{xy}{}^2 + \tau_{yz}{}^2 + \tau_{xz}{}^2\right)\right]
\end{aligned} \tag{3.34}$$

By considering the von Mises yield criterion, the equivalent stress or effective stress $\bar{\sigma}$ (MPa) can be represented as equation (3.35).

$$\begin{aligned}
\bar{\sigma} &= \sqrt{3J_2'} = \sqrt{\frac{3}{2}}\left[\sigma'_{xx}{}^2 + \sigma'_{yy}{}^2 + \sigma'_{zz}{}^2 + 2\left(\tau'_{xy}{}^2 + \tau'_{yz}{}^2 + \tau'_{xz}{}^2\right)\right]^{1/2} \\
&= \frac{1}{\sqrt{2}}\left[\left(\sigma_{xx} - \sigma_{yy}\right)^2 + \left(\sigma_{yy} - \sigma_{zz}\right)^2 + \left(\sigma_{zz} - \sigma_{xx}\right)^2 + 6\left(\tau_{xy}{}^2 + \tau_{yz}{}^2 + \tau_{xz}{}^2\right)\right]^{1/2}
\end{aligned} \tag{3.35}$$

Consequently, yielding occurs as shown in equation (3.36).

$$\bar{\sigma} = \sigma_0 \tag{3.36}$$

A criteria to determine the response of a material to a loading has reached the elastic-plastic transition curve is obtained. The possibilities are $f < 0$ for elastic response, $f = 0$ for plastic response and $f > 0$ has no physical meaning. Different values of $\bar{\sigma}$ defines admissible yield functions at different material states.

(b) Flow rule

The flow rule relates the state of stress to the corresponding increments of plastic strain when an increment of plastic flow takes place. The direction of plastic strain is expressed by the rule that is stated as equation (3.37).

$$\left\{\Delta\varepsilon^p\right\} = \left\{\frac{\partial Q}{\partial \sigma}\right\}\Delta\lambda \tag{3.37}$$

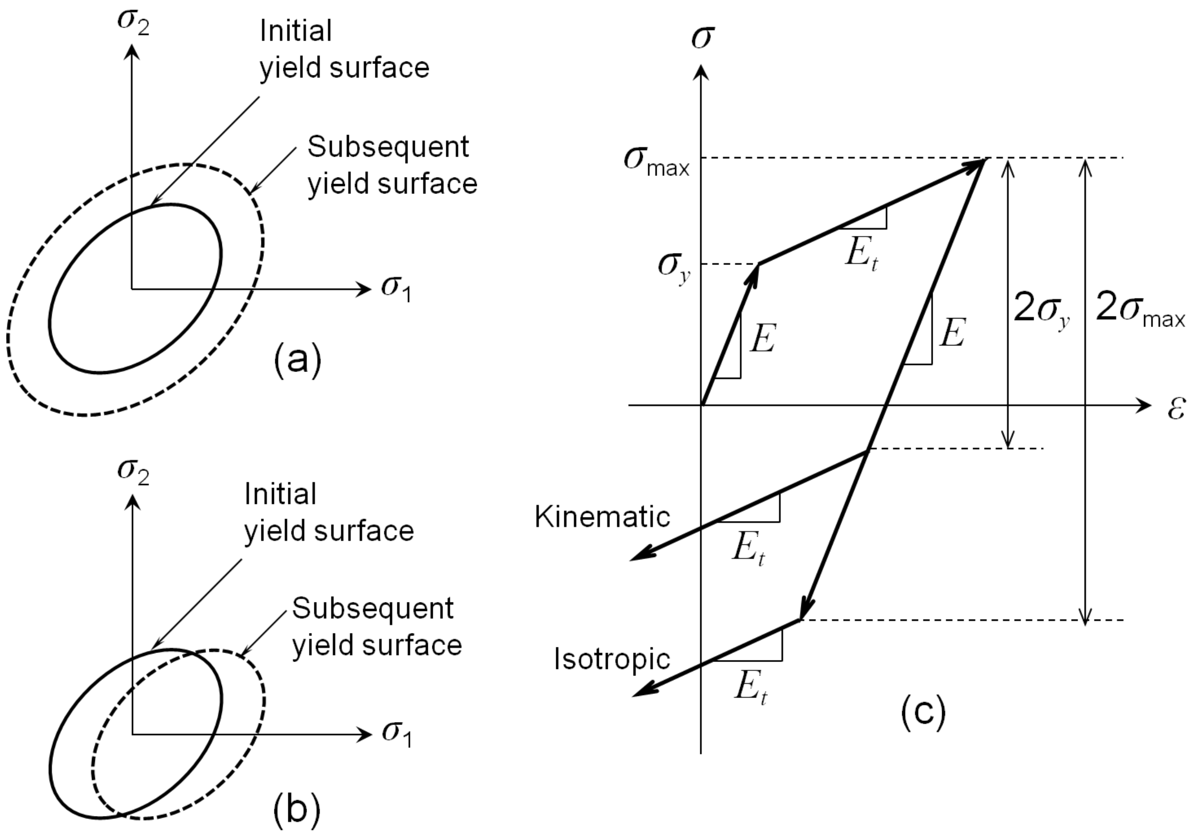

Figure 3.7 Graphical illustrations of (a) isotropic hardening rule, (b) kinematic hardening rule and (c) stress-strain relationship of hardening rule

where $\{\Delta\varepsilon^p\}$ is the vector of plastic strain increments, Q is the function of stress called a plastic potential, which determines the direction of plastic straining, and $\Delta\lambda$ is the plastic multiplier, which determines the direction of plastic straining.

(c) Hardening rule

The hardening rule describes how the yield criterion is modified as the strains develop beyond initial yield. Normally two hardening rules are used, which are the isotropic hardening and kinematic hardening. As shown in **Figure 3.7(a)**, according to the isotropic hardening rule, the elastic range is expanded from the initial value $2\sigma_y$ to the value $2\sigma_{\max}$ after reaching $\sigma_{\max}$. Therefore, the experimentally observed Bauschinger effect is not considered in this rule. In order to calculate the plastic strains by the isotropic hardening rule, the yield function of equation (3.33) can be written in the following form as shown in equation (3.38), because the yield surface remains centered about its initial centerline and expands in size as the plastic strains progress in the isotropic hardening rule.

$$f = \sqrt{3J_2'} - \sigma_0 = \bar{\sigma} - \sigma_0\left(\bar{\varepsilon}^p\right) = \bar{\sigma} - \sigma_0\left(\int d\bar{\varepsilon}^p\right) \tag{3.38}$$

where $\bar{\varepsilon}^{p}$ is the equivalent plastic strain.

In the kinematic hardening rule, the Bauschinger effect is taken into account by preserving an elastic range of $2\sigma_y$, but the possibility that the elastic range may increase is ignored. In order to calculate the plastic strains by the kinematic hardening rule, the yield function of equation can be written in the following form as shown in equation (3.39), which the yield surface remains the shape and size but merely translates in stress space as shown in **Figure 3.7(b)**.

$$f = f\left(\{\sigma\} - \{\alpha_0\}\right) \tag{3.39}$$

where α_0 is the centre of yield surface.

The incremental plastic strains can be obtained with substitution of equations (3.38) and (3.39) into equation (3.37). It can be seen from the result that the size of the plastic strain is related to the total increment in strain, the current stress state, and the potential yield surface. In the practical plastic analysis, the loads are applied as a series of small incremental load steps to enable the plasticity model to follow the load-response path as closely as possible.

3.4.3 Finite element formulation

(a) Principle of virtual work

The stress analysis can be performed by solving the virtual work equation as shown in (3.40).

$$\int_V \{\sigma\}\{\delta\varepsilon\}^T \, dV = \int_V \{f\}\{\delta u\}^T \, dV + \int_S \{P\}\{\delta u\}^T \, dS \tag{3.40}$$

where $\{\sigma\}$ is the stress vector, $\{f\}$ and $\{P\}$ are the body force vector in the body V and prescribed surface pressure vector on the surface A, $\{\delta\varepsilon\}$ and $\{\delta u\}$ are the kinematically admissible virtual strain vector and virtual displacement vector, respectively. Consider the two states at time t and $t + \Delta t$, respectively. By applying the virtual work, equation (3.40) to the state at $t + \Delta t$ yields the equation (3.41).

$$\int_V \left(\{\sigma^t\} + \{\Delta\sigma\}\right)\{\delta\varepsilon\}^T \, dV = \int_V \left(\{f^t\} + \{\Delta f\}\right)\{\delta u\}^T \, dV + \int_S \left(\{P^t\} + \{\Delta P\}\right)\{\delta u\}^T \, dS \tag{3.41}$$

where $\left(\{\sigma^t\} + \{\Delta\sigma\}\right)$, $\left(\{f^t\} + \{\Delta f\}\right)$ and $\left(\{P^t\} + \{\Delta P\}\right)$ are the stress, body force and surface pressure vectors at the time $(t + \Delta t)$, respectively. Equation (3.41) reduces to the virtual work equation at time t if there are no stress, body force and surface pressure increments, that is $\Delta\sigma = \Delta f = \Delta P = 0$. Note that the virtual strains and virtual displacements are arbitrary as long as they satisfy the compatibility conditions. By choosing the same virtual strains and virtual displacements for time states at t and at $t+\Delta t$, the following virtual work equation in the form of increments can be obtained as equation (3.42).

$$\int_V \{\Delta\sigma\}\{\delta\varepsilon\}^T dV = \int_V \{\Delta f\}\{\delta u\}^T dV + \int_S \{\Delta P\}\{\delta u\}^T dS \tag{3.42}$$

(b) Strain-displacement relations

Similar to the temperature field, the displacement increment Δu can be expressed in terms of the nodal displacement increments as equation (3.43).

$$\{\Delta u\} = [N]^T\{\Delta u_e\} \tag{3.43}$$

where $[N]$ is the element shape functions matrix and $\{\Delta u_e\}$ is the element nodal displacement increment vector. The total strain increments can be calculated from the displacement increments Δu using the well-known non-linear strain-displacement equation as shown in equation (3.44).

$$\{\Delta\varepsilon\} = [B]\{\Delta u\} = [B][N]^T\{\Delta u_e\} \tag{3.44}$$

where $\{\Delta\varepsilon\}$ is the total strain increments vector, $[B]$ is the strain-displacement matrix.

(c) Stress-strain relations

The total strain increment $\{\Delta\varepsilon\}$ can be divided into three parts as equation (3.45).

$$\{\Delta\varepsilon\} = \{\Delta\varepsilon^e\} + \{\Delta\varepsilon^p\} + \{\Delta\varepsilon^\theta\} \tag{3.45}$$

where $\{\Delta\varepsilon^e\}, \{\Delta\varepsilon^p\}, \{\Delta\varepsilon^\theta\}$ is the elastic, plastic and thermal strain increments, respectively. The difference between total strain increment and thermal strain increment gives mechanical strain increment, which consist of elastic and plastic strains increments and as expressed as equation (3.46).

$$\{\Delta\varepsilon\} - \{\Delta\varepsilon^\theta\} = \{\Delta\varepsilon^e\} + \{\Delta\varepsilon^p\} \tag{3.46}$$

Base on the theory of elastic-plasticity, the increments of elastic, plastic and thermal strains can be expressed as equations (3.47), (3.48) and (3.49), respectively.

$$\{\Delta\varepsilon^e\} = [D^e]^{-1}\{\Delta\sigma\} \tag{3.47}$$

$$\{\Delta\varepsilon^{p}\}=[D^{ep}]^{-1}\{\Delta\sigma\}-[D^{e}]^{-1}\{\Delta\sigma\} \quad , \quad [D^{ep}]=[D^{e}]+[D^{p}] \tag{3.48}$$

$$\{\Delta\varepsilon^{\theta}\}=\alpha\cdot\Delta\theta \tag{3.49}$$

where $\{\Delta\sigma\}$ is the stresses increment, $[D^{e}]$ is the elastic stiffness matrix, $[D^{p}]$ is the plastic stiffness matrix, $[D^{ep}]$ is the elastic-plastic stiffness matrix, $\Delta\theta$ is the temperature increment and α is the thermal expansion coefficient.

The finite element equilibrium equation can be obtained from the incremental form of virtual work equation of (3.42), which results in the following matrix form as equation (3.50).

$$\int_{V}[B]^{T}\{\Delta\sigma\}dV=\{\Delta R\}=[K]\{\Delta u\} \tag{3.50}$$

where $\{\Delta R\}$ is the vector of global element force increments and $[K]$ is the global stiffness matrix, and are written as equations (3.51) and (3.52), respectively.

$$\{\Delta R\}=\int_{V}[N]^{T}\{\Delta f\}dV+\int_{A}[N]^{T}\{\Delta P\}dA \tag{3.51}$$

$$[K]=\int_{V}[B]^{T}[D^{ep}][B]dV \tag{3.52}$$

The $\{\Delta R\}$ is the summation of element force increments vector $\{\Delta R_{e}\}$, which consist of thermal loading increments vector $\{\Delta F_{\mathrm{T}}\}$ and mechanical loading increments vector $\{\Delta F_{\mathrm{M}}\}$, and can be expressed as equation (3.53). While $[K]$ is the summation of element stiffness matrix $[K_{e}]$, consists of elastic stiffness matrix $[K^{e}]$ and plastic stiffness matrix $[K^{p}]$, and can be expressed as equation (3.54).

$$\{\Delta R\}=\sum\{\Delta R_{e}\}=\sum\left(\{\Delta F_{\mathrm{T}}\}+\{\Delta F_{\mathrm{M}}\}\right) \tag{3.53}$$

$$[K]=\sum[K_{e}]=[K^{e}]+[K^{p}] \tag{3.54}$$

Based on the von Mises yield criterion, the stress-strain relations or constitutive relations can be written as equation (3.55).

$$\{\Delta\sigma\}=[D^{ep}]\{\Delta\varepsilon\}-[C^{th}]\{\Delta\theta\} \tag{3.55}$$

where $\left[C^{th}\right]$ is the thermal stiffness matrix. This equation can be rewritten with the nodal increment as equation (3.56).

$$\{\Delta\sigma_e\}=\left[D^{ep}\right][B]\{\Delta u_e\}-\left[C^{th}\right][M]\{\Delta\theta_e\} \tag{3.56}$$

where $\{\Delta\sigma_e\}$ is the nodal stress increment matrix, $\{\Delta\theta_e\}$ is the nodal temperature increment matrix and $[M]$ is the temperature shape function. Therefore, the displacement increment and the stress increment can be solved from equation (3.xx).

(d) Incremental Newton-Raphson iteration method

In the analysis of plasticity that includes path-dependent non-linearities, the solution process has to be carried out by a step-by-step incremental analysis in order to correctly follow the load path. Therefore, the load vector $\{F^a\}$ is divided into many steps to be applied in increments, and the *N-R* iterations are performed at each step as expressed in equation (3.57).

$$\left[K_{n,i}\right]\{\Delta u_i\}=\{F_n^a\}-\{F_{n,i}^{nr}\} \tag{3.57}$$

where $\left[K_{n,i}\right]$ is the updated coefficient matrix for time step *n*, iteration *i*, $\{F_n^a\}$ total applied force vector at time step *n*, and $\{F_{n,i}^{nr}\}$ is the restoring force vector for time step *n*, iteration *i*.

This incremental *N-R* procedure is graphically illustrated in **Figure 3.8**. When the coefficient

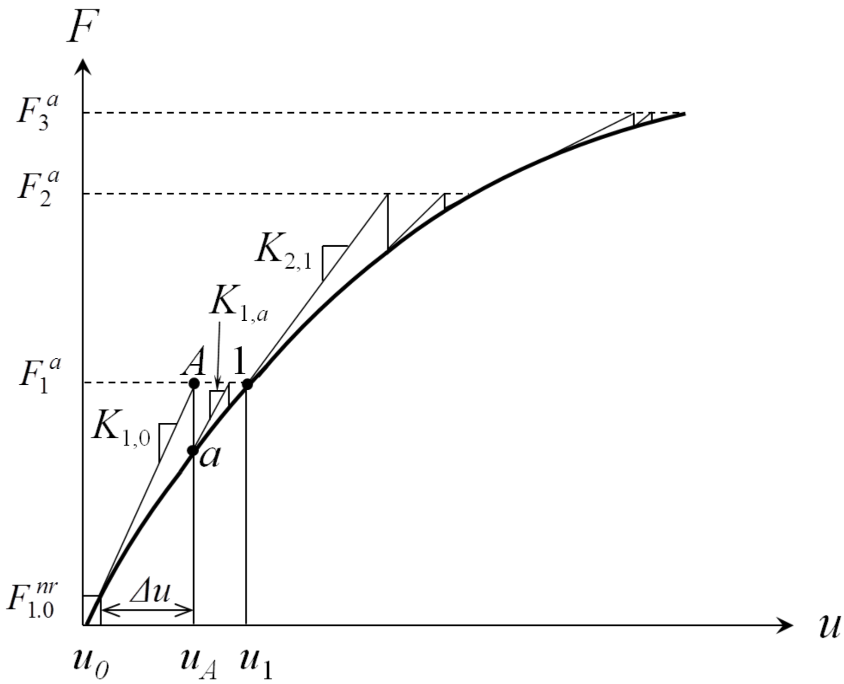

Figure 3.8 Graphical illustrations of incremental Newton-Raphson procedure

matrix $[K]$ is updated every iteration, the process is termed a full *N-R* solution procedure. Instead of updating $[K]$ in every iteration, $[K]$ can be used in many iterations in each step until convergence is obtained at each step. This solution method is the modified *N-R* method. Although more iterations are required in this method than the full *N-R* method, every iteration is accomplished more quickly avoiding repeated generation of $[K]$, which leads to computational cost reduction.

3.5 Finite element modeling

The thermo-mechanical simulation of welding deformation is carried out in two uncoupled analyses, which are thermal analysis and structural analysis. The thermal model is developed first with the heat conduction equation to obtain the temperature fields, which discussed in Chapter 2. Structural analysis is sequentially carried out with temperature distributions retrieved from thermal analysis are used as input or thermal loading for the mechanical model under the specific boundary. The mechanical model is used to estimate the weld induced stresses, strains and displacements. The mechanical model developed for the structural analysis is described in this section. **Figure 3.9** shows the numerical procedure of the uncoupled thermo-mechanical simulation.

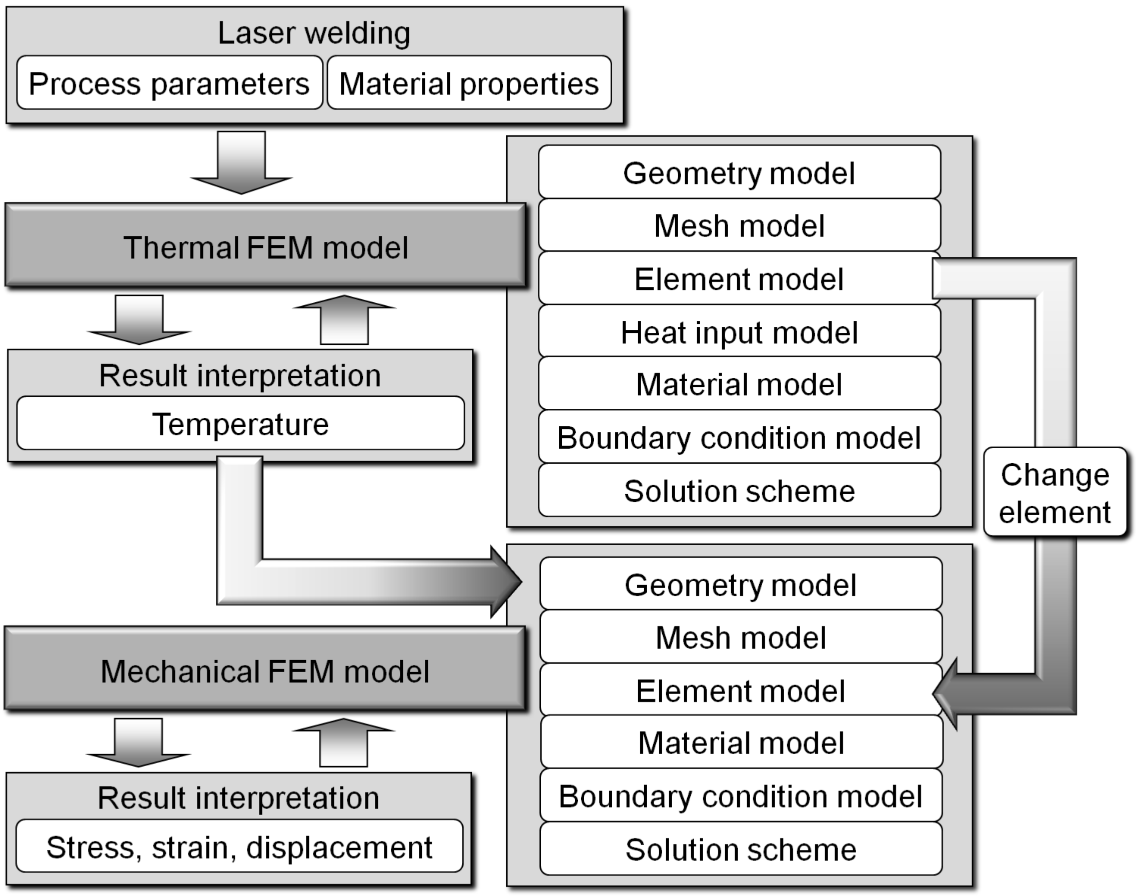

Figure 3.9 FEM procedure of uncoupled thermo-mechanical simulation

3.5.1 Geometry, mesh and element models

The same dimension and mesh used in the thermal analysis are used for the structural analysis as in section 2.4.1. This helps in maintaining the same geometrical and mesh for both thermal and structural analyses. In addition, since the stress was calculated by reading the nodal temperature field from the thermal analysis and applying it as a thermal load to the corresponding node in the mechanical model, the node labels for the structural mesh must match those from the thermal mesh. In structural analysis, the element types need to be changed and at the same time retaining the similar nodal and mesh information as in the thermal model. Therefore, the elements of PLANE77 and SOLID70 used in thermal analysis are automatically converted to PLANE183 and SOLID185 in structural analysis, respectively. These elements support plasticity, hyper-plasticity, stress stiffening, creep, large deflection and large strain capabilities.

3.5.2 Material model

The material modeling plays a crucial role in obtaining accurate results in thermo-mechanical simulations. The temperature dependent mechanical properties such as thermal expansion coefficient, Young’s modulus, Poisson’s ratio and yield stress are required in the structural analysis. The temperature dependent mechanical properties of austenitic stainless steel SUS304 are shown in **Figure 3.10**, which were taken from the literatures.[3.14), 3.26), 3.27)] The Young’s modulus or elastic modulus is a measure of the stiffness of a material. In other words, the elastic behavior of the material is determined by the Young’s modulus. While, the plastic behavior of the material is described by the temperature dependent yield stress and the strain hardening behavior.

Plastic behavior involved in the laser welding process begins when the induced stress exceeds the yield point of the material. The plasticity is characterized by non-linear relationship between stress and strain. Therefore, non-linear material properties are also required for plastic deformation using $\sigma - \varepsilon$ curve in the structural analysis. The stresses and strains resulting from the temperature difference created in the material are constructed into the $\sigma - \varepsilon$ curve to determine whether the thermal loading has resulted in an inelastic or plastic behavior. Numerical experiments have shown that using a plasticity model with isotropic strain hardening where the yield surface is expanding gives better results which have a better accordance with the measured deformation than a plasticity model with kinematic hardening.[3.28)] Many researchers employed isotropic strain hardening in the thermo-mechanical simulation of laser welding and other welding processes.[3.19), 3.29)–3.33)] In addition, the isotropic strain hardening gives an easier convergence. In this study, the multi-linear isotropic strain hardening model (von Mises yield criterion with associated flow rule, isotropic hardening rule and multi-linear isotropic hardening material) was chosen. **Figure 3.11** shows the stress-strain behavior of the multi-linear isotropic hardening material used in the analysis.

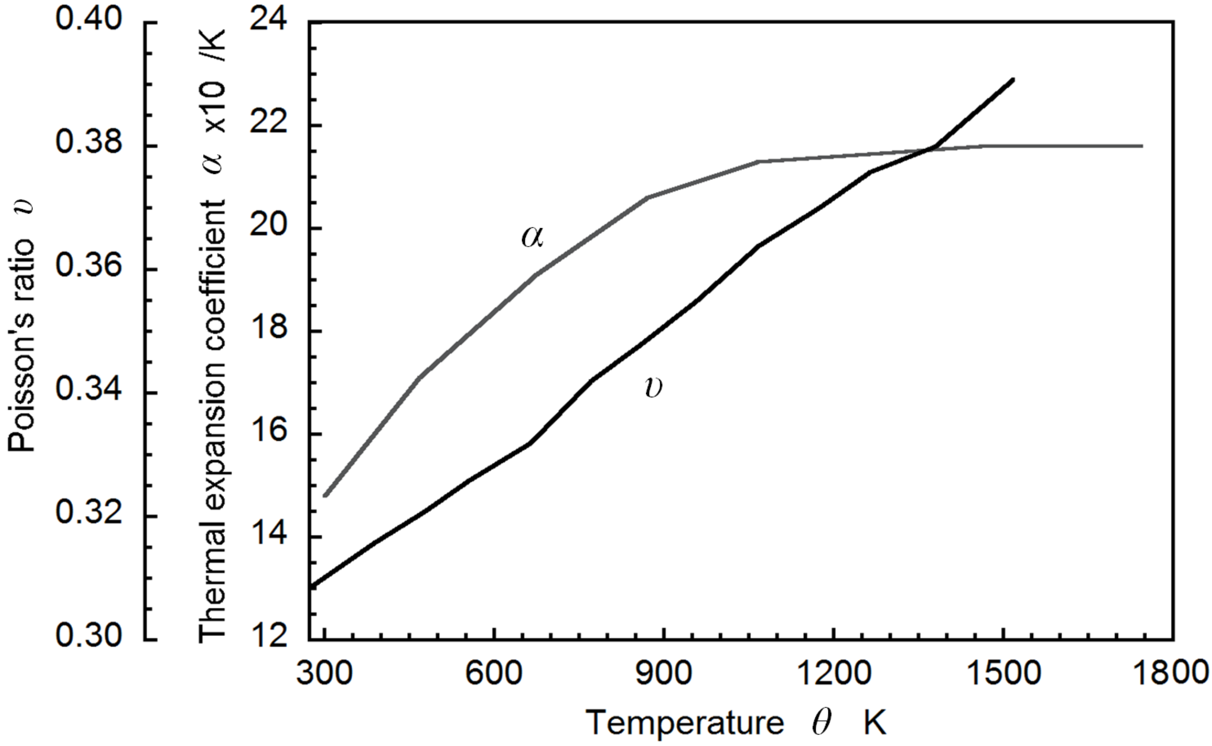

(a) Thermal expansion coefficient and Poisson's ratio

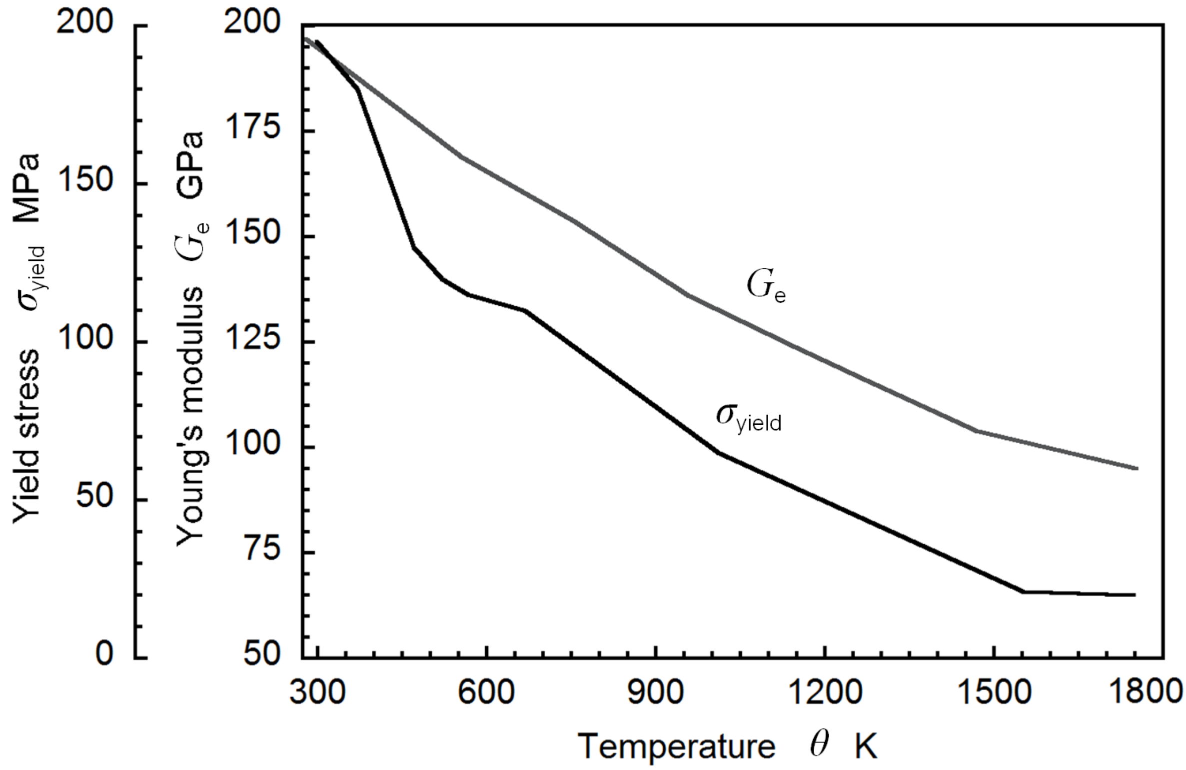

(b) Young's modulus and yield stress

Figure 3.10 Mechanical properties of austenitic stainless steel SUS304

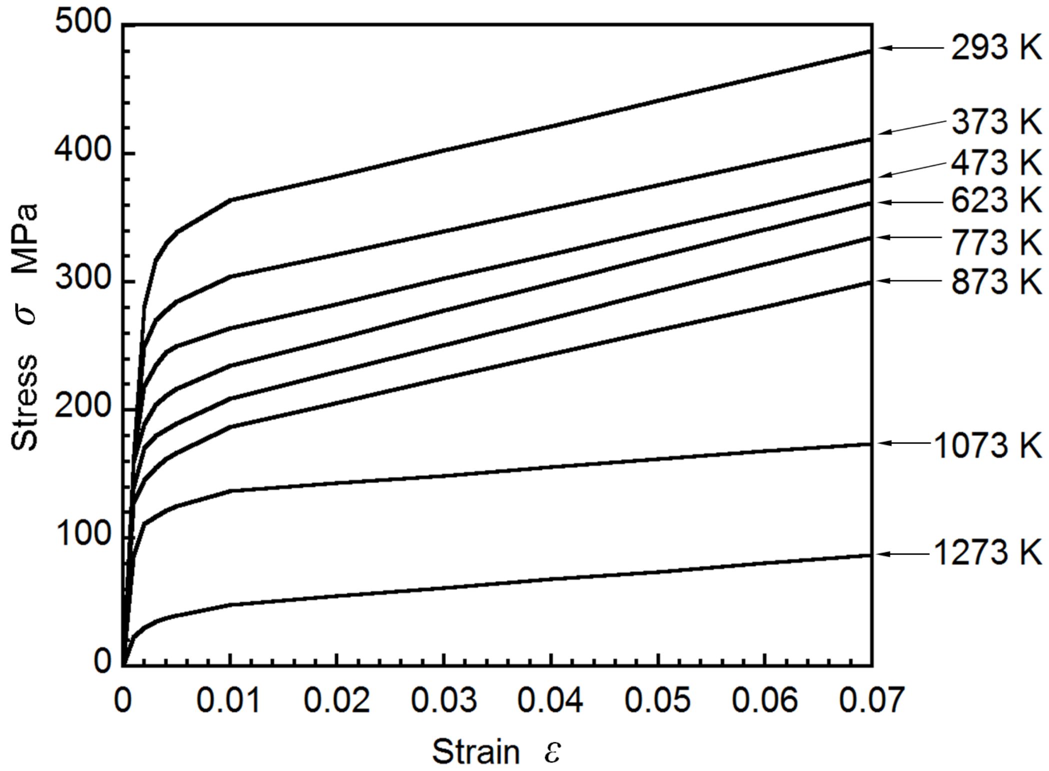

Figure 3.11 Multi-linear isotropic stress-strain model of austenitic stainless steel SUS304[3.34), 3.35)]

3.5.3 Boundary conditions model

After the temperature distribution is analyzed using the thermal analysis, the temperatures are applied with the predefined boundary conditions to predict any possible deformation and eventually study the stress distribution along the material. The boundary conditions for laser micro-welding represent the actual experimental position of the thin metal sheet during the process. The clamping of sheet on both ends are used as the boundary condition in structural analysis as shown in **Figure 3.12**. The boundary condition is zero displacement at the upper and lower of the end sheet, and it is fully constrained along the *x*, *y* and *z*-axes. The fully constraints were imposed to restraint the rigid body motions. If no appropriate constraints, the equations of FEM formulation can not be solved. Boundary conditions on the other surfaces are stress free.

3.5.4 Solution scheme

The structural analysis is a very important aspect of the computational weld mechanics for computing the stress and strain field. It was conducted after the thermal analysis was finished and the computation of time dependent temperature fields were determined during welding and subsequent cooling. In the thermal analysis, the computed thermal histories at all nodes are recorded and stored in a thermal analysis result file. These temperature fields were imported and applied in a transient structural analysis as a nodal or body load to perform the stress analysis. The corresponding

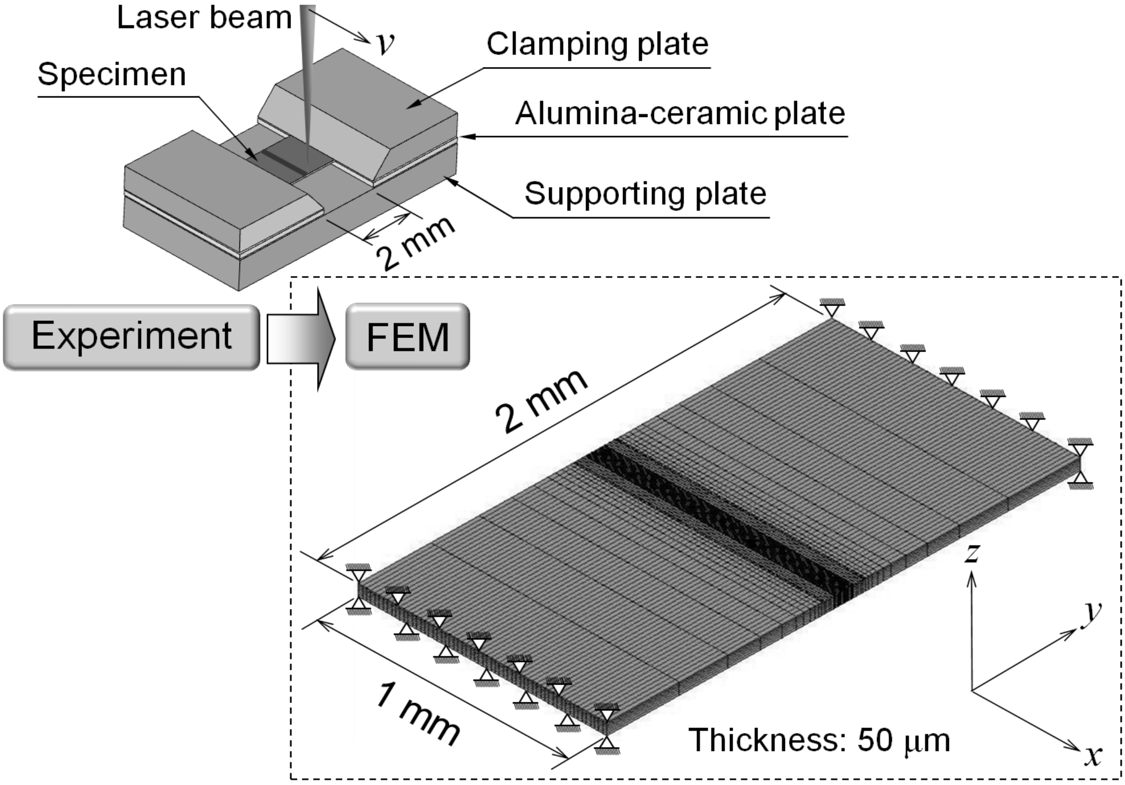

Figure 3.12 Boundary condition in structural analysis

structural analysis uses a command to read the temperature result file and map the thermal histories onto the nodes in the mechanical model. It is important that the thermal and mechanical models are meshed with same element topology for proper data mapping. These mapped nodal temperature fields at different times iteratively, replicate the similar transient method from thermal analysis. Also similar load steps from thermal analysis are used for the respective structural load steps.

Non-linear analysis requires large computation times and hence it is important to utilize all possible simplification in order to improve convergence of the solution. The path dependency of the solution during non-linear material behavior may also affect the final result attained. Therefore, the complex procedure of uncoupled thermo-mechanical simulation needs to be controlled by a structured algorithm. Convergence of solution for these nonlinear problems is generally possible by the use of a Newton-Raphson method. While many numerical integration schemes are available, the Newton-Raphson method is a widely used numerical approximation methods along with implicit numerical integration methods for non-linear structural problems. By this method, a tangent stiffness matrix is recalculated in each iteration, which provides a more accurate tangent stiffness matrix in each iteration. Finally, the interpretation and validation of results obtained at the end of structural analysis is also important aspect in FEM. In this study, four process conditions with various laser powers, scanning velocities and spot diameters are investigated as shown in **Table 3.1**. The model is validated by comparing the experimental results with established numerical simulation results.

Table 3.1 Laser parameters in FEM structural analysis

Case			1	2	3	4
Laser power	P	W	30	30	30	50
Scanning velocity	v	m/s	1.0	2.0	1.0	1.0
Spot diameter	d	μm	17.5	17.5	35.0	35.0

3.6 Equipments

A single mode CW fiber laser of SPI SP-100C was used in this study. In order to perform high-speed laser scanning, the laser scanning was carried out by a Galvano scanner. The detail descriptions of both equipments were mentioned in section 2.5.

In the experiment, the amount of deformation was measured by a laser displacement sensor (Keyence LK-G5000). The sensor head consists of two sensors as transmitter and receiver. The transmitter sensor emits the laser beam, while the receiver sensor receive the laser beam for measurement. Both sensor are protected with the glass covers. A laser emission LED located at the top of sensor head displays the target status. The green light, orange light and flashes light of LED show the target are at the center, within and outside the measurement range, respectively. The measurement range is ± 3 mm with 20 mm reference distance. **Table 3.2** shows the main specifications of laser displacement sensor. The controller synchronizes with sensor head to display the measurement reading and system status. The controller equipped with LK Navigator2 of computer software to connect with a microcomputer by external RS232 interface, which provides the system status and measurement settings can be simply monitored and controlled.

Table 3.2 Specifications of laser displacement sensor

Light source	Red semiconductor laser
Wavelength	650 nm
Output power	4.8 mW
Mounting mode	Diffuse reflection
Reference distance	20 mm
Measurement range	± 3 mm
Beam spot diameter	25 μm
Repeatability	0.02 μm
Sampling cycle	2.55/5/10/20/100/200/500/1000 μs

3.7 Experimental work

The austenitic stainless steel SUS304 was used as a specimen. The sizes of each specimen were 1 mm length, 10 mm width with thickness of 50 μm. A schematic diagram of experimental setup is shown in **Figure 2.12**. In this study, the wavelength of 1090 nm single-mode CW Yb fiber laser was used. The laser was delivered by an optical fiber and focused by a telecentric type $f\theta$ lens of 100 mm in focal length. The laser scanning was carried out by a Galvano scanner to achieve the high-speed beam scanning. The expander was installed between the isolator and the bending mirror to change the diameter of laser beam. In addition, the experiments with bead-on-plate welding were carried out in shielding gas of nitrogen under a constant pressure 100 kPa.

Before and after the experiment of laser welding, the deformation amounts were measured by laser displacement sensor (LDS). **Figure 3.13** shows the schematic diagram of deformation measurement setup. In order to ensure the straighten of specimen sheets, the clamping plate with an opening slot of 2 mm was used. Therefore, the deformation measurement was set to 2 mm width and 1 mm length. The clamping plate also was designed with tighten screws to hold the specimen down to the supporting plate. The LDS was located at a distance 20 mm away from the top surface of specimen. Since the beam spot diameter of LDS is 25 μm, 40 lines were set every 25 μm along with the welding path (x-axis). Each line was divided by 25 μm distance and 80 points in total were measured. The deformation value of specimen is defined as the different value between before and after measurement values. To achieve the accuracy in deformation measurement, the stage controller was synchronized with the controller of LDS by microcomputer, where the stage speed and sampling time of LDS were set to 125 μm/s and 100 ms, respectively.

3.8 Results and discussion

3.8.1 Temperature fields

Figure 3.14 illustrates the temperature fields on the top surface of welded material and the cross-sectional views of weld beads obtained by experiments and numerical simulations. The validation of the FE thermal model was realized by comparing the weld bead profiles in the transverse direction obtained from experiments with those predicted by numerical simulation. In the figure, the red region of isothermal contour at the weld bead profiles denotes the fusion zone where temperature exceeds the melting point (1720 K). The results of FE thermal model give a good estimation of the weld bead cross-section and the fair agreement indicates validity of the FE thermal model with the experimental results.

In general, the results show that the penetration and width of weld bead tend to decrease with

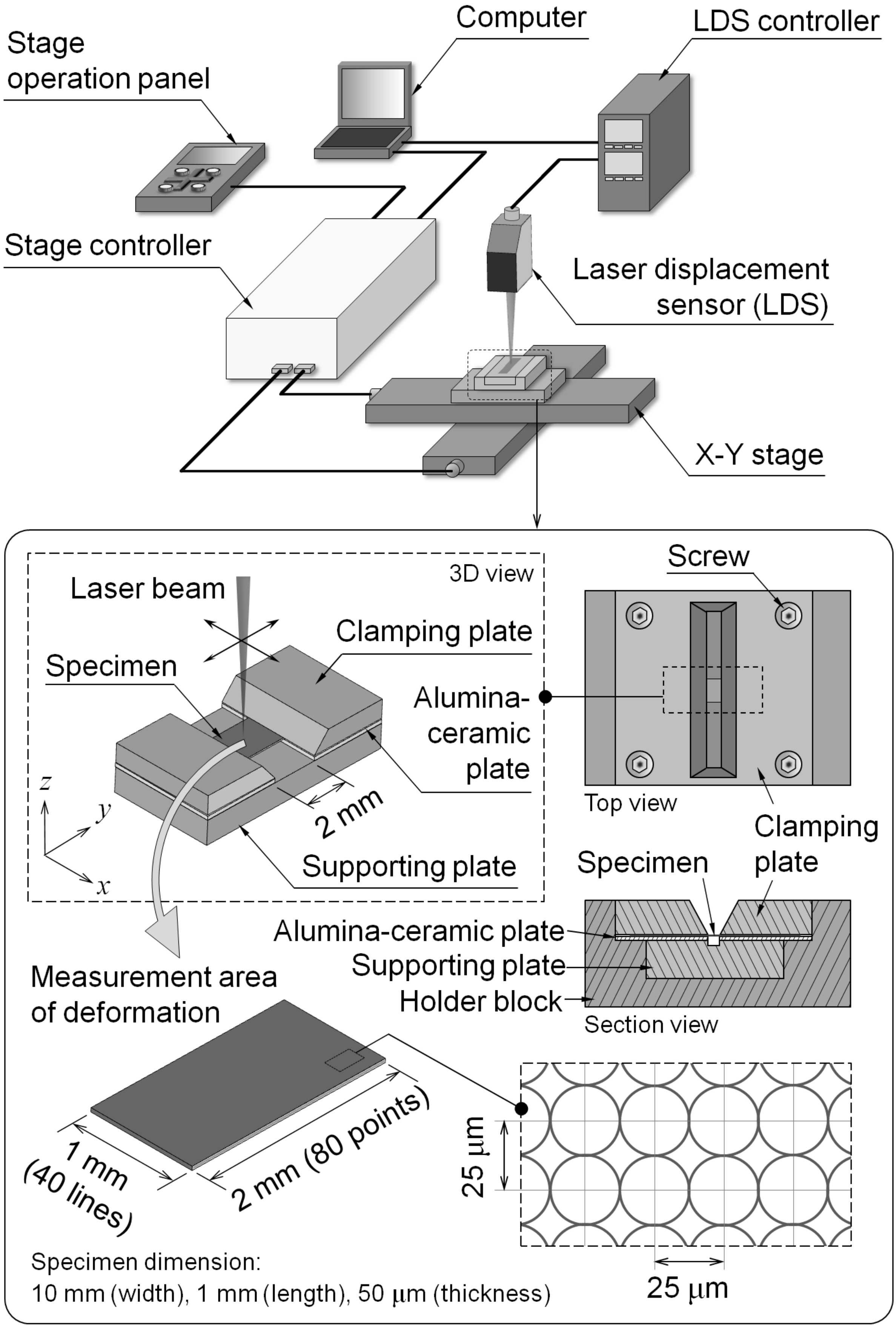

Figure 3.13 Schematic diagram of deformation measurement

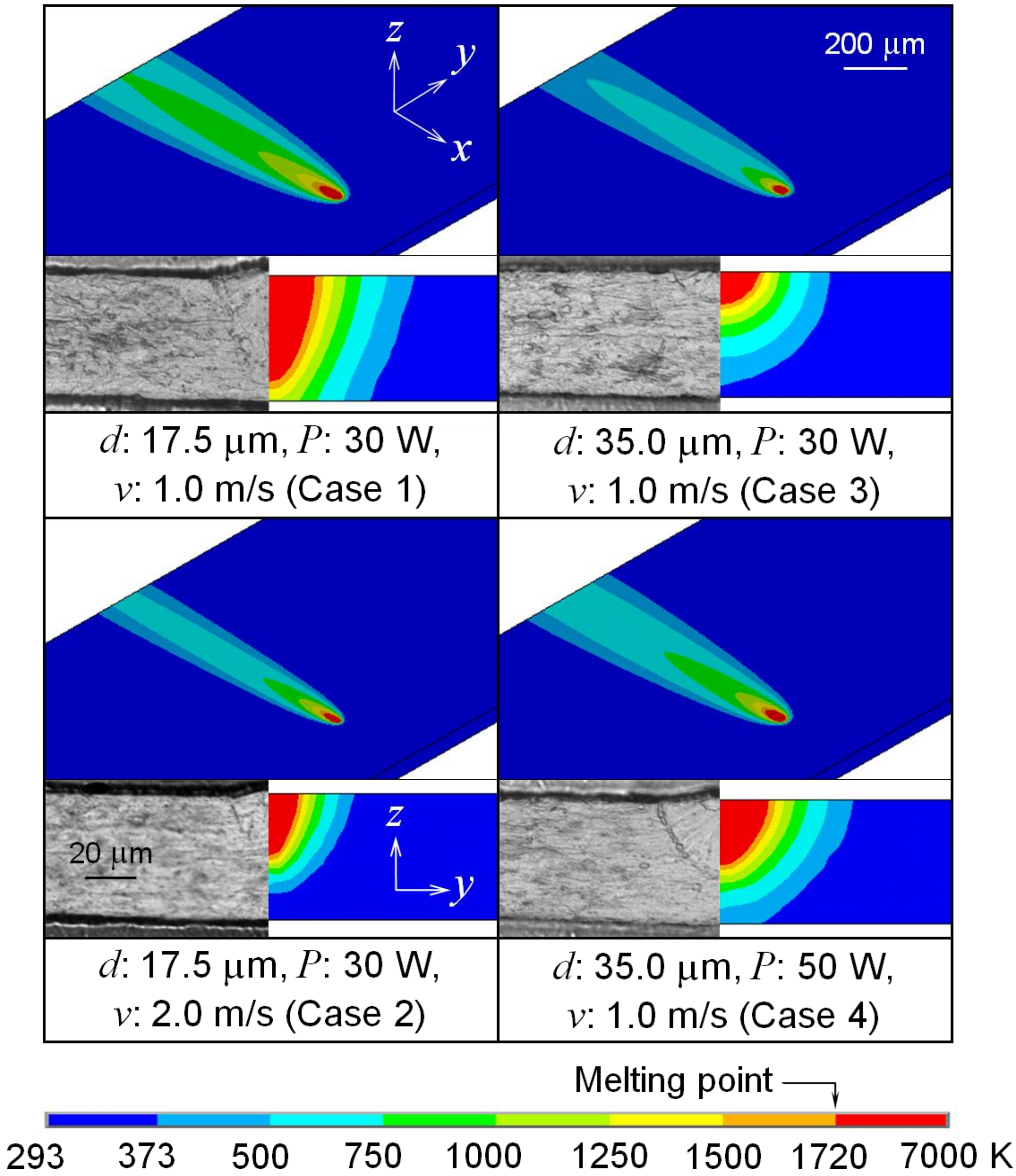

Figure 3.14 Temperature field contour at the top of weld surface and comparison of cross-sectional view between experimental and simulated weld bead geometry

the increase in the scanning velocity. The increase of scanning velocity reduced the interaction time between the laser beam and material. This time expansion caused the decreased of the maximum temperature value and heat input, causing a reduction of the molten volume. On the other hand, at constant scanning velocity, increasing laser power significantly affects the weld penetration. It is expected that the higher laser power leads to the greater weld bead geometry with increasing the power density (i.e. power per unit area).

In addition, since the laser spot diameter is an important factor in determining thermal processing characteristics, the power density can raise with a smaller spot diameter. The effect of laser spot diameter (Case 1 and 3) appears that a smaller spot diameter can yield a deeper weld penetration under the same laser power and scanning velocity. Furthermore, it can be noted that the weld penetration can be attained by smaller beam spot diameter with low laser power. From the results of thermal analysis, the stress, strain and deformation distributions are evaluated.

3.8.2 Welding stress fields

The stress evolutions are calculated based on the temperature field obtained by FE thermal analysis. **Figure 3.15** shows the contours of equivalent stress $\bar{\sigma}$ at different layers of *z*-axis. At this time, the laser beam location is 750 μm from the specimen edge (*x*=0) and it is irradiated on the specimen at 0.82 ms after the beginning of the laser irradiation and. It is clearly indicated that the higher equivalent stress concentration exists around the molten pool and there is a small level of stress in the molten pool. The equivalent stress attains low values in the molten pool because of the melting, which is free to expand in this region. These results in the blue spots located in the molten pool of the top surface, -25 μm and -35 μm layers. The same blue spot location can not be found in the bottom surface due to the fact that the weld penetration is slightly less than 35 μm and therefore, the material is solid at this bottom surface and being able to contain mechanical stress.

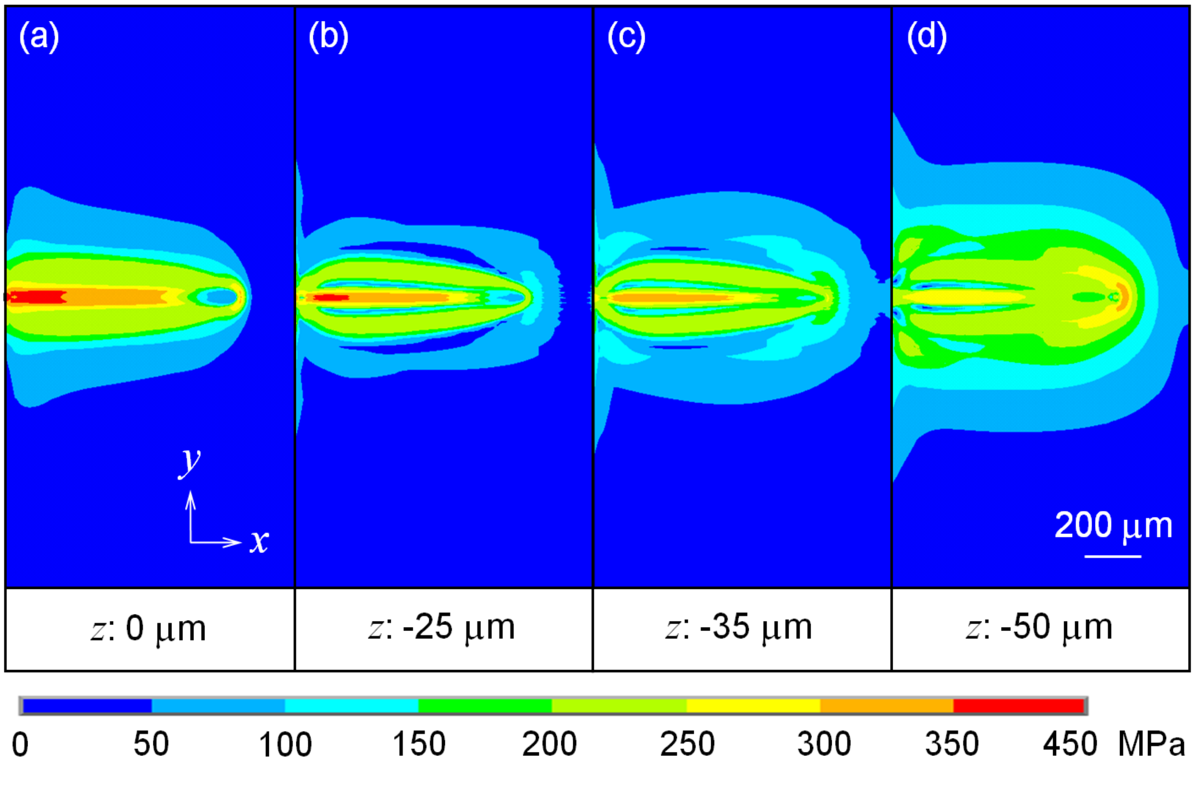

Figure 3.15 Equivalent stress distribution for different vertical layer of the specimen (*d*: 35.0 μm, *P*: 50 W, *v*: 1.0 m/s)

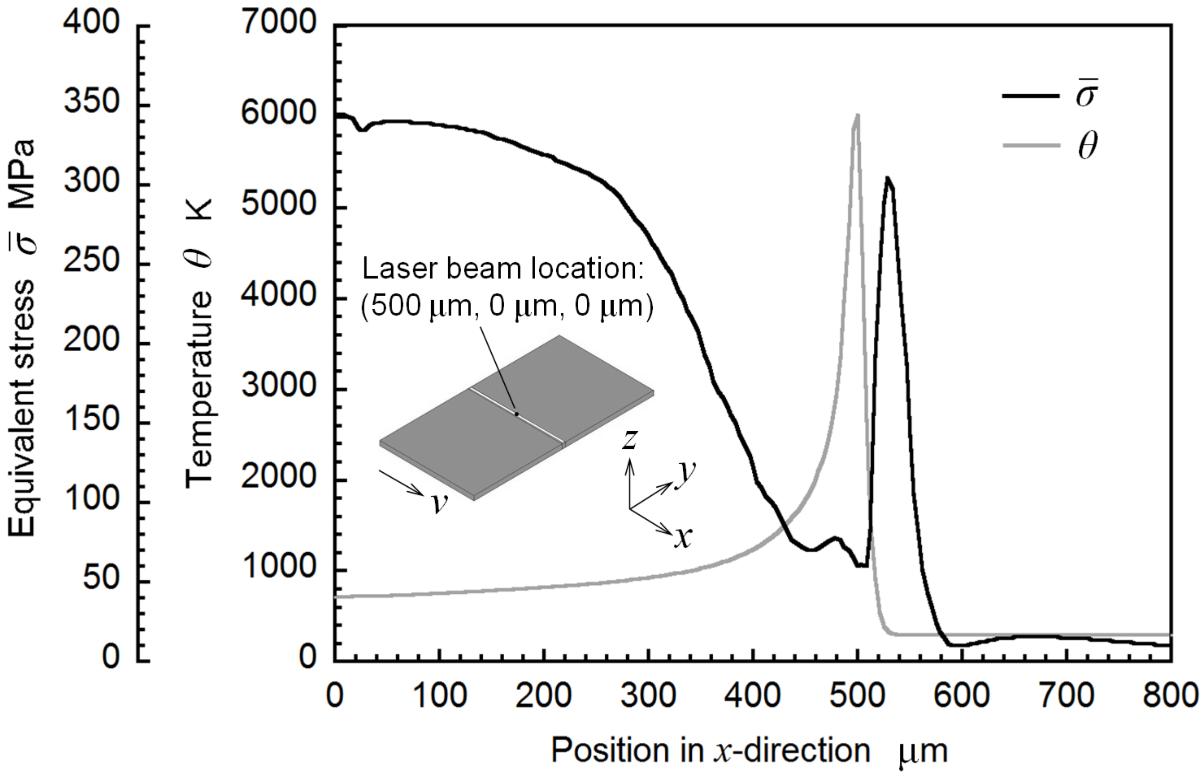

Figure 3.16 Distributions of temperature and equivalent stress at the top surface along the welding line (d: 35.0 μm, P: 50 W, v: 1.0 m/s)

Figure 3.16 shows the temporal distribution of temperature and equivalent stress calculated at the top surface along the welding line (x-axis) and the laser irradiated spot located at the middle of the specimen (x: 500 μm). It can be seen clearly in the front region to the laser irradiated spot, the equivalent stress attains high values because of the rapid increment of temperature and consequential large temperature gradient in this region. As time progresses, the equivalent stress reduces when temperature reaches its peak value at the laser irradiated region because of the elastic modulus or Young's modulus, which reduces with increasing the temperature. However, the temperature reduces as the cooling phase undergoes in the far region behind to the laser irradiated spot. Therefore, the equivalent stress increases once the temperature reduces. In addition, the equivalent stress becomes the residual stress in the solidified welding region. Based on the magnitude of equivalent stress exceeded the yield limit at 200 MPa, it can be confirmed that the plastic zone occurred at the front region to the laser beam and the cooled down region, which located far behind from the laser beam.

Figure 3.17 shows the equivalent stress distribution in the width direction along the y-axis at the middle of specimen (x: 500 μm) for a heating period (t: 0.55 ms) and three different cooling periods (t: 1.1 ms, 1 s, 300 s). When the laser irradiated spot reaches at the point A (t: 0.55 ms), the equivalent stress attains low values because of the attainment of high temperature in the region of irradiated spot center (y<17.5 μm). This is particularly true at the heating period, the occurrence of

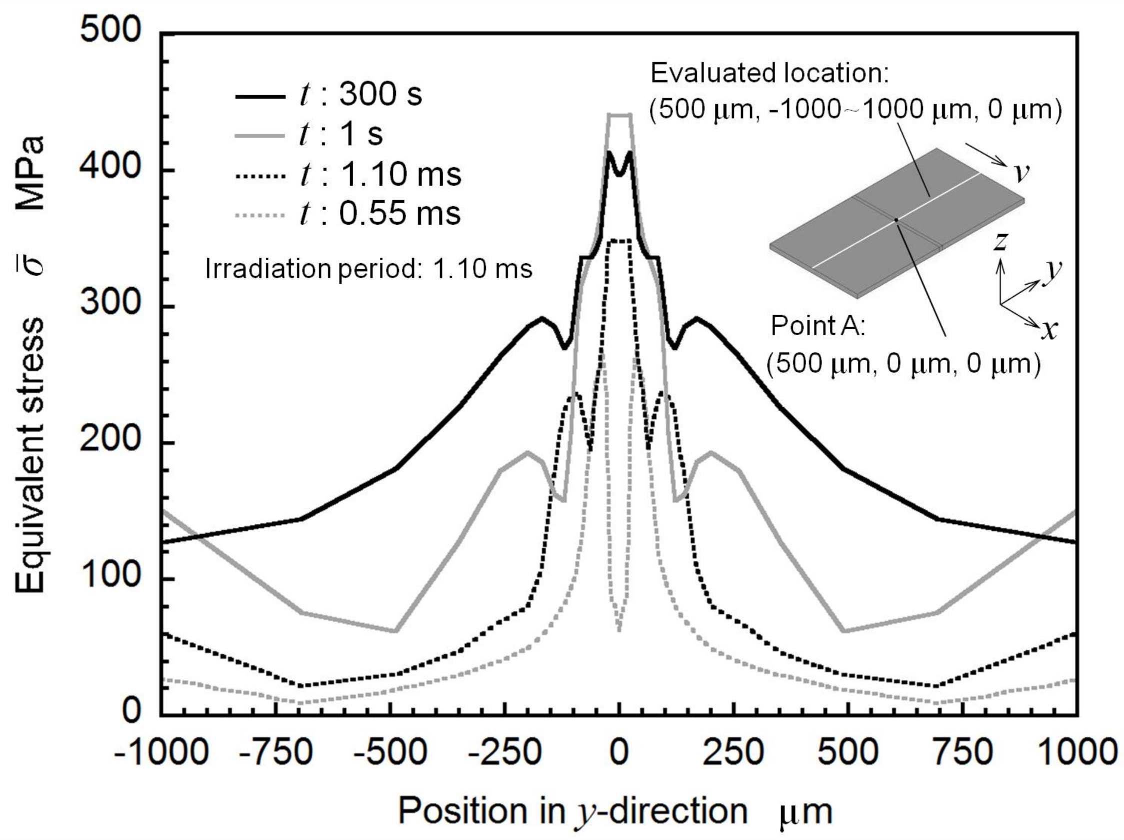

Figure 3.17 Equivalent stress distribution during laser irradiation and cooling along the width of specimen (d: 35.0 μm, P: 50 W, v: 1.0 m/s)

low equivalent stress is attributed to the low elastic modulus at elevated temperatures. It can be seen that the attainment of high stress levels in the region next to the irradiated spot edges, which has a high temperature gradient. In the early cooling period (t: 1.1 ms), the residual stress in the region of the irradiated spot center attains high level of equivalent stress. This is associated with the heat conduction, in which the high temperature gradient is developed in this region as a consequence of the temperature reduction. However, the residual stress remains low in the region next to the irradiated spot edge because of the low cooling rate. In addition, since the heat conduction transfer from the irradiated spot center towards its neighborhood is low because of the low temperature gradient developed in this region, it should be noted that the heat conduction enhances as the temperature gradient increases or vice versa. As the cooling period progresses further, the temperature reduces down to an initial temperature of the specimen and the equivalent stress attains higher values than those corresponding to the early cooling periods.

The distribution of normal and shear stresses during laser irradiation are shown in **Figure 3.18**. It can be clearly found that the magnitude of the normal stresses (σ_{xx}, σ_{yy}, σ_{zz}) are higher than those of shear stresses (τ_{xy}, τ_{yz}, τ_{xz}). Therefore, all the shear stress components being negligible since do not contribute significantly to the deformation.[3.19), 3.29)] **Figure 3.19** shows clearly that the

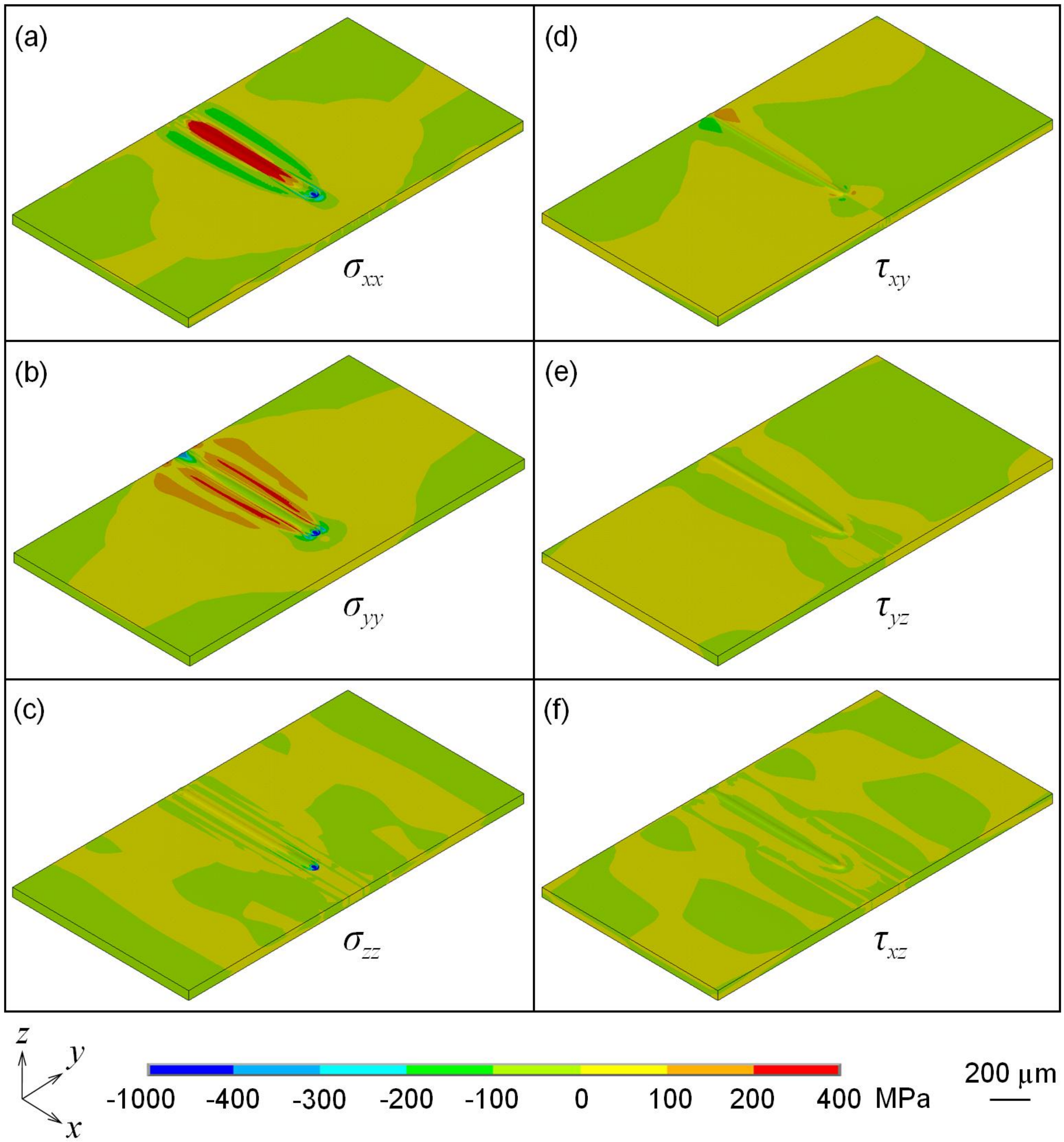

Figure 3.18 Distributions of normal stresses (a-c) and shear stresses (d-f) during laser irradiation (d: 35.0 μm, P: 50 W, v: 1.0 m/s)

magnitude of longitudinal stress σ_{xx} is higher in the front region to the molten pool and confirmed the plastic compression zone occurred because the expansion of this region is restrained by the surrounding material where the temperature is lower. It can be observed that the normal stresses consist high compressive stress with similar magnitude for each normal stress in the molten pool region. However, the through thickness stress σ_{zz} shows the less significant during the cooling period in the solidified weld zone and consequently resulted in low residual stress and similar with shear stresses, which does not contribute significantly to final deformation. Therefore, the two major stress components, viz. longitudinal σ_{xx} and transverse σ_{yy} stresses are discussed.

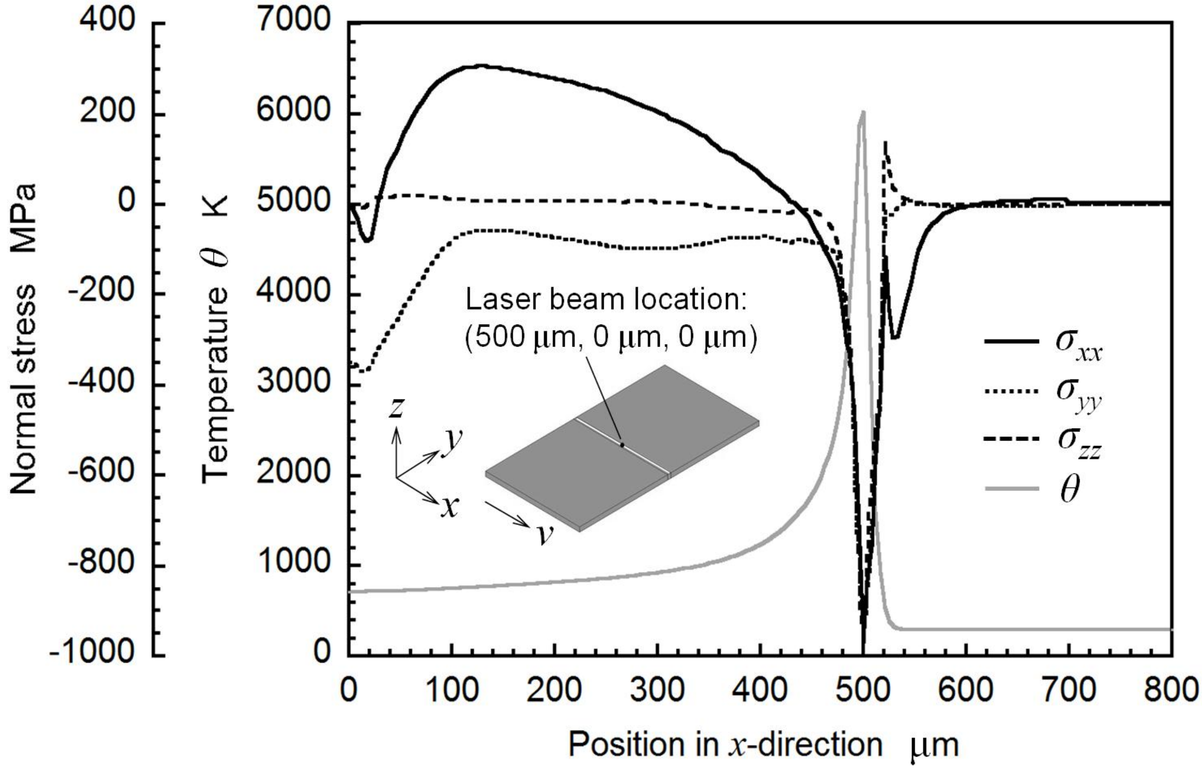

Figure 3.19 Distributions of temperature and normal stresses at the top surface along the welding line (d: 35.0 μm, P: 50 W, v: 1.0 m/s)

As shown in **Figures 3.18** and **3.19**, the longitudinal residual stress has the stronger influence over the solidified weld zone compared with the transverse residual stress. The longitudinal residual stresses are largely tensile and generated at the solidified weld zone and the HAZ, while compressive residual stresses were generated away from these zones. The transverse residual stresses are low compressive stresses near the weld zone and balance with tensile stresses in regions away from the weld zone. Since the longitudinal stress shows the most significant effect on stress distribution for entire welding cycle, the longitudinal stress distribution at four different time periods of the heating and cooling processes is discussed as shown in **Figure 3.20**. During the laser irradiation on the specimen (t: 0.55 ms), it shows that the regions of compressive stress in the molten pool is suddenly heated up when the laser beam reaches a neighboring location and generates a thermal expansion. In the front region to the molten pool, the unloading from yield surface proceeds elastically until the material yields in compression. As the heating proceeds, the molten pool is longitudinally in compression grows rapidly and attained the yield limit, in which the material undergoes plastic deformation. In addition, it is confirmed that the vicinity regions to the molten pool generates the tensile stress to balance with the compressive stress near the molten pool and counteract the thermal expansion constraining material in the surrounding. For regions behind the laser irradiation location, the cooling phase is taking place. Once the molten material starts to solidify, the self-balanced

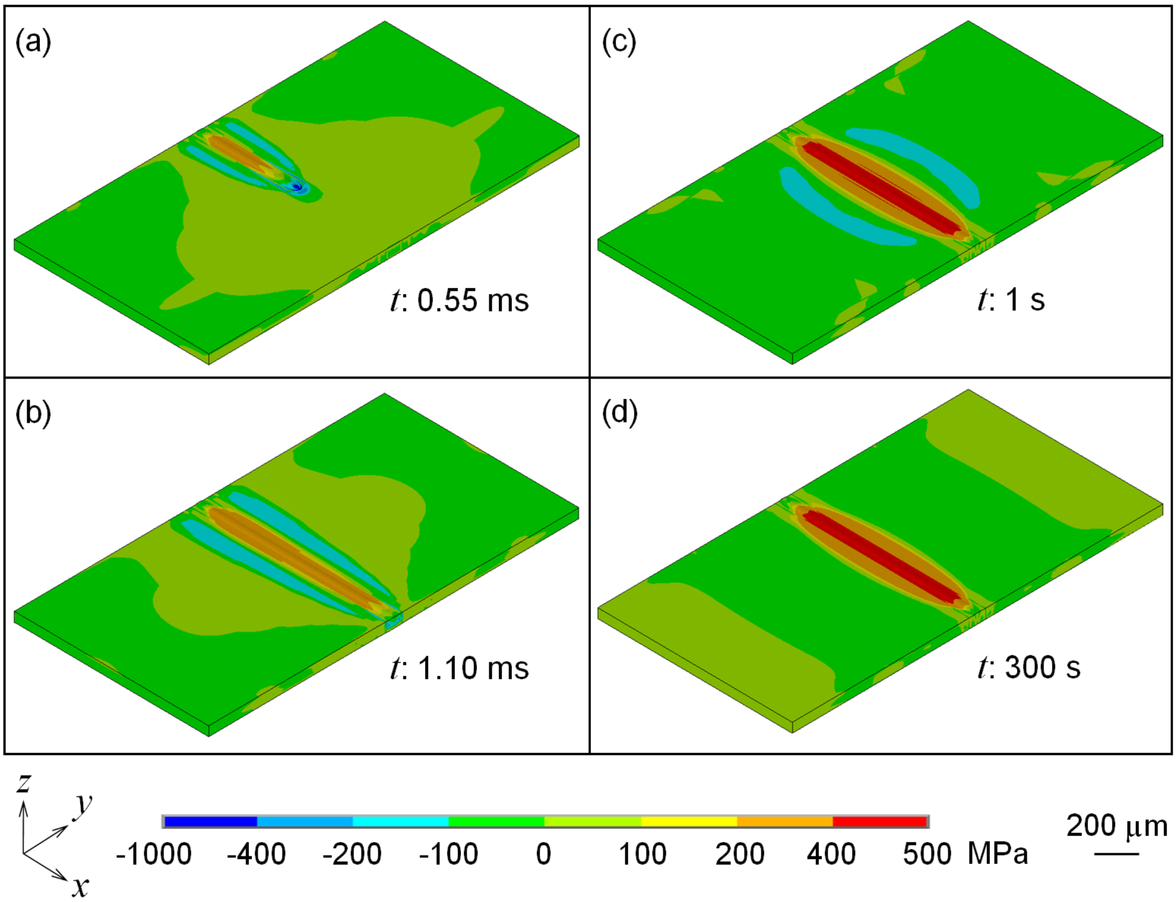

Figure 3.20 Distributions of longitudinal stress during (a) laser irradiation and (b-d) cooling (d: 35.0 μm, P: 50 W, v: 1.0 m/s)

residual stresses remaining without any external load. The material was cooled down and contracted rapidly in the region close to the weld zone, which causes a new positive sign of tensile residual stress. At the distance sufficiently far from the laser irradiation location, the further cooling and contraction generate higher residual tensile stress with the plastic tension zone and maintaining the deformation shape. It also can be seen that the longitudinal residual stress is almost uniformly distributed along the x-axis but reduces to zero at the free surfaces of the starting and ending edges of the welding line. Furthermore, the region far away from the solidified weld zone remained elastic during the entire welding cycle.

Figure 3.21 shows the longitudinal stress histories at two evaluated points located at the top (Point A) and bottom (Point B) surfaces, where the laser location is 500 μm from the specimen edge. It is found that the far ahead region to the irradiated spot undergoes lower tensile stresses, while the temperature is still in the ambient temperature. The compressive stresses start developed in the regions close to the irradiation spot. The point A rapidly undergoes the higher compressive stress because the expansion of the molten pool is restrained by the surrounding material, where the temperature is lower. At this time, the point B undergoes the tensile stress, and this stress is

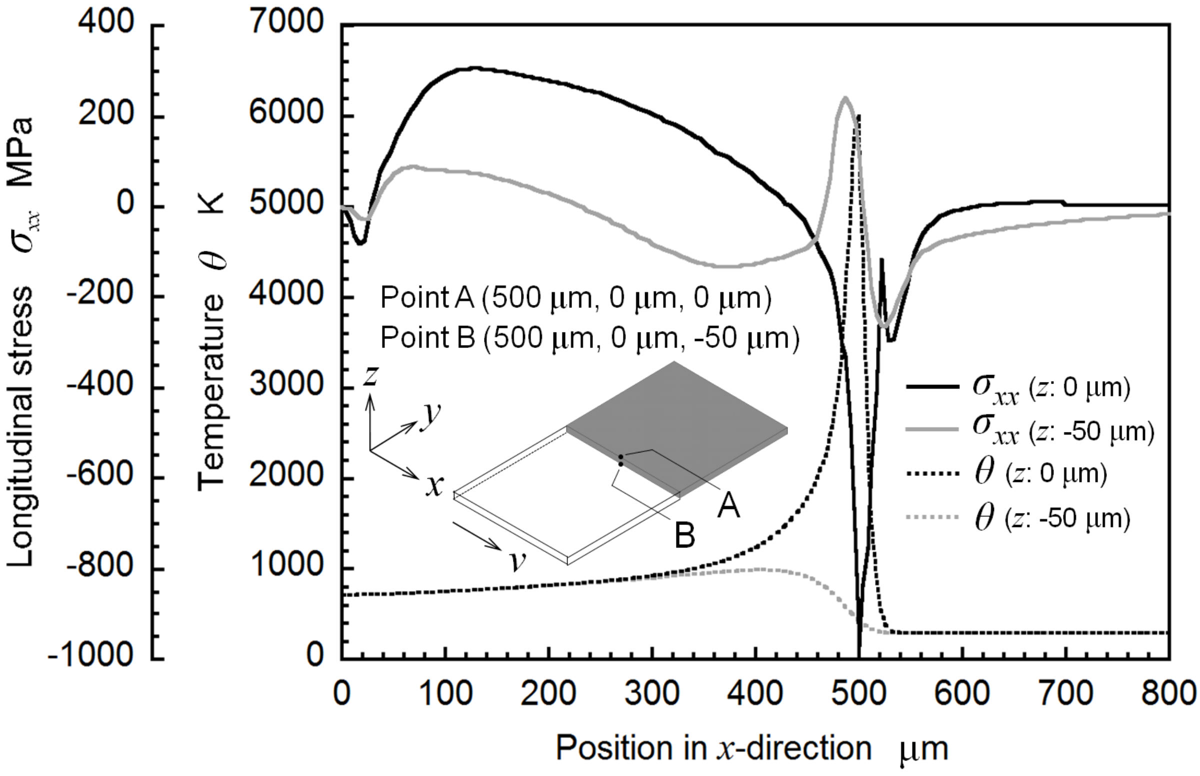

Figure 3.21 Temperature and longitudinal stress distributions of two evaluated points on the top and bottom surfaces (d: 35.0 µm, P: 50 W, v: 1.0 m/s)

attributed to the restriction of the surrounding material. After the laser beam moves away from the point A, the compressive stress rapidly decreases due to the rapid cooling in the region and change to the tensile stress due to the contraction of the material. On the contrary, during this period of time, the compressive stress is generated at the unmelted point B to balance the tensile stress at the top surface of point A. Because of the less cooling effect, the compressive stress at this point relatively smoothly decreases. As the further cooling periods, the both points attained tensile stress, which the stress magnitude is higher at top surface than lower surface. Therefore, the final deformation shape of specimen after the final cooling period is directly affected by the different stress magnitude between both surfaces.

Once the molten material starts to solidify, the shrinkage takes place in the weld zone, which then exerts stresses on the surrounding HAZ. These stresses reside in the material after welding and may result in unwanted distortions. The self-balanced stresses remaining without any external load are known as residual stresses. The two major residual stresses of longitudinal and transverse residual stresses are discussed with the influence of welding parameter such as spot diameter, laser power and scanning velocity on the welding residual stresses at the final cooling periods (t: 300 s). **Figures 3.22**, **3.23** and **3.24** show the longitudinal and transverse residual stresses at the top surface of specimen for different spot diameter, laser power and scanning velocity, respectively.

In general, the tensile residual stresses remain at the middle of specimen along the center of welding line after the welding process. While the compressive residual stresses occurs at the both edges of the welding line. The large tensile residual stress is generated in the molten zone and the magnitude of these residual stresses is larger than the yield strength of the weld material. However, it decreases as increasing in distance from the weld centreline. The magnitude and distribution of compressive residual stress is generated to balance with the regions under the tensile residual stress. It can be observed that the maximum stresses are present in the molten zone both in the case of longitudinal and transverse residual stresses. However, the longitudinal residual stress is more dominant over the transverse stress. The material in the welding significantly longitudinal tensile stresses because of the welding contraction during cooling, which the holding of the base material to the molten zone for maintain the original length. It causes the molten zone to be plastically deformed and considerable influence over the deformation. In addition, the transverse residual stress is smaller than the yield strength in the molten zone.

Figures 3.22(a), **3.23(a)** and **3.24(a)** show the residual stresses at the middle of the specimen width and its distribution along the length of welding line (*x*-axis). The transverse stress distribution in the molten zone shows two peaks at the free surfaces of the starting and ending edges of welding line. These transverse stresses are negative values, which indicates that the material at the two edges undergoes compression laterally although the material in the middle section of the specimen length undergoes tension laterally. This is resulted from the base material trying to maintain its original length significantly during cooling. Referring to the results of longitudinal residual stress distribution, it is clear that the weld material is plastically deformed and significant tensile stresses along the length of the specimen are evident.

Figures 3.22(b), **3.23(b)** and **3.24(b)** show the residual stresses at the middle of the specimen length (x: 500 μm) and its distributions along the width of y-axis. It can be seen that along the transverse direction, the longitudinal stress becomes negative (compressive) in the region with some distance away from the welding line. However, the longitudinal tensile stress in the molten zone is significantly greater than the longitudinal compressive stress in the base material and passing through zero at a small distance from the weld centerline. It can be noted that the tensile stress is counterbalanced by the compressive stress and this attributed to the correctly modeled shape of the molten zone. In addition, it shows that the stress gradient within the molten zone is very steep and it is strongly affected by high temperature gradient on that region, which locally concentrated by the heat source of laser beam. Transverse residual stresses are much smaller than longitudinal stresses and reaches its peak value close to the molten zone or HAZ, and gradually reduces toward to the edge of the specimen. Moreover, other areas of the welding plate, the residual stresses are much lower than the material yield strength and indicating that the transverse shrinkage is mainly resulted from

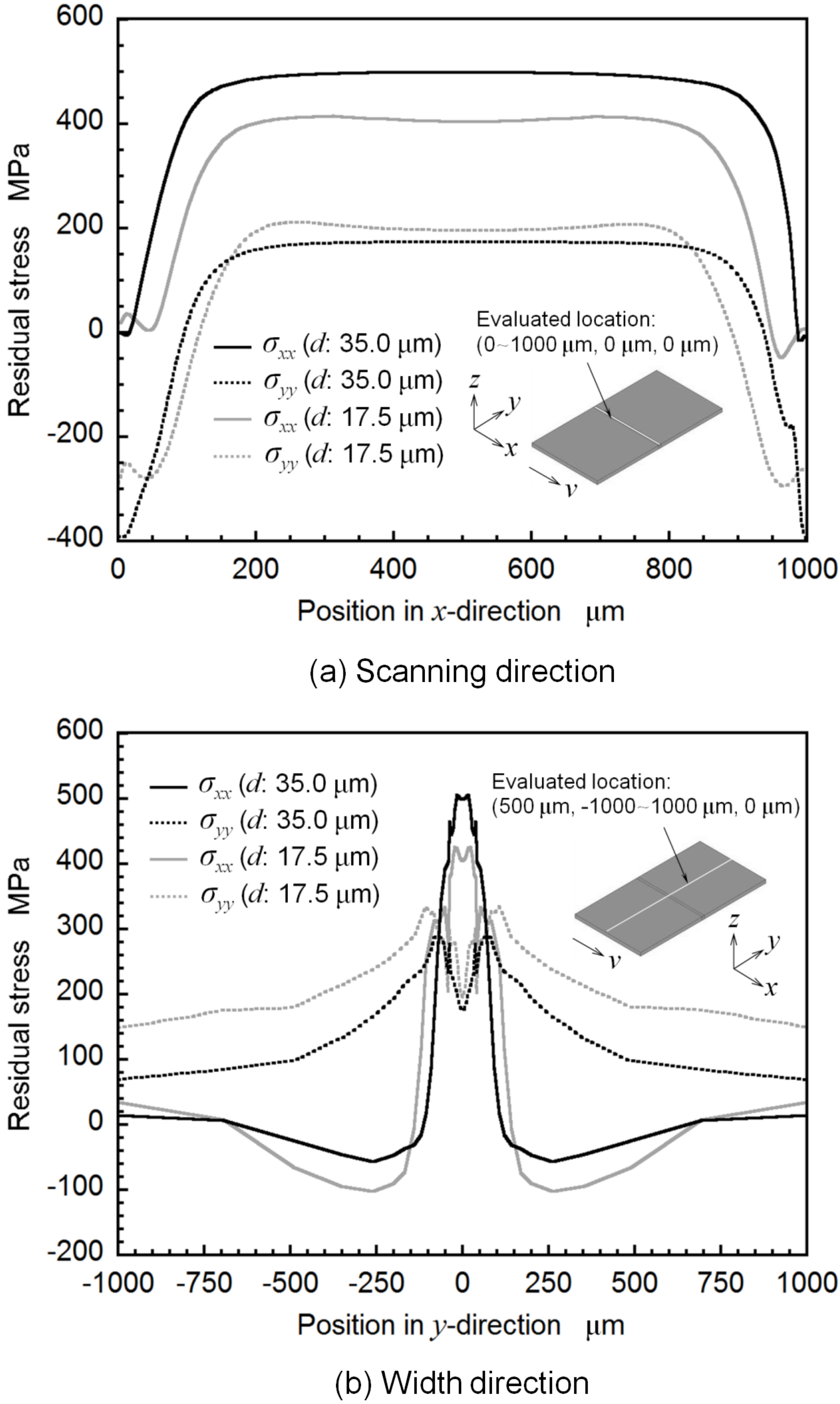

Figure 3.22 Longitudinal (σ_{xx}) and transverse (σ_{yy}) residual stress distributions along (a) x-axis and (b) y-axis under different spot diameter (P: 30 W, v: 1.0 m/s)

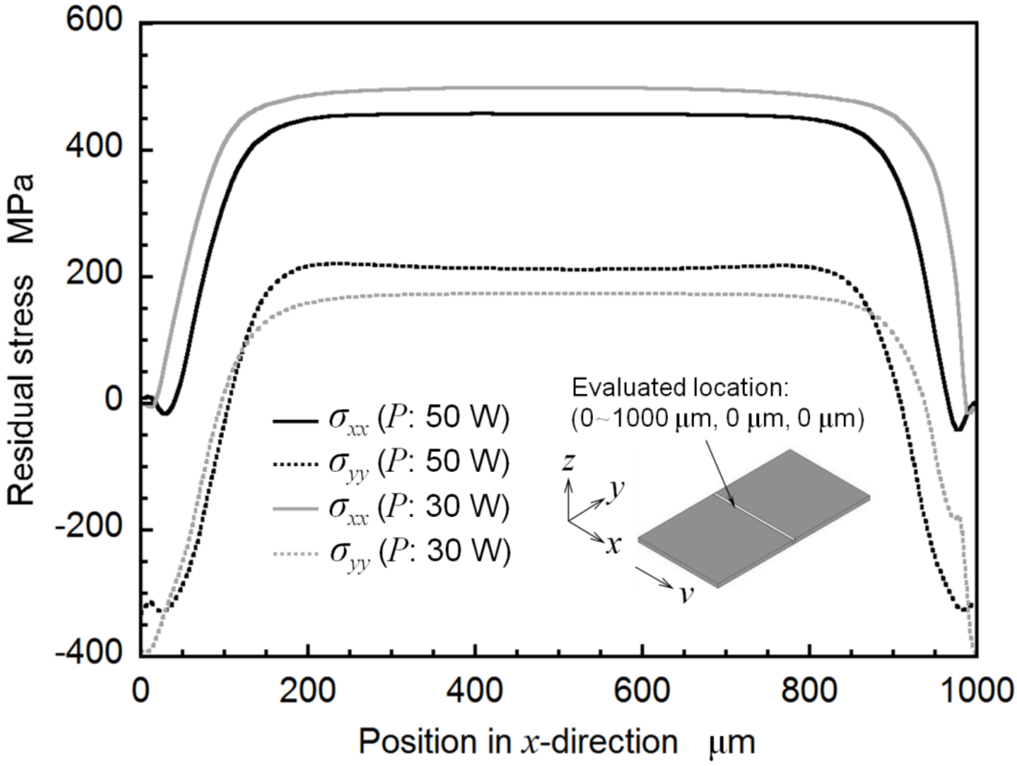

(a) Scanning direction

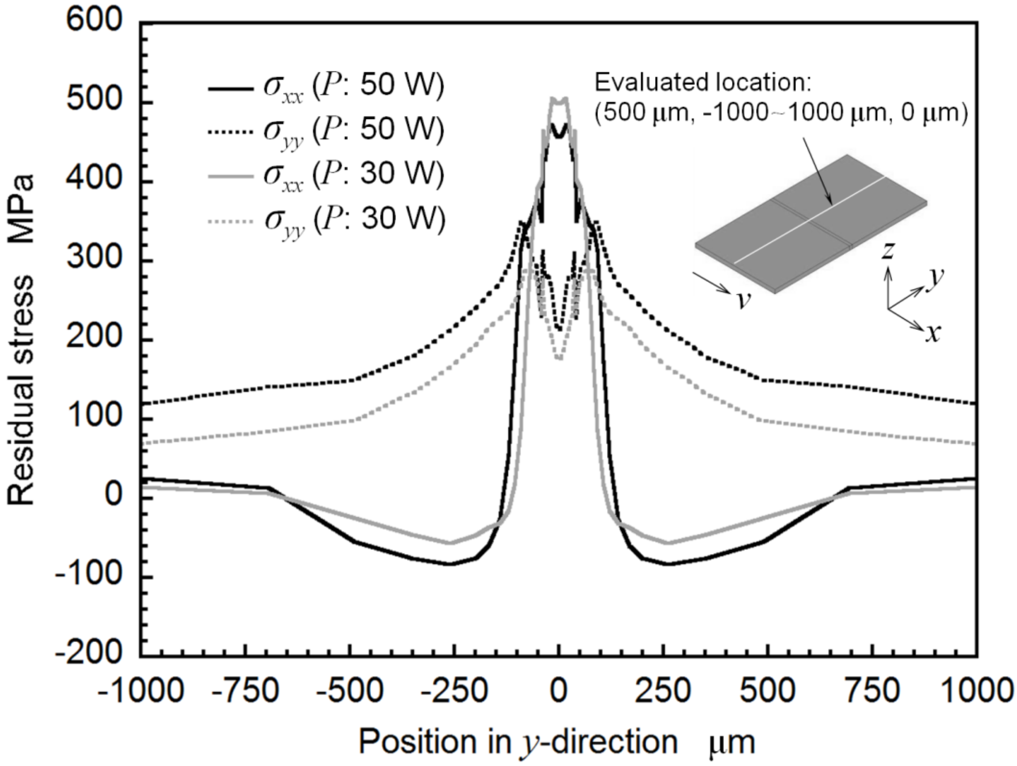

(b) Width direction

Figure 3.23 Longitudinal (σ_{xx}) and transverse (σ_{yy}) residual stress distributions along (a) x-axis and (b) y-axis under different laser power (d: 35.0 μm, v: 1.0 m/s)

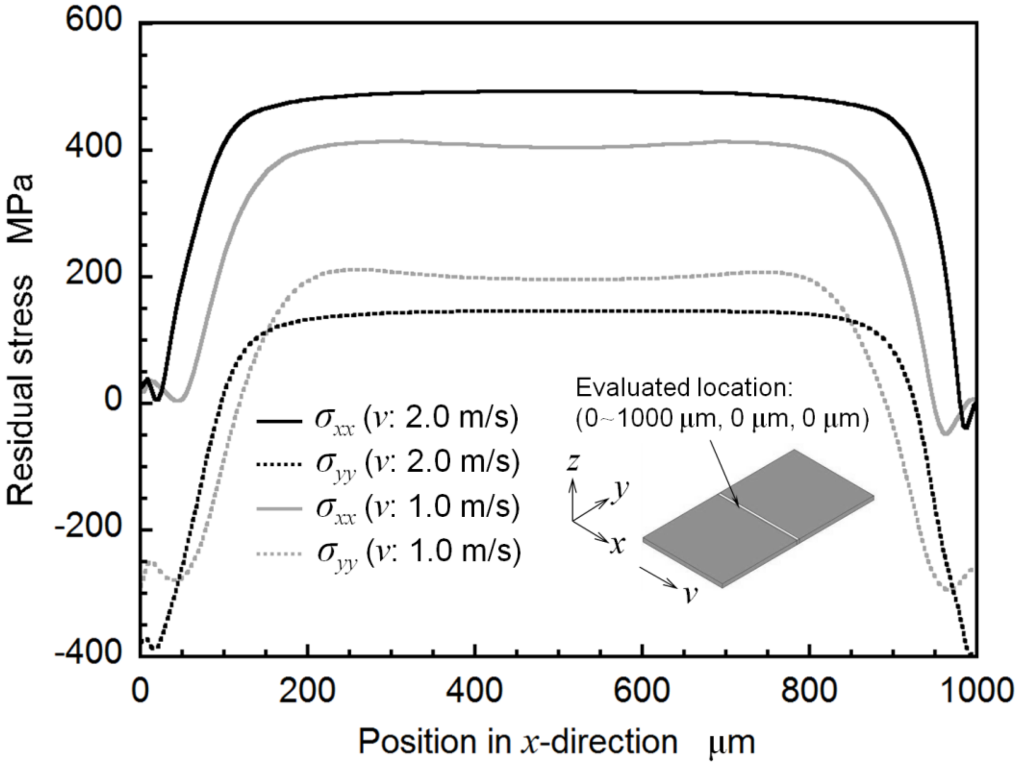

(a) Scanning direction

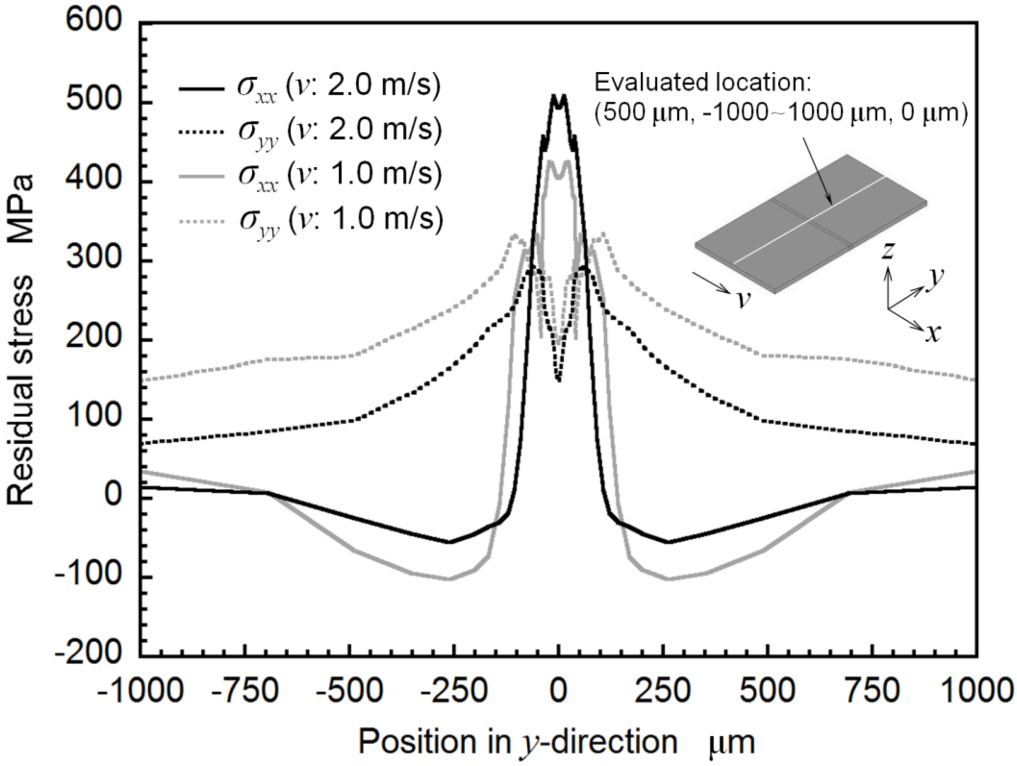

(b) Width direction

Figure 3.24 Longitudinal (σ_{xx}) and transverse (σ_{yy}) residual stress distributions along (a) x-axis and (b) y-axis under different scanning velocity (d: 17.5 μm, P: 30 W) thermal strains during expansion and contraction in the welding process.

As shown in **Figure 3.22**, the varying spot diameter affects the width of the tensile residual zone at the surrounding of weld centerline. Since the large spot diameter generates lower energy density and resulted narrower weld bead as shown in **Figure 3.14** (Case 3), it can be observed that the narrower tensile residual zone at the weld centerline and balanced with lower compressive residual stresses around the weld line. However, the higher level of longitudinal tensile residual stress generated on the solidified molten zone by larger spot diameter. This is due to the lower temperature during irradiation compared to the small spot diameter, which caused the earlier cooling period started at the solidified molten zone. Consequently, the early stress transformation to tensile stress makes the final residual stress at the weld centerline is higher with larger spot diameter. It can be clearly observed in **Figure 3.25**, which shows the equivalent stress distribution on the top surface of specimen during the intermediate of laser irradiation and the end of cooling period. The higher tensile stress already generated at the solidified zone with the large spot diameter at the same location and time during irradiation period. On the contrary, the residual stress distributions show that the wider tensile residual zone at the weld centerline and balanced with higher compressive residual stresses around the weld line are generated by the small spot diameter at the end of cooling period. Therefore, the different between size of spot diameter will significantly affected on the specimen deformation.

Laser power is one of the most important process parameters governing the heat input, which is directly proportional to energy supplied to the weld material. As shown in **Figure 3.23**, the residual stresses increase with increasing the laser power. This is due to the slower cooling rate resulted by increased the laser power. In other words, the effect of laser power directly influences the temperature distributions and consequently the residual stress profile in the welded material. High laser power generates wider residual stress field on both longitudinal and transverse residual stresses. It also generated a relatively wide plastically deformed zone, which caused the residual stress tends to be large with the increasing laser power along the transverse direction. It also can be seen clearly in **Figure 3.25**, where the distribution of final residual stress with high laser power is wider and higher magnitude.

Scanning velocity represents the distance travelled by the laser beam along the welding line per unit time. Since the scanning velocity inversely proportional to the heat input, the heat input decreases with the increasing of scanning velocity and as the result, the weld bead size is reduced. As shown in **Figure 3.24**, a low residual stress generated by faster scanning velocity due to the faster cooling rate and smaller volume of weld. In addition, as the temperature of the heated area is low by faster scanning velocity, the reduced local shortening leads to a low residual stresses. For the low scanning velocity, the temperature is higher than that at the high scanning velocity. The increase of

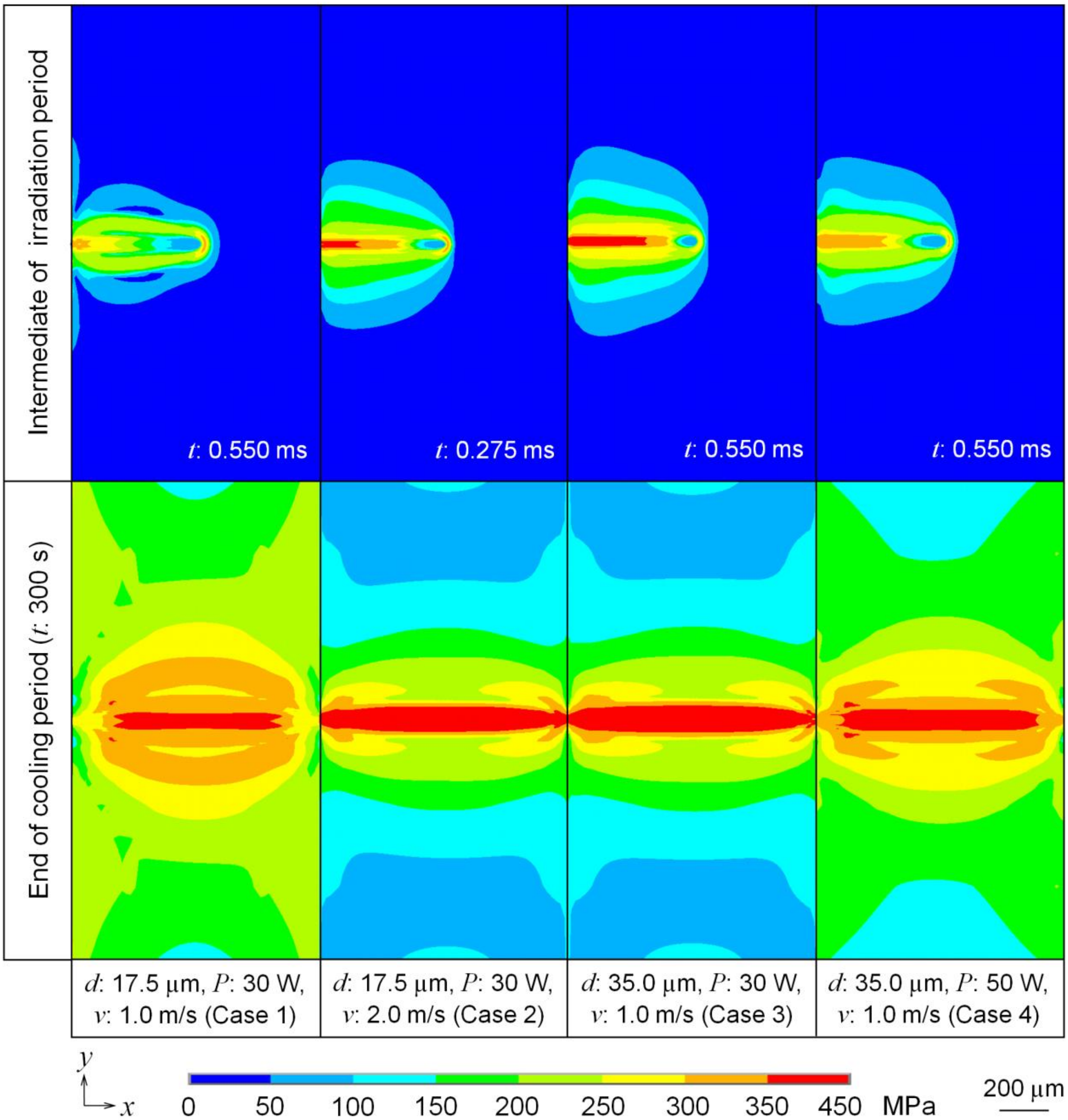

Figure 3.25 Equivalent stress distribution on the top surface of specimen during intermediate of laser irradiation and end of cooling period for four welding conditions

stress beyond the minimum value results from the thermal expansion of the material immediately after the current location. For the same reason, the rise of stress is higher at the lower scanning velocity. As a result, the residual stresses are lower for the specimen scanned at higher velocity than at the lower scanning velocity.

Refer to the **Figure 3.25**, it can be clearly seen that the higher level of longitudinal tensile residual stress generated at the solidified molten zone by the lower laser power, larger spot diameter and faster scanning velocity is a consequence of the lower temperature during irradiation period caused the earlier cooling period started at the solidified molten zone. In addition, the early stress transformation to tensile stress makes the final residual stress at the weld centerline higher with these level of process parameters. Referring to the residual stress results, the influence of heat input significantly affected to the distribution of residual stresses in the weld material. Furthermore, it can be noted that the formation of stress fields which also persist after the specimen temperature returns to room temperature and may still be present when the specimen is used in subsequent welding process.

3.8.3 Plastic strain fields

Thermal stresses occur in the weld zone and the adjacent areas due to the non-uniform expansion and contraction of the weld metal and surrounding base metal by heating and cooling cycles during welding,. During the heating phase, the strains always generates induce plastic deformation of the material. The stresses resulting from these strains combine and react to generate internal forces that cause a variety of welding deformations. **Figure 3.26** shows the equivalent strain distribution of the specimen during the laser irradiation and cooling phase. The regions below the

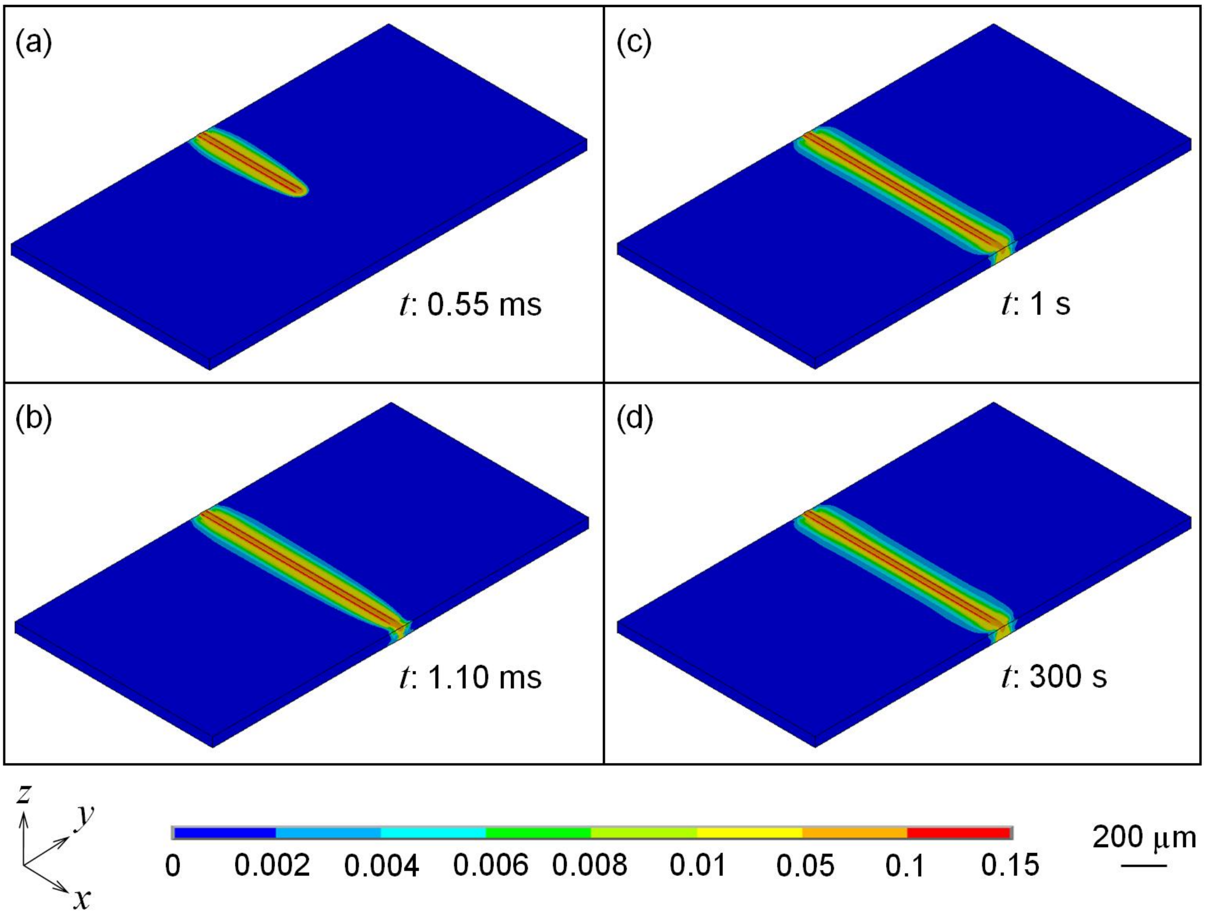

Figure 3.26 Equivalent strain distribution during (a) laser irradiation and (b-d) cooling (d: 35.0 μm, P: 50 W, v: 1.0 m/s)

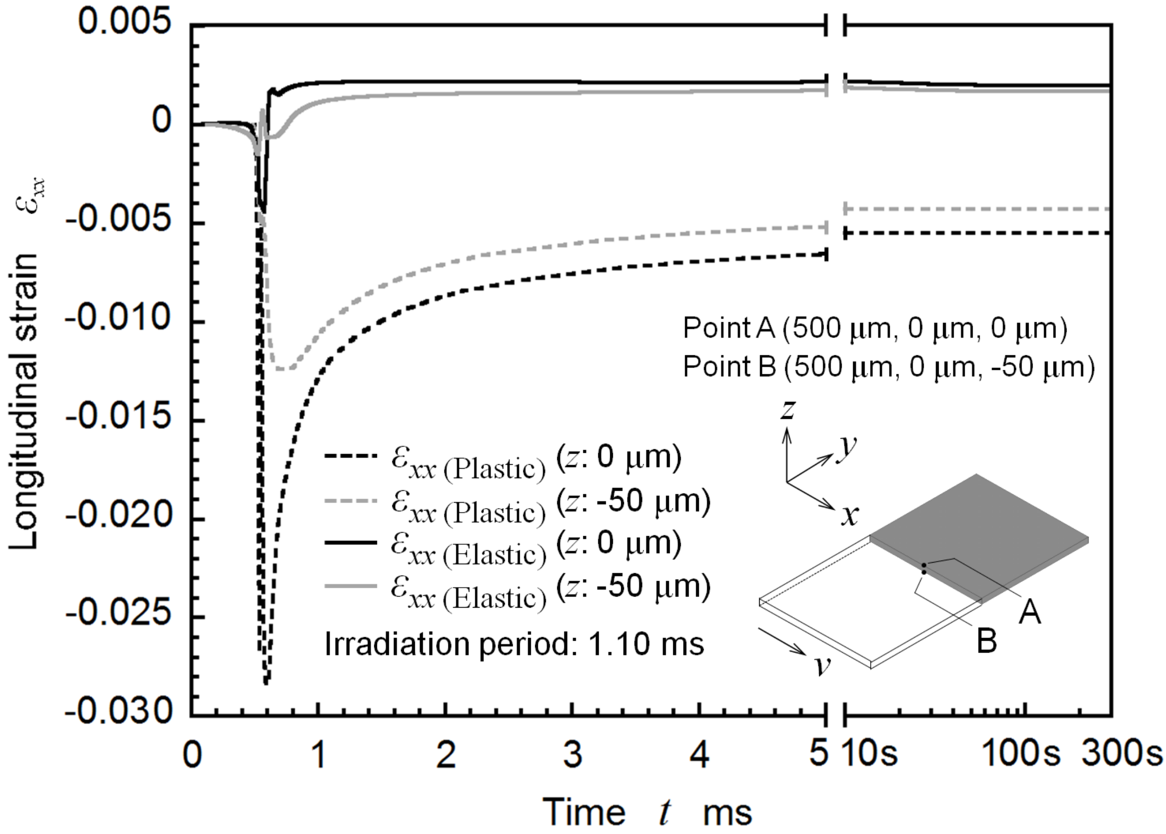

Figure 3.27 Longitudinal strain histories of two evaluated points on the top and bottom surfaces (d: 35.0 μm, P: 50 W, v: 1.0 m/s)

laser beam want to expand, while the expansions are prohibited by the surrounding regions heated to lower temperatures causing compressive plastic strains in regions near the laser beam. These compressive strains are the cause of the deformation that remains after the specimen cooled down to room temperature. It can be observed that at the beginning of the welding, the strains are non-uniform and the specimen is deformed from the edge of laser entry to the irradiated areas. At the end of the welding process and especially after cooling, the strain become more uniform.

Figure 3.27 shows the the strain histories at the middle of specimen (x: 500 μm) on the top and bottom surfaces. The total strain is considered to be sum of elastic and plastic strains. Since the plastic strain is very high compared with the elastic strain and dominate during heating and cooling periods, the strain field is only discussed on the plastic strain distribution. It can be seen that the top surface rapidly undergoes the high compressive strain started from 0.55 ms when the laser irradiation reaches at the point A (Middle point of welding line on top surface) and sufficiently high temperature is reached, which resulted the specimen deforms downward against the laser beam. This is due to the thermal expansion of the irradiated zone is constrained by the surrounding cool base materials. Both the top and bottom surfaces tended to thermally expand during laser irradiation. It can be seen that the plastic strain is higher compressive at the top surface of specimen and slightly low compressive on the bottom surface. However, as the thermal expansion was restricted by the surrounding material and especially by the restriction of clamping edges, it led to the compressive plastic strain remaining until the cooling period. Moreover, since the top surface was heated to a higher temperature and had a stronger tendency to expand. Compressive plastic strain was more induced at the top surface, which makes the specimen deforms with reversed upward direction in cooling period, while the bottom surface undergoes a slight compression resulted from the heating period. In addition, the plastic strain is reduced and it changes only in magnitude as the material cools down but remains different from zero even the specimen temperature returns to a homogeneous state in cooling period.

Figure 3.28 shows the distributions of temperature, stress and plastic strain at the middle of specimen (*x*: 500 μm) along some distance of the *y*-axis for a heating period (*t*: 0.55 ms) and three different cooling periods (*t*: 1.1 ms, 1 s, 300 s). Since the plastic strains are significantly affected on the molten zone and its surrounding areas, the evaluated location of plastic strain was carried out up to 250 μm from weld centerline. The temperature field at specimen surface rapidly increase to peak temperature during laser beam irradiation and high temperature gradients occurred at the area close to the weld centreline, which resulted the higher stress gradient. Due to the rapid diffusion of the heat into the surrounding materials in the laser irradiation zone, the specimen temperature gradually reduces to room temperature in cooling periods. Based on the stress distribution, the molten pool and HAZ expand thermally at the laser irradiation period and the expansion is restricted by the base material. This cause the area to be effectively in compression resulting in a plastic strain. The plastic strain was developed when this compressive stress exceeds the yield stress at elevated temperature. It can be observed that the large compressive strain develops in the weld center line and the plastic deformation occurs. However, the tensile strain generated near to the center line and affected directly from the low compressive stress on that region to keep force equilibrium, which the narrow molten pool was generated on the initial heating period when irradiation spot just reaches on the center of the specimen. When the temperature is reduced at the initial of the cooling time (*t*: 1.1 ms), the compressive stress at the central area of irradiation spot and surrounding area changes to tensile stress due to the yielding strength of material increases with decreasing temperature, which the plastic strain decrease with the temperature and part of the compressive strain generated in the irradiation period is cancelled out in the cooling period. As the cooling period progresses further to the ambient temperature, the residual stresses along the specimen are tensile, while the compressive residual strains are distributed and remained until the end of the cooling period. These compressive residual strains cause shrinkage in the laser irradiated area and lead to the final deformation angle. However, a tensile residual strain is found at the locations near to the weld zone due to the tensile force generated by thermal shrinkage during cooling period.

Figure 3.29 shows the temporal distributions of plastic strain for the four different welding

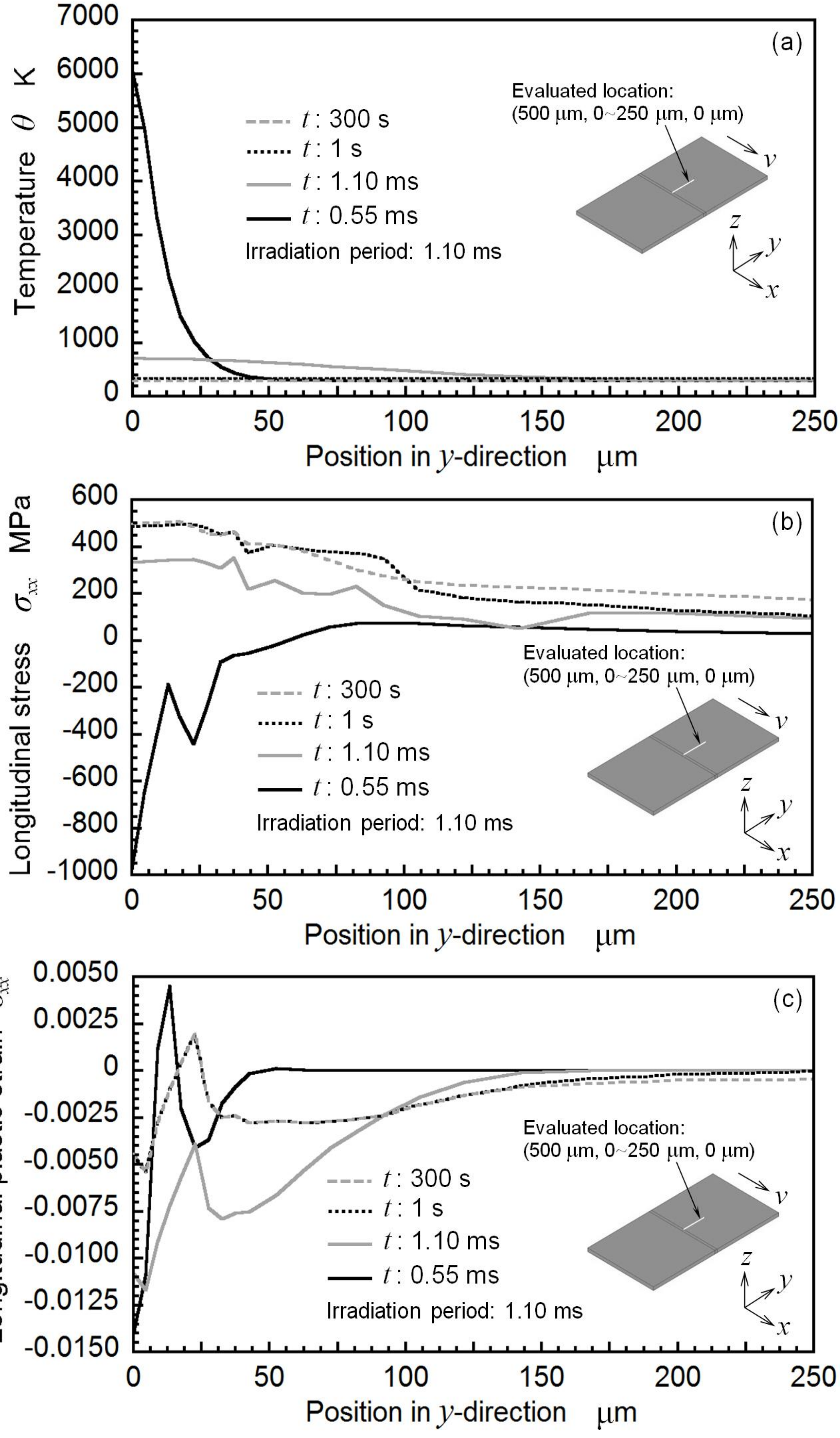

Figure 3.28 Distribution of (a) temperature, (b) stress and (c) plastic strain during laser irradiation and cooling periods (d: 35.0 μm, P: 50 W, v: 1.0 m/s)

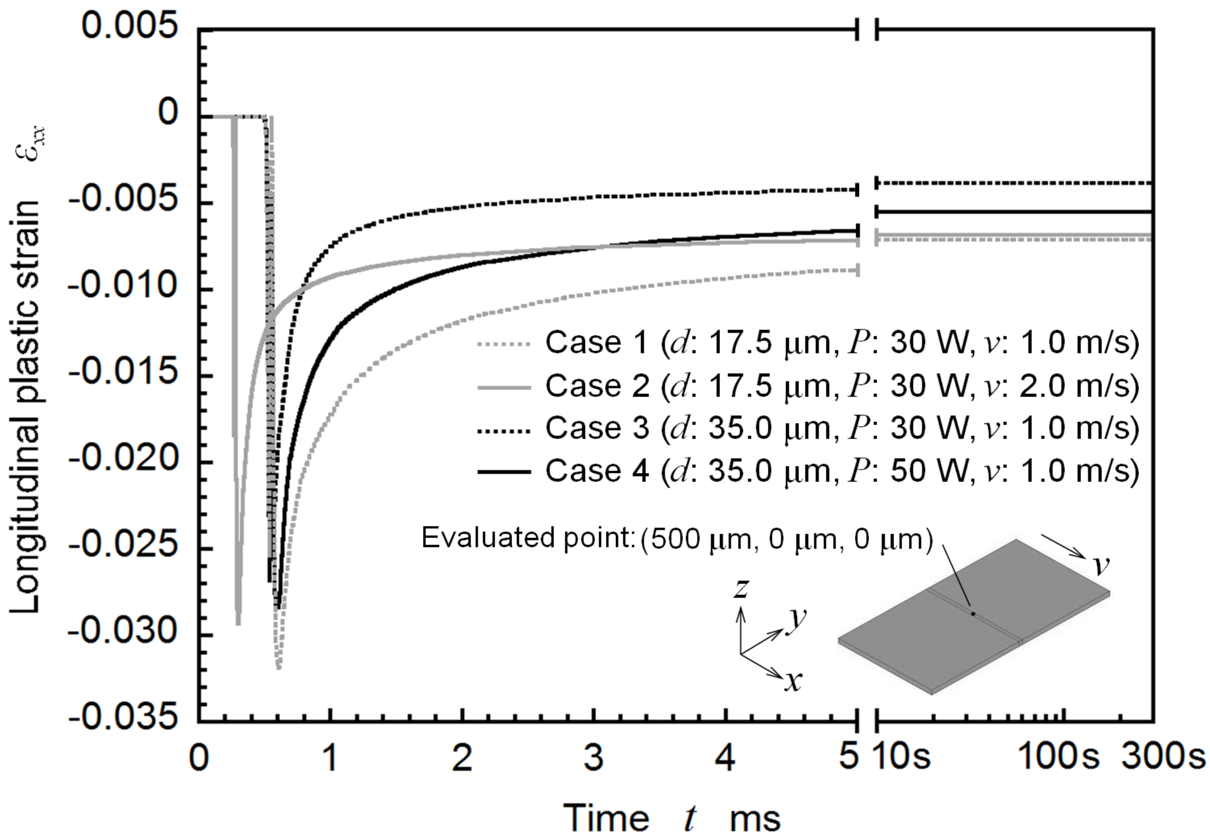

Figure 3.29 Temporal distribution of longitudinal plastic strain for four welding conditions

conditions. It can be seen that the slower scanning velocity, higher laser power and smaller spot diameter induced the higher magnitude compressive strain on the top surface at the irradiation period and continues with higher contraction strain at the cooling period. In addition, the tendency of higher contraction strain on these level of process parameters are due to the slower cooling rate which resulted by higher energy density. Therefore, it can be noted that the plastic strain fields during irradiation and cooling periods are directly affected from the temporal distributions of temperature and stress. On the contrary, the rapid reduction of compressive plastic occurred by the faster scanning velocity, lower laser power and larger spot diameter strains after the laser beam moves away from the top surface center of specimen (x: 500 μm). Furthermore, the deformation shapes of specimen during irradiation and cooling periods are also influenced by strain fields as well as affected from the temperature and stress distributions, which are discussed in the next section of welding deformations.

3.8.4 Welding deformations

Welding deformation is caused by non-uniform heating and cooling during welding. The strains produced during the heating stage of welding are always accompanied by plastic deformation of the material. The stresses resulting from these strains combine and react to produce internal forces

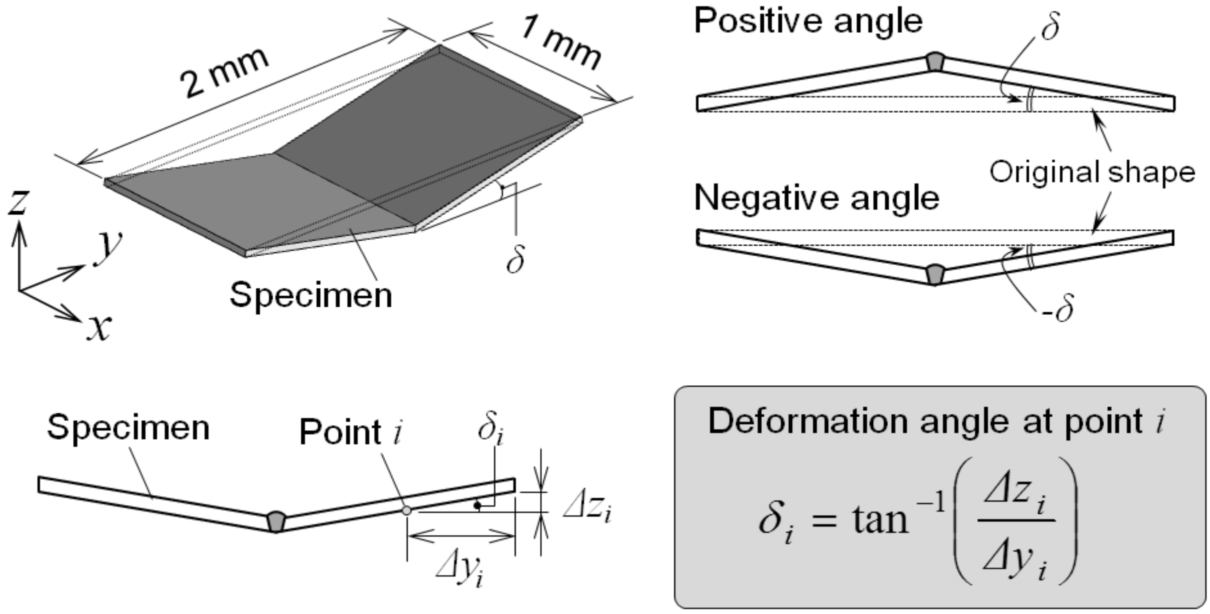

Figure 3.30 Schematic diagram of deformation angle calculation

that cause a variety of welding deformations. In addition, the other reason for the deformation changes is the existence of a temperature gradient in the through thickness direction. In this study, the welding deformation is evaluated in deformation angle of specimen as shown in **Figure 3.30**. The deformation angle for individual point *i* is calculated from the measurement of the displacement in the *z*-direction over the length from specimen edge as expressed in equation (3.58).

$$\delta_i = \tan^{-1}\left(\frac{\Delta z_i}{\Delta y_i}\right) \tag{3.58}$$

The positive angle is defined as the deformation towards the laser beam, while negative angle is the deformation downwards against the laser beam. In the calculation of deformation angle, the measurement locations are carried out on the bottom surface of specimen due to the expansion of weld bead was generated with convex curvature on the top surface along the specimen centerline. It can be observed from **Figure 3.31**, which shows the time history of deformation angle at the center of the top and bottom surfaces to demonstrate the changes of deformation angle with time. The positive deformation angle on the top surface of welding centerline was generated by thermal expansion along the positive *z*-direction because of the free surface boundary condition. Therefore, the angular deformation of specimen is discussed on the deformation of bottom surface. Starting from the moment when the laser beam enters the specimen, the negative deformation angle started to grow significantly in the weld centreline. As the laser beam scans along the *x*-axis, the deformation angle continues to rise. When the laser beam reaches the end edge of the specimen, the whole specimen is warmed up to a certain temperature and softened along the weld line. At the initial

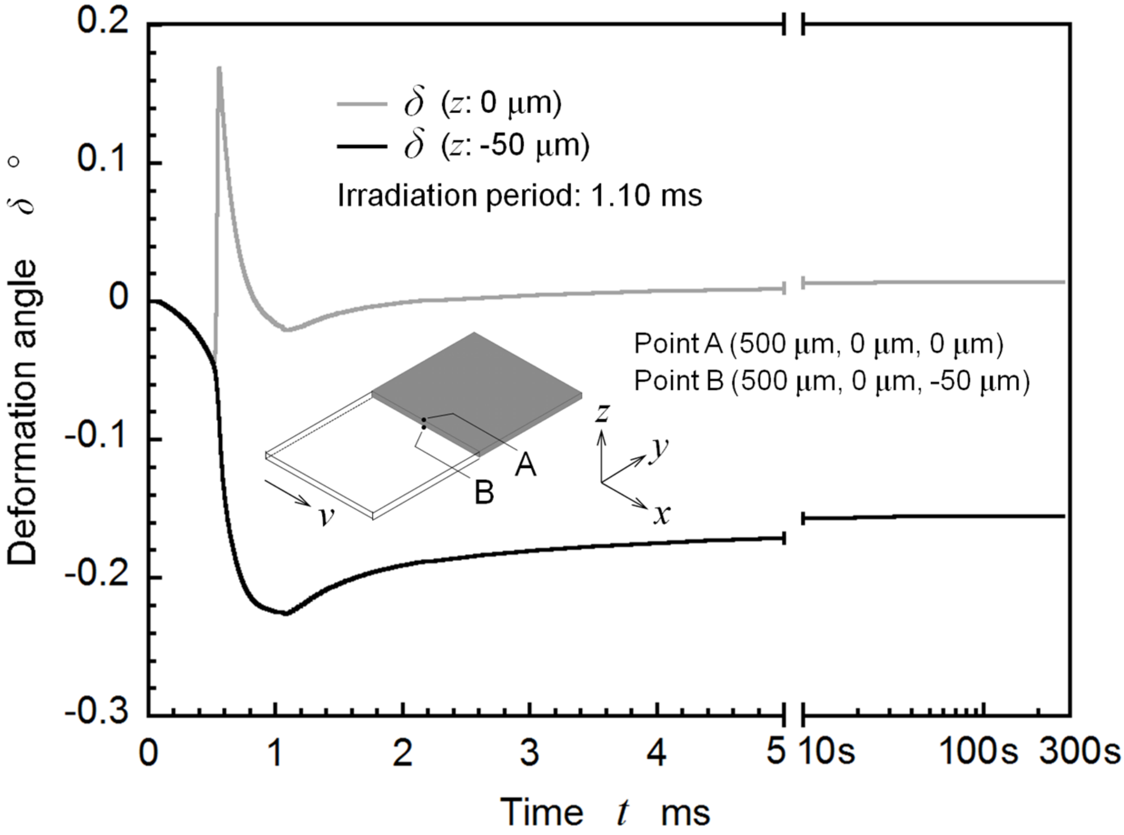

(a) History of deformation angle at the top and bottom surface of center point

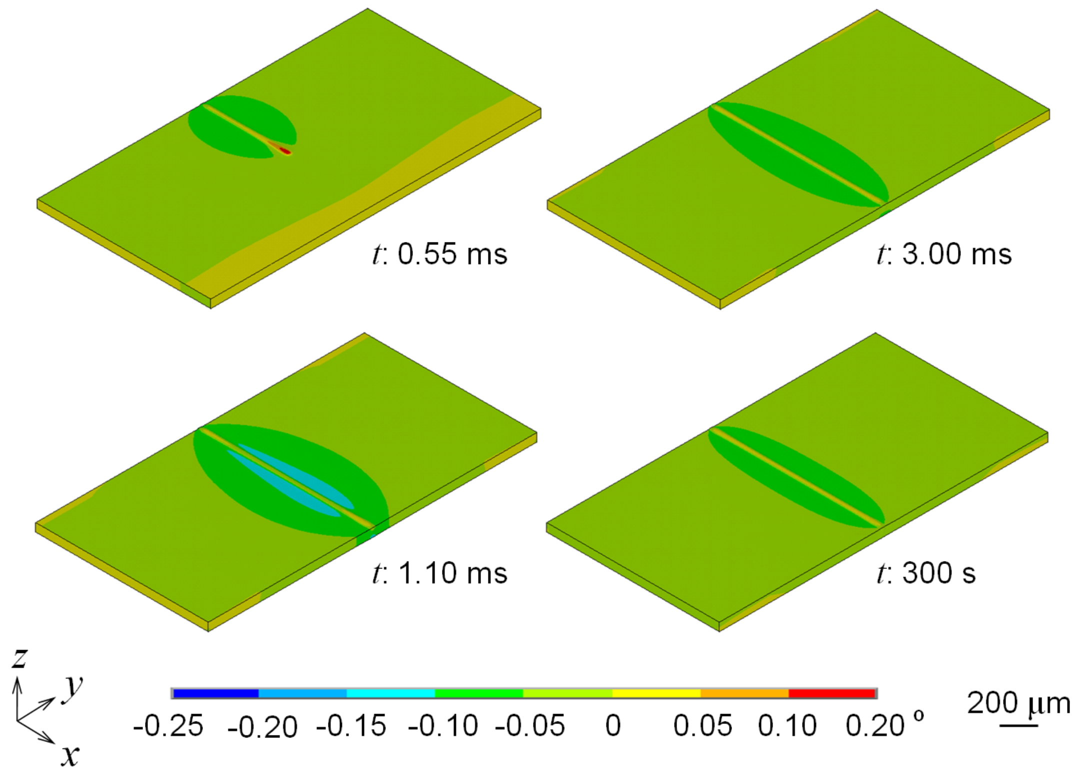

(b) Distributions of deformation angle

Figure 3.31 Temporal distributions of deformation angle at the top and bottom surfaces of specimen (d: 35.0 μm, P: 50 W, v: 1.0 m/s) cooling period (t: 1.1 ms), the deformation slightly increased at the evaluated point for maximum displacement of 0.02 μm, which resulted the negative deformation angle of 0.23°. However, the specimen deformation gradually decrease in reversed upward direction and remained with concave shape in the further cooling period and the deformation process ends approximately at 30 s due to the slow cooling process. The deformation angle of specimen also shown in the below of **Figure 3.31** during laser irradiation (t: 0.55 ms) and cooling periods (t: 1.1 ms, 3 s, 300 s). It is observed that during irradiation period, the deformations are non-uniform and the specimen is deformed more at the region near to the laser beam. However, the deformation become more uniform and their distribution is almost linear from the weld line to the both restricted edges of the specimen at the cooling period.

Figure 3.32 shows the relationship between deformation angle with temperature, stress and strain in time history. It is again shown that the specimen first undergoes compressive stress cause by the constraint of the rapid expansion of the material when the laser beam reaches the top surface center of welding line (x: 500 μm). It can be observed that the large compressive plastic strain develops in the weld center line and the plastic deformation occurs. After the laser beam moves away from the top surface center, the contraction of the center material changes the stress state to tensile stress and still remains in the plastic state, while the plastic strain gradually decreases to the lower compressive strain until the end of the cooling period. It can be seen that the changes of deformation grow rapidly right after the laser beam has passed over the top surface center (Point A). In other words, the deformation which driven by thermal expansion (temporary effect) and residual stresses (permanent effect) continuously raised from the irradiation process start instant to the end of laser–material interaction (t: 1.1 ms). From now on, the deformation of the specimen deforms in upward direction and does not change much with further cooling. In addition, the restriction of clamping plates also not allowing further deformation in the thickness direction (z-direction), which gives significant effect on the deformation angle.

Figures 3.33 and **3.34** show the displacement which are evaluated at the bottom surface of specimen along the width and welding directions, respectively. The displacements are magnified in these figures to make them clearly visible. Furthermore, the circles on the curves indicate the location of the laser beam. As can be seen from **Figure 3.33**, the angular deformation of specimen shows the tendency to be concave from the laser irradiation until the end of cooling period. It is shown that the specimen first deforms downward against the laser beam, and then deforms in reversed upward direction but still remained with the concave shape. The compressive stress induced by the heat expansion leads to negative displacements during heating stage of welding, while a large tensile stress generated by the thermal contraction forces the specimen with upward direction after the specimen cools. It also happens because the same forces caused by the non-uniform temperature

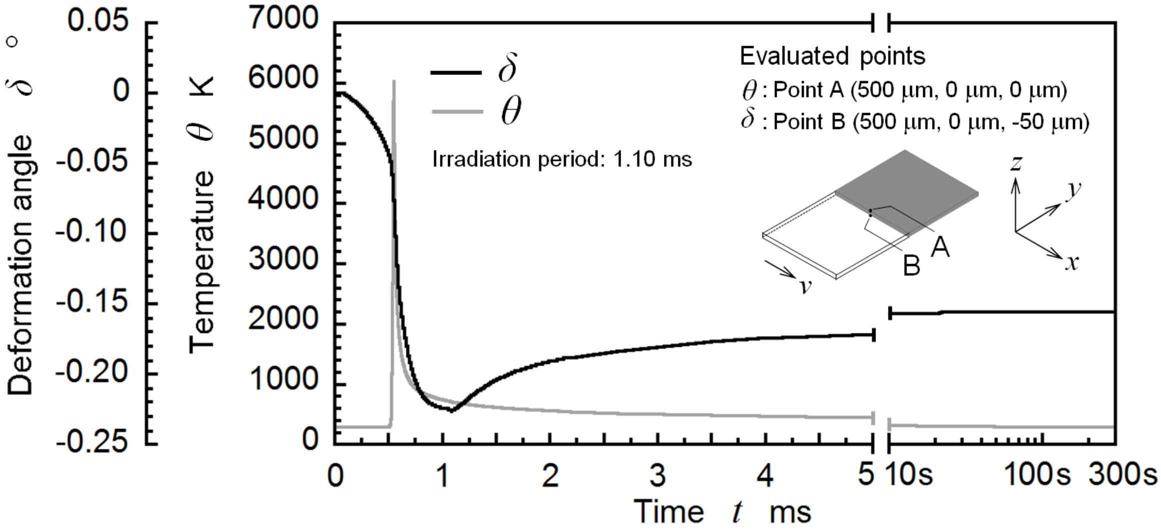

(a) Temperature and deformation angle

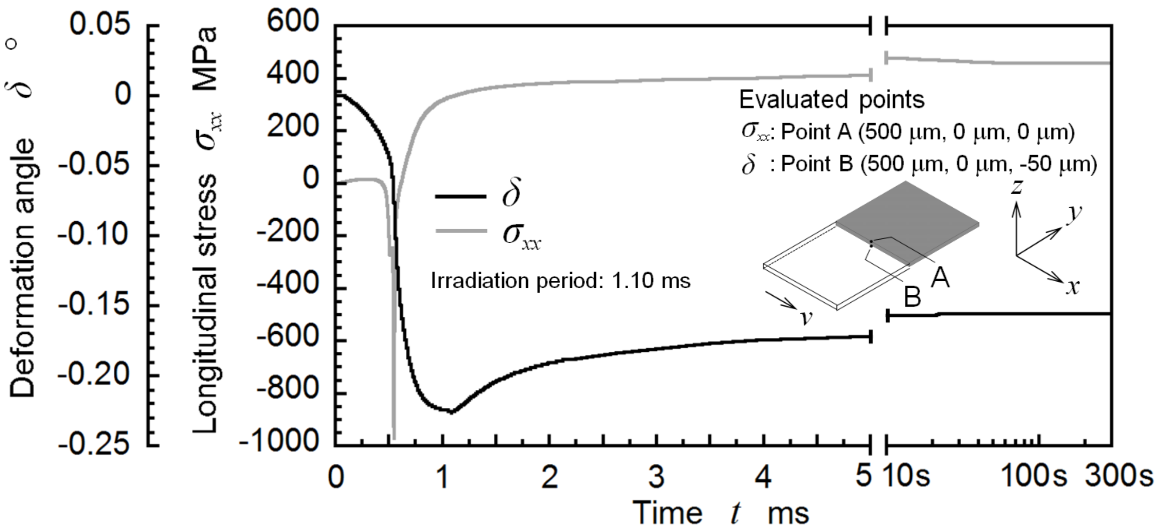

(b) Stress and deformation angle

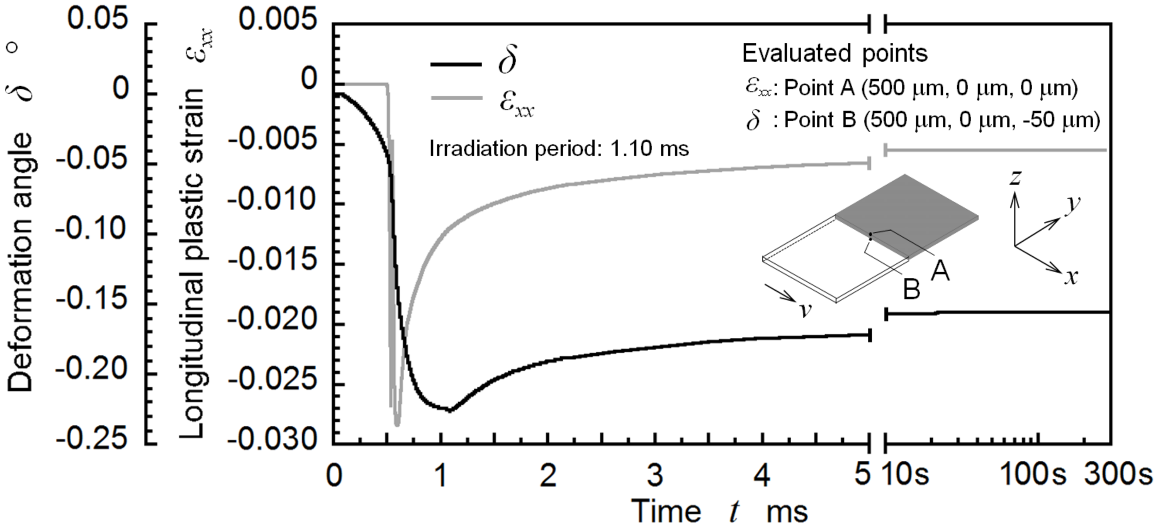

(c) Plastic strain and deformation angle

Figure 3.32 Relationship of deformation with (a) temperature, (b) stress and (c) plastic strain during laser irradiation and cooling periods (*d*: 35.0 μm, *P*: 50 W, *v*: 1.0 m/s)

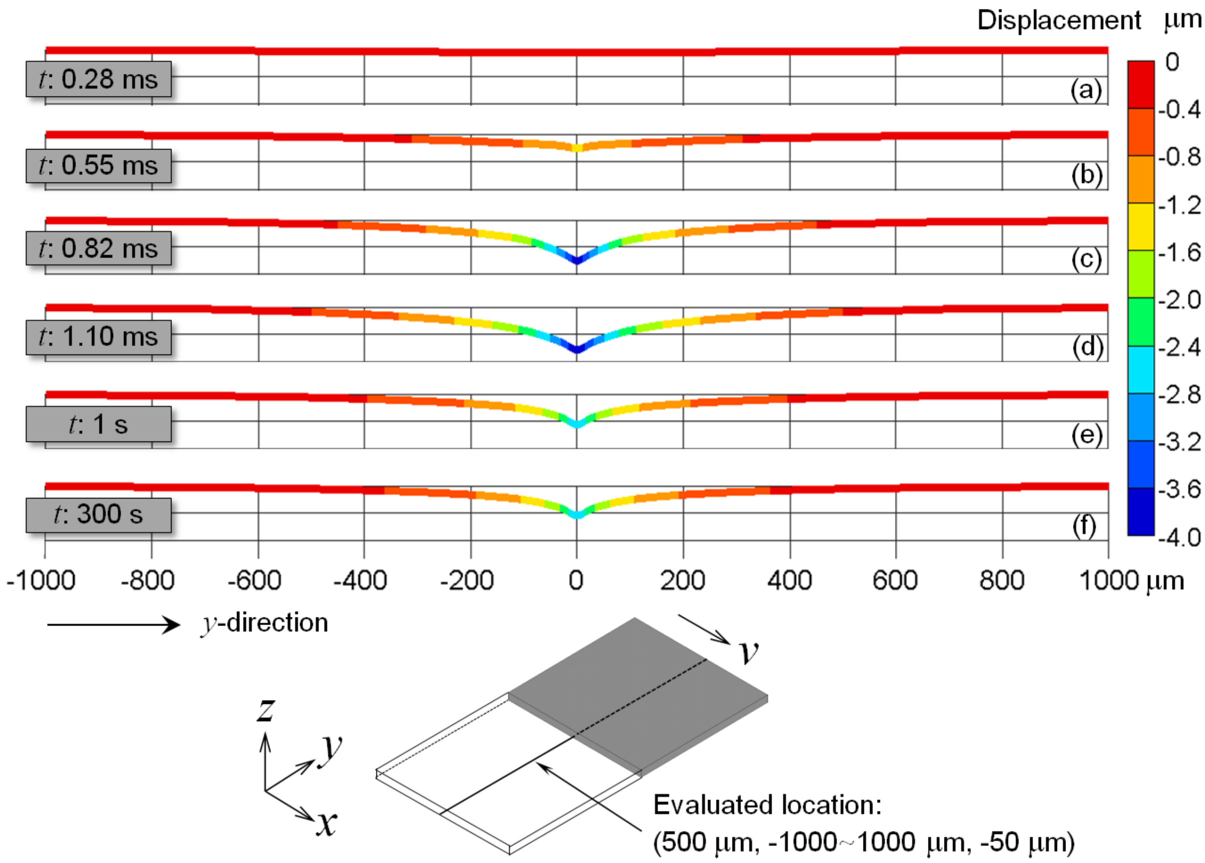

Figure 3.33 Displacement along the width direction during (a) laser irradiation and (b-d) cooling (*d*: 35.0 μm, *P*: 50 W, *v*: 1.0 m/s)

distribution in the through thickness direction, which can result in larger deformation if they are applied to the softer material. The significant displacement growth starts only when the plates are sufficiently heated on the bottom surface as well as on the top surface. In other words, in order to proceed with angular change formation, a softened region of the metal should exist along the centerline of the cross-section.

As can be seen from **Figure 3.34**, the material deformations were non-uniform at the beginning of the process near the side edge of the laser beam entry instantaneously after the laser beam enters the specimen, which an area of the specimen close to the laser beam tends to expand stronger than the cooler regions during irradiation period. In other words, the drop of the displacement after the laser enters the specimen is caused by the stronger surrounding constraint in the middle of the specimen. It leads to a situation where the bottom surface of the specimen are falling down. In addition, the expanding region does not have a freedom to expand as much as it needs and caused the rest of the specimen resists, which resulted a plastic deformation in the hot region. It also can be observed that buckling deformation occurred during irradiation period, which is caused by compressive stresses. In general, the material was buckled when the compressive stresses in that

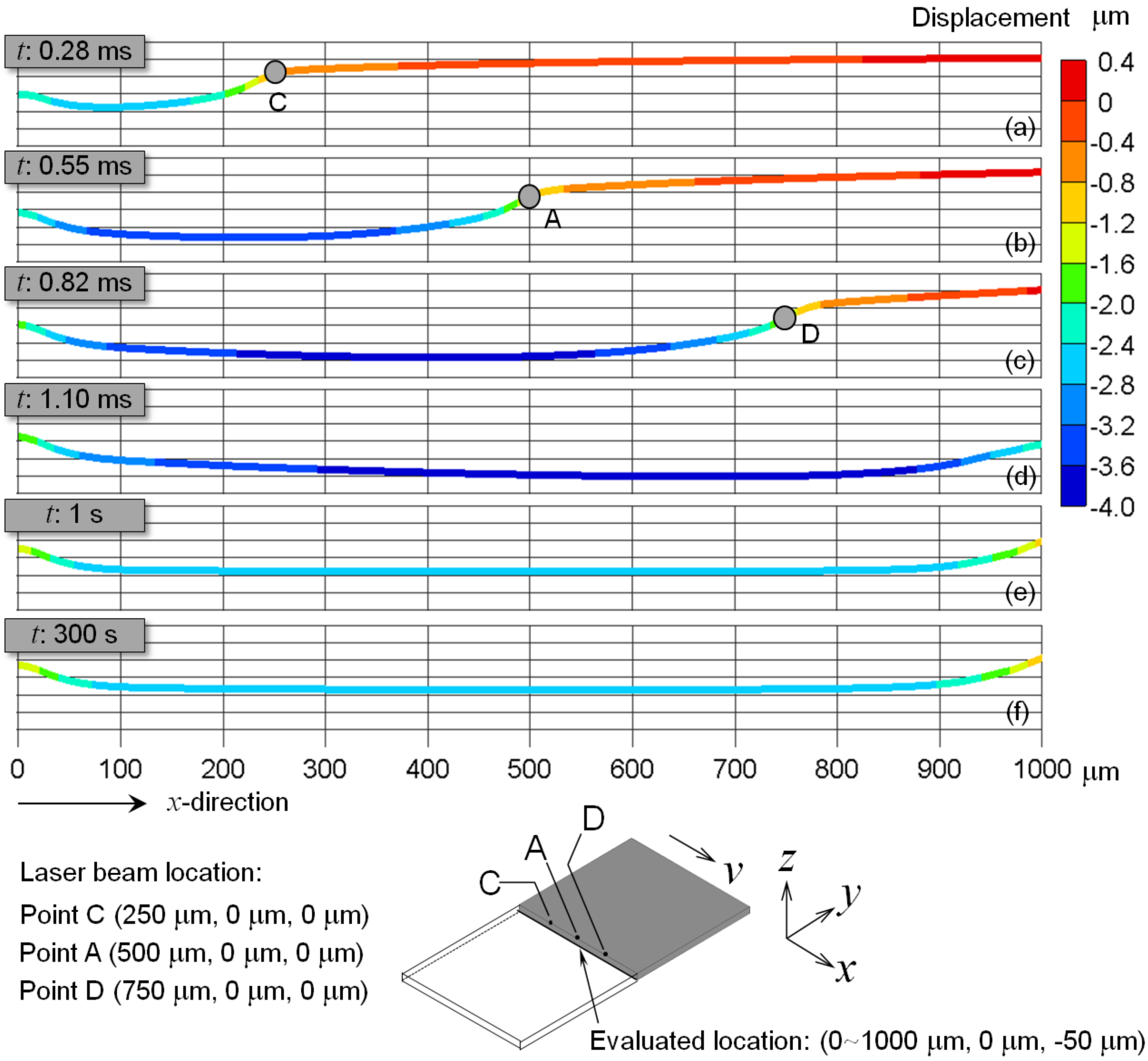

Figure 3.34 Displacement along the welding direction during (a) laser irradiation and (b-d) cooling (d: 35.0 µm, P: 50 W, v: 1.0 m/s)

material exceed a certain critical buckling stress level and mostly occurred in thin sheet welding.[3.22), 3.36)] After the laser irradiation period or initial cooling period at 1.1 ms, the largest value of the deformation was achieved. In the cooling period, the contraction of the top surface combined with the thermal expansion of the bottom surface and a positive movement of deformation was induced. The specimen deformation became more uniform at the end of the cooling stage, which is resulted by the redistribution of the thermal stresses. At the end of the cooling phase (t: 300 s), a permanent deformation has been found. Moreover, it can be noted that the amount of deformation in bending deformation after the welding cycle is smaller than the buckling deformation during laser irradiation.

The specimen deformation is greatly affected by process parameters, which also directly influenced by the weld bead profile. **Figure 3.35** shows the temporal distributions of deformation angle for the four different welding conditions. In addition, **Figures 3.36** and **3.37** show the final

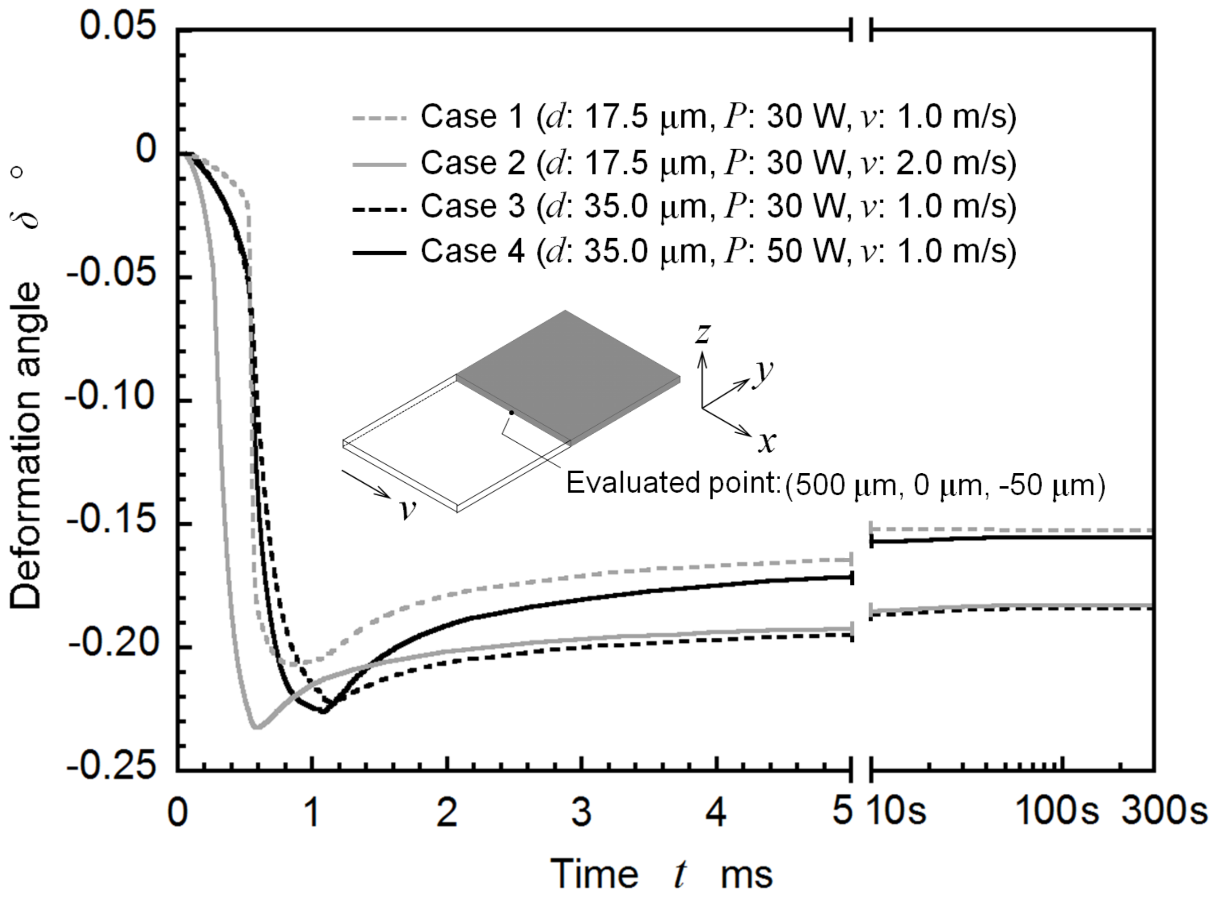

Figure 3.35 Temporal distributions of deformation angle for four welding conditions

deformation shapes which are evaluated at the bottom surface of specimen along the width and welding directions, respectively. The displacements in these figures are also magnified to make them clearly visible. It is shown that the permanent deformations under all welding conditions are formed with negative angle or concave curvature downwards against the laser beam. As shown in **Figure 3.35**, the formation of specimen deformation by smaller spot diameter was starts more slowly and subsequently continues with more rapidly increment to maximum deformation. Since the heat distribution through material thickness on the irradiated zone with smaller spot diameter is almost uniform and resulted the less difference of stress magnitude between top and bottom surfaces, the deformations are mainly affected surrounding the molten pool. Furthermore, the residual stress distributions show that the wider tensile residual zone at the weld centerline and balanced with higher compressive residual stresses around the weld line significantly reduced the final specimen deformation with small spot diameter as shown in **Figure 3.22(b)**. While the specimen deformation with large spot diameter is affected up to the further away regions from the weld, and resulted from the large different between residual stress at weld centerline and it further away region which can be clearly seen in **Figure 3.36**. In addition, it can be observed that the higher magnitude in maximum deformation is generated with large spot diameter and compared to the small spot diameter, it keeps

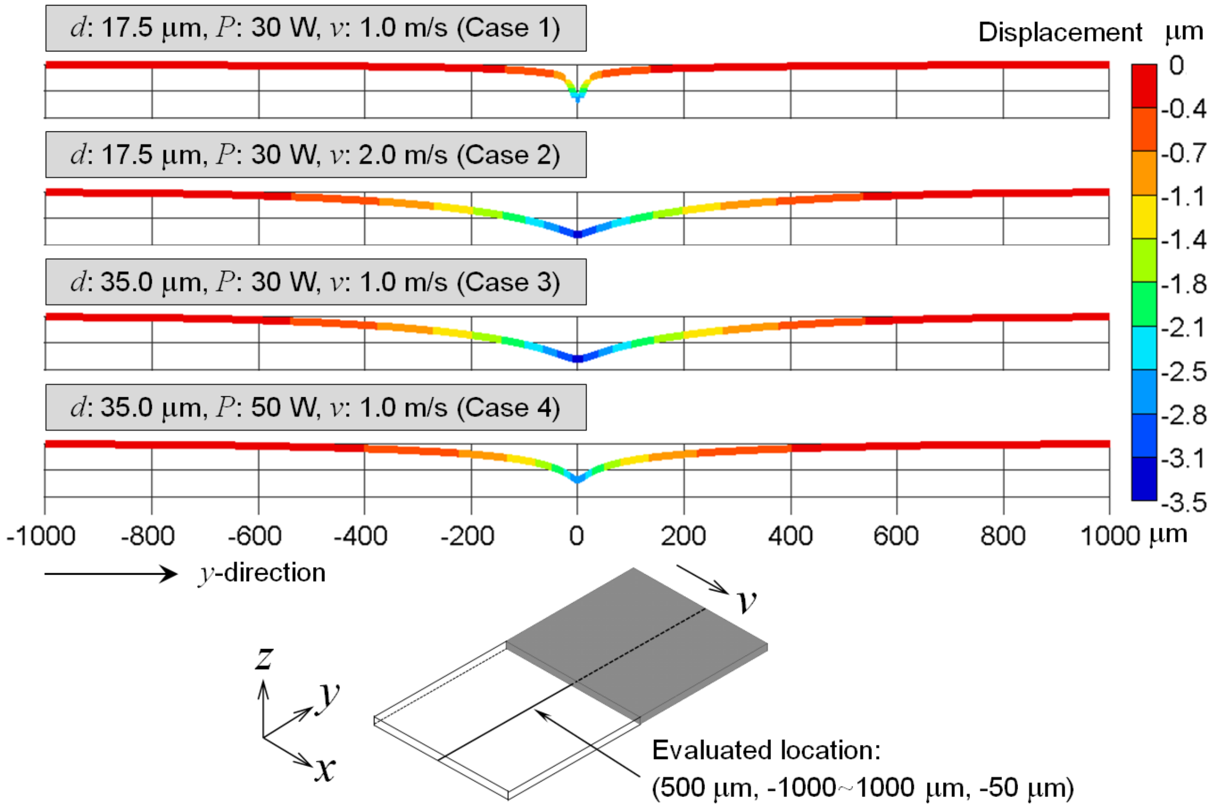

Figure 3.36 Final displacement along the width direction for four welding conditions

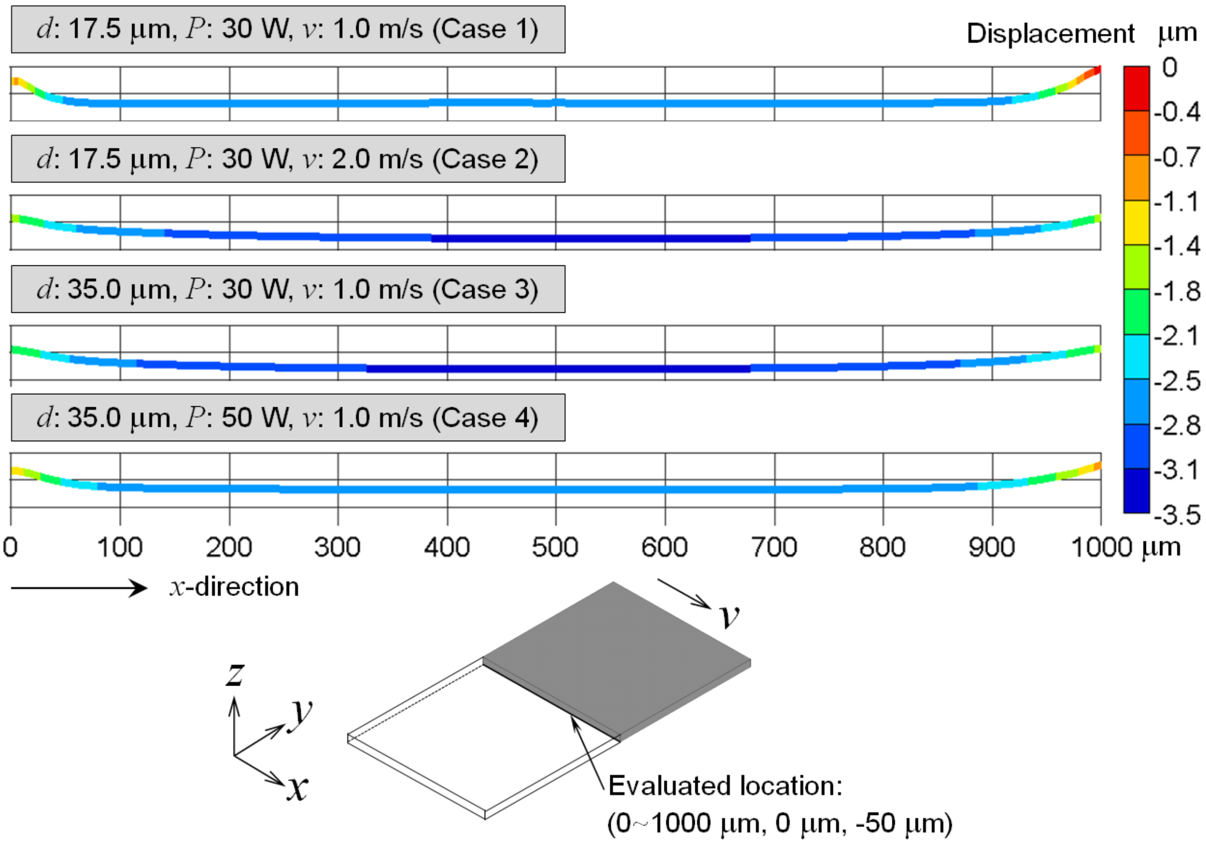

Figure 3.37 Final displacement along the welding direction for four welding conditions

larger deformation until the cooling period.

Since the thermal contraction forces the specimen with upward direction in the cooling period, the reversed deformation is used to evaluate the effect of process parameters in the specimen deformation. The reversed deformation is defined as the difference magnitude between the maximum deformation on the welding cycle and the final deformation on the final cooling period as shown in **Table 3.3**. It shows that the small spot diameter generated larger reversed deformation and resulted a lower final deformation angle under the constant scanning velocity and laser power. Therefore, the deformation angle decreases with decrease in the spot diameter.

Table 3.3 Reversed deformation for four welding conditions

Case			1	2	3	4
Maximum deformation angle	δ_{max}	°	-0.207	-0.232	-0.222	-0.226
Time of δ_{max}	$t_{\delta_{max}}$	ms	0.86	0.59	1.14	1.08
Final deformation angle	δ_{final}	°	-0.152	-0.183	-0.184	-0.155
Time of δ_{final}	$t_{\delta_{final}}$	s	300			
Reverse deformation	δ_{rev}	°	0.055	0.049	0.038	0.071

In general, it has been usually reported that the high heat input generates larger angular deformation and resulted the positive deformation angle.[3.32), 3.37)] However, in this study, since the both specimen edges were clamped during irradiation and cooling periods, it was found that the angular deformation conversely became small with remaining a negative deformation angle by higher laser power. This is due to the restriction of clamping edges not allowing further increment of specimen deformation in the through thickness direction, which makes the deformation angle is small with negative deformation angle. In addition, even the low laser power generates slightly less maximum deformation angle, the large reversed deformation by high laser power resulted the smaller final deformation angle and it is also directly affected from the distribution of final residual stress on the specimen.

The specimen deformation is largely influenced by the scanning velocity. Similar effect as the spot diameter, the slower scanning velocity generates higher amount of heat energy input received by the material during the welding process, which the heat distribution through thickness material on the irradiated zone is almost uniform and resulted the less difference of stress magnitude between top and bottom surfaces. It can be seen that the deformations by slower scanning velocity are mainly affected surrounding the molten pool. While the specimen deformation with faster scanning velocity is affected up to the further away regions from the weld, which can be seen clearly in **Figure 3.36**.

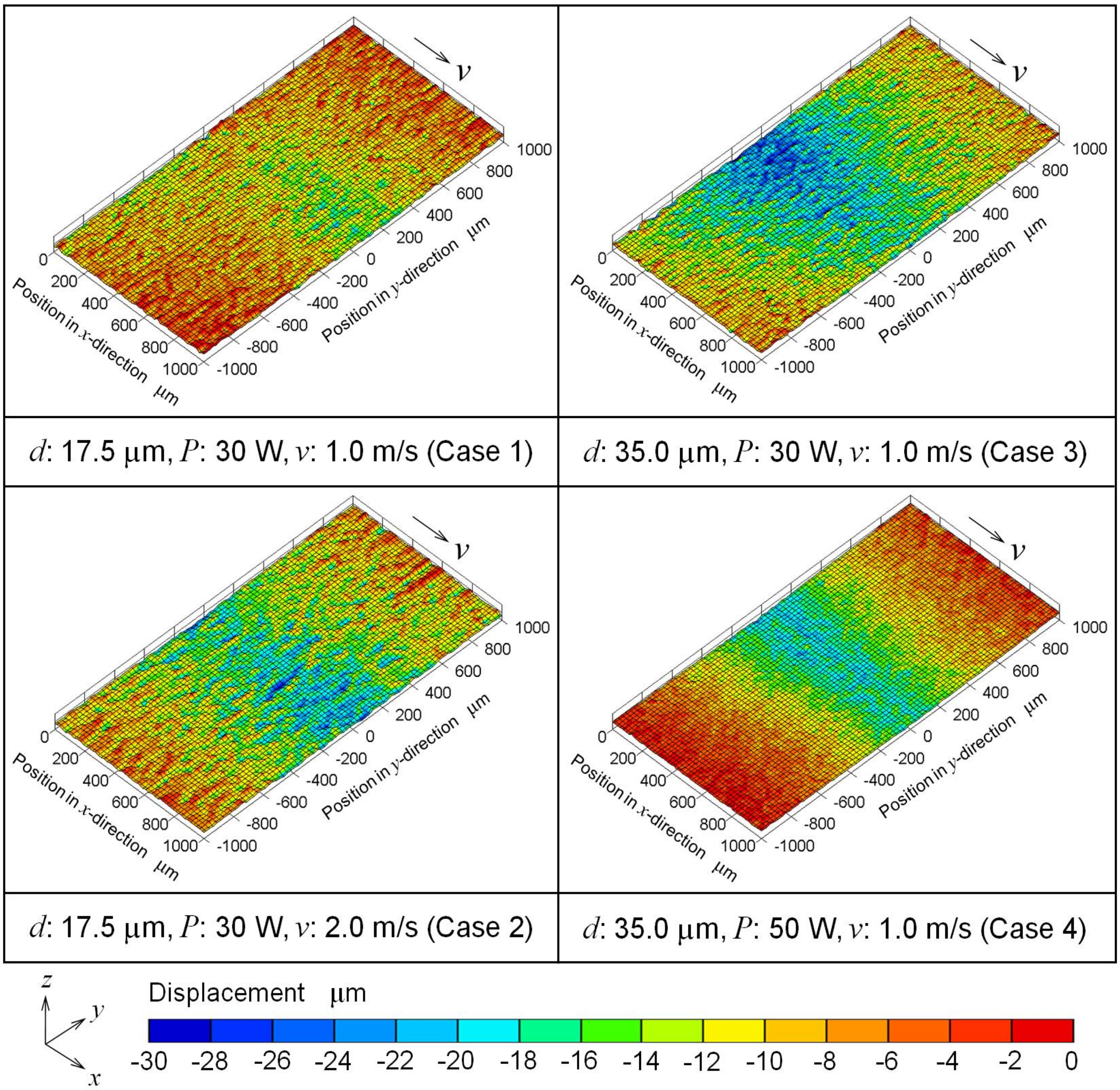

Figure 3.38 Measured displacement for four welding conditions

Furthermore, since the faster scanning velocity generates low residual stress distributions, the reversed deformation by high level of scanning velocity is smaller compared than slower scanning velocity even the maximum deformation was obtained by faster scanning velocity. Therefore, the final deformation angle decreases with decrease in the scanning velocity.

In order to validate the mechanical FE model, the numerical results of the deformation were compared by using the measured and calculated experimental data of displacements. **Figure 3.38** shows the experimental result of out-of-displacement at the top surface of specimen using a laser displacement sensor. Out-of-plane displacement is the subtraction value between the final displacement after welding experiment and the initial displacement prior to welding, since the developed FE model is based on the assumption of an initially flat specimen. The calculated deformation angles obtained experimentally are compared with numerical values as shown in **Figure**

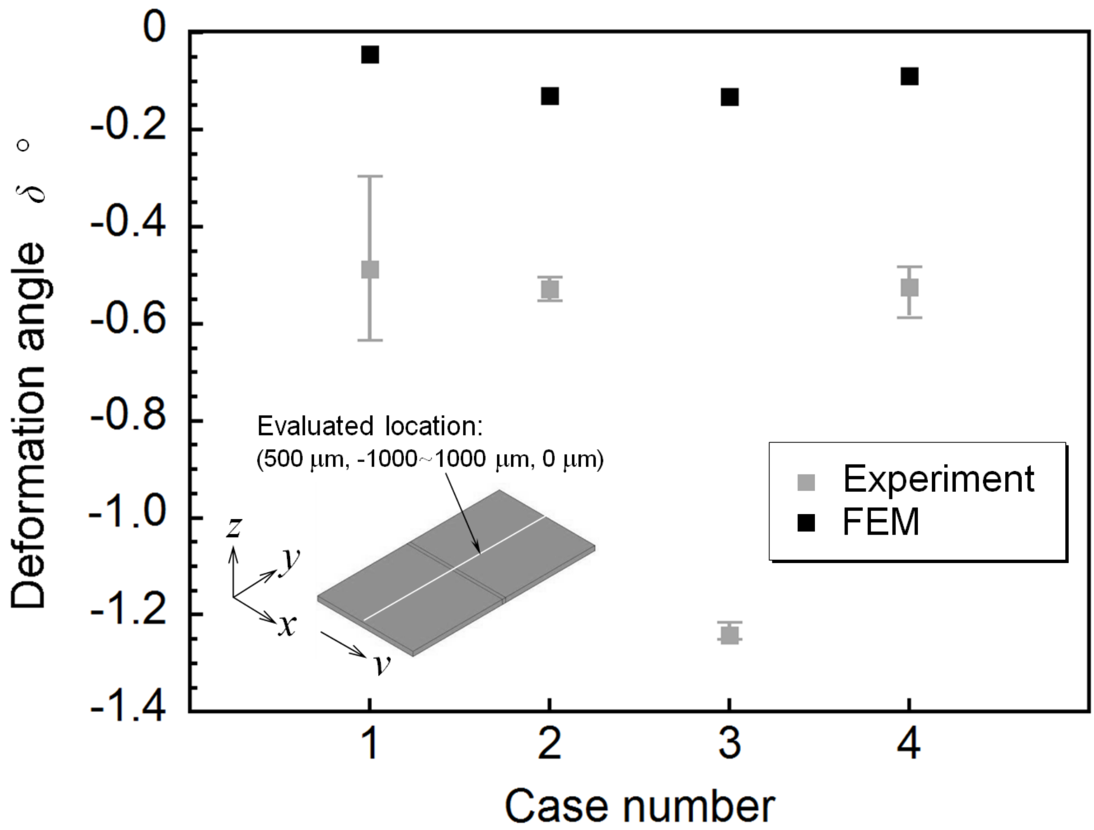

Figure 3.39 Comparison between experimental and simulated deformation angle

3.39. The experiments were repeated three times and the repeatability is shown in terms of error bars around the data points. In this comparison, the deformation angles on the top surface were used for numerical results. It is found that the trends of the deformation predictions are in fair agreements with the experimental results for different scanning velocity, laser power and spot diameter. However, the comparison of deformation angle reveals that in Case 3, the simulation give underestimated values due to the different welding mode than that in the Cases 1, 2 and 4. Refer to the **Figure 3.15**, it is observed that the conduction welding generated in the Case 1, while quasi-penetration welding for other cases. Therefore, it can be noted that the different welding mode significantly affected on the results of developed mechanical FEM model.

It is difficult to exactly simulate experiments in detail because the deformation is quite sensitive to variations in welding conditions. For the error of deformation values between the numerical simulation and experimental results, it may be from two factors. One is due to without considering the initial residual stress of the base metal, and another is because of an isotropic hardening plasticity model used in this study to consider the plastic mechanic behavior of welded material, which actually has a little difference with the true stress-strain curve of the material. The inaccuracies in the measurement of deformation may also contribute to the differences. From these viewpoints, it still needs further improvement in the both simulation and measurement.

For understanding of the mechanisms of laser micro-welding, an exact match between experimental and numerical results is not necessary. However, the key mechanisms need to be captured in the developed models. The numerical results emphasize the ability of this method to understand the characteristics and phenomenon of laser micro-welding, especially in the stress, strain and deformation fields characteristics. The fair agreement suggests that the current developed model can be used as a tool for a parametric examination of the laser micro-welding process, which will lead to optimize values of the welding parameters. The current model also can be easily used to simulate the welding of real engineering application.

3.9 Conclusions

A three-dimensional finite element model has been developed to simulate the stress, strain and deformation field during laser micro-welding of thin steel sheet. Main conclusions obtained in this chapter are as follows:

(1) Laser micro-welding could be performed weld with low distortion. The compressive stress induced by the heat expansion led to negative deformation angles downwards against the laser beam during the heating stage of welding, while a large tensile stress generated by the thermal contraction forces the specimen in upward direction but still remained with the concave shape after the specimen cools.

(2) High temperature gradient was generated in the vicinity of the molten pool, and elastic modulus reduced equivalent stress in the molten pool during the laser irradiation. The equivalent stress attained high values in the region of high temperature gradient in the cooling period.

(3) The welding residual stresses and deformation were formed due to the plastic deformation during irradiation and cooling periods. The residual stress is higher than yield strength of material and had strongest affect upon the welding deformation.

(4) Longitudinal residual stress usually prevailed over the transverse residual stress and reaching the yield limit along most of the molten zone. The transverse residual stress was substantial and reaching the yield limit at the both ends of weld.

(5) High tensile stress generated in and around the molten zone and balanced by the compressive stress further away from the weld towards the restricted specimen edges.

(6) The stresses were developed by the constrained thermal expansion and contraction of the material during weld cycle and lead to the formation of plastic strains.

(7) Scanning velocity, laser power and spot diameter have a significant effect on the stress and strain fields as well as final deformation.

References

3.1) K. Masubuchi : Prediction and Control of Residual Stresses and Distortion in Welded Structures, Transactions of JWRI, (1996), Vol. 25, No. 2, 53-67.

3.2) D. Radaj : Heat Effects of Welding, Springer-Verlag, (1992), 1, 9-11, 14, 149.

3.3) D. Deng and H. Murakawa : Prediction of Welding Distortion and Residual Stress in a Thin Plate Butt-welded Joint, Computational Materials Science, (2008), Vol. 43, 353-365.

3.4) C. Carmignani, R. Mares and G. Toselli : Transient Finite Element Analysis of Deep Penetration Laser Welding Process in a Singlepass Butt-welded Thick Steel Plate, Computer Methods in Applied Mechanics and Engineering, (1999), Vol. 179, 197-214.

3.5) E. Armentani, R. Esposito and R. Sepe : The Effect of Thermal Properties and Weld Efficiency on Residual Stresses in Welding, Journal of Achievements in Materials and Manufacturing Engineering, (2007), Vol. 20, No. 1-2, 319-322.

3.6) D. Camilleri and T.G.F. Gray : Computationally Efficient Welding Distortion Simulation Techniques, Modelling and Simulation in Materials Science and Engineering, (2005), Vol. 13, 1365-1382.

3.7) A.P. Mackwood and R.C. Crafer : Thermal Modelling of Laser Welding and Related Processes – A Literature Review, Optics and Laser Technology, (2005), Vol. 37, 99-115.

3.8) K. Satoh, K. Sao, K. Iwai and D. Takahashi : Thermal Elasto-plastic Analysis on Stress and Strain in Weld Metal During Multi-pass Welding, Transactions of JWRI, (1973), Vol. 2, No. 2, 33-43.

3.9) L.J. Yang and Z.M. Xiao : Elastic-plastic Modelling of the Residual Stress Caused by Welding, Journal of Materials Processing Technology, (1995), Vol. 48, 589-601.

3.10) W. Liang, S. Itoh, A. Vega and H. Murakawa : Numerical Study of Inherent Deformation Produced in Thick Plate Through Bending by Line Heating, Transactions of JWRI, (2006), Vol. 35, No. 1, 77-82.

3.11) D. Deng and H. Murakawa : Prediction of Welding Distortion and Residual Stress in a Thin Plate Butt-welded Joint, Computational Materials Science, (2008), Vol. 43, 353-365.

3.12) T. Schenk, I.M. Richardson, M. Kraska and S. Ohnimus : A Study on the Influence of Clamping on Welding Distortions, Computational Materials Science, (2009), Vol. 45, 999-1005.

3.13) Y. Namba and T. Katayama : Three-dimensional Thermal Elastic-plastic Analysis of Laser Forming Process, Journal of Precision Engineering (in Japanese), (1999), Vol. 65, No. 9, 1330-1334.

3.14) S. Amada and N. Shirai : Bending Deformation of Thin Plate Heated Locally by Laser, Proceedings of the Japan Society of Mechanical Engineers (in Japanese), (1996), Vol. 62, No. 604, 120-125.

3.15) T. Terasaki : Numerical Analysis of Laser Forming, Journal of Japan Laser Processing Society (in Japanese), (2003), Vol. 10, No. 3, 17-22.

3.16) R. Spina, L. Tricarico, G. Basile and T. Sibillano : Thermo-mechanical Modeling of Laser Welding of AA5083 Sheets, Journal of Materials Processing Technology, (2007), Vol. 191, 215-219.

3.17) G.A. Moraitis and G.N. Labeas: Residual Stress and Distortion Calculation of Laser Beam Welding for Aluminum Lap Joints, Journal of Materials Processing Technology, (2008), Vol. 198, 260-269.

3.18) G.A. Moraitis and G.N. Labeas : Prediction of Residual Stresses and Distortions due to Laser Beam Welding of Butt Joints in Pressure Vessels, International Journal of Pressure Vessels and Piping, (2009), Vol. 86, 133-142.

3.19) M. Zain-ul-Abdein, D. Nelias, J.F. Jullien and D. Deloison : Experimental Investigation and Finite Element Simulation of Laser Beam Welding Induced Residual Stresses and Distortions in Thin Sheets of AA 6056-T4, Materials Science and Engineering A, (2010), Vol. 527, 3025-3039.

3.20) S. Kou : Welding Metallurgy (Second Edition), John Wiley & Sons, Inc., (2003), 122-124.

3.21) E. Kannatey-Asibu : Principles of Laser Materials Processing, John Wiley & Sons, Inc., (2009), 363-364.

3.22) E.M. van der Aa : Local Cooling During Welding – Prediction and Control of Residual Stresses and Buckling Distortion, Doctoral Dissertation, Delft University of Technology, (2007), 1, 6-7.

3.23) A. Sluzalec : Theory of Thermomechanical Processes in Welding, Springer, (2005), 158.

3.24) N. Noda, R.B. Hetnarski and Y. Tanigawa : Thermal Stresses, Taylor & Francis, (2003), 140.

3.25) E.H. Smith : Mechanical Engineer's Reference Book, Butterworth-Heinemann, (1994), 8/7.

3.26) T. Katayama : Three-dimensional Thermal Elastic-plastic Analysis of Laser Forming Process by Finite Element Method, Master Dissertation, Chubu University (in Japanese), (1998), 34-35.

3.27) JSSA : Stainless Steel Databook, The Nikkan Kogyo Shimbun (in Japanese), (2002), 209.

3.28) B.S. Martin : Simulation of Welding Distortions in Ship Section, Doctoral Dissertation, Technical University of Denmark, (1999), 100.

3.29) M. Zain-ul-Abdein, D. Nelias, J.F. Jullien and D. Deloison : Prediction of Laser Beam Welding-induced Distortions and Residual Stresses by Numerical Simulation for Aeronautic Application, Journal of Materials Processing Technology, (2009), Vol. 209, 2907-2917.

3.30) L. Chuan, Z. Jianxun and N. Jing : Numerical and Experimental Analysis of Residual Stresses in Full-penetration Laser Beam Welding of Ti6Al4V Alloy, Rare Metal Materials and Engineering, (2009), Vol. 38, No. 8, 1317-1320.

3.31) P. Ferro, A. Zambon and F. Bonollo : Investigation of Electron-beam Welding in Wrought Inconel 706 – Experimental and Numerical Analysis, Materials Science and Engineering A, (2005), Vol. 392, 94-105.

3.32) H. Long, D. Gery, A. Carlier and P.G. Maropoulos : Prediction of Welding Distortion in Butt Joint of Thin Plates, Materials and Design, (2009), Vol. 30, 4126-4135.

3.33) D. Deng and S. Kiyoshima : Numerical Simulation of Residual Stresses Induced by Laser Beam Welding in a SUS316 Stainless Steel Pipe with Considering Initial Residual Stress Influences, Nuclear Engineering and Design, (2010), Vol. 240, 688-696.

3.34) P.J. Cheng and S.C. Lin : An Analytical Model to Estimate Angle Formed by Laser, Journal of Materials Processing Technology, (2001), Vol. 108, 314-319.

3.35) S.H. Park, J.K. Kim and J.H. Kim : Materials with Complex Behaviour – A Statistical Study on Stress-strain Relation of AISI 304 Stainless Steel Under Elevated Temperatures, Springer, (2010), Vol. 3, No. 1, 3-18.

3.36) E.M. van der Aa, M.J.M Hermans and I.M. Richardson : Welding with a Trailing Heat Sink – How to Optimise the Cooling Parameters?, Proceedings of the 7th International Conference on Trends in Welding Research, (2005), 577-582.

3.37) R. Wang, S. Rashed, H. Serizawa, H. Murakawa and J. Zhang : Numerical and Experimental Investigations on Welding Deformation, Transactions of JWRI, (2008), Vol. 37, No. 1, 79-90.

Chapter 4:
Direct Micro-joining of Brass and Copper of FPC by Pulsed Nd:YAG Laser

4.1 Introduction

As one of the most important developments in manufacturing processes, machining operations can significantly contribute to profitability. The best techniques can result in the low production costs and keep the competitiveness of products. The development of the direct joining method is important for major applications in the automobile and electronic fields. Among various joining techniques, it is well-known that the laser welding is an effective technique for joining metals because the laser beam has a high power density to melt materials easily at a high processing speed with a precise positioning.[4.1)–4.3)] Electronic industry is becoming increasingly interested in a laser welding technology to joint electronic components. Starting from July 2006, the WEEE/RoHS laws in Europe forbids the usage of lead in solders, which is very harmful to the human body and the environment.[4.4), 4.5)] The laws gave impetus to the solder-free in the laser welding as a promising solution to replace the conventional joining technique.

A flexible printed circuit (FPC) is strongly expected as a connection component because of its high reliability for movable parts of electronic device. FPC has greatly contributed to make devices thinner, lighter and more compact. Copper and its alloys are some of the most versatile materials and widely used in the electrical and electronic components because of its high ability to conduct the energy and transmit the signals.[4.6)] However, the high thermal conductivity of copper has a great influence on weldability.[4.7)] In the welding process, the heat is rapidly conducted into the copper, which might lead to the incomplete fusion in the weld metals. Moreover, the welding process of copper can be essentially described in the same way as that on other metals. However, the primary difficulty in the laser welding of copper is the crucial time to form the weld pool at the beginning of the process because of its high reflectivity and the high thermal conductivity, which makes it difficult to initiate a reliable welding process.[4.8)] Furthermore, the main challenging in the laser welding of copper-alloy brass is the generation of porosity due to the evaporation of alloyed zinc from a brass,[4.9)] since the boiling point of zinc is lower than the melting point of copper. Therefore, the achievement of high reliability is mandatory for applying the laser welding technique in the industrial production lines.

In the laser micro-welding of high reflective materials, the use of a standard pulse profile is limited to weld the dissimilar metals of copper and brass in the overlap joint geometry, since the

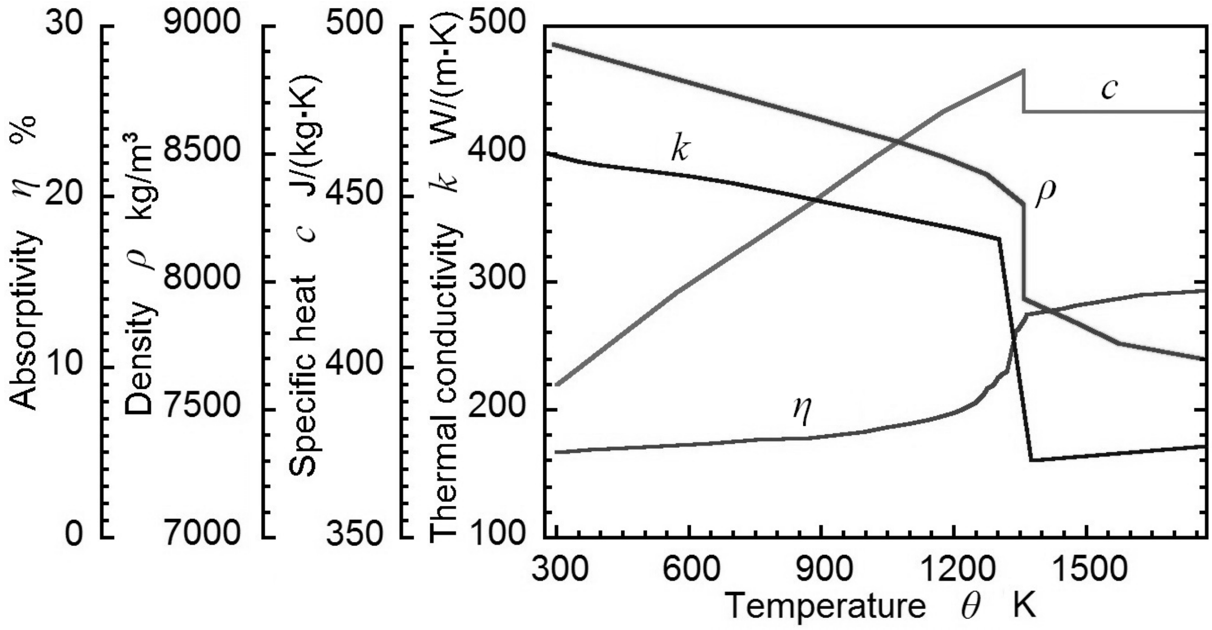

Figure 4.1 Thermophysical properties and absorptivity of copper for 1064 nm wavelength

uncontrolled heat input generates an overshoot, which produce undesirable welded joints. The control of heat input is very important for achieving a suitable welding penetration, preventions of overheating condition and unacceptable welding defects. Moreover, the combinations of these materials are unique, and the precise heat control is essential to perform the stable welding process.

In this chapter, the overlap welding between a FPC, which consist of a thin copper circuit on a polyimide film, and a thick brass electrode by a pulsed Nd:YAG laser were experimentally and numerically investigated with the control of pulse waveform. The numerical analysis was conducted based on the fundamental analysis of the heat transfer problem during the laser micro-welding by finite element method (FEM). The weld strength was also evaluated by shearing test for the overlap welding with and without the control of pulse waveform.

4.2 Overview of approach

Reflectivity varies depending on the temperature; when a material becomes hotter, the absorption of the incident light increases. However, in the case of copper, the high thermal conductivity prevents from getting hotter, thereby maintaining the high reflectivity. **Figure 4.1** shows the absorptivity of copper for 1064 nm wavelength and its thermophysical properties as a function of temperature.[4.10), 4.11)] At room temperature, the absorption rate of the Nd:YAG laser is low, approximately 5 %. It is difficult to obtain a stable laser micro-welding process, since the absorptivity increases drastically. On the other hand, the thermal conductivity decreases when the material reaches its melting point. In other words, when the laser beam is irradiated on the target, its high reflectivity permits only a small absorption of the incident energy. At the same time, the absorbed energy is quickly removed from the interaction point due to the high thermal conductivity. Then, the temperature rises slowly and the formation of the keyhole is consequently delayed. The weld condition of highly reflective materials can be improved with an essential technique of pulse waveform.[4.12)]

There are several published papers related to the laser welding using the pulse waveform technique on the materials with the high reflectivity and thermal conductivity such as copper and aluminum. Biro, E. et al.[4.13)] reported that the weld bead quality was improved by the ramp-down pulse waveform in the laser welding of copper. In addition, the controlled heat input by pulse waveform adjustment was effective in controlling the weld behavior of copper.[4.5)] Meanwhile, it has been reported that the laser welding of aluminum alloy was successfully applied with controlled pulse waveform and also an effective technique to reduce and eliminate the weld defects.[4.14), 4.15)] With respect to the laser welding with controlled pulse waveform, only a limited number of papers[4.16)–4.18)] have experimentally investigated on the welding of dissimilar materials. However, no work has been reported concerning the welding behavior of copper on polyimide and brass in overlap laser welding using controlled pulse waveform. In order to achieve a better understanding into the relationship between the different material properties, complex pulse waveform and its effects on the weld bead, the pulse waveform followed by numerical analysis are strongly required. These points would make the welding of dissimilar materials to a challenging technological problem for applying the laser welding in the industrial application.

In this research, it was carried out to control a pulse waveform, which is a technique used to temporally distribute energy within a single laser pulse by controlling the power and the time period of laser pulse in real time. It can be also defined as a variation in power supplied for a laser to change the shape of the output pulse and subsequently the heat distribution within one pulse. Changing the energy distribution within a pulse can completely change the melting or process behavior of a material. The weld penetration and quality could be improved by changing the laser pulse waveform in these difficult-to-weld applications**. Figure 4.2(a)** shows a setting profile of a standard laser pulse. This is known as a rectangular pulse waveform with the power densities remaining nominally constant throughout the pulse. Rectangular pulse waveform is the simplest and most extensively used laser pulse waveform containing only one energy sector. **Figures 4.2(b)** and **(c)** show the setting input and actual output of a ramp-down and ramp-up pulse waveforms, respectively. These pulses either emit the majority of their power early or late within the pulse. This equates to either a gradual cooling or gradual heating of material. Materials with dissimilar melting points, a ramp-down pulse waveform reduces weld cracks and porosity. [4.12)] For the latter, materials with low melting points and

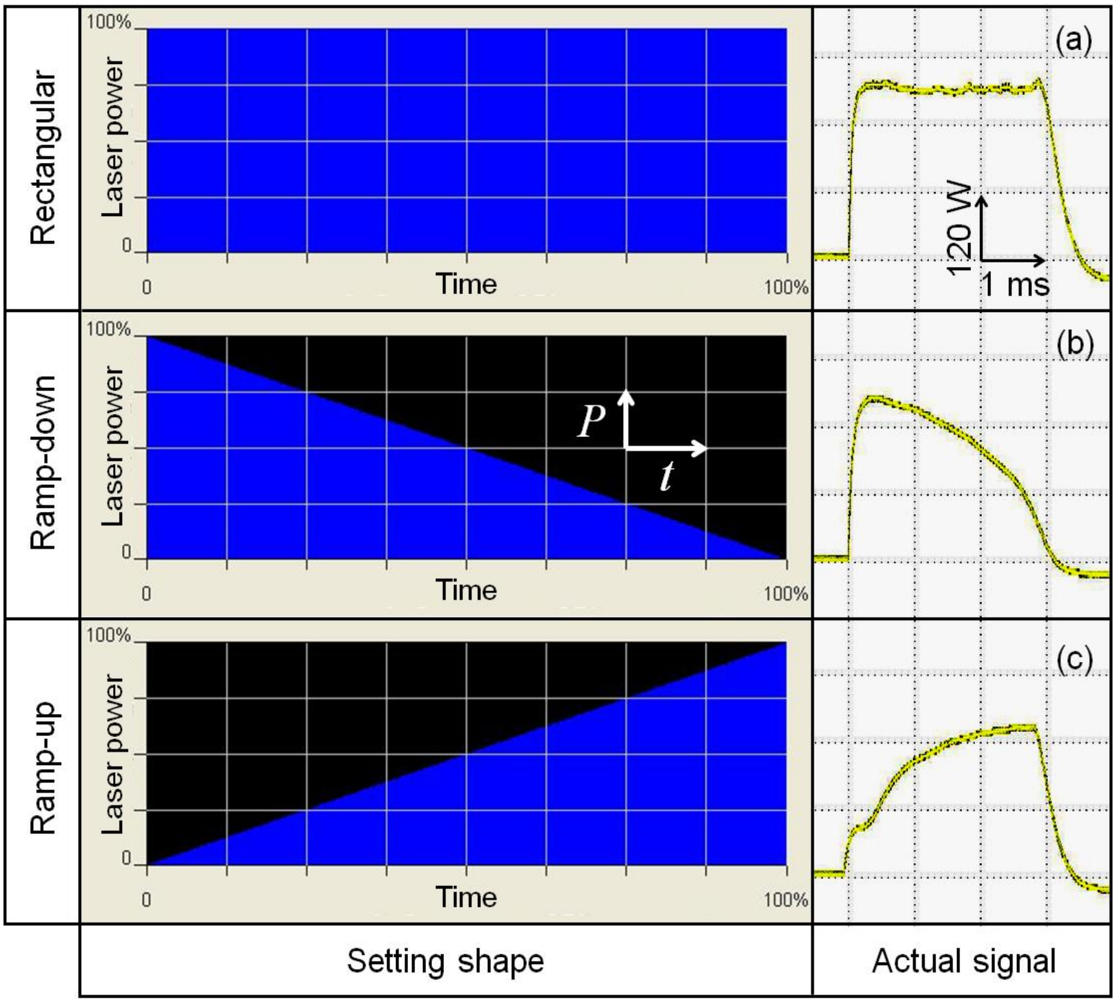

Figure 4.2 Setting shape and actual signal of pulse waveform (P: 300 W, τ: 3 ms)

high reflectivity will benefit from ramp-up pulse waveform during welding. This waveform slowly increases the intensity in weld pulse until much later in the melt.

4.3 Equipments

4.3.1 Pulsed Nd:YAG laser

Figure 4.3 schematically shows the pulsed Nd:YAG laser source of LASAG SLS200 CL8 used in this study. It has been developed for the purpose of reliable micro-welding applications. The excellent beam quality makes it possible to fit optical fibers of down to 50 μm core diameter at a low aperture. The real-time power supply (RTPS) also makes it more attractive for precision welding applications with high demands on pulse-to-pulse stability down to a peak power of 20 W. The flexible pulse waveform capabilities and pulses of up to 100 ms duration allow superior welding strategies targeting applications, where minimal thermal side effects are mandatory. The main specifications of laser source are listed in **Table 2.1**. A 50 μm fiber diameter (Numerical aperture,

N_A=0.11) and maximum laser peak power of 1 kW were used as welding laser source for the experiments. Square shape pulse is the standard output of this laser. The available range for the laser parameters were 0.5–100 ms for pulse width and 0.1–200 Hz for pulse repetition rate.

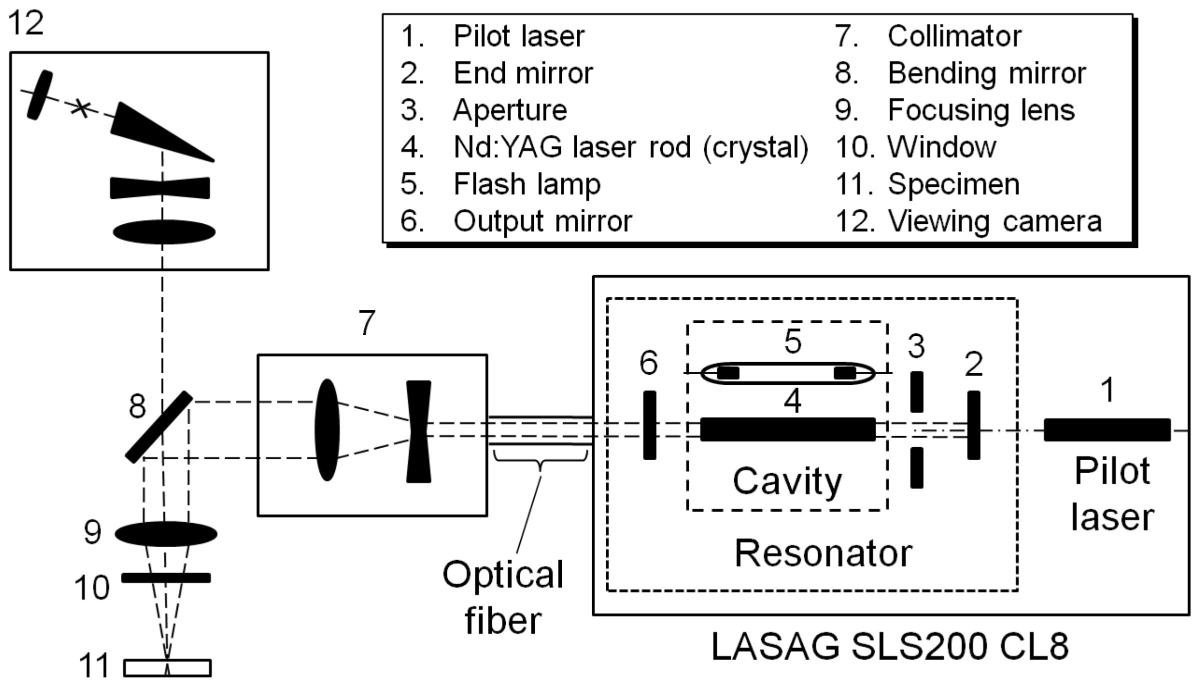

Figure 4.3 Schematic illustration of pulsed Nd:YAG laser

Table 4.1 Specifications of pulsed Nd:YAG laser

Wavelength	1064 nm
Pulse width	0.5–100 ms
Pulse repetition rate	0.1–200 Hz
Maximum pulse energy	5 J
Maximum average power	5 W
Maximum peak power	1 kW @ 3 ms
Minimum peak power	0.02 kW

(a) Parameters of laser pulse

In the pulsed laser, the molten zone geometry generated by each laser pulse is determined by the peak power and pulse width. The number of pulses per a second, the pulse overlap and the scanning velocity additionally affect a seam width. The peak power of laser pulse, measured in Watts (W), controls the weld penetration depth and it is a direct parameter that can be set on the laser operation. It controls the maximum power of each pulse and directly affects the power density measured in

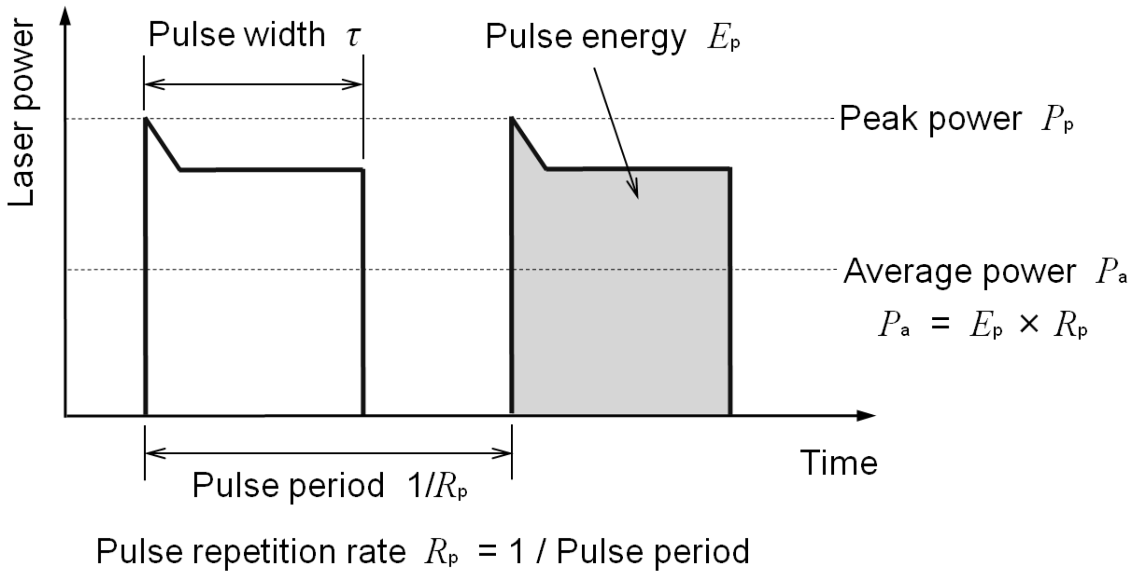

Figure 4.4 Schematic illustration of pulsed output

W/cm^2. The pulse width is the time period of the laser pulse. It controls the amount of heat into a part, the weld width and the thermal cycle. The pulse width is usually measured in milliseconds (ms) in the laser source. The pulse repetition rate also controls the amount of heat into a part and the thermal cycle. It equates to the number of flash-lamp pulse per a second, and it would be expressed as Hertz (Hz). In addition, the pulse energy is calculated by a multiplication of peak power and pulse width. Furthermore, the average power represents the power averaged in one second over the period of the pulse. **Figure 4.4** shows the important parameters of the laser pulse, including the peak power, the pulse width, the pulse repetition rate, the pulse energy and the average power.

(b) Pulse waveform

The pulse waveform has been recognized as one of the essential technique to challenge the high reflective materials and can avoid the problem of an unstable process. As briefly described in section 4.2, the changing shape of laser pulse might improve the weld penetration and quality in the difficult-to-weld applications. The LASAG SLS200 CL8 of pulsed Nd:YAG laser equipped with computer software to create and control a pulse shape. **Figure 4.5** shows the menu of pulse waveform in the PC-Terminal 2 software, which is connected to the laser source of LASAG SLS200 CL8. The time period of each added sector varies from 0.2 to 100 ms with 0.1 ms increments. The height of each sector can be adjusted from 0 to 100 % of the laser power. Vertical and horizontal axes show the laser power and pulse width in percentage from the current setting values, respectively. To create a complex pulse waveform, a single pulse shape can be plotted with a minimum 17 points. In order to determine the position of a defining points accurately, the right underneath of the menu shows the current cursor position or setting values of peak power and pulse width.

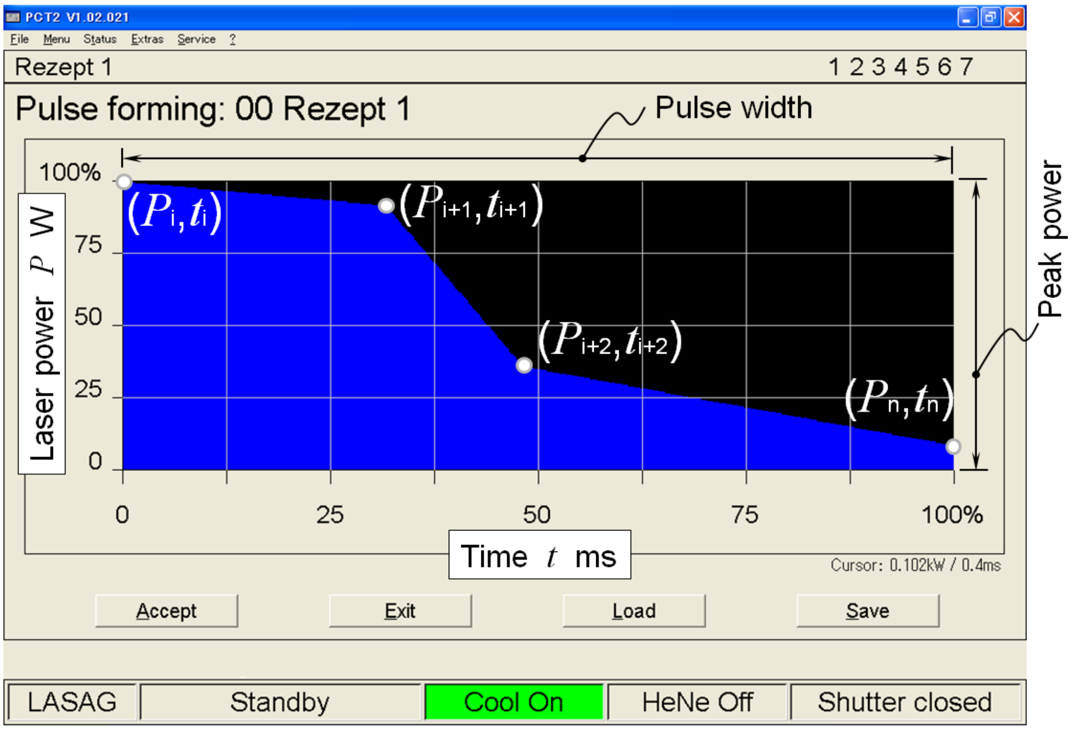

Figure 4.5 Setting of pulse waveform in PC-Terminal 2 software

4.3.2 Field emission scanning electron microscope

In this study, a field emission scanning electron microscope (FE-SEM) manufactured by JEOL (Model: JSM-7001F) was used for microstructure observation and elemental analysis. The performance and stability enables up to 1000000x magnification. The specimen chamber handles specimens up to 200 mm in diameter. The JSM-7001F features a unique in-lens field emission gun that delivers more than 200 nA of beam current to the sample. An extremely small probe diameter at low kV and high current is optimal for characterization of nanostructures with a resolution of 1.2 nm at 30 kV. It also supports full integration of energy dispersive spectroscopy (EDS), wavelength dispersive spectroscopy (WDS), e-beam lithography and image database. Stage automation is standard with a 5-axis computer control of *x*, *y*, *z*, tilt and eucentric rotation. The FE-SEM can be configured for both high-vacuum and low-vacuum operation.

4.3.3 Universal testing machine

An universal testing machine (Shimadzu EZ-L) with 1000 N load cell was used in the shearing test. The testing machine supports a wide range of measurement applications, which the test force measurement accuracy ±1 % of indicated value with a test force between 1/250 and 1/1 load cell. It has the test speed ranging from 0.05 mm/min to 1000 mm/min. The rapid return speeds significantly reduce the cycle time for repetitive testing. Furthermore, the auto-calibration of test force ensures the stable measurement value.

4.4 Experimental procedures

A FPC and a brass electrode were used as specimens as shown in **Figures 4.6** and **4.7**, respectively. The FPC, which consists of five layers with four different materials, i.e. adhesive (two layers), polyimide (PI), copper (Cu) and tin (Sn). The sizes of copper circuit were 30 mm length, 2 mm width and 70 μm thickness with the 6 μm tin coating around the copper surfaces, while the adhesive and polyimide layers are 22.5 μm and 25 μm thickness, respectively. The components of brass electrode are copper (70 %) and zinc (30 %). The brass electrode with 650 μm width and 640 μm thickness was also coated with tin layer of 0.01 μm.

A schematic diagram of experimental setup is shown in **Figure 4.8**. In this study, a pulsed Nd:YAG laser (LASAG SLS200 CL8) of 1064 nm in wavelength was used as a laser source. The laser beam was delivered by an optical fiber of 50 μm core diameter. The collimator was installed between the optical fiber and the bending mirror, and the focusing point was coordinated by a lens of 50 mm in focal length. In order to avoid the back-reflection of incident laser beam, the processing

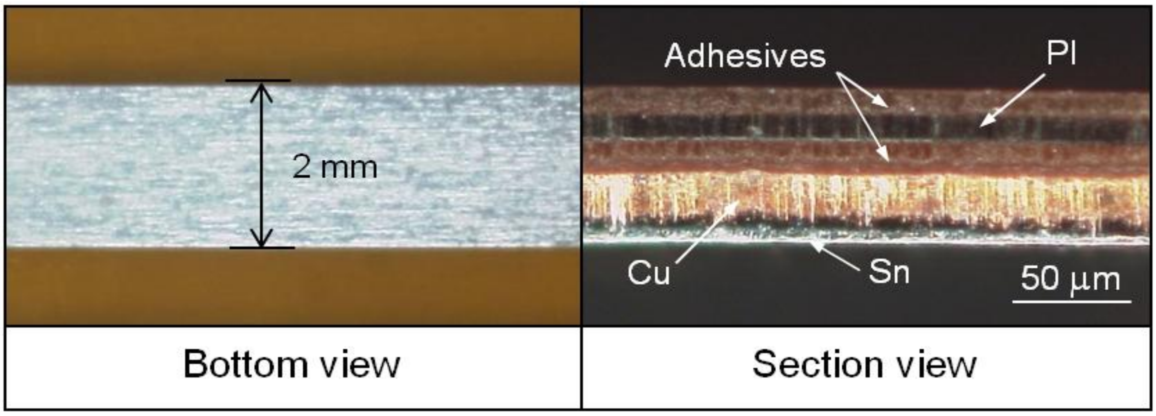

Figure 4.6 Photograph of flexible printed circuit

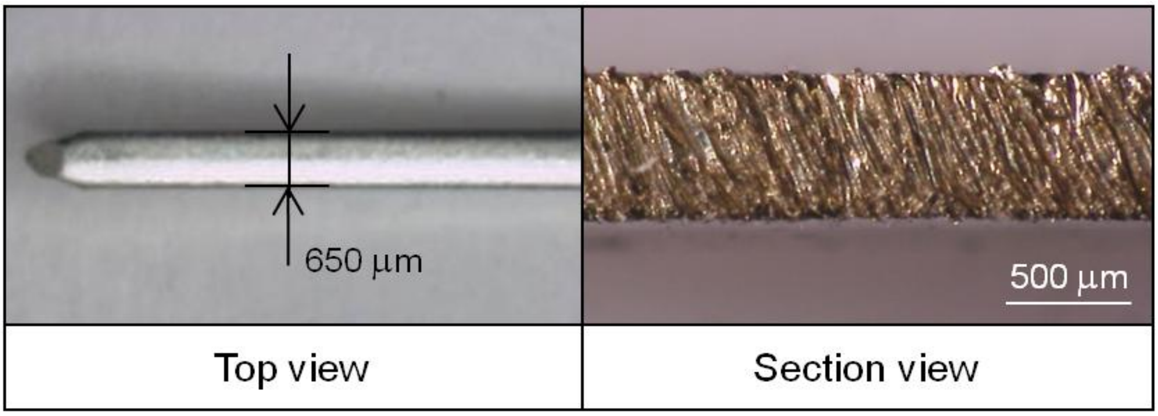

Figure 4.7 Photograph of brass electrode

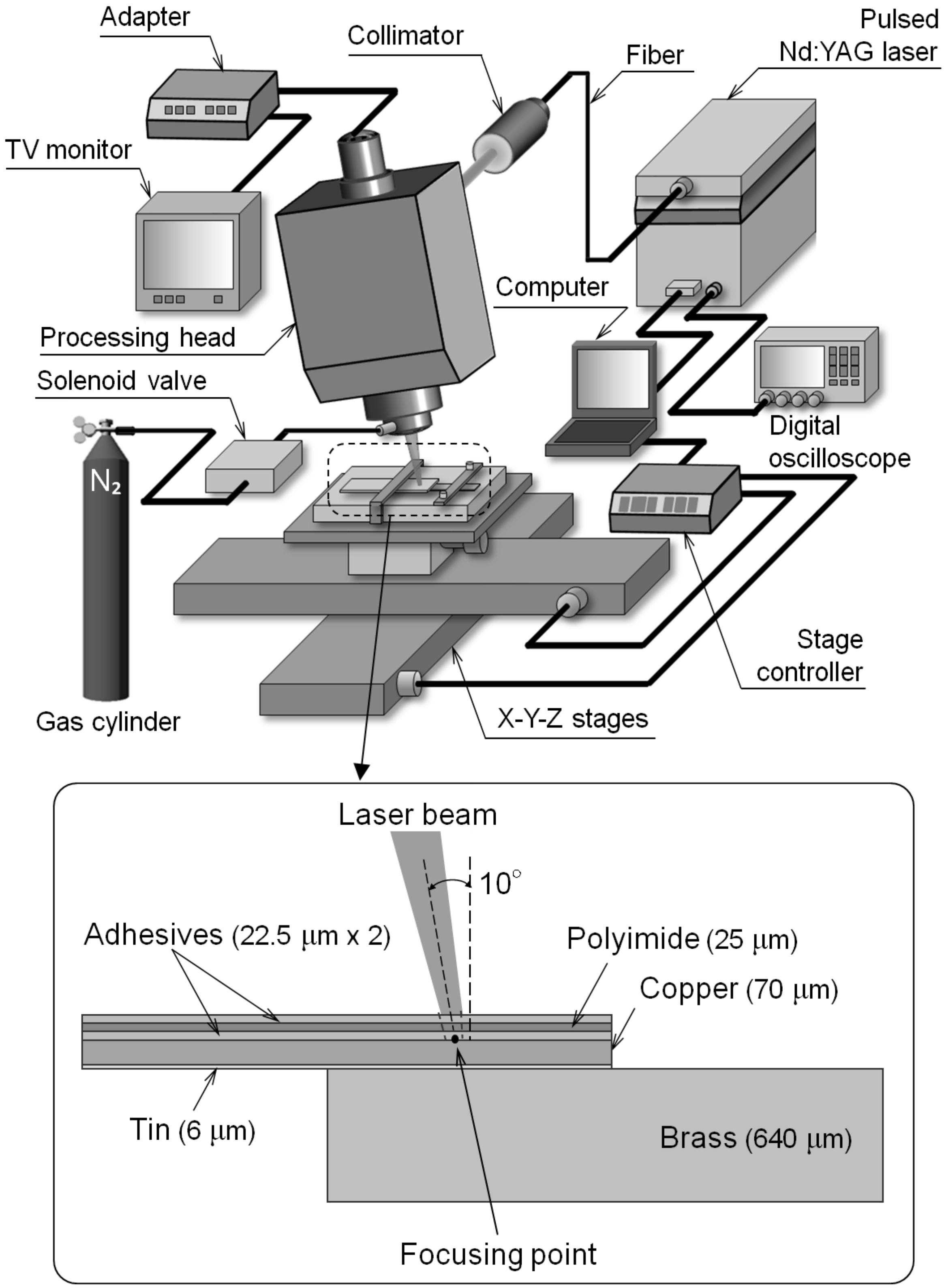

Figure 4.8 Schematic diagram of experimental setup

head was aligned 10 degrees to the perpendicular axis of specimen surface. The specimens were welded in an overlap joint geometry, where the thin copper circuit of FPC overlapped on a brass electrode under a shielding gas of nitrogen with 13 L/min flow rate. The position of laser irradiation was confirmed using a CCD camera located at the top of processing head. The setting shape of pulse waveform was controlled by the computer software, which is connected to the laser source machine. The actual signal of current waveform was measured by the digital oscilloscope, while the actual signal of pulse waveform was monitored and measured by the photodiode.

After the laser welding, the sectioned surface of welded specimen was ground, polished and etched for the observation of weld bead by an optical microscope, scanning electron microscope (SEM) and energy dispersive spectroscopy (EDS). In addition, the shearing test was carried out to measure the shear strength of the overlap welded joints with a Shimadzu EZ-L test machine. Since the test specimens of FPC and brass electrode are thin, the shearing test jig (**Figure 4.9(a)**) was used to ensure the test specimens firmly hold at the shear axis. The figure shows the clamping of test specimen during shearing test and the observation of fracture point on the top surface of brass electrode after the shearing test (**Figure 4.9(b)**). The cross-head speed was set to 1 mm/min. The specimen was gripped by the clamps, which are placed in the fixture blocks. Then, a shear load was slowly increased at the suitable increments by the mechanical lever system until the welded joint of specimen was fractured. The shear strength was calculated by using fracture load and welding area. The value of shear strength was the average of three specimens. Then, the fracture surfaces were observed with SEM.

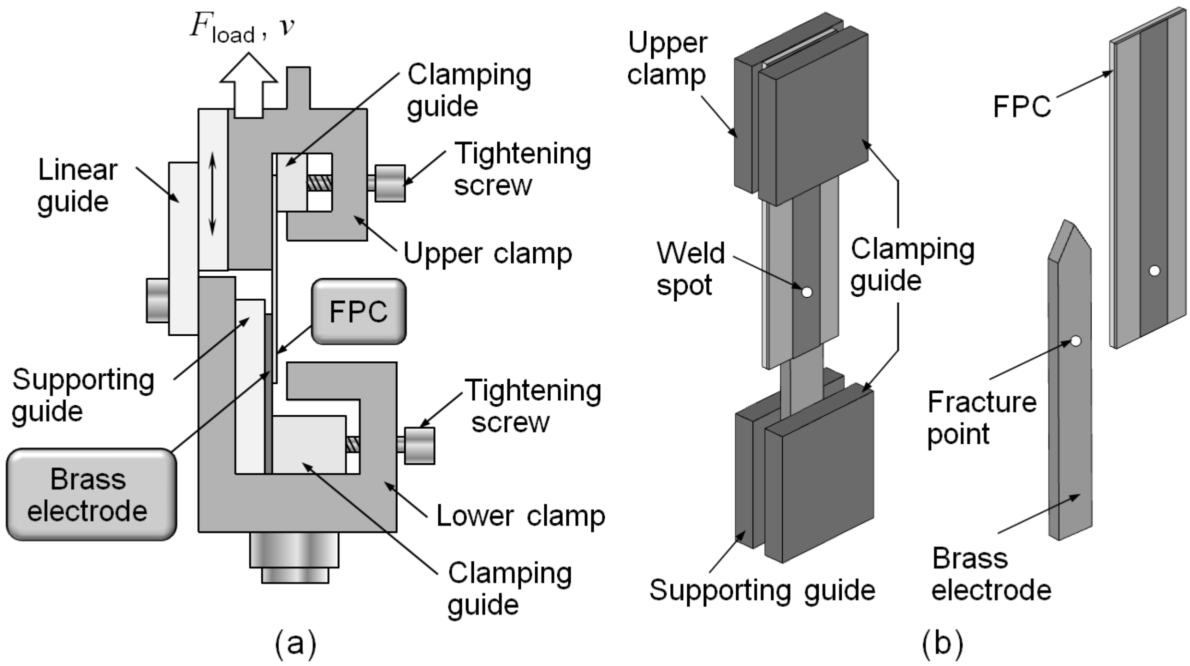

Figure 4.9 Schematic illustration of (a) shearing test jig and (b) observation of fracture point

4.5 Numerical analysis

In this study, the further analysis of the welding phenomenon was conducted by the heat conduction analysis with the finite element method (FEM). The analysis model is based on the fundamental heat transfer for laser micro-welding process. Based on the first law of thermodynamics, the equation written as equation (2.9) for heat flow in a three-dimensional solid was used.

Figure 4.10 shows the developed finite element model, and also shows the magnified mesh view near the interface. Fine mesh resolution is given at and near the heat source, while a fairly coarse mesh density is at the region far from the heat source. A portion of the specimens was designed in the analysis model in order to reduce the calculation time. As the heat source of laser beam is symmetric in the *y*-*z* plane, only half the heat source is considered. The heat source comprises a Gaussian plane heat source on the top surface and a conical shape heat source along the thickness of the specimen. To simplify the analysis, the assumption has been made that the alignment of laser spot was perpendicular to the specimen surface. The convective heat transfer condition of air was considered after the set time of laser irradiation. Except for a laser beam irradiated area, the convective heat transfer condition of air was also assumed. The analytical conditions are shown in **Table 4.2**. Since the temperature dependent on thermal properties are important for the accurate calculation of a temperature distribution. The temperature dependent thermal properties of copper are shown in **Figure 4.1**. However, to simplify the analysis the changes in thermal properties with temperature dependent for adhesive, polyimide, tin and brass during laser processing were not considered as shown in **Table 4.3**.

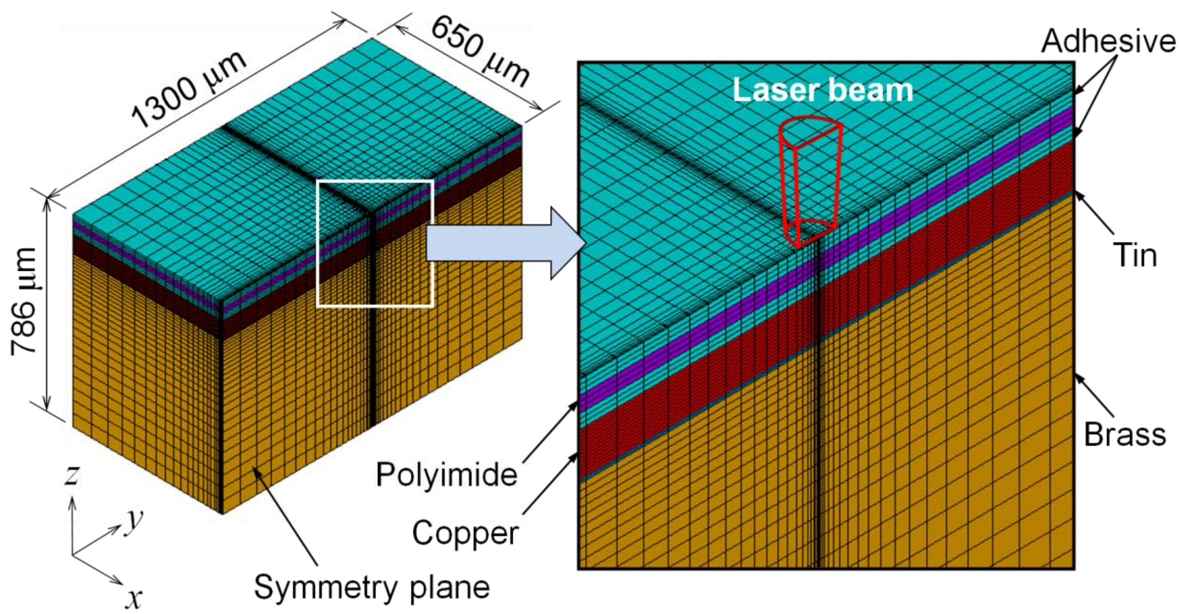

Figure 4.10 Finite element model for heat conduction analysis

Table 4.2 FEM analysis conditions

Parameter / condition			Value
Laser power	P	W	50–400, 500
Pulse width	τ	ms	3.0, 4.1
Beam diameter	d	μm	50
Heat transfer coefficient	h_c	$W/(m^2 \cdot K)$	10
Room temperature	θ_∞	K	293

Table 4.3 Thermal properties for adhesive, polyimide, tin and brass

Material	Thermal conductivity k W/(m·K)	Specific heat c J/(kg·K)	Density ρ kg/m^3
Adhesive	0.13	1085	1255
Polyimide	0.14	1090	1380
Tin	67	228	7280
Brass	120	375	8530

4.6 Results and discussion

4.6.1 Rectangular pulse waveform

Figure 4.11 shows the cross-section views for various pulse energies with the rectangular pulse waveform. As shown in the **Figure 4.11(a)**, the copper layer was not molten at 400 W laser power and 1 ms pulse width (E_p: 400 mJ/pulse). It can be observed that only the brass was molten with the presence of hole due to the lower melting point of brass (1228 K) compared with that of copper (1358 K). Furthermore, since the reflectance of laser beam on a copper is high, the absorbed laser energy is too low to melt a copper. Thus, the molten zone appeared only in the brass at the end of laser pulse. **Figure 4.11(b)** shows the cross-section view for higher 500 W laser power and the same 1 ms pulse width (E_p: 500 mJ/pulse). A penetration hole through a copper layer can be observed with the molten region of brass around the hole. In this case, the higher heat input of laser spot would accelerate the evaporation of alloyed zinc in the brass, which has low boiling point (1180 K). The higher laser power enhances to increase the surface temperature of copper and induces more laser energy absorbance. However, this higher laser power resulted in the evaporation at the beginning of laser pulse. Subsequently, for longer 3 ms pulse width with 500 W laser power (E_p: 1500 mJ/pulse) as shown in **Figure 4.11(c)**, it was clear that the hole became larger due to the long interaction time,

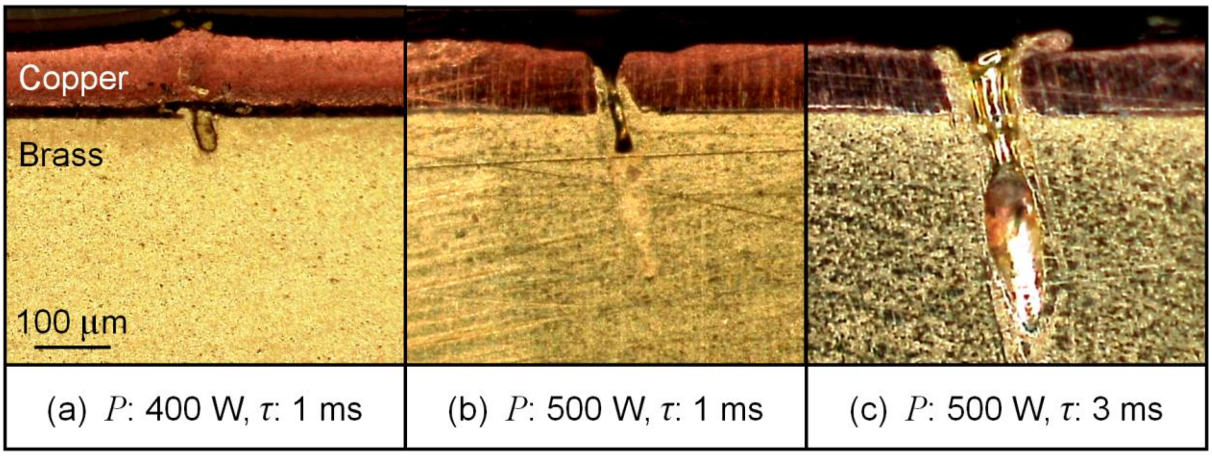

Figure 4.11 Cross-section view of welding results with rectangular pulse waveform

which caused the excessive evaporation of alloyed zinc in the brass. From these viewpoints, for joining copper and brass, the 500 W laser power with 1 ms pulse width can be used as a basic model in the thermal analysis.

Figure 4.12 shows the calculated temperature distributions at the central cross-section of specimen with 500 W laser power and 3 ms pulse width at the time of 1 ms, 2 ms and 3 ms after the beginning of laser irradiation. The evaporation areas of adhesive and polyimide layers were defined as the gray color in the upper part. After the removal of element in the gray color area, the thermal analysis was performed on the outer of evaporation area of adhesive and polyimide layers. It can be seen that the half-bottom of copper does not reach the melting point at 1 ms from the beginning of laser irradiation. It can be clearly clarified that the absorbed energy on the copper was quickly diffused due to its higher thermal conductivity. In addition, the absorptivity of copper is very low below melting point, which also make the longer heating time is required to rise the temperature from the laser irradiated point of top edge to the bottom edge of copper layer before the joining between copper and brass. Although the laser spot cannot penetrate the copper, the alloyed zinc has reached the boiling point. It can be confirmed that the holes are already formed during this period. Even the longer pulse width increased the temperature to achieve the full-penetration in the copper layer, the size of holes in brass became larger since the absorbed energy was simultaneously increased. In other words, it is considered that the difference in the absorptivity and the specific heat between copper and brass led to the selective evaporation of brass, and a large hole was remained.

Figure 4.13 shows the temperature histories of three points selected in the analysis model, where the points of A, B and C are located at the top edge of copper, at the bottom edge of copper and at top edge of brass as shown in **Figure 4.12**, respectively. The red dashed line indicates the melting point of copper. There is an interval time of about 0.8 ms to melt at the bottom edge of copper after the melting of copper at the top edge. Meanwhile, it can be seen that the evaporation of alloyed zinc is growing in point C during that interval time. Alloyed zinc in the brass evaporates easily, and the formation of the hole is inevitable in the laser irradiation with a rectangular pulse waveform.

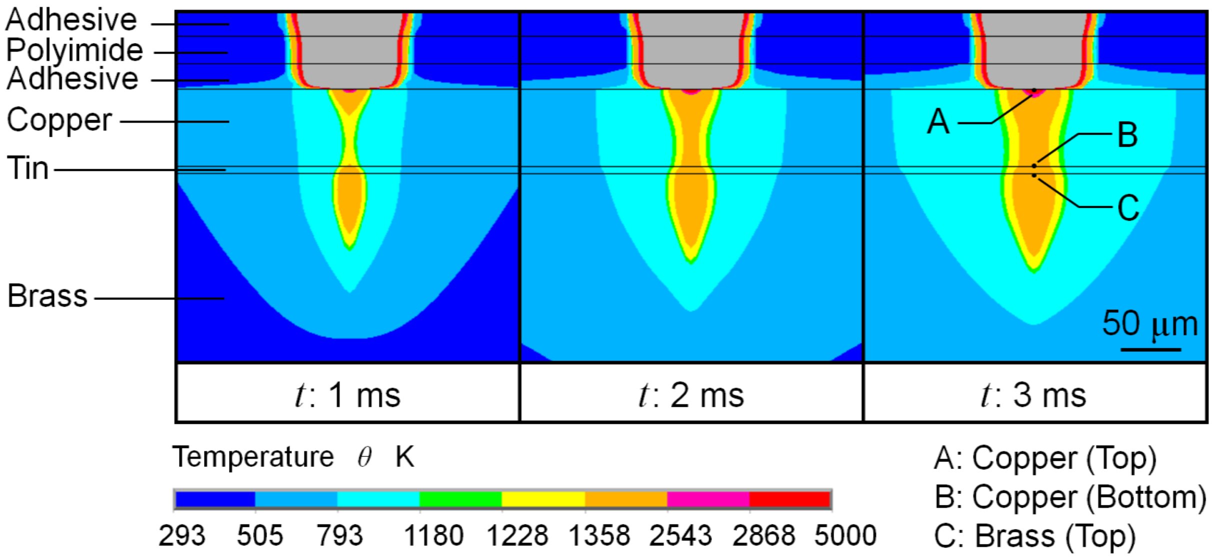

Figure 4.12 Spatial temperature distribution at 500 W – 3 ms with rectangular pulse waveform

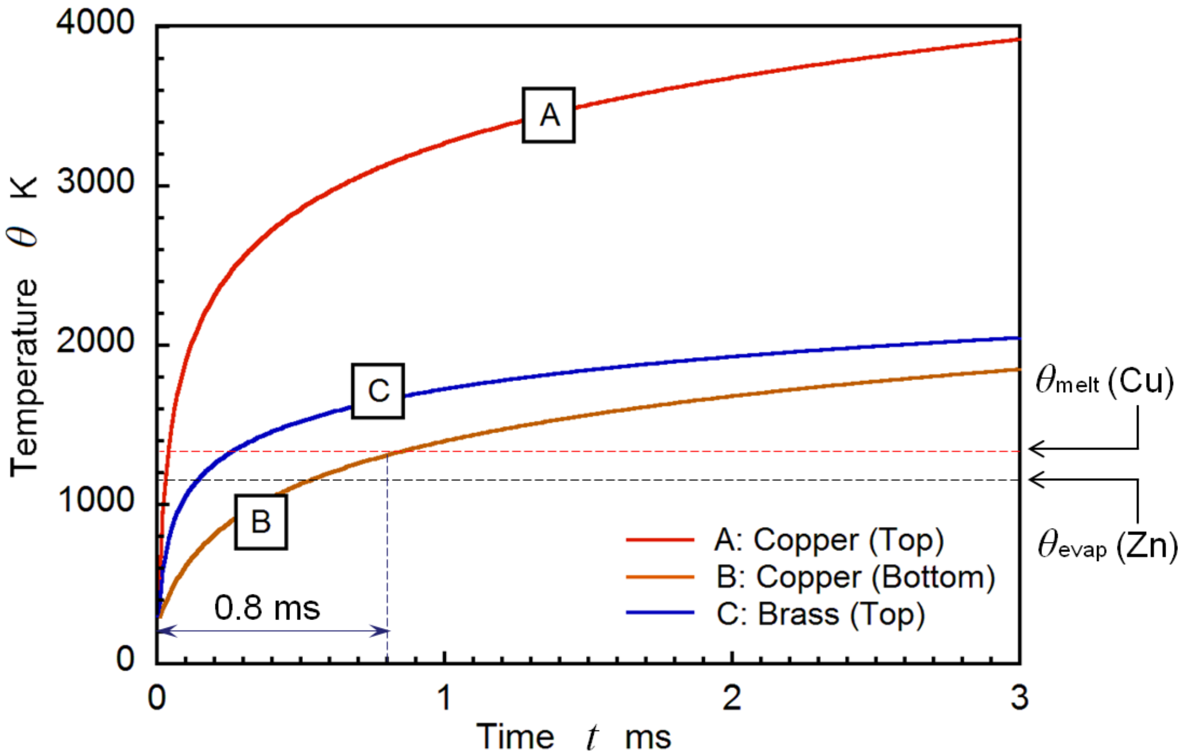

Figure 4.13 Temporal temperature distribution at 500 W – 3 ms with rectangular pulse waveform

4.6.2 Pulse waveform with pre-heating effect

According to the **Figure 4.1**, the absorptivity of copper increases approximately three times from the solid state phase at room temperature to the molten phase. Therefore, a solution is to pre-heat the copper that overcome the low initial absorptivity, and it is the most common method used to counteract the high thermal conduction.[4.19)] Based on this point, the pre-heating effect was applied before the joining of FPC and brass electrode on the pulse waveform to prevent from the formation of a large hole. Since the FPC consists of two main layers of thin copper circuit and adhesive/polyimide films, the pre-heating effect was divided into two phases. As shown in **Figure 4.14**, the phase 1 is started with lower pulse energy to eliminate the adhesives and polyimide films. This phase also initiates the heat conduction on the copper surface to increase the absorptivity of laser beam. In the phase 2, the higher laser power with an appropriate interaction time is required to generate the molten zone in the copper layer without the melting of brass. It is expected that the phase 2 would prevent from the occurrence of hole in molten area. After the pre-heating effect on the pulse waveform, in the phase 3, the increasing of laser power was employed for joining copper and brass.

The variation of the laser power with time was analyzed by the thermal analysis. Compared with the temperature distributions of the rectangular pulse waveform condition, **Figure 4.15** shows that the temperature rises from the laser irradiated point of top edge to the bottom edge of copper layer. It also can be seen that a sufficient interaction time about 3 ms with 300 W laser power is

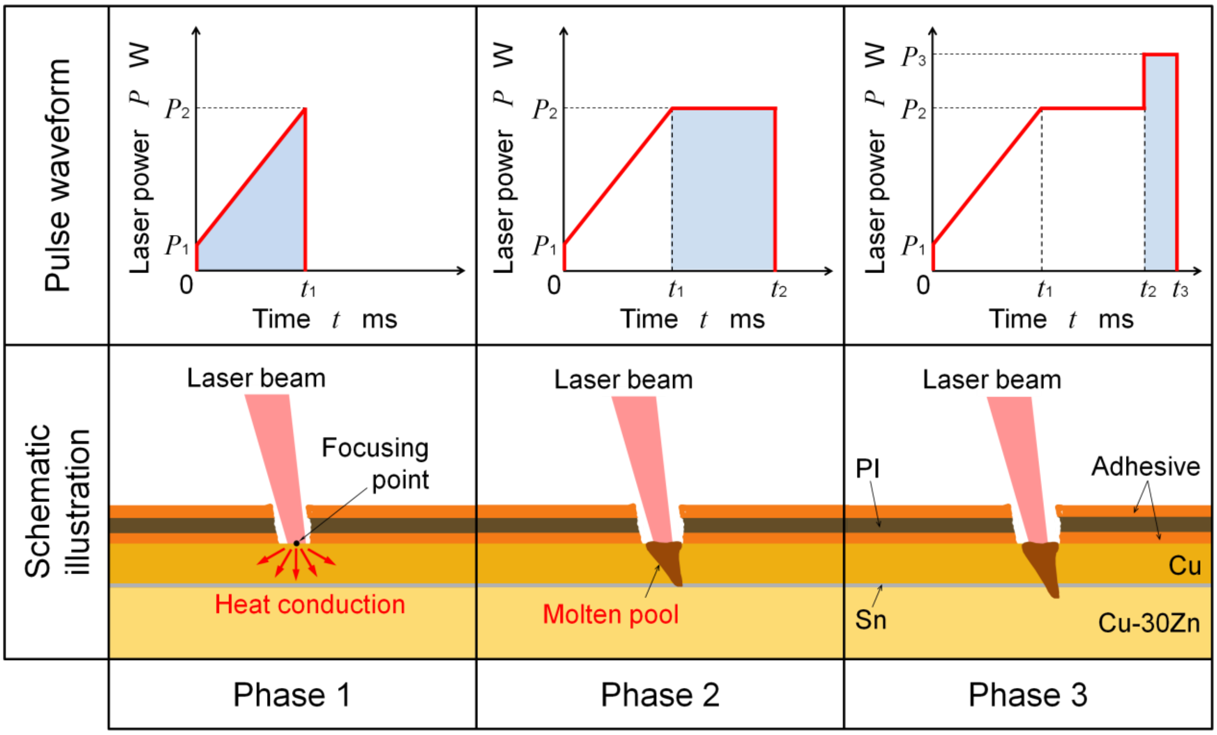

Figure 4.14 Schematic illustration of welding mechanism with pre-heating

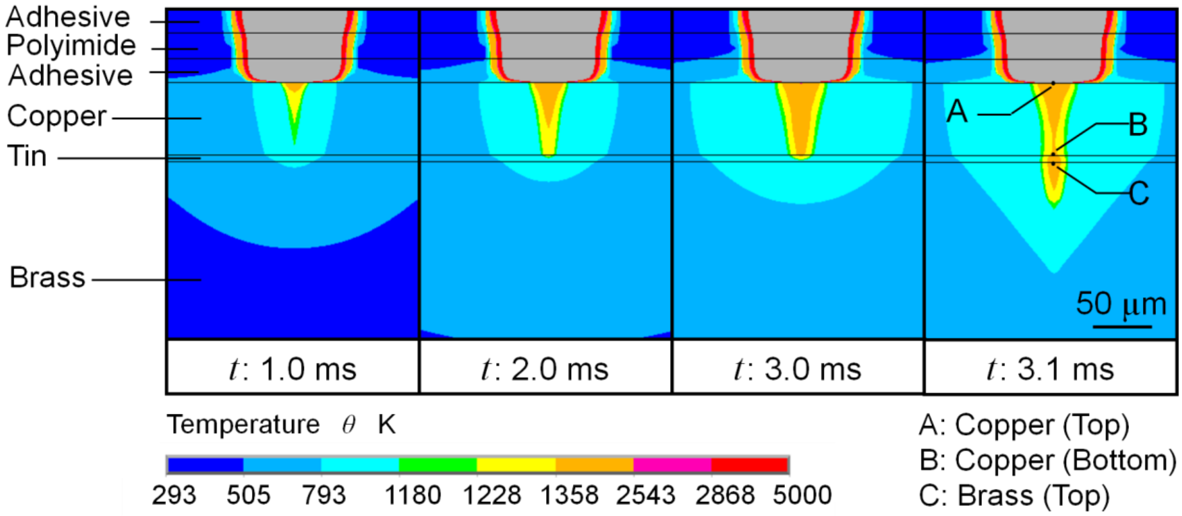

Figure 4.15 Spatial temperature distribution with pre-heating effect on pulse waveform

required to generate the molten zone in the copper layer without melting of brass in the phases 1 and 2. As shown in **Figures 4.15** and **4.16**, the temperature of copper layer rises from the top to the bottom edge of copper layer. It indicates that only the temperature of point C (top surface of brass) rapidly increases during the irradiation time between 3 ms to 3.1 ms in the phase 3, after the full-penetration of the copper layer is achieved. Since the temperature continually increases in the short time, the evaporation of alloyed zinc in the brass could be controlled.

The controlled pulse waveform was divided into three phases including the two phases of pre-heating in the beginning of the pulse. The phase 1 is started with laser power P_1 up to P_2 under the duration of pulse width τ_1. P_2 and P_3 are the laser powers used in the phase 2 and 3, respectively. The duration of phase 2 is performed with τ_2 of pulse width, while the phase 3 with pulse width τ_3. According to the laser irradiation of the phase 1, which is to remove the adhesive and polyimide films of FPC, the laser power was fixed from 50 W to 300 W and the pulse width were set at 1.5 ms. **Figure 4.17** shows the removal parts of adhesive and polyimide films until the phase 1. It can be observed the top surface of copper at the end of phase 1, and this phase is essential to initiate the heat conduction to increase the absorptivity before the phase 2. The pre-heating effect of pulse waveform in the phase 2 was carried out with the laser power of 300 W, while the pulse width varied from 0.5 to 2.5 ms.

Figure 4.18 shows the bottom views of the FPC until the phase 2. The heat-affected zone and molten zone could not be confirmed from the cross-section view. As can be seen from the inappropriate conditions of 300 W laser power with the irradiation time of 2 ms and 2.5 ms, the laser spot fully penetrated through the copper layer, and the blowhole was generated. From these results, the 300 W laser power with 1.5 ms pulse width is appropriate condition to generate molten zone without the penetration hole for the phase 2 of pulse waveform.

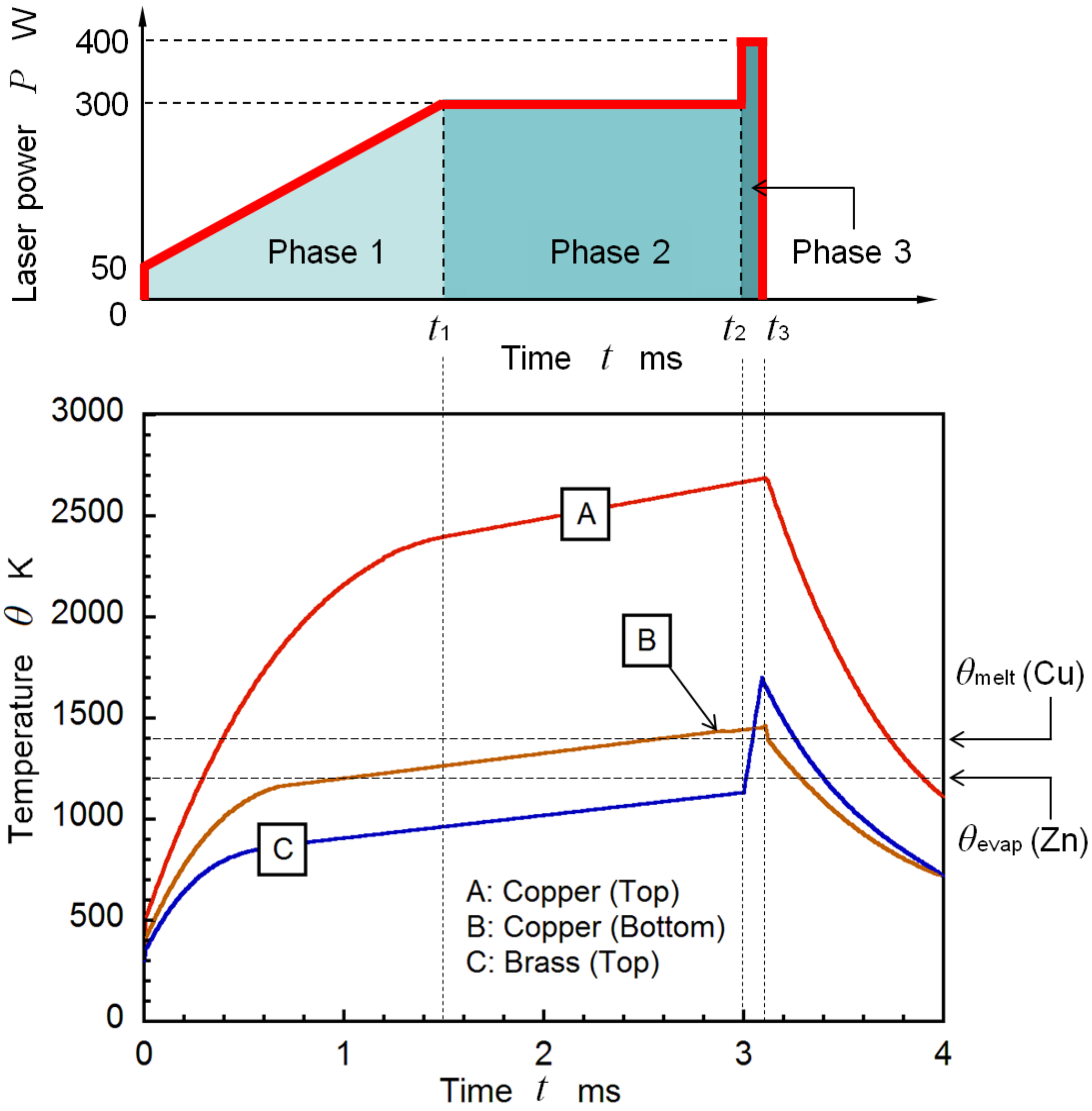

Figure 4.16 Temporal temperature distribution with pre-heating effect on pulse waveform

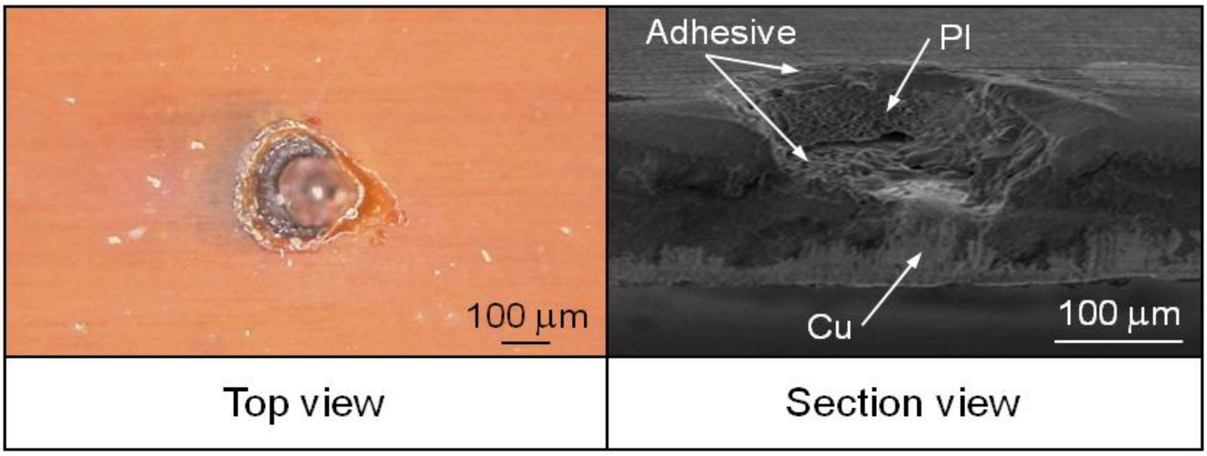

Figure 4.17 Removal part of adhesive and polyimide films in phase 1 of controlled pulse waveform (P_1: 50–300 W, τ_1: 1.5 ms)

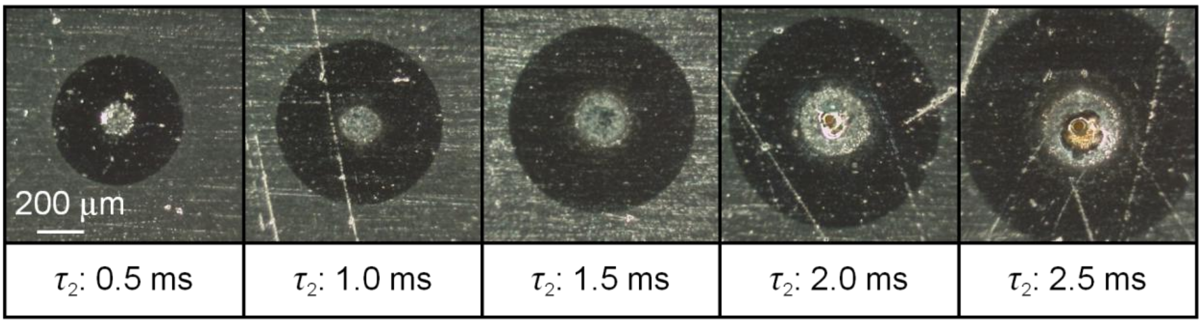

Figure 4.18 Bottom view of FPC in phase 2 of pulse waveform with pre-heating effect (P_2: 300 W)

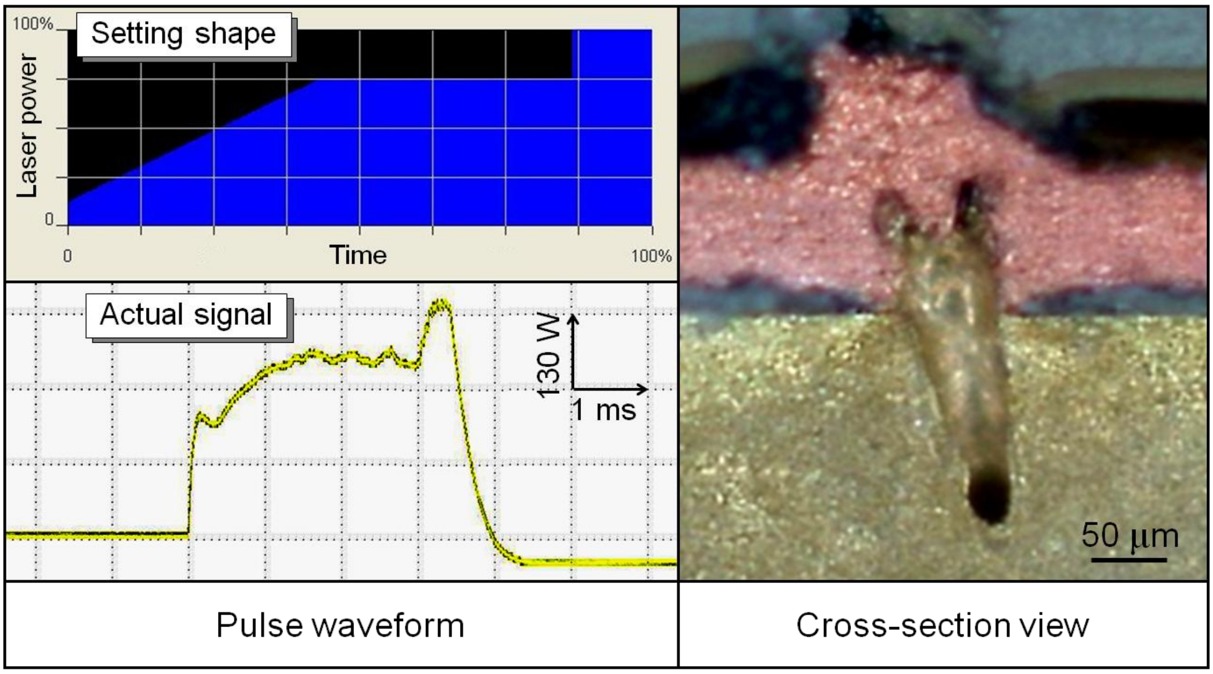

Figure 4.19 Welding result of pulse waveform with pre-heating effect (P: 400 W, τ: 3.5 ms)

Next, the phase 3 of pulse waveform was carried out for the joining of copper and brass. The laser power and pulse width were set at 400 W and 3.5 ms, respectively. The pulse waveform and cross-section view of welding result are shown in **Figure 4.19**. The porosity and bump defects were observed in contrast to the expected result. Porosity is formed due to the instantaneously increase of laser power in phase 3. Another cause of porosity is the trapped gases of alloyed zinc from the bottom of the weld keyhole, which is occurred under a high pressure.[4.20] It can be noted that the high pressure of trapped gasses pushed upward the molten copper to generate bump, and it was solidified immediately at the end of laser pulse irradiation. Therefore, the post-heating effect on the pulse waveform was considered for the copper-brass joining without weld defects.

4.6.3 Pulse waveform with pre- and post-heating effects

The phase 4 of post-heating is a subsequent function of the phase 3 by adding the heat to melt the bump generated in phase 3. This re-melting process was intended to fill the hole in order to obtain a better joining condition. **Figure 4.20** shows the configuration of pulse waveform with the pre- and post-heating effect and the cross-section observation. As a new phase 4 in the configuration of pulse waveform, the laser power gradually decreases to stream down the bump below the evaporation point of brass. As a result, it can be seen that the use of post-heating configuration has a positive effect on molten pool to remove the bump. However, the use of longer pulse width (τ_4: 3 ms) generated an undercut defect on the copper layer. This result would be caused by the overheating, where most of the copper and zinc have been evaporated. Therefore, it is considered that the post-heating should be modulated with small and sustainable heat input by introducing an approach of rest time in the post-heating phase of pulse waveform.

At the particular time in the post-heating of phase 4, the laser power was set to zero for the reduction of the heat input as shown in **Figure 4.21**. The waveform of post-heating is divided into three pulses with the rest time inserted between pulses. It can be noted that the hole was filled without any weld defects in both conditions. It can be proved that an appropriate heat input on the post-heating phase melted the bump and filled the hole in the brass layer. Furthermore, the rest time can be expected to avoid the overheating and to stabilize the weld joint. Therefore, it can be clearly confirmed that the direct joining of a FPC and a brass electrode was realized without any weld

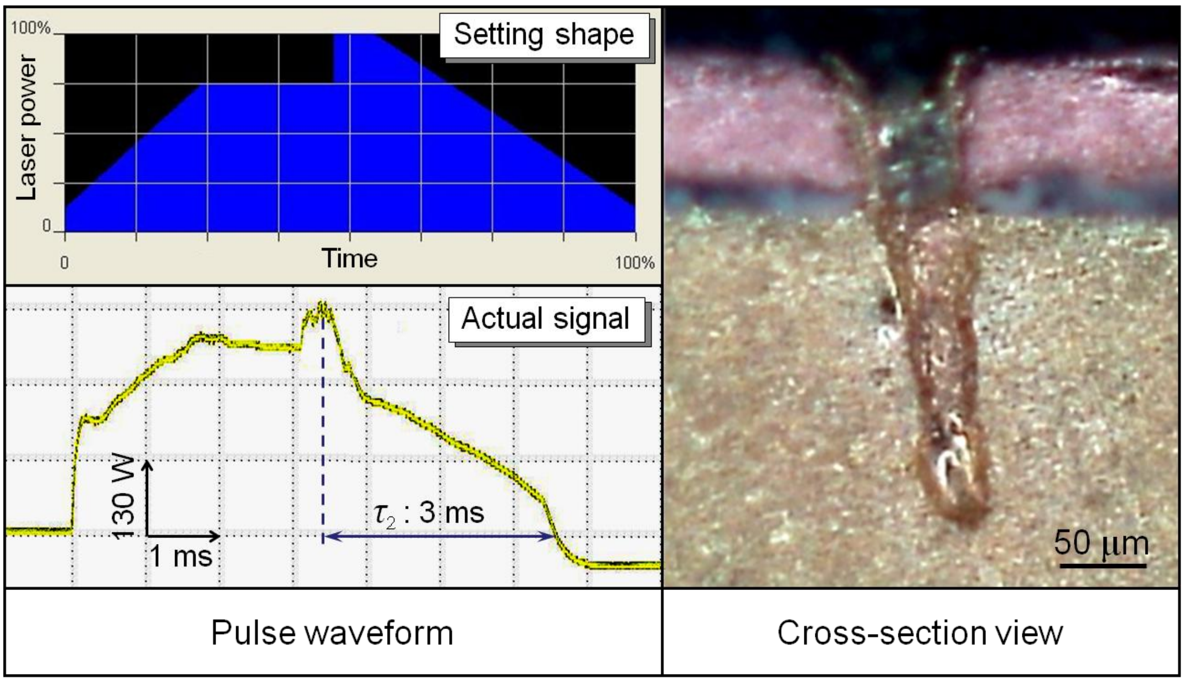

Figure 4.20 Welding result of pulse waveform with pre- and post-heating effects (P: 400 W, τ: 6.5 ms)

defects by the pulse waveform with pre- and post-heating effects including the rest time.

In addition, the elemental analysis was performed to observe the element distribution at the welded parts, such as Cu, Zn and Sn using a scanning electron microscope (SEM) equipped with the energy dispersive spectroscopy (EDS). **Figure 4.22** shows the EDS mapping and spot analysis results of overlap welding by pulse waveform with pre- and post-heatings including rest time (**Figure 4.21(a)**). According to the distribution map of element, the small amount of Zn element was uniformly distributed in the molten zone of copper layer. It was confirmed by the EDS spot analysis,

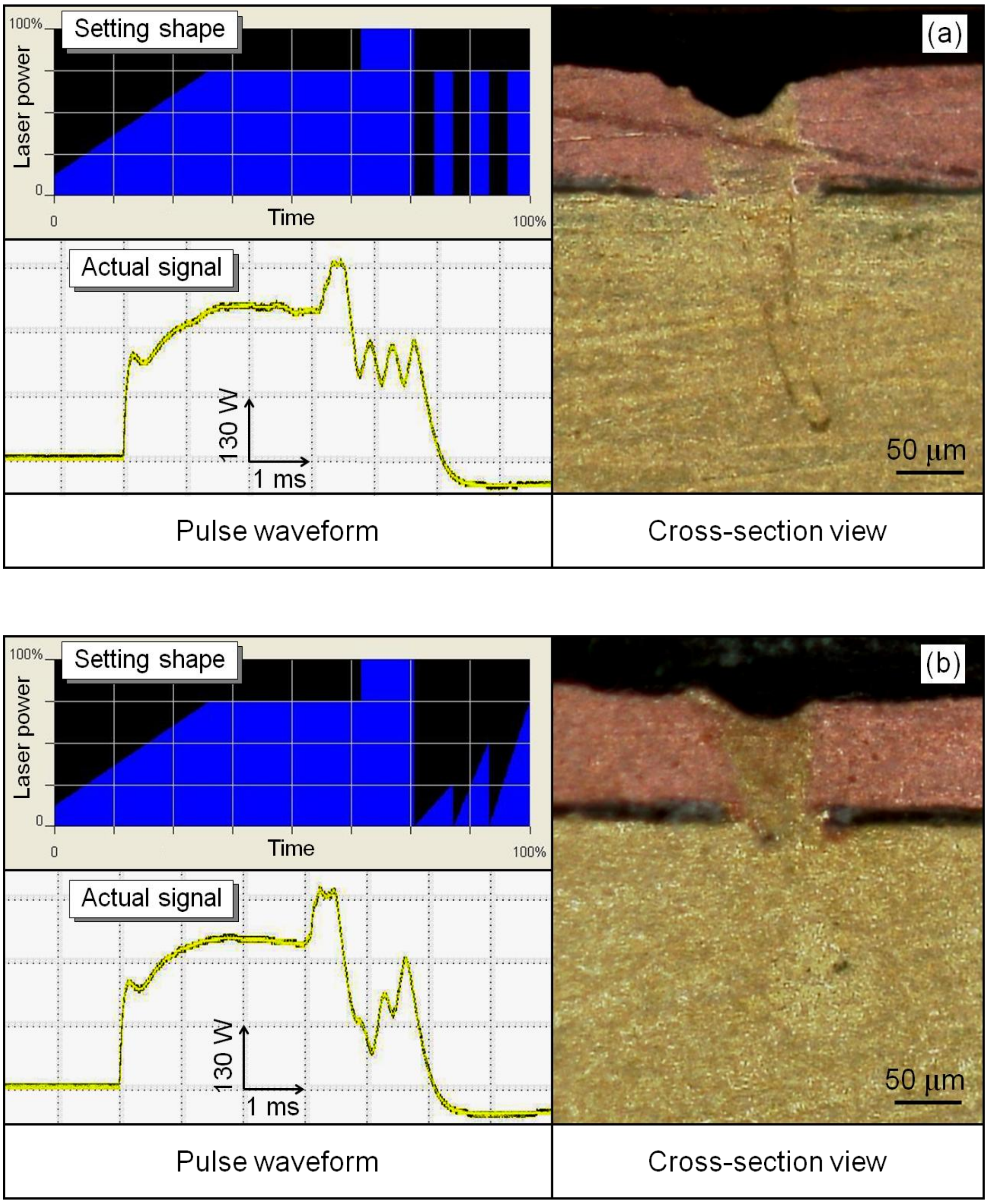

Figure 4.21 Welding result of pulse waveform with pre- and post-heating effects including rest time (P: 400 W, τ: 4.7 ms)

where the slightly high percentage of Zn in the molten zone of copper layer (Point 1 and 2) compared than the copper metal away from the molten zone (Point 5). It can be noted that the small amount of Zn element from the brass material of electrode was moved to the top of molten zone during the joining process. Moreover, the spot analysis shows that the amount of Cu and Zn in the molten zone located between copper and brass layers (Point 3), and in the molten zone of brass layer (Point 4) were not much difference compared than the brass metal away from the molten zone (Point 7). This result shows that evaporation of Zn obtained in the direct laser micro-welding, is being prevented by appropriate controlled pulse waveform.

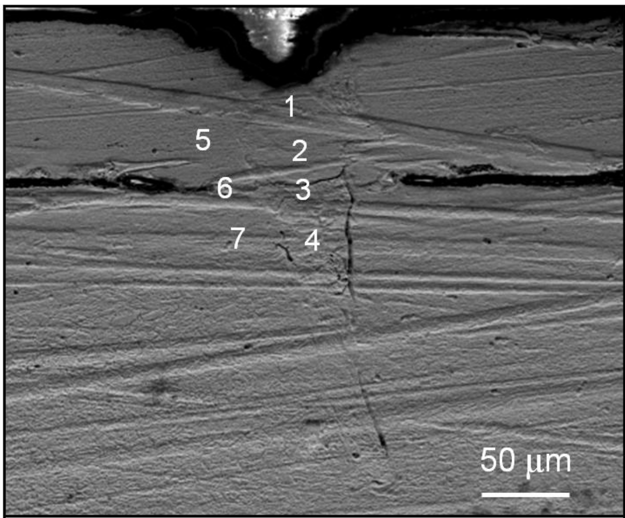

SEM image

No.	Cu (wt.%)	Zn (wt.%)	Sn (wt.%)
1	95.01	4.17	0.82
2	94.61	4.72	0.67
3	71.89	27.70	0.42
4	68.40	29.75	1.86
5	98.46	1.09	0.45
6	49.33	2.29	48.38
7	70.71	28.80	0.49

EDS spot analysis

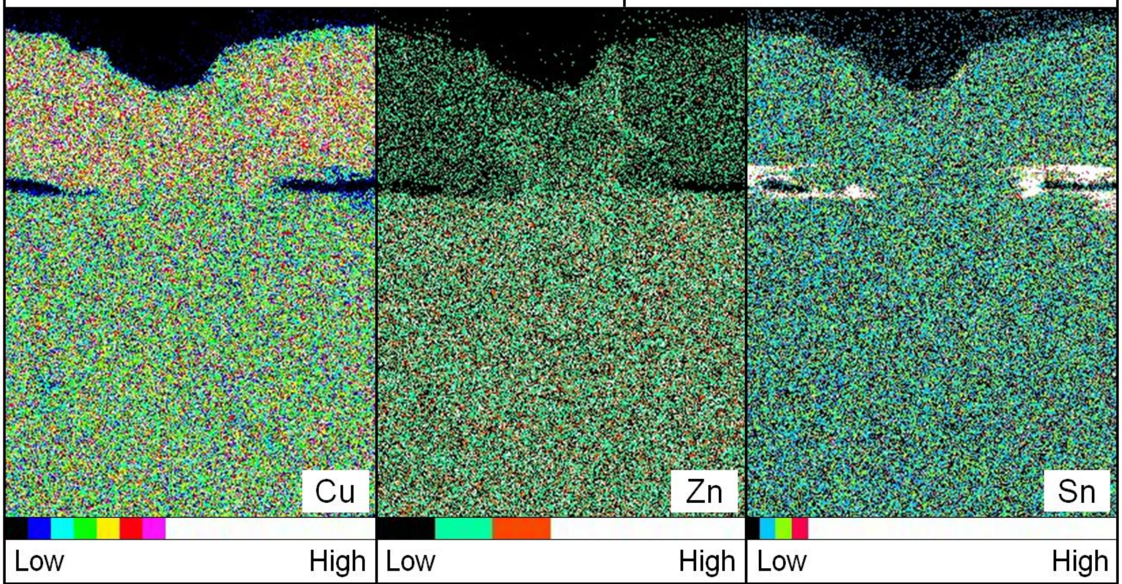

EDS mapping

Figure 4.22 SEM image, EDS spot and mapping analysis of pulse waveform with pre- and post-heatings including rest time

4.6.4 Evaluation of weld strength

In order to evaluate the weld strength on the overlap welding with and without the control of pulse waveform, the shearing test was carried out. **Figure 4.23** shows the various laser pulse waveforms used for the shearing test. Based on the **Figure 4.9(b)** for the observation of fracture point in the shearing test, **Figure 4.24** shows the fracture part on the top surface of brass electrode after the shearing test. It shows that, in the laser welding with the rectangular pulse waveform condition, the fracture occurred with the presence of hole. On the other hand, in the welding with the control of pulse waveform, the fracture occurred without the defect of hole. As can be seen from **Figure 4.25**, the shear strength of welded specimen with the rectangular pulse waveform (Case 1-3) showed a lower value than that with the controlled pulse waveform (Case 4-8). As shown in **Figures 4.11** and **4.24**, it could be noticed that the existences of hole and porosity defects had obvious influence on the weakness of weld joint strength, even if the rectangular pulse waveform generated larger heat input. With the control of pulse waveforms, there was decreasing in heat input, while the shear strength increased. The pulse waveform with only pre-heating (Case 4) was less significant on the weld strength, since the bump and porosity defects were occurred on the weld joint as shown in

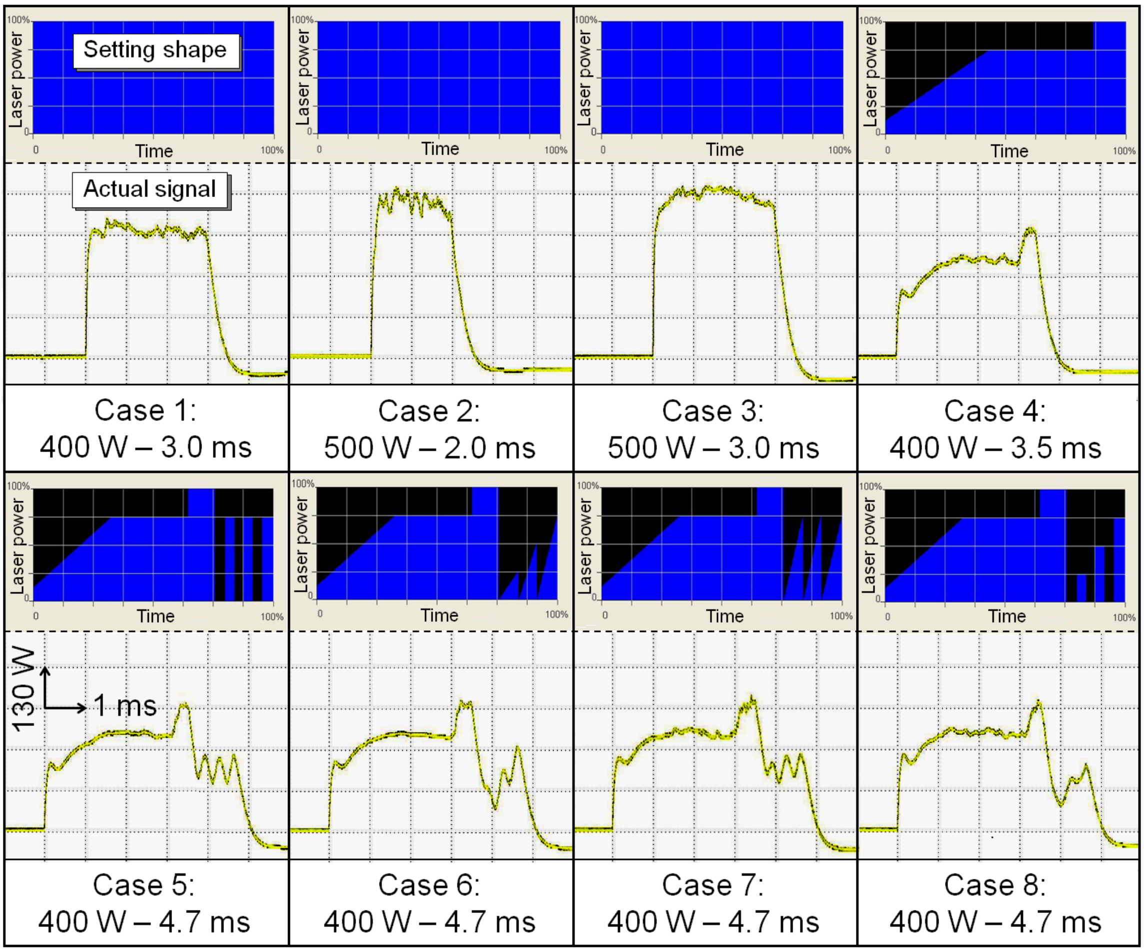

Figure 4.23 Pulse waveforms used for the shearing test

Figure 4.19. Compared with the pulse waveform with the pre- and post-heatings, the insertion of rest time on the post-heating phase is expected to avoid the overheating and weld defects. It showed the higher shear strength, even it yields smaller welded joint area. However, it shows that the pulse waveform with the pre- and post-heatings of Case 7 and 8 were less significant to increase the weld strength. It can be noted that the inappropriate pulse shape on the post-heating phase was directly affected on the lower weld strength. Therefore, it is clearly that the appropriately controlled laser pulse configurations are effective to produce a higher strength of joint for a direct joining between a FPC and a brass electrode.

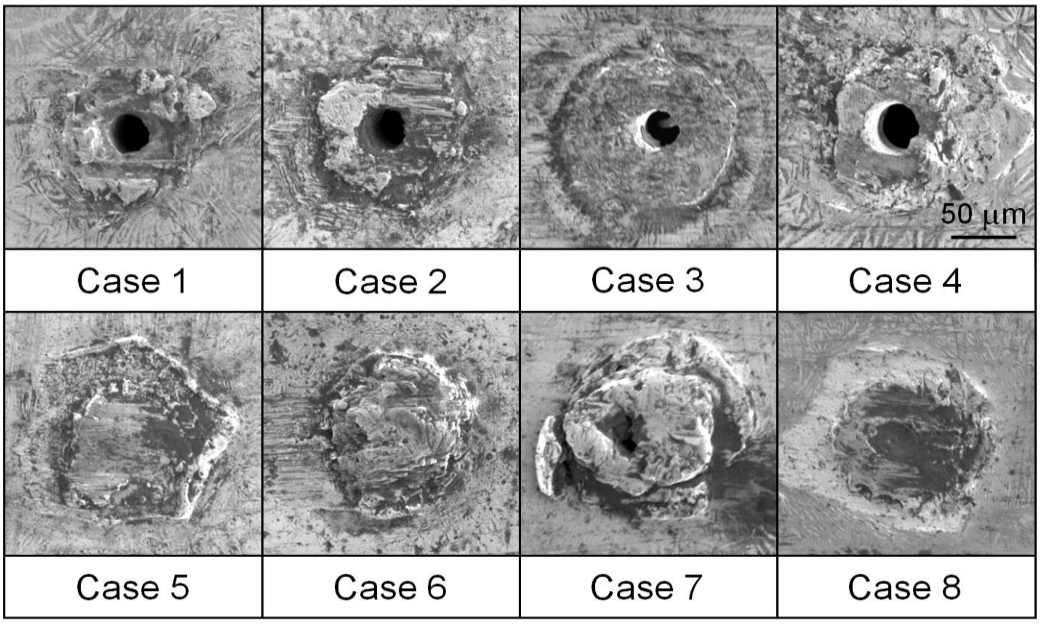

Figure 4.24 Fracture on the top of brass electrode

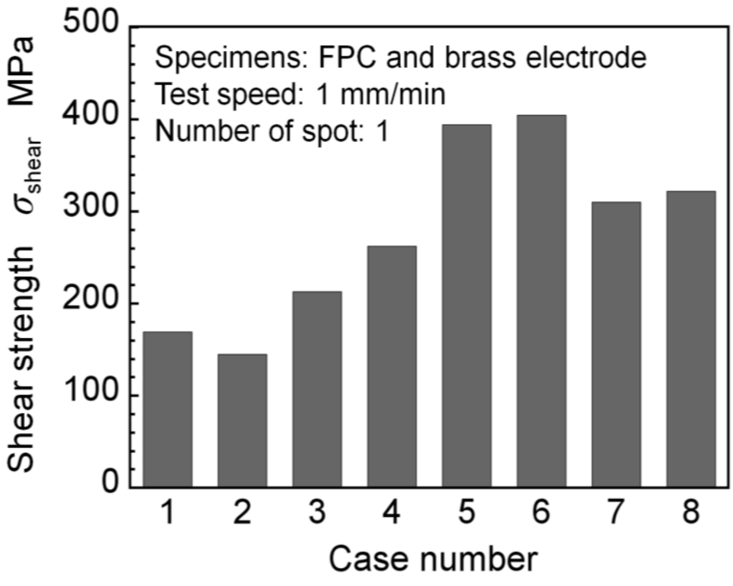

Figure 4.25 Shear strength of the welding with and without the control of pulse waveform

4.7 Conclusions

The overlap micro-welding of thin copper circuit and thick brass electrode by using the control of pulse waveform and heat input was experimentally and numerically investigated. Main conclusions obtained in this chapter are as follows:

(1) Alloyed zinc in the brass was evaporated easily, and the formation of porosity was inevitable in the laser irradiation with the rectangular pulse waveform.

(2) Pre-heating effect of the pulse waveform was essential to increase the surface temperature of copper and induced higher absorption of laser energy at the beginning of laser pulse.

(3) Post-heating effect of the pulse waveform performed a positive result to remove the bump defect. However, the inappropriate heat input led to the undercut defect in copper layer.

(4) Better weld joint without weld defects could be achieved by adding a rest time in the post-heating phase.

(5) The higher shear strength could be obtained by the control of pulse waveform to perform the good joining without weld defects.

References

4.1) S. Katayama and Y. Kawahito : Laser Direct Joining of Metal and Plastic, Scripta Materialia, (2008), Vol. 59, 1247-1250.

4.2) Y. Ozeki, T. Inoue, T. Tamaki, H. Yamaguchi, S. Onda, W. Watanabe, T. Sano, S. Nishiuchi, A. Hirose and K. Itoh : Direct Welding Between Copper and Glass Substrates with Femtosecond Laser Pulses, Applied Physics Express, (2008), Vol. 1, 082601.

4.3) J.W. Kim and C.G. Kim : Design of a Laser Welded Thin Metal Tube Structure Incorporating Welding Distortion and Residual Stress, International Journal of Precision Engineering and Manufacturing, (2010), Vol. 11, No. 6, 925-930.

4.4) F. Otte, U. Stute and A. Ostendorf : Micro Welding of Electronic Components with 532nm Laser Radiation, Proceedings of SPIE, (2007), Vol. 6458, 645804.

4.5) K. Takahashi, T. Watanabe, S. Matsusaka and T. Wada : Direct Microjoining of Copper Materials Using Laser Beams, JSME International Journal, Series C, (2006), Vol. 49, No. 1, 128-134.

4.6) G. Shahnon and P. Severloh : Laser Microwelding of Copper, Industrial Laser Solutions, (2009), January, 1-3.

4.7) AWS : Welding Copper and Copper Alloys, American Welding Society, (1997), 10-13.

4.8) L. Migliore : Laser Materials Processing, Marcel Dekker, (1996), 176-178.

4.9) J.C. Ion : Laser Processing of Engineering Materials, Elsevier Butterworth-Heinemann, (2005), 431-433.

4.10) A. Blom, P. Dunias, P.V. Engen, W. Hoving and J.D. Kramer : Process Spread Reduction of Laser Micro-spot Welding of Thin Copper Parts Using Real-time Control, Proceedings of SPIE, (2003), Vol. 4977, 493-507.

4.11) JSTP : Thermophysical Properties Handbook, Japan Society of Thermophysical Properties, (2008), 23-25.

4.12) M. Naeem : Controlling the Pulse in Laser Welding, Welding, (2004), June, 1-4.

4.13) E. Biro, D.C. Weckman and Y. Zhou : Pulse Nd:YAG Laser Welding of Copper Using Oxygenated Assist Gases, Metallurgical and Materials Transactions A, (2002), Vol. 33A, 2019-2030.

4.14) M. Rohde, C. Markert and W. Pfleging : Laser Micro-welding of Aluminum Alloys – Experimental Studies and Numerical Modeling, International Journal of Advanced Manufacturing Technology, (2010), Vol. 50, 207-215.

4.15) J. Zhang, D.C. Weckman and Y. Zhou : Effect of Temporal Pulse Shaping on Cracking Susceptibility of 6061-T6 Aluminum Nd:YAG Laser Welds, Welding Journal, (2008), Vol. 87, No. 1, 18s-30s.

4.16) M. Schmidt and M. Weigl : Laser-bonding in High Power Electronics, Journal of Laser Micro/Nanoengineering, (2010), Vol. 5, No. 3, 242-247.

4.17) R. Witte, R. Liebers, R. Holtz, J. Wilden and T. Neumann : Laser Welding with Pulsed Solid State Lasers – Strategies and New Developments, Proceedings of LPM 2010 – the 11th International Symposium on Laser Precision Microfabrication, (2010).

4.18) M. Naeem : Microwelding Performance Comparison Between a Lower Power (125 W) Pulsed Nd:YAG Laser and a Low Power (100–200 W) Single Mode Fiber Laser, Proceedings of PICALO 2008 – The 3rd Pacific International Conference on Application of Lasers and Optics, (2008).

4.19) W.W. Duley : Laser Welding, John Wiley & Sons, (1999), 25-27.

4.20) J.F. Ready and D.F. Farson : LIA Handbook of Laser Materials Processing, Laser Institute of America, (2001), 320-322.

Chapter 5:
Micro-welding of Super Thermal Conductive Composite by Pulsed Nd:YAG Laser

5.1 Introduction

The diffusion of generated heat in the electronic devices is an important issue. The heat would be diffused from electronic devices by passive strategies, which would be carried out by the use of high thermal conductivity materials as a heat sink. The development of advanced materials with the superior high-thermal properties and the high strength-to-weight ratio has led to new metal matrix composites (MMCs) as a great attractive material in the electrical and electronic industries. Aluminum and its alloys are widely used for the manufacturing of MMCs, which have reached the industrial stage in some areas.[5.1)] In order to manufacture practical components from MMCs, a technique for joining MMCs to other similar composites or to monolithic materials is strongly required. Therefore, the development of reliable and economic joining technique is important for extending the applications of MMCs. It is well-known that laser welding is the most flexible and versatile welding technology, and it has succeeded in the welding of MMCs.[5.2), 5.3)]

Recently, a super thermal conductive (STC) aluminum-graphite (Al-Gr) composite with the low coefficient of thermal expansion (CTE) was developed.[5.4)] The properties of thermal conductivity versus thermal expansion coefficient are summarized in **Figure 5.1**, where the upper ellipse zone shows the STC composite materials, and the other of conventional thermal conductive materials such as Cu, Al, Al-SiC, Cu-W, Cu-Mo, AlN and Si are also indicated. It is difficult to weld STC Al-Gr composite material compared with existing MMCs, since the graphite material only can be melted under the high pressure with the high temperature.[5.5)] In the laser welding, the use of standard pulse profile is limited to joint this material, since the uncontrolled heat input generates an overshoot, which leads to undesirable welded joints. The control of heat input by a pulse waveform is very important to achieve a suitable welding penetration, preventions of overheating and unacceptable welding defects.

In this chapter, the welding of STC Al-Gr composite was experimentally and numerically investigated by using a pulsed Nd:YAG laser with the control of pulse waveforms, which can provide a well-controlled heat input with high energy density. These investigations have led to an optimum welding condition proposed for a pulsed laser welding with minimum weld defects. The experimental work was carried out in two sections, namely the bead-on-plate welding of STC Al-Gr composite, and the overlap welding of pure aluminum and STC Al-Gr composite. The welding characteristics of

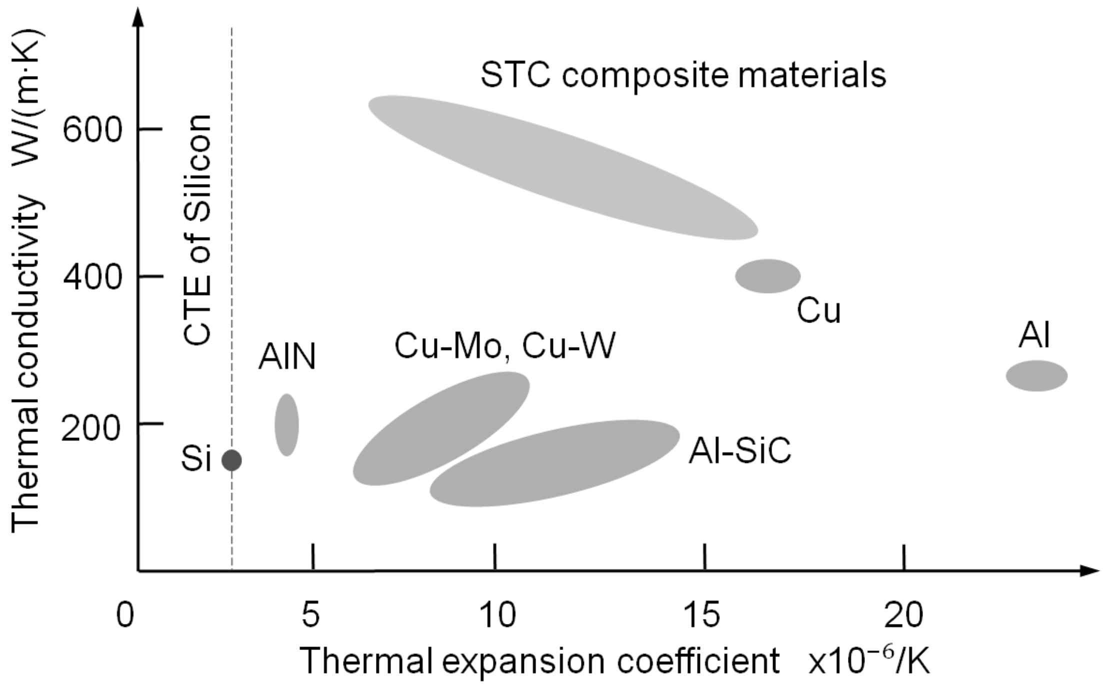

Figure 5.1 Thermal conductivity and thermal expansion coefficient of STC composites and other materials

STC Al-Gr composite were discussed by the observation of joint part with optical microscope, scanning electron microscope (SEM) and energy dispersive spectroscopy (EDS). Moreover, the temperature distributions in the laser micro-welding process were numerically analyzed to discuss the proper heat input. The weld strength was also evaluated by a shearing test for the overlap welding with and without the control of pulse waveform.

5.2 Background and overview

Each material has its own unique properties. In many applications, it has been found that there is a need for the combination of several material properties together. These desired material property combinations can be achieved by the development of new composite materials. Composite materials are usually classified by the type of material used for the matrix. The four primary categories of composites are polymer matrix composites (PMCs), metal matrix composites (MMCs), ceramic matrix composites (CMCs) and carbon-carbon composites (CCCs).[5.6] In this study, the viewpoint was MMCs, which having the properties of lightweight, high specific strength, wear resistance, and a low coefficient of thermal expansion.

Aluminum has many properties such as high thermal and electrical conductivity, high corrosion resistance, low cost and lightweight that make it ideal for use in MMCs. In addition, aluminum can be recycled and offers intriguing environmental and economical opportunities.[5.7]

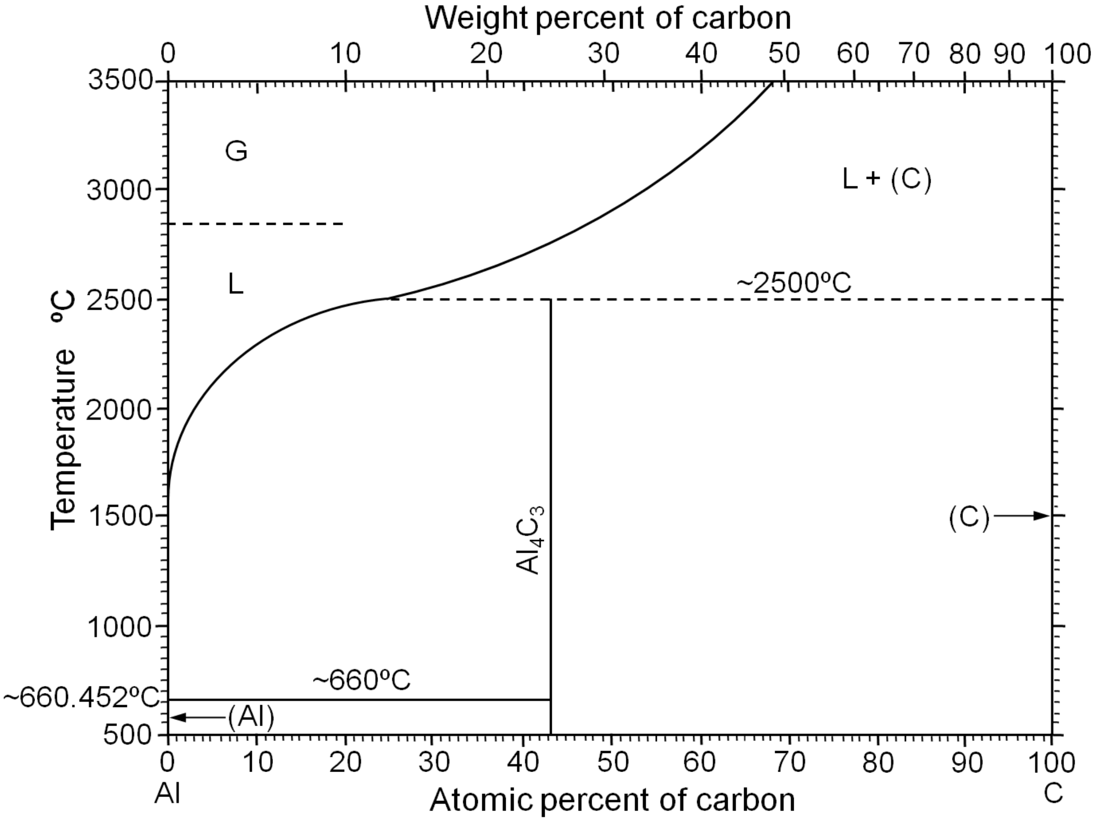

Figure 5.2 Al-C phase diagram

From the chemical point of view, the aluminum reacts with carbon to form only aluminum carbide (Al_4C_3) intermetallic compounds as shown in the **Figure 5.2**. The Al_4C_3 is known as the only stable intermediate in the Al-C binary system. However, it is very brittle at the ambient temperature.[5.8)] Based on the Al-C phase diagram,[5.9)] it can be seen that the coexistence of liquid aluminum and solid carbon requires the existence of an intermediate phase Al_4C_3. At equilibrium phase, it is impossible to directly dissolve solid carbon into liquid aluminum unless the temperature is above the melting point of Al_4C_3.[5.8)] Graphite, in the form of fibers or particulates has been recognized as a high-strength and low density material.[5.1)] The material combination of aluminum and graphite could produce an advanced aluminum-graphite (Al-Gr) composite, which has an unique thermal properties, due to to the opposite thermal expansion coefficients of aluminum and graphite.

Recently, a super thermal conductive(STC) Al-Gr composite was developed, which have been prepared by utilizing a pulsed electric current sintering method[5.1)] to realize the properties of higher thermal conductivity and lower thermal expansion coefficient. The material properties of STC Al-Gr composite are shown in **Table 5.1**. It shows that the thermal conductivity, thermal expansion coefficient and bending strength are anisotropic due to the directional properties of graphite and their designed orientation in *xy* plane-direction (top view) and *xz* thickness-direction (section view) as shown in **Figure 5.3**.

Table 5.1 Material properties of STC Al-Gr composite

Material properties			Value
Thermal conductivity	k_{xx} , k_{yy}	W/(m·K)	450
	k_{zz}	W/(m·K)	40
Specific heat	c	J/(kg·K)	810
Density	ρ	kg/m³	2450
Thermal expansion coefficient	α_{xx} , α_{yy}	/K	17×10^{-6}
	α_{zz}	/K	8×10^{-6}
Bending strength	M_{xx}	MPa	65
	M_{zz}	MPa	7
Tensile strength	$\sigma_{\mathrm{tensile}}$	MPa	49
Young modulus	G_{e}	GPa	31
Electrical resistivity	R	Ωm	17×10^{-8}

The demand for lighter and thinner products has led MMCs to be manufactured, especially in welding process. The welding process of MMCs has attracted various industries by the reduction of material weight and costs, and improvement of design flexibility. Therefore, the development of efficient, flexible and reliable joining technique is significantly important to increase the potential of MMCs. Compared with the conventional fusion welding techniques, laser welding has numerous advantages such as narrow heat-affected zone (HAZ), good quality of weld bead, precise positioning and control of irradiation beam and its movement, the ease of automation and the high production speed.[5.9), 5.10)] Laser welding is characterized by intermittent laser beam powers that would allow melting and solidification consecutively. The great advantage of laser welding is keyhole effect by very high power densities involved in the laser welding, which makes laser welding technique widely used in many industrial productions.

Since the STC Al-Gr composite is a new composite in MMCs, no work has been reported concerning the welding behaviour on this composite by laser welding technique. There are several published papers related to the laser welding of MMCs, especially in the composites with combination of Al and SiC. Niu et al.[5.2)] reported that the welding of Al-SiC can be successfully realized by using laser welding. It is possible to control the geometry of weld bead by precisely controlling the laser output parameters.[5.12)] However, the reaction between SiC and Al in the weld zone generates a formation of needle-like brittle Al_4C_3, which can degrade the mechanical properties of Al-SiC composite. It dissolves in aqueous environments resulting in a loss of integrity to the weld zone.[5.13)] In addition, the Al_4C_3 formation reduces the toughness of the weld bead, even it results in

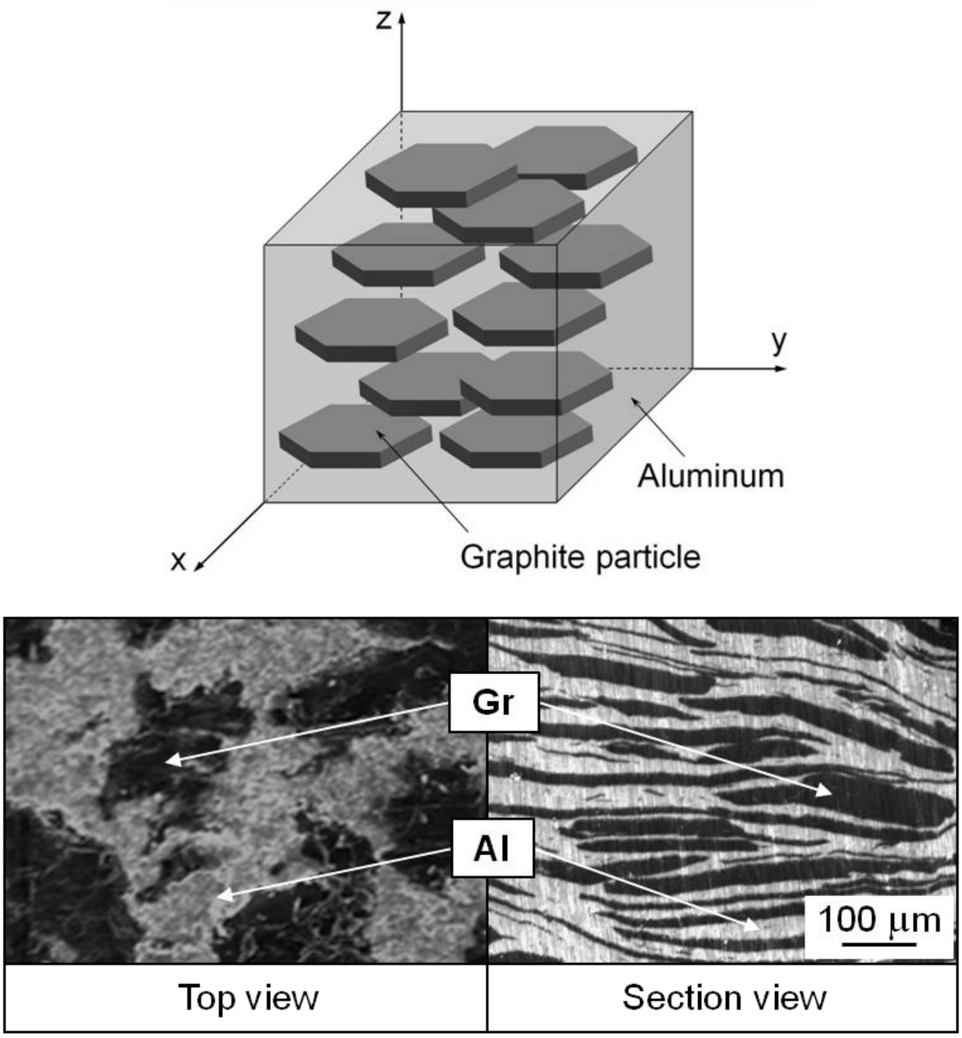

Figure 5.3 Schematic illustration and optical micrographs of STC Al-Gr composite

the increase of hardness.[5.3)] Therefore, preventing the formation of the Al_4C_3 during welding process is important for successful welding of Al-SiC composites.[5.14)]

There are severe heterogeneity of the material structure and the great difference in both physical and chemical properties between the aluminum matrix and graphite particles. This point would make the welding of STC Al-Gr composites to a challenging technological problem for applying the laser welding technique in the industrial application. In this study, the pulsed Nd:YAG laser was used as a laser source. Square shape pulses are the standard output of this laser with the constant power distribution during its duration time. By utilizing the ability of pulsed Nd:YAG laser to shape the temporal power profile of each pulse offers the high flexibility in optimising the weld parameters. This pulse waveform allows the control of penetration, melt pool geometry and keyhole formation. It also has been reported that pulse waveform to be an effective method to reduce or eliminate the weld defects.[5.15)]

5.3 Equipments

A pulsed Nd:YAG laser source of LASAG SLS200 CL8 used in this study. The detail descriptions of this laser source were mentioned in section 4.3.1. The microstructure observation and elemental analysis were carried out using a JSM-7001F of field emission scanning electron microscope (FE-SEM). The features of FE-SEM were described in the section 4.3.2. For the evaluation of mechanical strength, the shearing test was carried out using the Shimadzu EZ-L of Universal testing machine, and the features of testing machine were described in the section 4.3.3.

5.4 Experimental procedures

A schematic diagram of experimental setup is shown in **Figure 5.4**. In this study, a pulsed Nd:YAG laser (LASAG SLS200 CL8) of 1064 nm in wavelength was used as a laser source. The laser beam was collimated to 15 mm in diameter and delivered by an optical fiber of 50 μm core diameter. The collimator was installed between the optical fiber and the bending mirror, and the collimated laser beam was focused on the specimen surface by a lens of 50 mm in focal length. In order to avoid the back-reflection of incident laser beam, the processing head was aligned by 10 degrees to the perpendicular axis of the specimen surface. The irradiation experiments were carried out in two sections, namely the bead-on-plate welding of STC Al-Gr composite, and the overlap welding of pure aluminum and STC Al-Gr composite. The welding experiments were done in a shielding gas of nitrogen with 13L/min flow rate. The stage controller could determine the movement of X-Y-Z stage, and it also synchronized the laser pulse.

After the laser welding, the sectioned surface of welded specimen was ground, polished and etched for the observation of weld bead by an optical microscope, scanning electron microscope (SEM) and energy dispersive spectroscopy (EDS). In addition, the shearing test was carried out to measure the shear strength of the overlap welded joints with a Shimadzu EZ-L test machine. The specimen for shear strength of overlap welding was designed with five seam lines and 1.5 mm distance between each line as shown in **Figure 5.5**. The cross-head speed was set to 0.5 mm/min. The specimen was gripped by the clampers, which are placed in the fixture blocks. Then, a shear load was slowly increased at the suitable increments by the mechanical lever system until the welded joint of specimen was fractured. The shear strength was calculated by using fracture load and welding area. The value of shear strength was the average of three specimens. Then, the fracture surfaces were examined with SEM and EDS analysis.

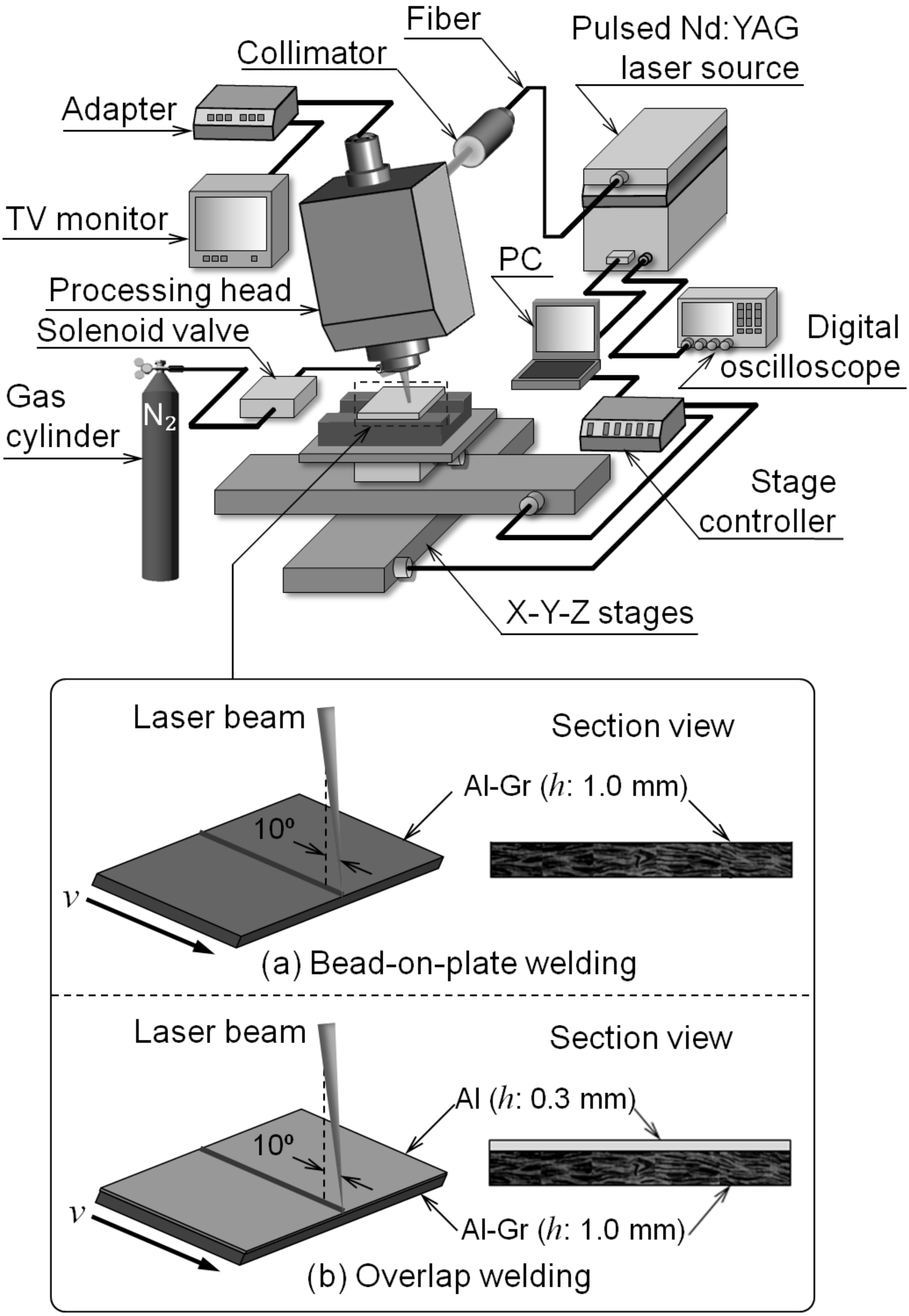

Figure 5.4 Schematic diagram of experimental setup

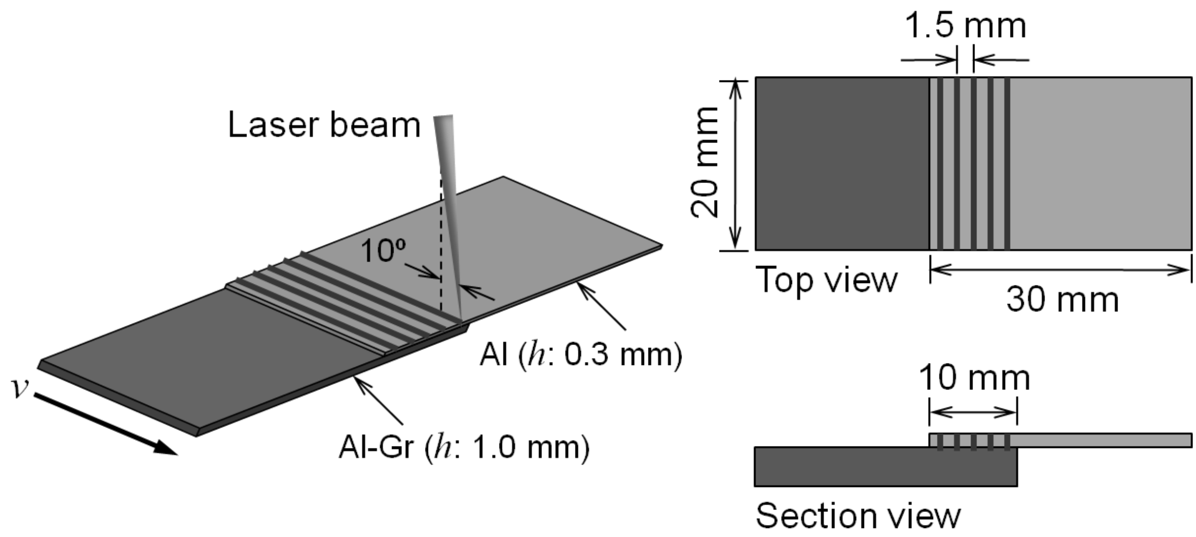

Figure 5.5 Configuration of shearing test specimen

5.5 Numerical analysis

In this study, the further analysis of the welding phenomenon was discussed by the heat conduction analysis with finite element method (FEM) to simulate the thermal process of laser welding. The analysis model is based on the fundamental heat transfer for the laser welding process. Based on the first law of thermodynamics, the heat flow in a three-dimensional solid can be expressed as equation (2.9).

Figure 5.6 shows the developed finite element models for bead-on-plate welding and overlap welding. Fine mesh resolution is given at and near the heat source, while a fairly coarse mesh density is considered at the region far from the heat source. A portion of the specimens was designed in the analysis model in order to reduce the calculation time. In addition, the half model with symmetric conditions is used in the analysis. As the heat source of laser beam is symmetric in the y-z plane, only half the heat source is considered. The heat source comprises a Gaussian plane heat source on the top surface and a conical shape heat source along the thickness of the specimen. To simplify the analysis, the assumption has been made alignment of laser spot was perpendicular to the specimen surface and a single spot of laser irradiation was utilized in the heat conduction analysis. The convective heat transfer condition of air was considered after the set time of laser irradiation. Except for a laser beam irradiated area, the convective heat transfer condition of air was also assumed. The main FEM analytical conditions are shown in **Table 5.2**. The thermal properties for STC Al-Gr composite were shown in **Table 5.1**. To simplify the analysis, the changes in thermal properties with temperature dependent of STC Al-Gr composite during this laser processing were not considered. However, the temperature dependent thermal properties of pure aluminum are important and required in the thermal analysis for overlap welding with STC Al-Gr composite and are shown in **Figure 5.7**.

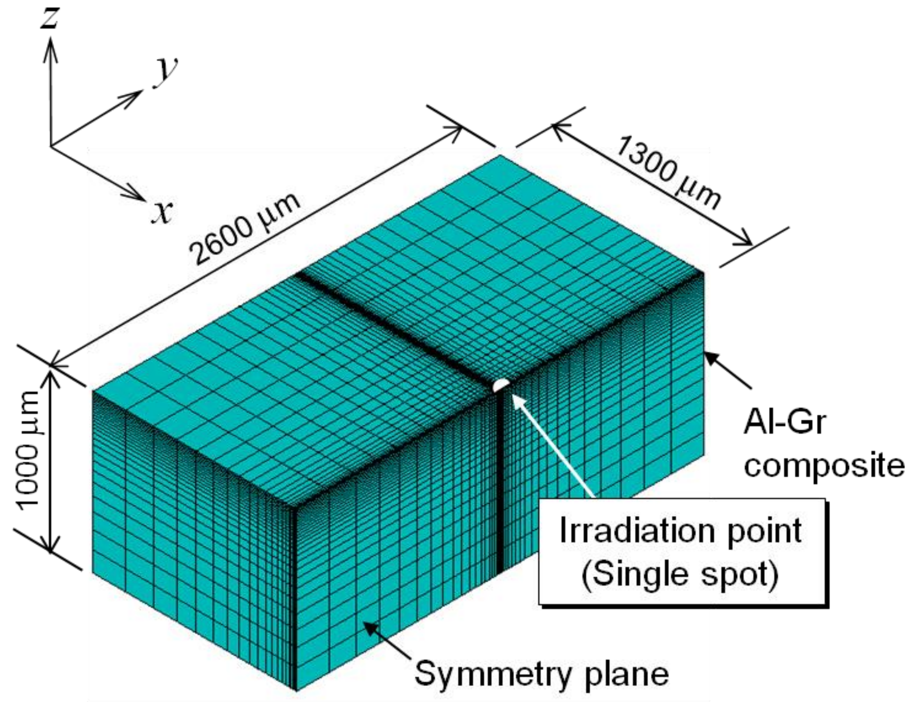

(a) Bead-on-plate welding of Al-Gr composite

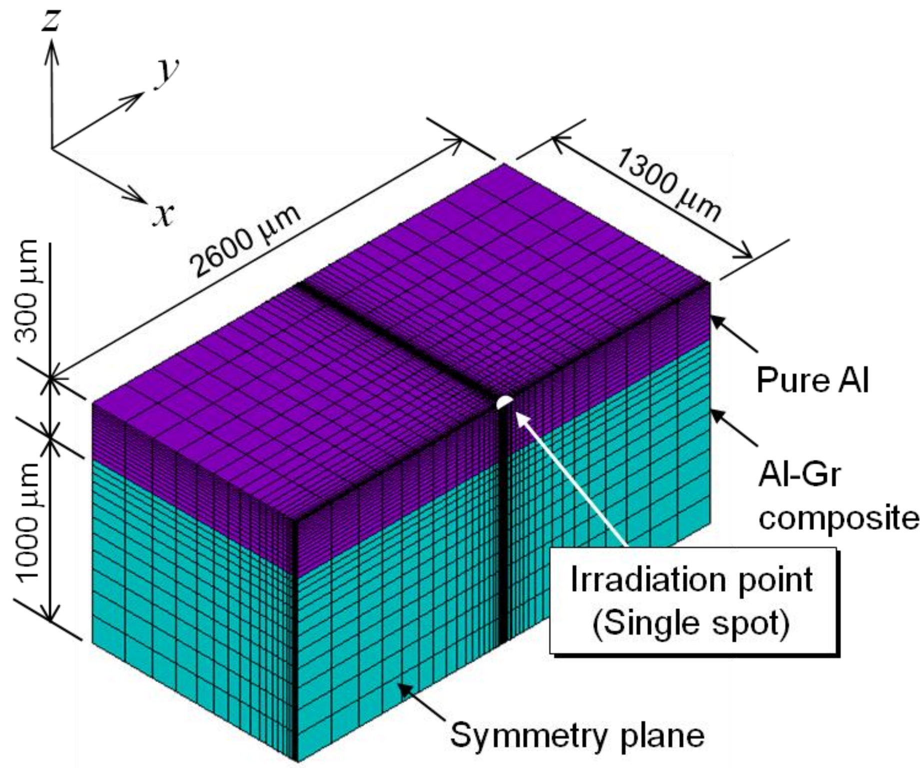

(b) Overlap welding of pure Al and Al-Gr composite

Figure 5.6 Finite element models for investigation of temperature distributions

Table 5.2 FEM analysis conditions

Parameter / condition			Bead-on-plate welding	Overlap welding
Laser power	P	W	20, 30, 40	400
Pulse width	τ	ms	1.5	2.7, 3.0, 5.0
Beam diameter	d	μm	50	
Heat transfer coefficient	h_c	W/(m²·K)	10	
Room temperature	θ_∞	K	293	

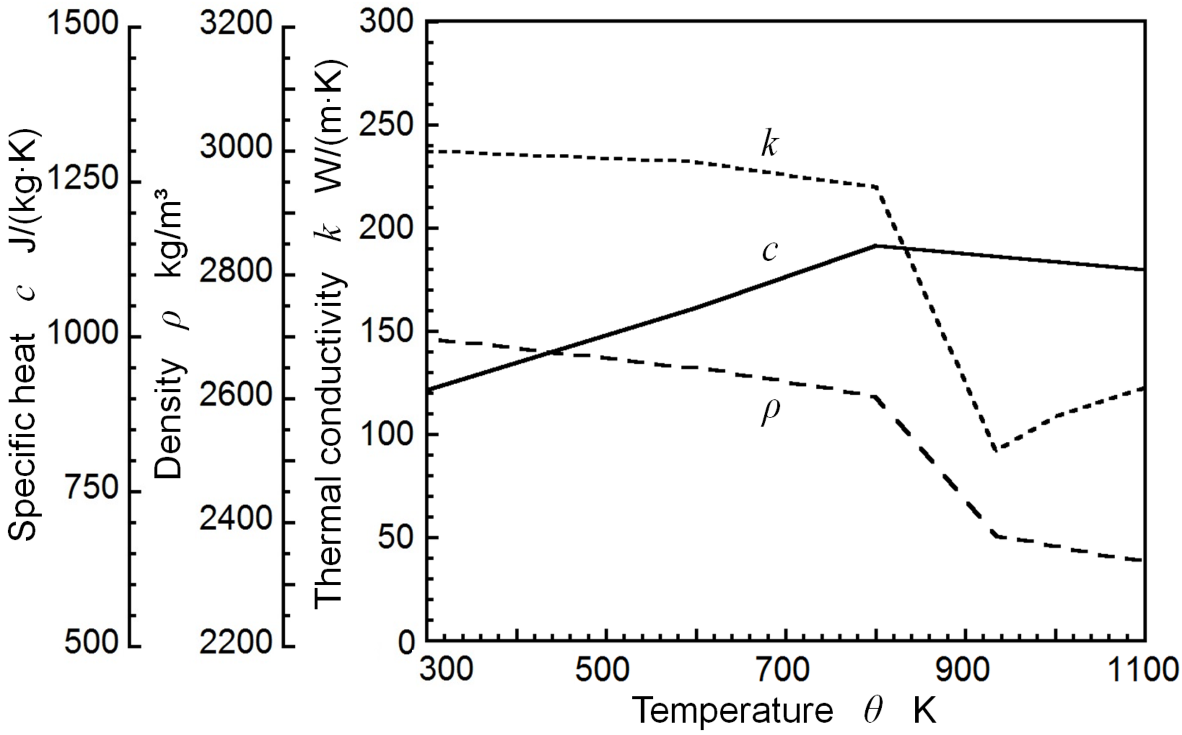

Figure 5.7 Thermophysical properties of pure aluminum

5.6 Results and discussion

5.6.1 Bead-on-plate welding

In the bead-on-plate welding experiment, the STC Al-Gr composite of 1 mm thickness was used as the specimen. The specimen was mounted by a clamping fixture with the alumina-ceramic plates, which are located on the bottom surface of specimen to minimize the heat loss during welding experiments. The rectangular shape of laser pulse was fixed as the standard output of laser source. The experiments were conducted with laser power up to 50 W, pulse width from 1 to 5 ms and scanning velocities varied between 12 to 72 mm/min.

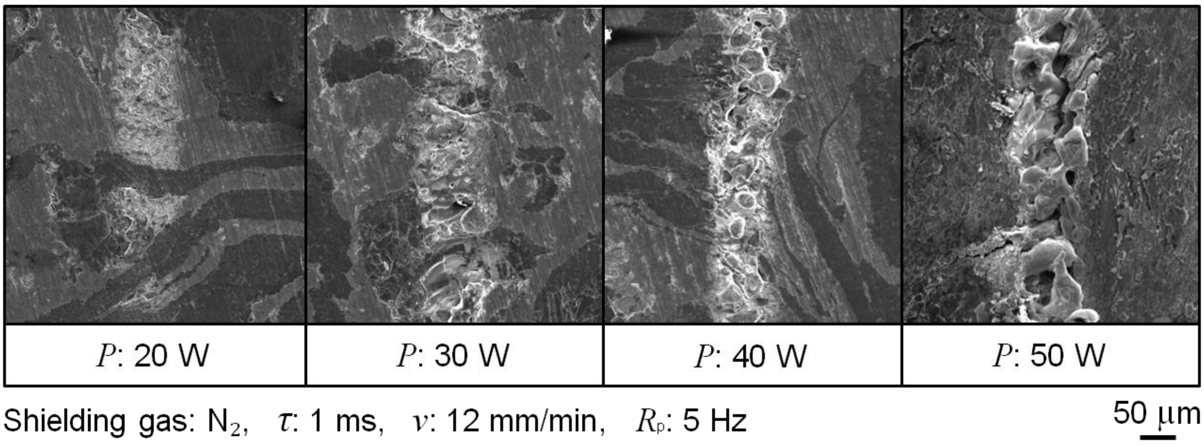

Figure 5.8 Influence of laser power on the top surface of weld bead

(a) Influence of welding parameters

In the first experiment, the welding condition on the top surface of Al-Gr composite was investigated by changing the power of laser pulse. The pulse width, pulse repetition rate and scanning velocity were kept constant at 1 ms, 5 Hz and 12 mm/min, respectively. The results of this experiment are shown in **Figure 5.8**. It can be noticed that the laser power significantly affected the welding condition. As shown in figure, when the laser power is insufficient high, the molten zone was discontinuous. At the lower 20 W of laser power, the molten zone can be observed only on the aluminum material, while the graphite material is non-molten phase. It is consider that the insufficient laser energy would not react the graphite material.

It is assumed that too high laser power leads to the generation of weld defects with increasing the power density. In practice, the power density below 10^7 W/cm^2 is generally advisable to avoid severe ejection of molten material.[5.16)] At the 50 W of laser power, it seems too high power density resulting blowholes and a poor quality of weld surface. The power density on the specimen surface can be reduced to prevent the porosities at the weld pool surface by reducing the laser power. Therefore, the acceptable condition of weld surface is obtained between 30 W to 40 W of laser power. However, since the graphite element only can be melted under the high pressure with high temperature,[5.5)] the existence of this element in the molten zone of Al-Gr composite is important to identify. It might be considered that the required laser power to generate molten zone in this composite is relatively smaller than the welding of pure aluminum, even it has a higher thermal conductivity.

In order to identify the presence of graphite element in the molten zone, the energy-dispersive X-ray spectroscopy (EDS) technique was used for the elemental analysis. **Figure 5.9** shows the distribution map of elements Al and C on the top surface of molten zone. As shown in the figure, the element Al is the main composition detected in the molten zone. However, the EDS mapping shows that only small particles of graphite were observed on the top of the solidified aluminum. Judging

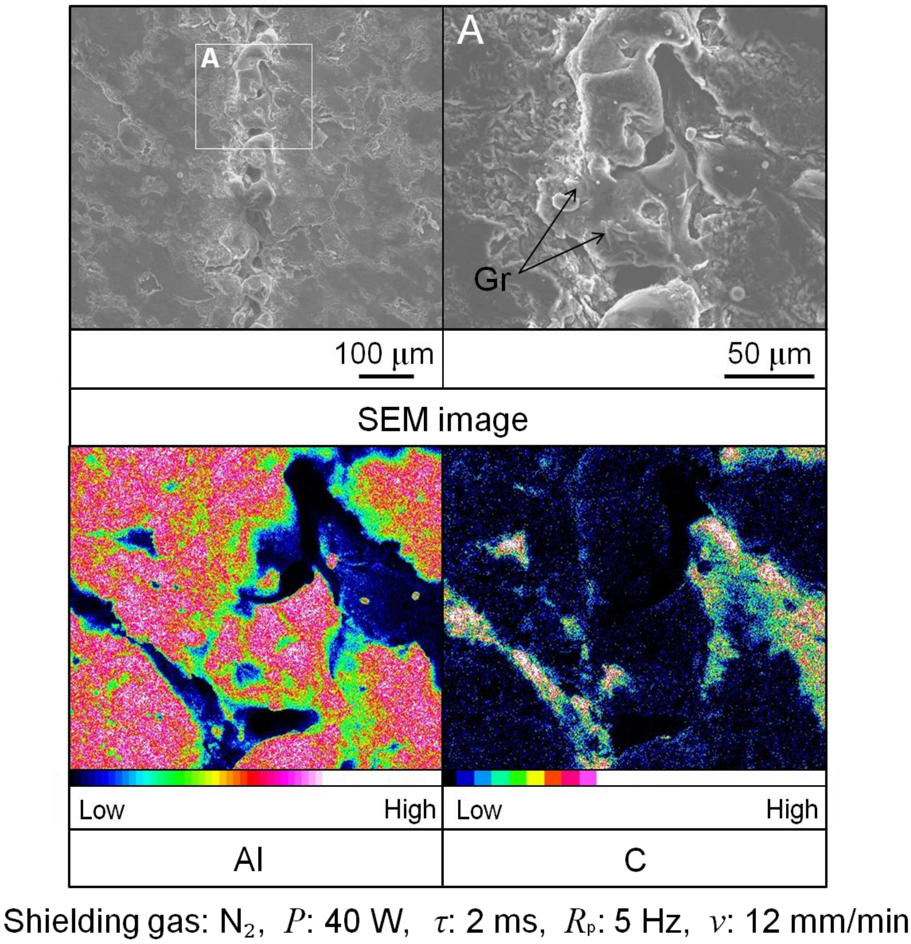

Figure 5.9 SEM photographs and element mapping of Al and C

from the distribution maps of elements, it can be presumed that the graphite was not mixed with aluminum, and it was ruptured into small particles. Even the aluminum material of Al-Gr composite was melted with the low laser power, the graphite material could not be melted. Because, the graphite only can be melted at the high temperature (θ_{melt}: 4765 K) under the high pressure (F_{melt}: 100 bar) [5.17] compared with the melting point of aluminum (θ_{melt}: 933 K). In addition, since the graphite is soft and brittle material, the graphite would be smashed only by direct irradiated laser beam to form the small particles during keyhole welding process.

In the second series of welding experiments, the influence of pulse width was investigated. **Figure 5.10** shows the appearance of weld beads under the various pulse widths at a constant laser power. It shows that the longer pulse width would generate more molten volume because the weld pool remains for an extended period of time. The widest welds are generated by the longer pulse width, which is considered due to the longer heating time. As a result, the irregular shapes and large size of cavities or blowholes are generated periodically when the pulse width was more than 1 ms. The tendency of blowhole occurrence and weld bead imperfections were drastically increased in the case of longer pulse width due to instabilities of the keyhole. In addition, the adverse effect of long

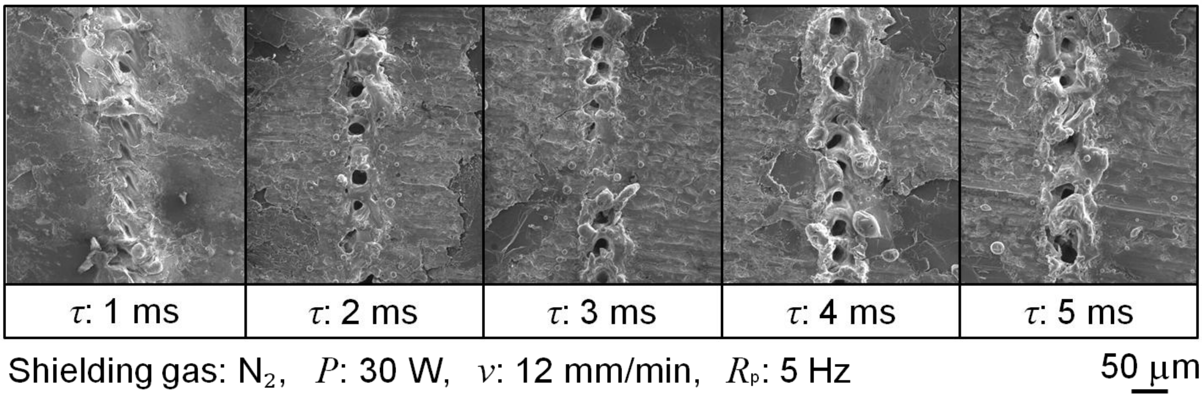

Figure 5.10 Influence of pulse width on the top surface of weld bead

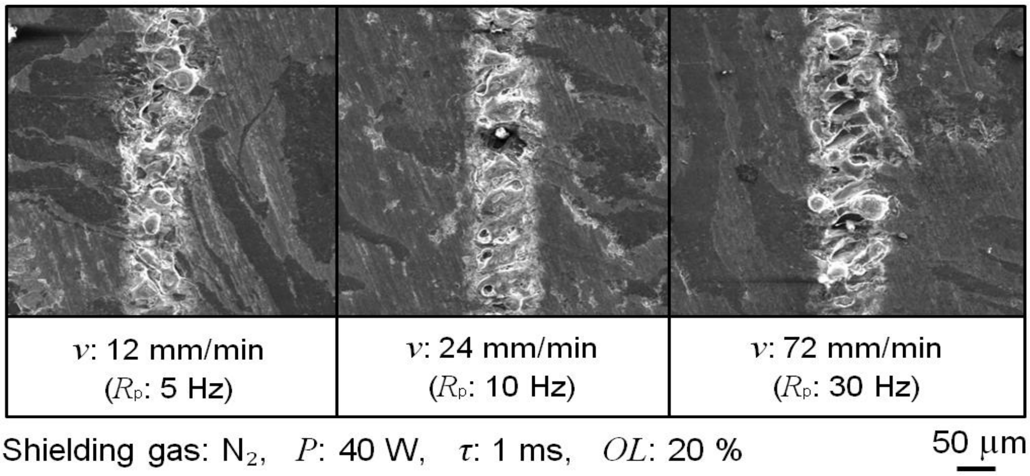

Figure 5.11 Influence of scanning velocity on the top surface of weld bead

pulse width on the weld penetration was believed due to a higher proportion of heat conducted laterally into the specimen. The results reflect that the higher energy input would enlarge processed zone. As mentioned later in section 5.6.1(b), based on the thermal analysis by FEM, a very short pulse width is enough to initiate the melting of aluminum and the evaporation of graphite on the welding of Al-Gr composite.

In order to keep the continuity of the penetration, the overlapping ratio was kept constant at 20 %. An increase in scanning velocity would increase the pulse repetition rate in the pulsed laser welding. The influence of scanning velocity on the top surface of weld bead was shown in **Figure 5.11**. It is noted that with the decrease of scanning velocity led to the enhancement of the molten zone surface, in which the weld seam surface showed an uniform surface ripple formation without blowholes. It can be seen that the effect of the remaining energy of the previous pulse is significant to interact the Al-Gr composite by the subsequent laser pulse. However, the size of molten zone was wider at the higher scanning velocity with the blowholes and poor quality of weld surface. Because the scanning velocity matches an opposite with the heat input, and the increasing of the scanning velocity means

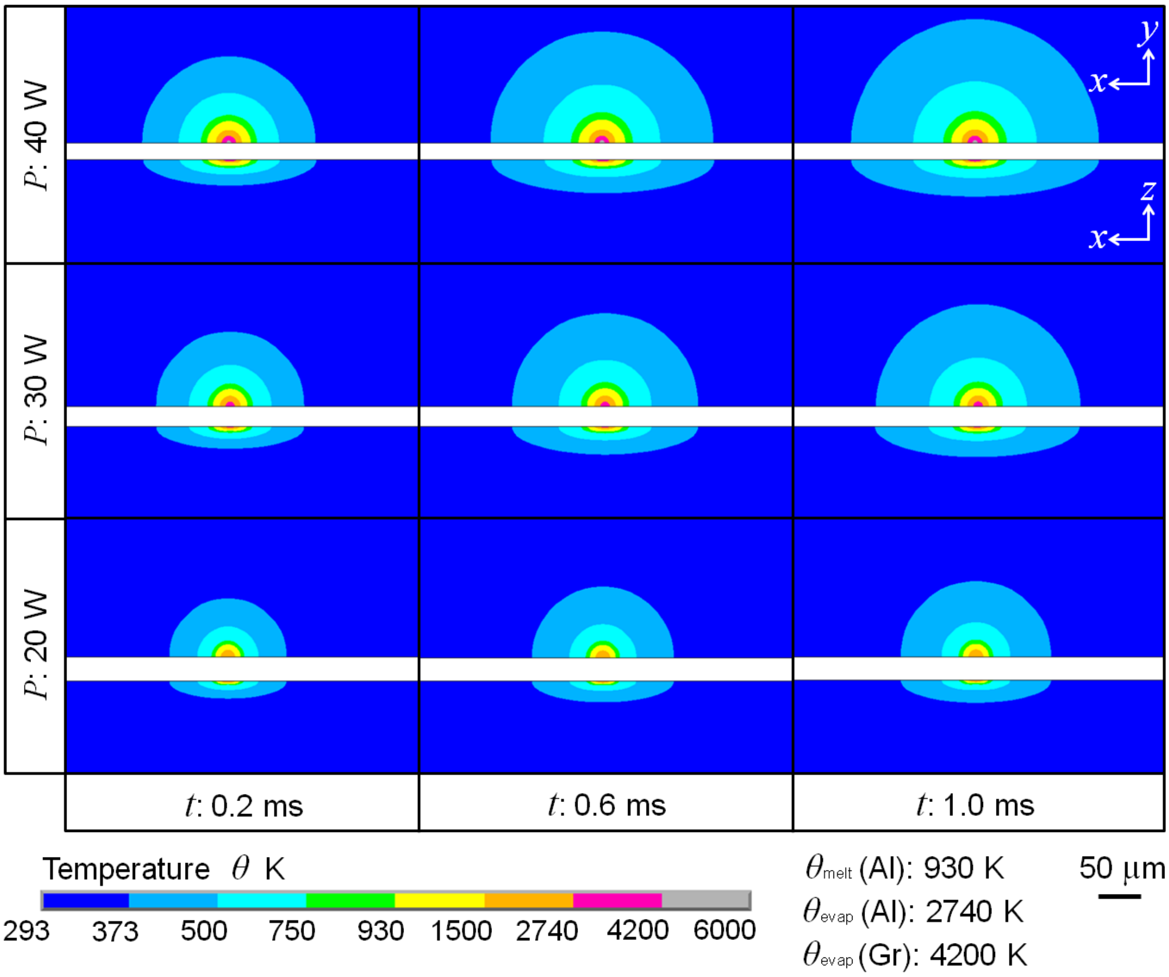

Figure 5.12 Spatial temperature distributions in bead-on-plate welding

the decreasing of the average power per unit weld length exerted on the welding line, thereby producing a small amount of intermixed melt. Therefore, the lower scanning velocity is required to produce acceptable welded joints and maintain welding quality.

(b) Temperature field induced in STC Al-Gr composite

A thermal analysis was carried out in order to study the temperature field induced in the welding process of Al-Gr composite**. Figures 5.12** and **5.13** show the influence of laser power and pulse width on temperature distribution of Al-Gr composite spatially and temporally. It can be clearly clarified that the absorbed energy on the Al-Gr composite was quickly removed in *x*-direction compared to the *z*-direction due to the higher thermal conductivity in *x*-direction (k_{xx}: 450 W/(m·K)), which is more than ten times of the thermal conductivity in *z*-direction (k_{zz}: 40 W/(m·K)). It can be seen that the increase of laser power and pulse width could enable an elevated temperature. This can be described that an enhanced laser energy input is absorbed by Al-Gr composite. In particular, when the low laser power of 20 W and 30 W are applied, the maximum temperatures are approximately

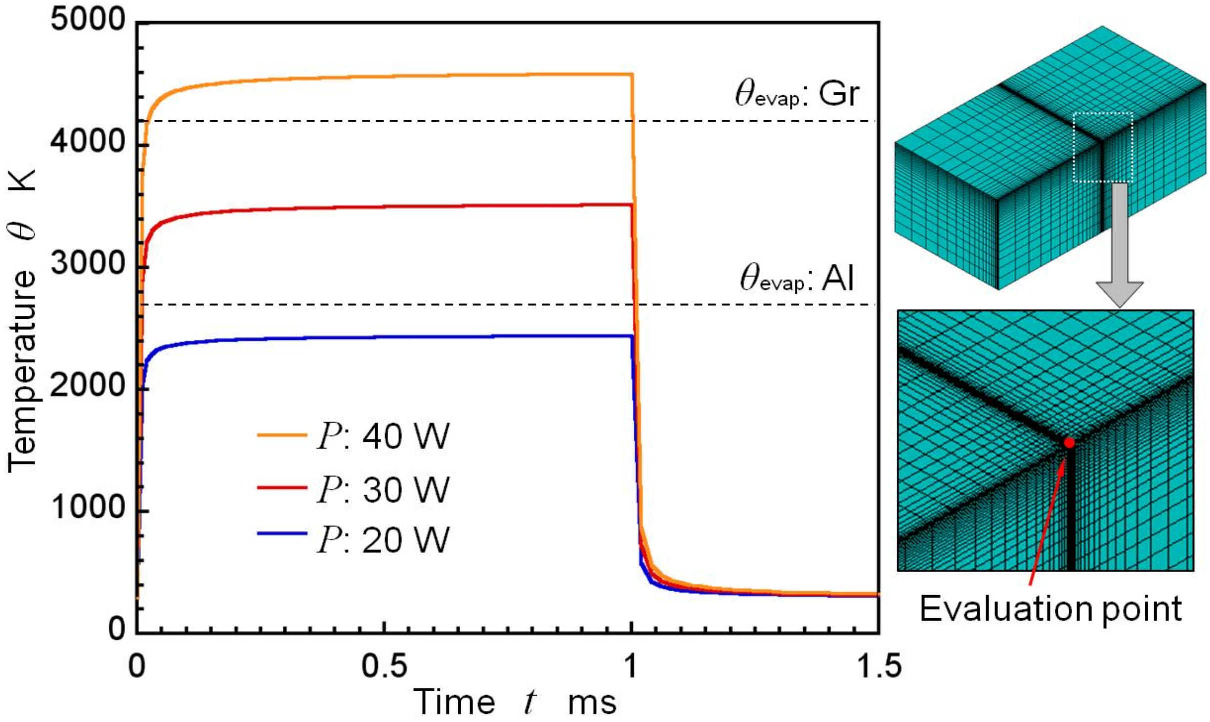

Figure 5.13 Temperature histories in bead-on-plate welding

2400 K and 3500 K, respectively, which reaches to the melting and evaporation temperature of aluminum material below evaporation temperature of graphite material. At the higher laser power of 40 W, the evaporation of graphite material occurs because the peak temperature of 4607 K exceeds the evaporation temperature of graphite. However, the influence of pulse width shows the slight increasing on the temperature after the melting of aluminum or evaporation of graphite was achieved. According to the thermal analysis results, it can be concluded that the laser power is significantly influenced on the evaporation of graphite. Judging from these results, a very short pulse width is required to initiate the melting of aluminum and the evaporation of graphite on the welding of Al-Gr composite.

5.6.2 Overlap welding

In the overlap welding experiment, the pure aluminum sheet of 0.3 mm thickness and the STC Al-Gr composite of 1 mm thickness were used as the specimens. In order to achieve an optimum welding condition, the rectangular and controlled pulse waveforms of laser pulses were utilized as the output of laser source.

(a) Rectangular pulse waveform

The variations of laser power from 300 to 550 W with constant 1 ms pulse width were irradiated on the specimen of 0.3 mm thickness aluminum and 1.0 mm Al-Gr composite plate as shown in

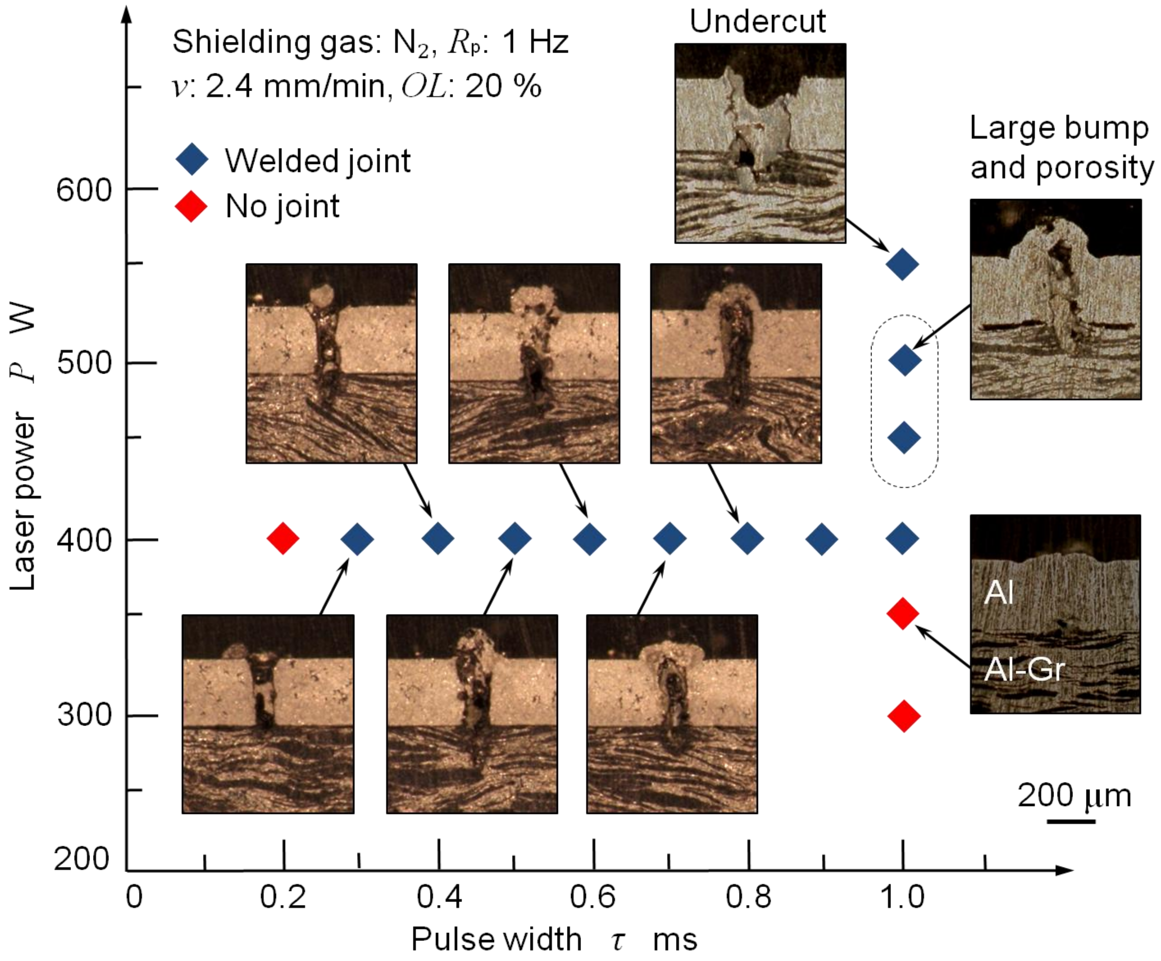

Figure 5.14 Welding results with rectangular pulse waveform

Figure 5.14. It could be seen that the laser pulse energy less than 400 mJ/pulse was insufficient to form a molten geometry for joining both materials, in which the penetration depth was shallow. The higher pulse energy was crucial to achieve the sufficient penetration depth and control the formation of molten geometry. However, the cross-section view above 450 mJ/pulse showed signs of porosity and bump defects. Moreover, the undercut defect was observed at the higher pulse energy of 550 mJ/pulse. Judging from these observation results, it was confirmed that the higher laser power (more than 400 W) causes destructive effects, and the lower laser power (less than 400 W) will restrict the penetration depth and joining. From these viewpoints mentioned above, the next welding experiments were carried out under the constant 400 W laser power with various pulse widths in the rectangular pulse waveform.

Figure 5.14 shows welding results with the rectangular pulse waveform for various pulse widths and laser powers. As shown in the figure, the width of laser pulses had a significant role on the penetration depth. The weld joint between aluminum plate and Al-Gr composite can be seen at the pulse widths more than 0.3 ms. The penetration depth and bead width gradually increased with increasing the pulse width. However, these increments led to the increase of bump size in the weld

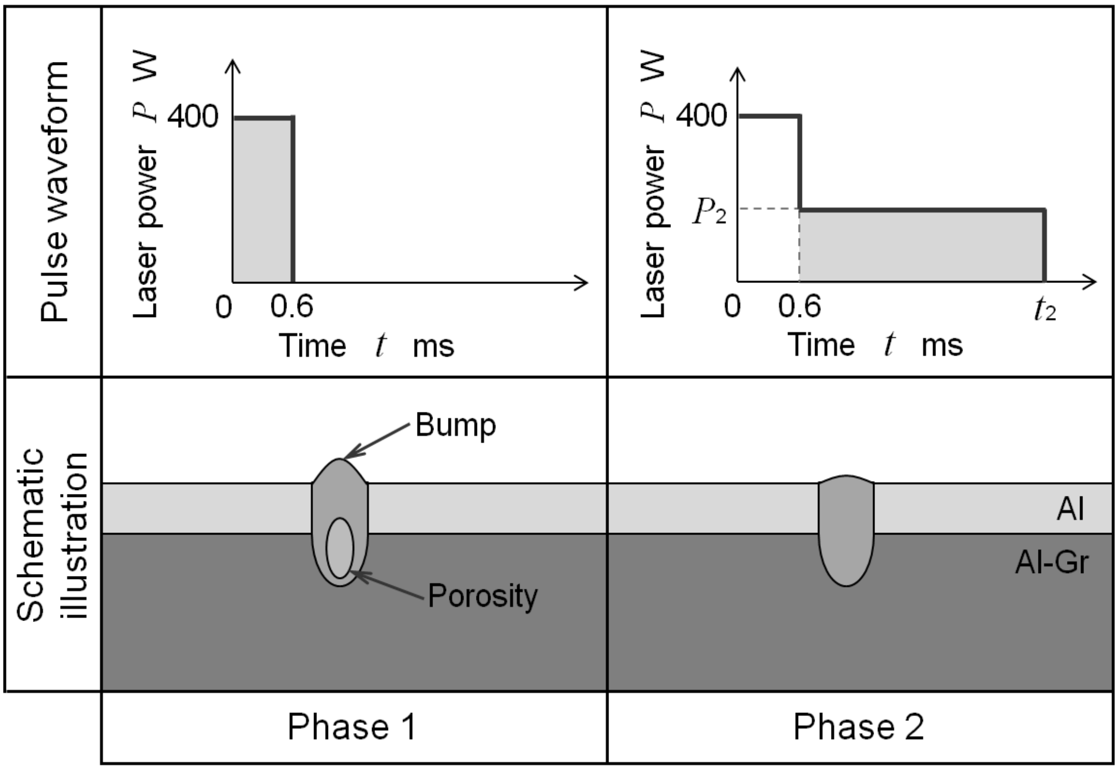

Figure 5.15 Schematic illustration of welding process with spike pulse waveform

joint. On the other hand, the penetration depth increased gradually with increasing the laser pulse energy, and a joining part between pure aluminum plate and Al-Gr composite was obtained with porosity and bump defects. According to the observation results of cross-section in the welding with rectangular pulse waveform, the pulse width of 0.6 ms was better condition with the deeper penetration, smaller porosities and bumps.

(b) Controlling pulse waveform

As mentioned in the above observation results of normal rectangular pulse waveform, the bump and porosity defects were the major problem in the overlap welding between pure aluminum and Al-Gr composite. In order to overcome these problems, a controlled pulse waveform is discussed, since it is considered that an appropriate controlled laser pulse waveform could generate a better welded joint. **Figure 5.15** shows the controlled pulse waveform named as a spike pulse waveform. The spike pulse waveform is divided into two phases. At the phase 1, the laser power of 400 W and pulse width of 0.6 ms were selected according to the previous experimental results of rectangular pulse waveform. Phase 2 is a subsequent function of the phase 1 by adding the heat to melt the bump generated in the phase 1. This re-melting process is intended to remove the porosity in order to obtain a better joining state. Therefore, the experiments were carried out to discuss an appropriate value of laser power P_2 and time period t_2 at the phase 2 of spike pulse waveform.

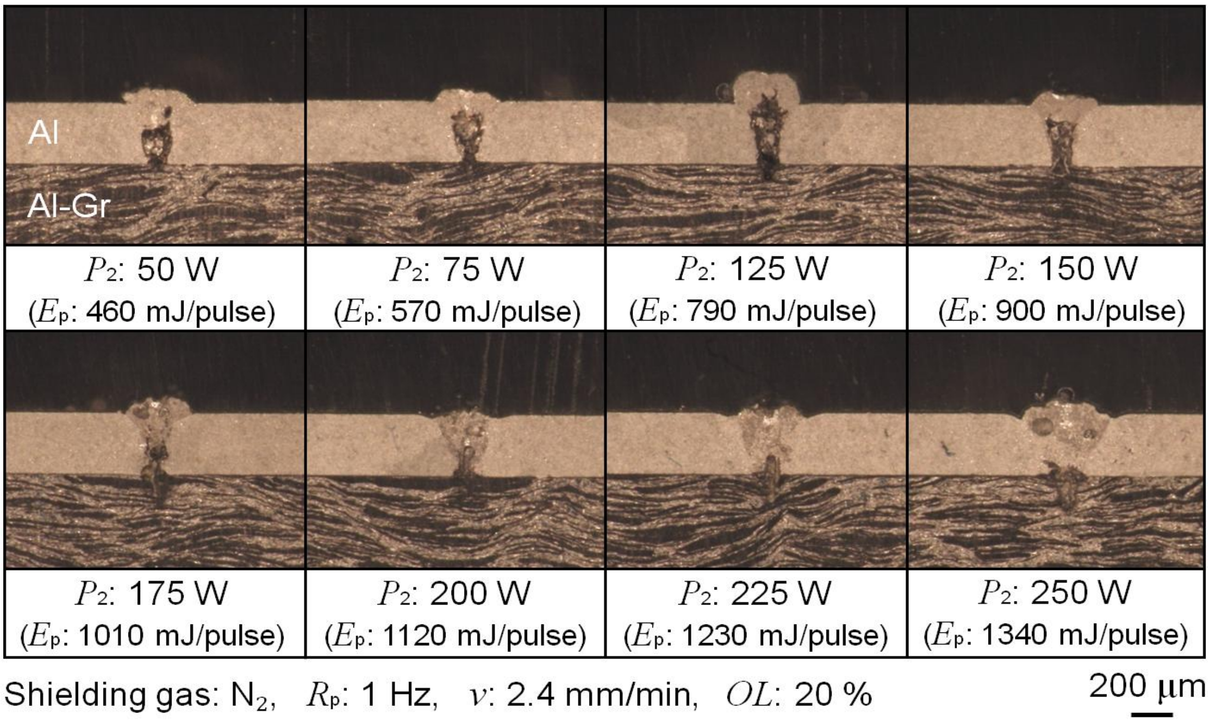

Figure 5.16 Influence of laser power (P_2) in phase 2 of spike pulse waveform

From the cross-section observation as shows in **Figure 5.16**, it was seen that the porosity and bump have remained at a range of laser power 50–125 W, while an undercut was generated at the laser power more than 200W. The observation results of laser power 150 W and 175 W showed acceptable joining conditions, and 175 W was selected as the laser power of phase 2 (P_2) for the deeper penetration and less porosity defect. The next experiment was carried out to define an optimum pulse width to set the time period t_2 at the phase 2 of spike pulse waveform as shown in **Figure 5.15**.

The pulse width was set less than 5 ms due to the limitation of maximum pulse width in the laser system used in this study. **Figure 5.17** shows the cross-section views for various pulse widths under the same laser power of phase 2 to define the appropriate value of pulse width at the phase 2 for the spike pulse waveform. An appropriate irradiation time is necessary to melt and reduce a bump during a welding process. Within the range 1.5–2.5 ms of pulse width (t_2), the results show that the welding defect of bump was not removed. Moreover, it could be cleared that the longer irradiation time (t_2: 3.5–5.0 ms) generated the larger size of bump. On the other hand, the pulse width t_2 of 3 ms showed an acceptable penetration depth. Judging from these results, 3 ms is selected as an appropriate value of t_2 at the phase 2 in the case of spike pulse waveform due to the stable penetration and smaller bump without porosities.

In addition, the elemental analysis was performed to observe the element distribution at the welded parts using a SEM equipped with the energy dispersive spectroscopy (EDS). **Figure 5.18**

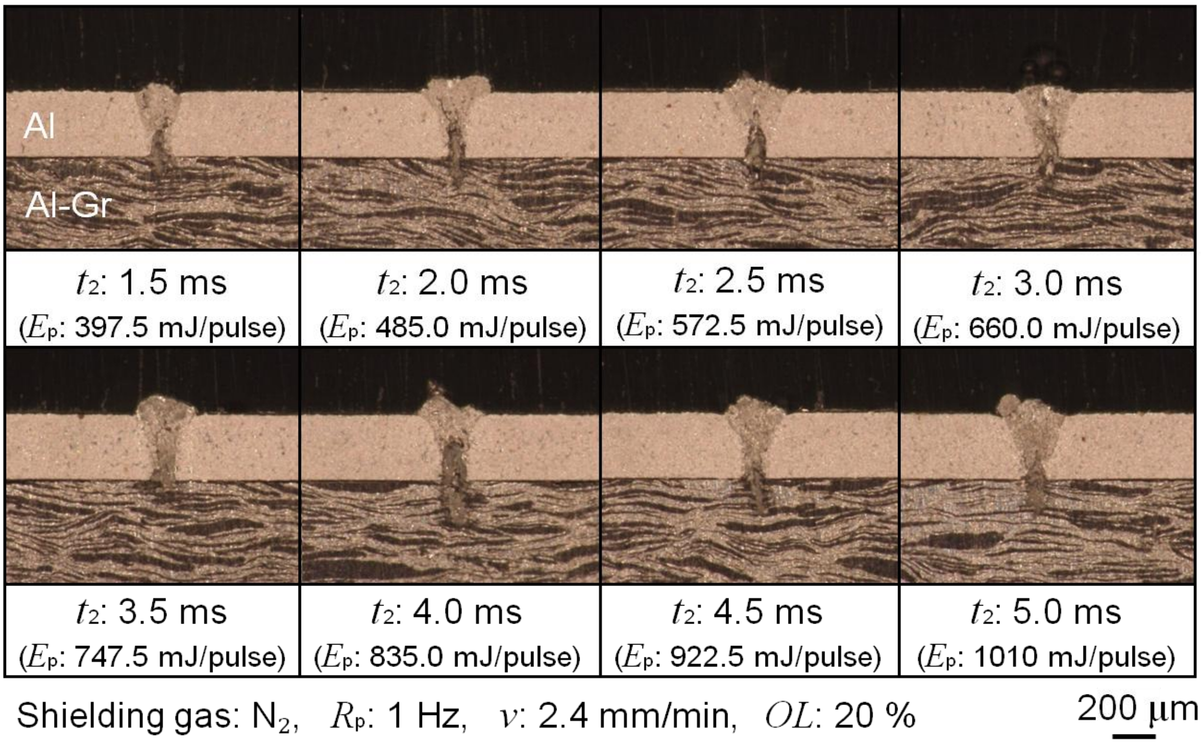

Figure 5.17 Influence of pulse width (t_2) in phase 2 of spike pulse waveform

showed the results of EDS mapping analysis in the case of spike pulse waveform. The shape of molten zone at the Al-Gr composite can not be seen clearly because of too much carbon particles on the molten zone, which can not be melted during the welding process. It could be seen that the coarse carbon located at the welded joint between pure aluminum and Al-Gr composite. It is considered that the severe convection of graphite particles with aluminum materials might be occurred in the molten zone. In other words, when Al-Gr composite is evaporated, an over-pressure is developed in the keyhole. This phenomenon would cause graphite particles pushed up from the prior zone in Al-Gr composite to the zone in the upper pure aluminum with melting phase, and finally the carbon particles would be redistributed during the re-solidification. However, it could be seen that a lack of fusion defect was generated by the spike pulse waveform. It could be detected by using an accurate microscopic observation in the high magnification condition. The lack of fusion defect in the molten zone can be identified by its string-like appearance, and it had randomly oriented curvature. It is considered that the lack of fusion defect is not pore, since the carbon element could be seen in this area.

From the observation results by the spike pulse waveform, the use of controlled pulse waveform has a positive effect on molten zone to remove the porosity and minimize the bump. However, the rapid cooling after welding process would generate the coarse carbon particles and lack of fusion defect in the molten zone. Therefore, an improvement of heat input at the end of laser pulse is necessary by introducing an approach of ramp-down on the phase 2 to relieve the internal stress

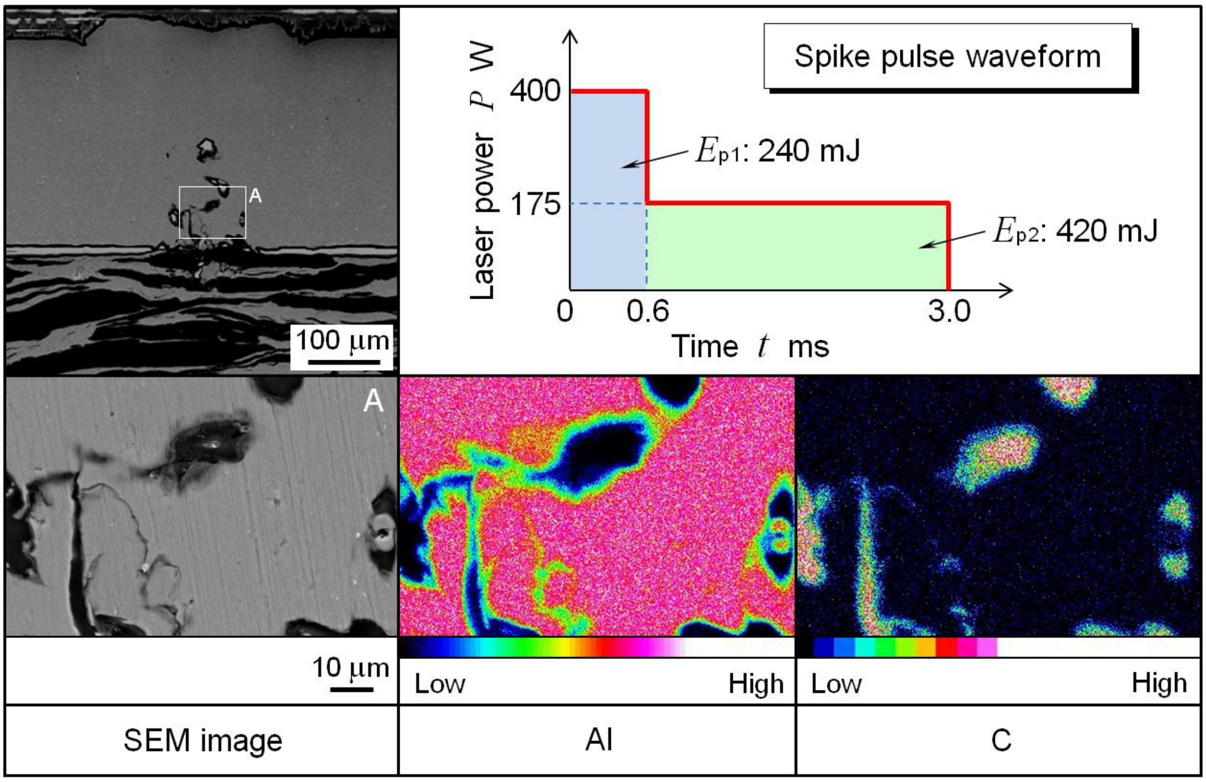

Figure 5.18 SEM images and EDS mappings with spike pulse waveform

during re-solidification process, which would generate a better welded joint. The new controlled pulse waveforms are expressed as the annealing pulse waveform, and the trailing pulse waveform is also shown in **Figure 5.19**, in which the setting profile and the actual signal of three controlled pulse waveforms are also shown. Since the phase 2 of spike pulse waveform generated a stable weld bead compared with the rectangular pulse waveform, the amount of energy at the phase 2 for the annealing and the trailing pulse waveforms was conducted under the same energy of 420 mJ. The main difference between the annealing and the trailing pulse waveforms are the laser power and irradiation time during the phase 2. The annealing pulse waveform has the higher laser power with the shorter interaction time, while the trailing pulse waveform has the lower laser power with the longer interaction time.

The difference of temperature change by spike, annealing and trailing pulse waveforms was investigated with the thermal calculation. Spike, annealing and trailing pulse waveforms are finished at the time of 3.0 ms, 2.7 ms and 5.0 ms, respectively. The temperature distributions were similar until 0.6 ms for three pulse waveforms, since they have similar pulse shape (laser power and pulse width) at the phase 1. The main difference appeared at the pulse shape of phase 2 even under the same energy (E_{p2}: 420 mJ). **Figures 5.20** and **5.21** show the temperature histories and distributions by these three controlled pulse waveforms. It can be seen that spike pulse waveform shows the constant temperature distribution during the phase 2. Therefore, it is considered that the rapid cooling

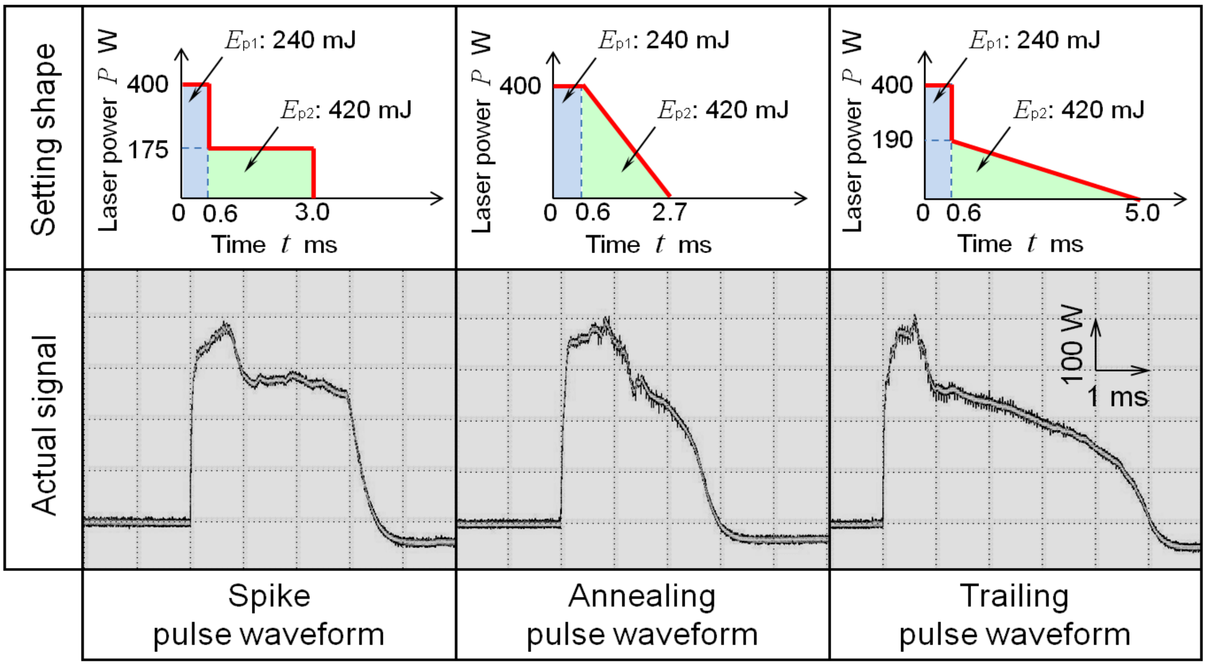

Figure 5.19 Setting shape and actual signal of controlled pulse waveform

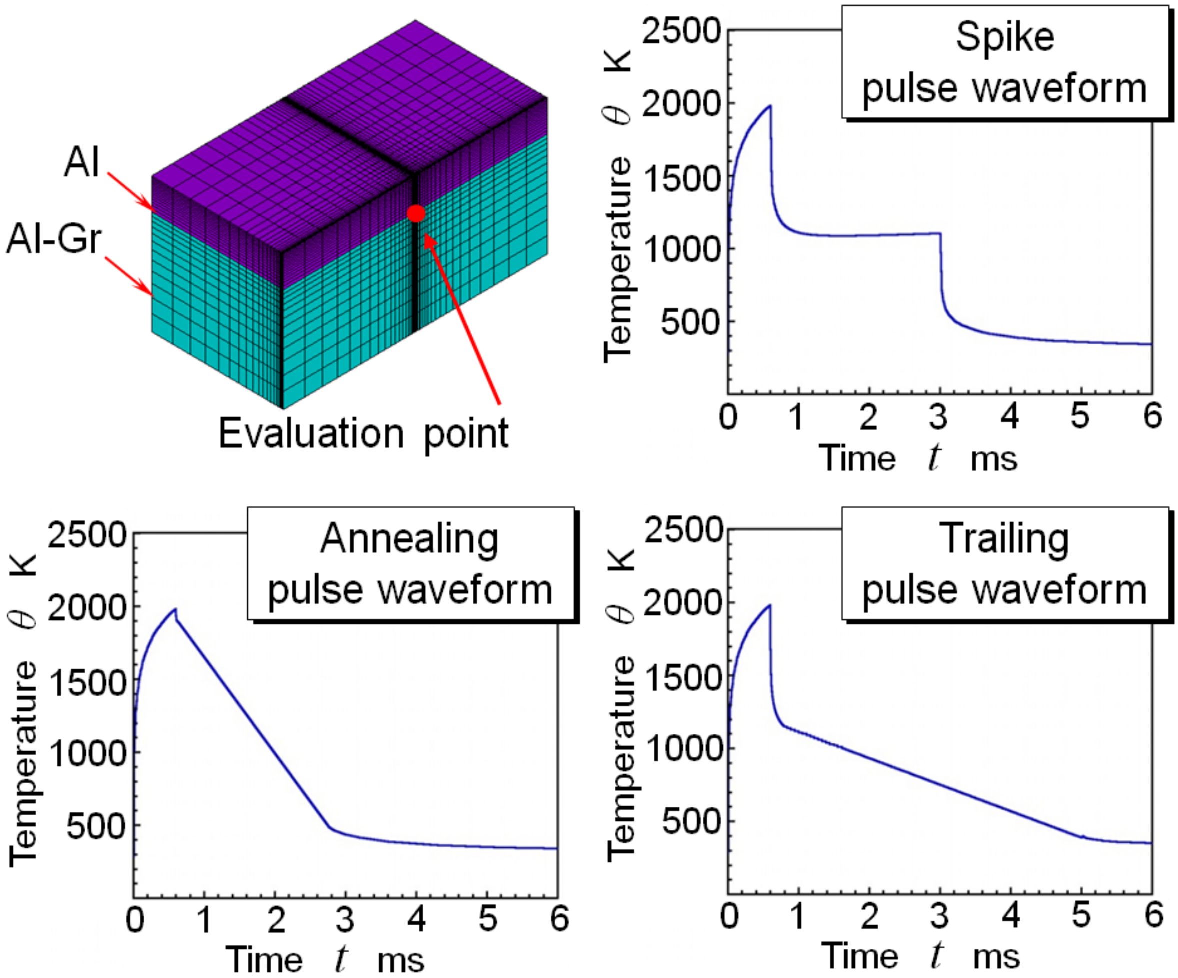

Figure 5.20 Temperature histories by three controlled pulse waveforms

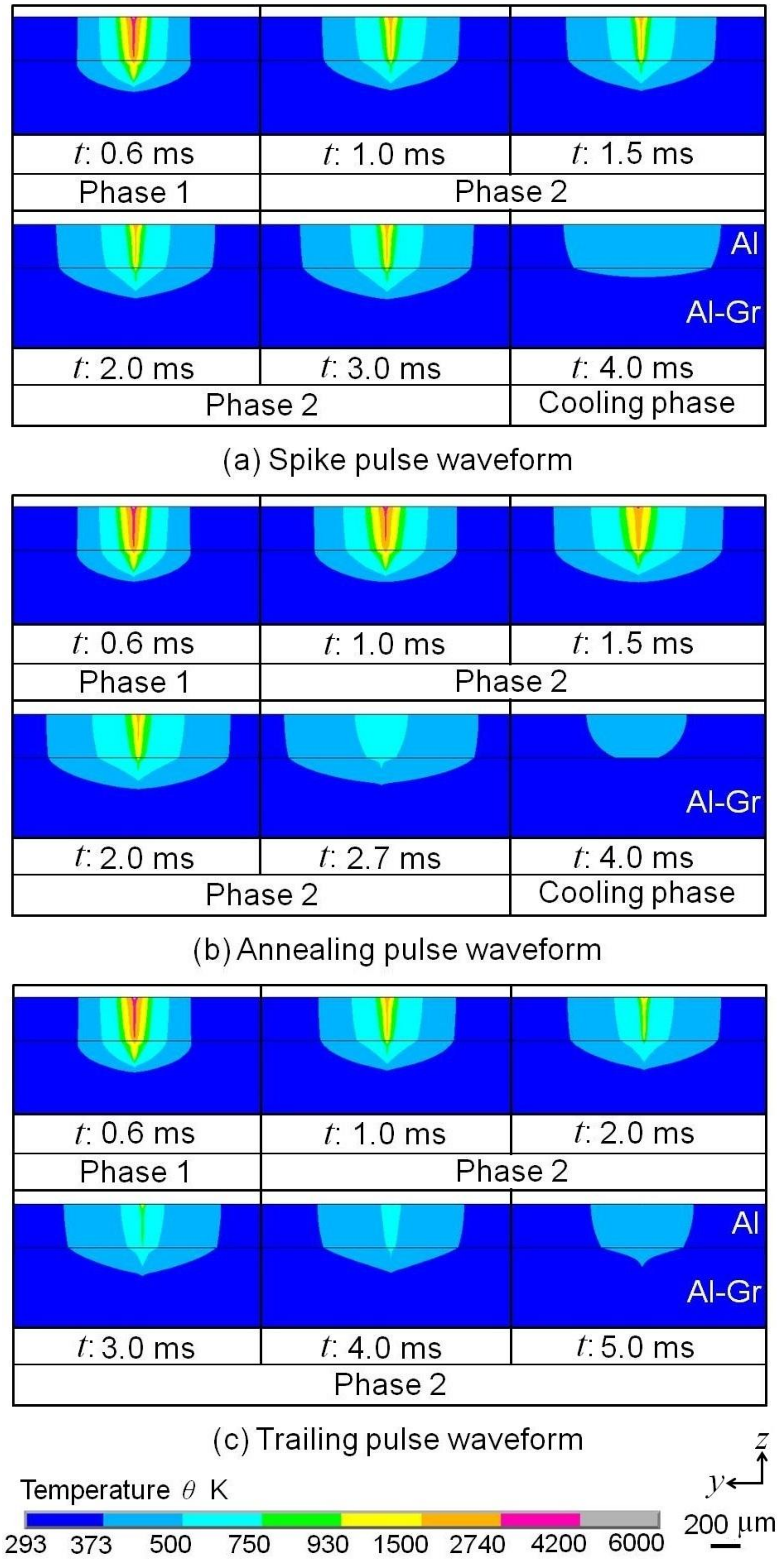

Figure 5.21 Spatial temperature distribution by three controlled pulse waveforms

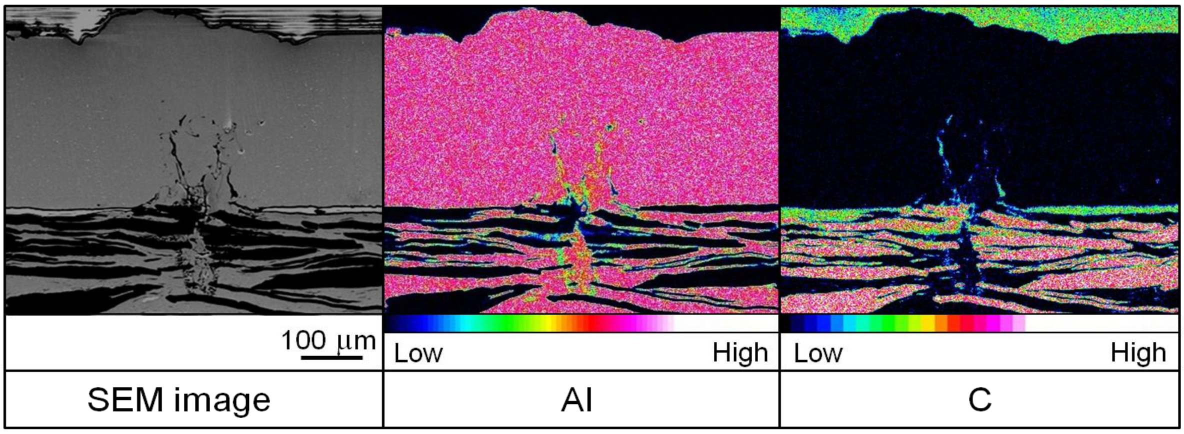

(a) Annealing pulse waveform

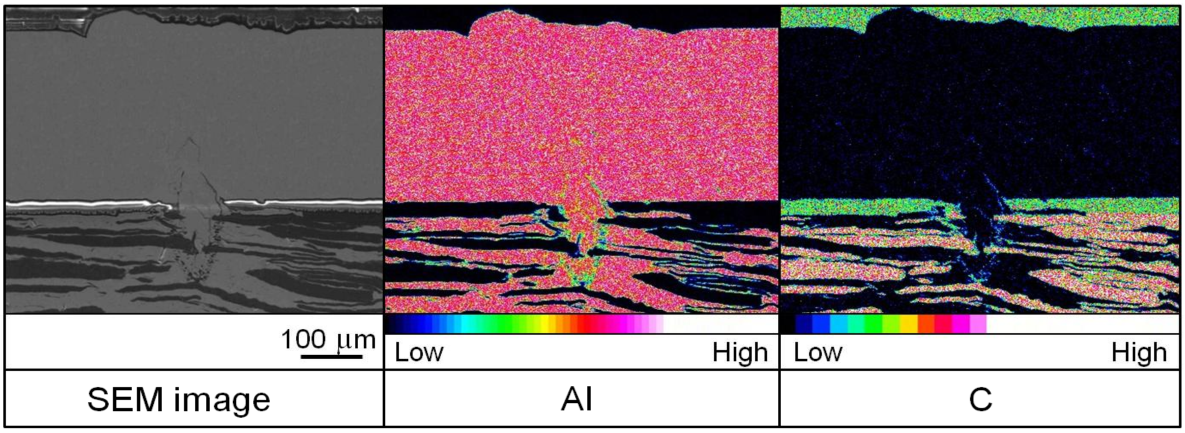

(b) Trailing pulse waveform

Figure 5.22 SEM images and EDS mappings of cross-section with (a) annealing and (b) trailing pulse waveforms

at 3 ms during the solidification generates the internal stress, and it might cause the lack of fusion defect. From this disadvantage of spike pulse waveform, the slow cooling process is required during the solidification phase. As shown in the figures, the annealing pulse waveform shows the rapid decreasing of temperature distribution at the phase 2. On the other hand, the trailing pulse waveform indicates the gradual decreasing of temperature distribution at the phase 2, which means that slow cooling could be realized. In other words, the longer time of laser irradiation is useful at the phase 2 in order to overcome the lack of fusion problem.

SEM images and EDS mappings of cross-section with annealing and trailing pulse waveforms are shown in **Figure 5.22**. In the SEM image, the shape of molten zone can be seen clearly if there are existences of aluminum element on the Al-Gr composite material. Compared with the spike pulse waveform, the size of carbon particles was much smaller in the case of annealing pulse waveform. However, it shows that the lack of fusion was appeared around the carbon particles. In the case of trailing pulse waveform, it can be seen that the specimens have been molten well with an acceptable

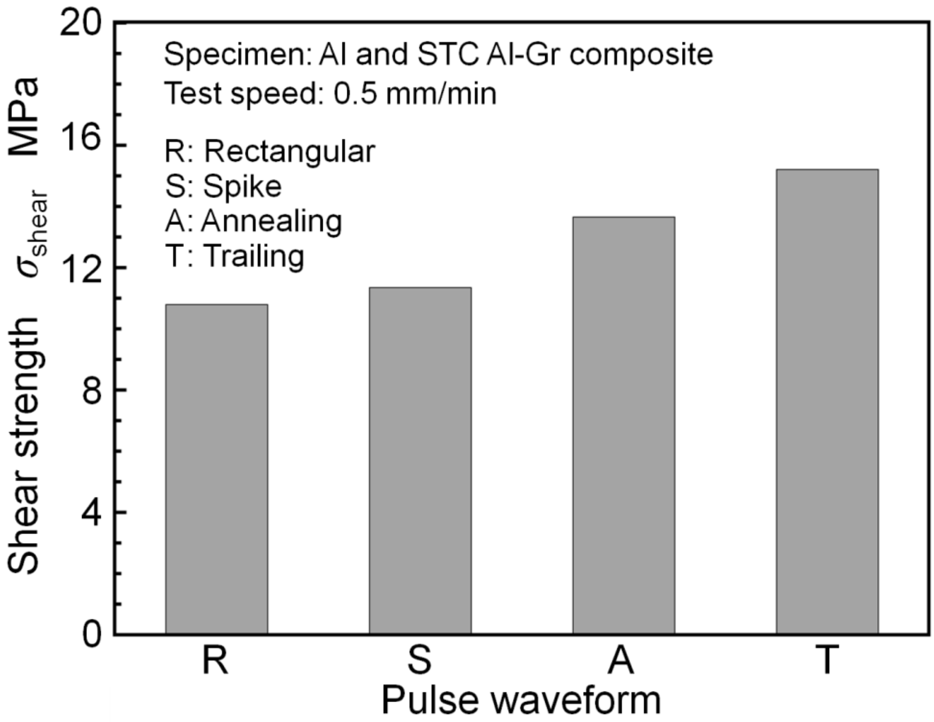

Figure 5.23 Shear strength of the welding with and without the control of pulse waveforms

weld bead state without lack of fusion defect. It also shows that a better weld bead state was obtained by applying the trailing pulse waveform. Furthermore, the sufficient long time during the welding process. In other words, the slow cooling process during re-solidification is necessary to avoid the appearance of carbon particles and minimize the lack of fusion defect in the molten zone.

5.6.3 Evaluation of mechanical strength

In order to evaluate the weld strength of the overlap welding with and without the control of pulse waveform under the constant laser pulse energy (E_p: 660 mJ/pulse), the shearing test was carried out. **Figure 5.23** shows the shear strength for various laser pulse waveforms. As shown in the figure, the weld joint with controlled trailing pulse waveform indicated the greater weld strength compared to the uncontrolled pulse waveform. The lower strength of the uncontrolled pulse waveform is attributable to the fact that the existence of porosity reduced the strength of weld joint. Meanwhile, it shows that the spike pulse waveform was less significant to increase the weld strength compared to the uncontrolled pulse waveform. It can be noted that the lack of fusion defect was affected on the lower weld strength. Therefore, it is cleared that the appropriate controlled laser pulse configurations are effective to improve the weld joint between aluminum and STC Al-Gr composite.

Figure 5.24 shows the fracture part on the top surface of Al-Gr composite after the shearing test. As can be seen from the figure, the fracture with uncontrolled pulse waveform occurred at the weld bead boundary in the Al-Gr composite and the presence of groove could be observed. It could

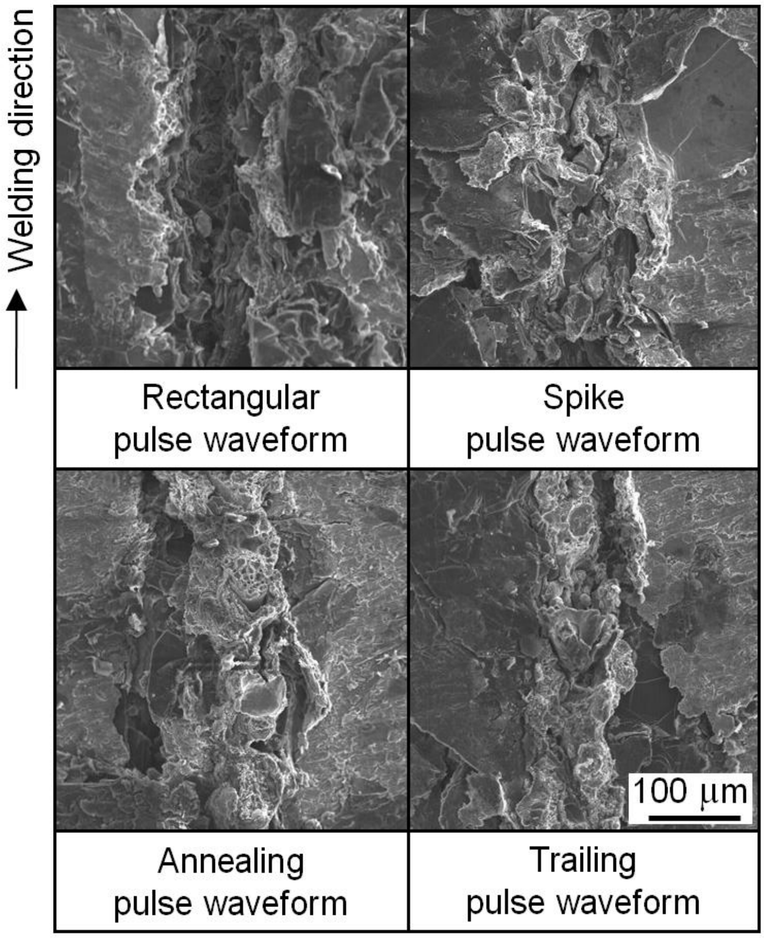

Figure 5.24 SEM photographs of fracture on the top of STC Al-Gr composite

be noticed that the existence of groove defect clearly influenced the weakness of weld joint strength. However, the fracture in the welding with the control of pulse waveform appeared inside the weld bead, which is located at the interface between pure aluminum and Al-Gr composite without the groove defect. In other words, the interfaces of aluminum and STC Al-Gr composite were expected to be the weak points of the weld joint. It is also considered that a weld joint without weld defects would increase the weld strength.

Figure 5.25 shows the side fracture surface of aluminum and STC Al-Gr composite, which were obtained from the shearing test under the welding condition with trailing pulse waveform. It can be seen that the fracture appearances show the brittle fracture. This fracture along the welding interface would deteriorate the weld strength of aluminum and STC Al-Gr composite joint. **Figure 5.25** also shows the distribution map of elements Al and C on the fracture zone, where spot analysis of points 1 to 10 are listed in **Table 5.3**. It can not be detected the aluminum carbide Al_4C_3 at the fracture zone, since the solid graphite can not be solidified into liquid aluminum. EDS mapping on the bottom surface of aluminum confirms that after the shearing test, the fine and coarse graphite particles were found sticks on melted aluminum without mixture with solidified aluminum.

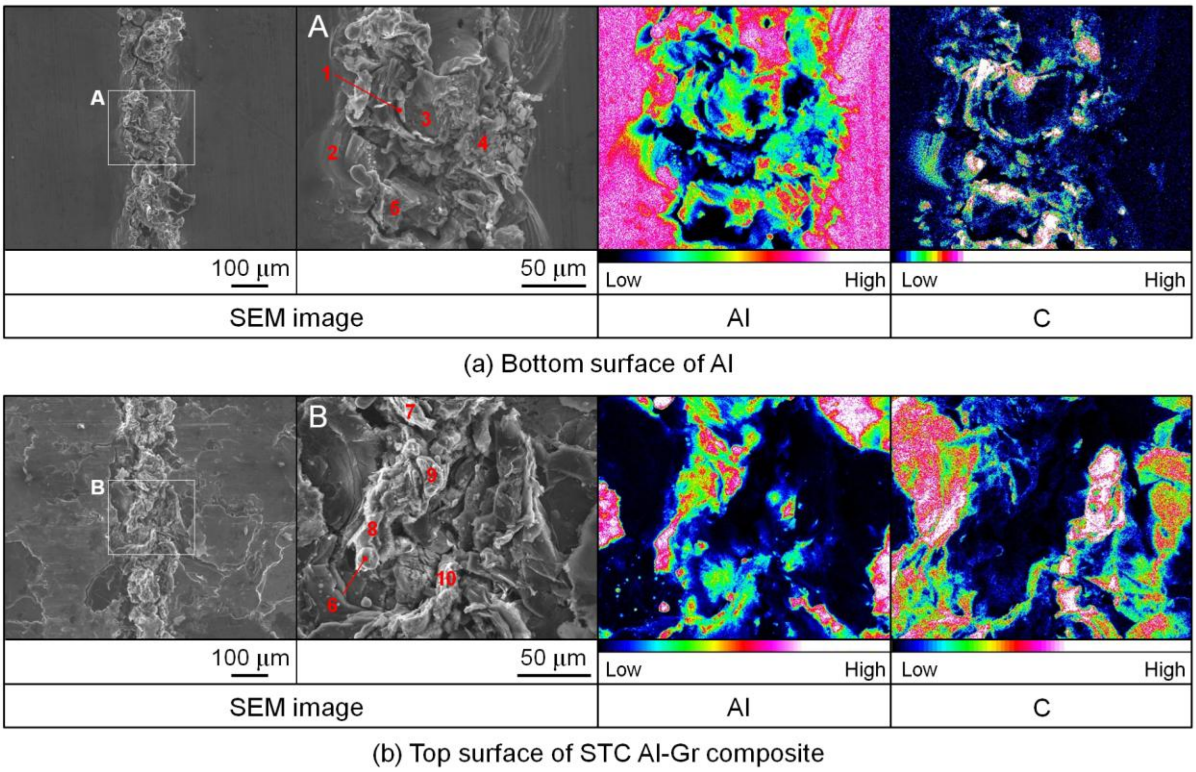

Figure 5.25 SEM photographs and EDS mappings of fracture with trailing pulse waveform on the (a) bottom surface of aluminum and (b) top surface of STC Al-Gr composite

In the case of fracture zone on the top surface of STC Al-Gr composite, it also can be seen that the solidified aluminum was squeezed out towards the edge of weld joint region, which showed the aluminum and graphite can not mixed together between both materials. Furthermore, the formation of the Al_4C_3 during welding process was successfully prevented during the welding process, which could deteriorate the strength of weld joint. In addition, the SEM observation revealed the crack was propagated in the fracture zone, which restricts the further strength of weld joint. However, compared with the bending strength of STC Al-Gr composite which is 7 MPa in the thickness direction, the weld strength between the aluminum and STC Al-Gr composite showed the relatively higher strength. Therefore, it is clearly performed that the controlled laser pulse configurations are effective to produce a higher strength of joint for welding between an aluminum and STC Al-Gr composite.

Table 5.3 Element composition of points 1–10 in **Figure 5.25**

Point No.	1	2	3	4	5	6	7	8	9	10
Al (wt. %)	49.67	30.94	62.84	41.16	64.45	52.45	35.68	48.66	64.65	48.01
C (wt. %)	50.33	69.06	37.16	58.84	35.55	47.55	64.32	51.34	35.35	51.99

5.7 Conclusions

The micro-welding of a super thermal conductive (STC) aluminum-graphite composite was experimentally and numerically investigated by pulsed Nd:YAG laser. Main conclusions obtained in this chapter are as follows:

(1) In the bead-on-plate welding of STC Al-Gr composite, the laser power and pulse width had a great influence on the top surface condition of weld bead.

(2) Laser power more than 30 W was required to melt the STC Al-Gr composite without evaporation of the graphite element in the composite.

(3) The graphite was not mixed with aluminum during welding process to prevent the formation of aluminum carbide, which can degrade the weld joint.

(4) The overlap welding of aluminum and STC Al-Gr composite was successfully carried out using an appropriate controlled pulse waveform.

(5) Porosity and bump were observed as remarkable weld defects in overlap welding without a control of laser pulse.

(6) The proper control of laser power and pulse width could perform a positive result with free of weld defects and a relatively small bump.

(7) The controlled pulse waveform with slow cooling at the end of laser pulse was essential to relieve internal stress during solidification, since the lack of fusion was observed on the joining zone due to the rapid cooling.

(8) The higher shearing strength could be obtained by the control of pulse waveform compared with the uncontrolled rectangular pulse waveform.

References

5.1) N. Baraker, S. Tzamtzis, B.K. Dhindaw,J. Patel, N.H. Babu and Z. Fan : Processing of Aluminum-Graphite Particulate Metal Matrix Composites by Advanced Shear Technology, Journal of Materials Engineering and Performance, (2009), Vol. 18, No. 9, 1230-1240.

5.2) J. Niu, L. Pan, M. Wang, C. Fu and X. Meng : Research on Laser Welding of Aluminum Matrix Composite SiCw/6061, Vacuum, (2006), Vol. 180, 1396-1399.

5.3) P. Bassani, E. Capello, D. Colombo, B. Previtali and B. Vedani : Effect of Process Parameters on Bead Properties of A359/SiC MMCs Welded by Laser, Composites: Part A, (2007), Vol. 38, 1089-1098.

5.4) T. Ueno, T. Yoshioka, J. Ogawa, N. Ozoe, K. Sato and K. Yoshino : Highly Thermal Conductive Metal/Carbon Composites by Pulsed Electric Sintering, Synthetic Metals, (2009), Vol. 159, 2170-2172.

5.5) A.V. Kirillin and A.V. Kostanovskii : Melting Point of Graphite and Liquid Carbon, Physics-Uspekhi, (2003), Vol. 46, No. 12, 1295-1303.

5.6) M. Kutz : Handbook of Materials Selection, John Wiley & Sons, Inc., (2002), 358.

5.7) V. Canilloo, A. Sola, M. Barletta and A. Gisario : Surface Modification of Al-Al_2O_3 Composites by Laser Treatment, Optics and Lasers in Engineering, (2010), Vol. 48, 1266-1277.

5.8) H. Lu, D.H. Shen, X.F. Deng, Q.K. Xue, N. Froumin, N. and M. Polak : Study of the Al/Graphite Interface, Chinese Physics, (2001), Vol. 10, No. 9, 832-835.

5.9) T.B. Massalski, H. Okamoto, P.R. Subramanian and L. Kacprzak : Binary Alloy Phase Diagrams (Vol.1), ASM International, (1990), 131.

5.10) K. Behler, J. Berkmanns, A. Ehrhardt and W. Frohn : Laser Beam Welding of Low Weight Materials and Structures, Materials and Design, (1997), Vol. 18, No. 4/6, 261-267.

5.11) L.K. Pan, C.C. Wang, Y.C. Hsiao and K.C. Ho : Optimization of Nd:YAG Laser Welding onto Magnesium Alloy via Taguchi Analysis, Optics and Laser Technology, (2004), Vol. 37, 33-42.

5.12) T.M. Yue, J.H. Xu and H.C. Man : Pulsed Nd:YAG Laser Welding of SiC Particulate Reinforced Aluminium Alloy Composite, Applied Composite Materials, (1997), Vol. 4, 53-64.

5.13) T.J. Lienert, E.D. Brandon and J.C. Lippold : Laser and Electron Beam Welding of SiCp Reinforced Aluminum A-356 Metal Matrix Composite, Scripta Metallurgica, (1993), Vol. 28, 1341-1346.

5.14) H.M. Wang, Y.L. Chen and L.G. Yu : In-situ Weld-Alloying/Laser Beam Welding of SiCp/6061Al MMC, Materials Science and Engineering, (2000), Vol. A293, 1-6.

5.15) J. Zhang, D.C. Weckman and Y. Zhou : Effect of Temporal Pulse Shaping on Cracking Susceptibility of 6061-T6 Aluminum Nd:YAG Laser Welds, Welding Journal, (2008), Vol. 87, No. 1, 18s-30s.

5.16) X. Cao, W. Wallace, C. Poon and J.P. Immarigeon : Research and Progress in Laser Welding of Wrought Aluminum Alloys – Laser Welding Processes, Materials and Manufacturing Processes, (2003), Vol. 18, No. 1, 1-22.

5.17) M. Joseph, N. Sivakumar and P. Manoravi : High Temperature Vapour Pressure Studies on Graphite Using Laser Pulse Heating, Carbon, (2002), Vol. 40, No. 11, 2031-2034.

Chapter 6: Conclusions

High brightness lasers offer the capabilities of operating with smaller spots, longer focal lengths and greater distances than conventional heat sources. These physical properties allow the laser to be used in novel ways with unique processing mechanisms. As applications of laser beam become more widespread in various industries, there is strong requirement to understand the fundamental issues of laser micro-welding process, such as the relationship between the numerous process parameters and the weld quality. In addition, laser micro-welding has become a significant industrial process because there are many outstanding advantages over the conventional welding process. In this thesis, a study of micro-welding in thin, difficult-to-weld and high performance materials by high brightness lasers was carried out. Furthermore, since the finite element based numerical techniques has proven to be very useful and efficient for research, design development and production engineering. This thesis also has investigated the laser micro-welding via the finite element analysis. One of the advantages of the finite element model is that the model allows parameter variations that can not be easily obtained by experimental techniques. For understanding of the mechanisms of laser micro-welding, an exact match between experimental and numerical results is not necessary. However, the key mechanisms need to be captured in the developed models.

The investigation into the laser micro-welding began in chapter 1 by highlighting the needs and problems for this process in industrial application, and leads to the following conclusions based on the experimental studies and numerical analyses, which has contributed to a better understanding in the laser micro-welding. In chapter 2, a numerical approach was carried out to calculate and simulate dynamically the temperature distribution of thin stainless steel sheet in CW laser micro-welding, which is essential to predict the weld bead geometry. For this purpose, a three-dimensional thermal FEM model was developed. The developed numerical model using a combination of surface heat source and adaptive volumetric heat source could well represent the real welding as the heat source penetrating into the material. The numerical results showed that the laser irradiation pre-heats a very small area in the front of the laser beam, while a tail profile behind the laser beam due to the heat transfer during the cooling process. The weld pool became more elliptical shape with higher laser power and scanning velocity compared to that of lower laser power and scanning velocity. In addition, the weld pool shape of lower laser power and scanning velocity with larger spot diameter led to the circular shape of weld pool. Moreover, the simulated results showed that the heat input to the weld pool was transferred quickly in the thickness direction and then in the width direction to reach uniform distribution. The temperature difference through the specimen thickness can affect the final deformation of the specimen, which it was clear that the heat conduction played an important role in the heat flow and the surface convection. The developed model predicted the weld bead geometry and agreed well with the experimental results, which could be used as inputs for the thermo-mechanical analysis of laser welding of thin steel sheet.

In chapter 3, the thermal deformation of thin stainless steel sheet in CW laser micro-welding was extensively investigated through numerical simulation, since thermal deformation is very important factor and it is necessary to understand the deformation caused by thermal processing. A three-dimensional mechanical FEM model was developed to simulate the welding stress and plastic strain fields, which has provided valuable insight into the laser micro-welding process and was also essential to predict the thermal deformation. The numerical results showed that the laser micro-welding could weld with low distortion, which the compressive stress induced by the heat expansion led to negative deformation angles downwards against laser beam during heating stage of welding, while a large tensile stress generated by the thermal contraction forces the specimen in upward direction but still remained with the concave shape after the specimen cools. The welding stress and deformation were generated by plastic deformation during the heating and cooling periods. In addition, the residual stress was higher than yield strength and had strongest affect upon the welding deformation. The sensitivity of thermal deformation can be evaluated against the process parameters to emphasize the fundamental understanding of the laser micro-welding process. It confirmed that the stress state and final deformation vary for various process parameters. Consequently, the welding mode should be chosen to match the material and welding process. The numerical simulated results have proved that the developed finite element model was effective to predict thermal histories, thermally induced stresses and welding deformations in the thin material. Moreover, it helped to understand the process mechanism in the laser micro-welding of thin material. Further improvements in the material model and assumptions should improve the developed mechanical FEM model.

In chapter 4, an approach of pulse waveform in laser pulse was implemented to weld the difficult-to-weld materials. The overlap welding between a FPC, which consists of a thin copper circuit on a polyimide film, and a thick brass electrode by a pulsed Nd:YAG laser were investigated. The investigation has involved the establishment and evaluation of an effective pulse waveform to determine the optimum welding results as well as the development of three-dimensional finite element model to understand the characteristics of laser micro-welding in these materials. The results showed that the uncontrolled pulse waveform generates excessive evaporation and resulted an unstable process. The pulse waveform with pre-heating effect was essential to increase the surface temperature of copper and induced higher absorption of laser energy at the beginning of laser pulse. While, the post-heating effect on the pulse waveform performed a positive result to remove the bump defect. It was found that the excessive evaporation and unstable process could be controlled the combination of pre- and post-heating effects on the pulse waveform. Furthermore, a better weld joint without weld defects could be achieved by adding a rest time in the post-heating phase, which avoids the overheating and stabilizes the weld joint. It was proved that the higher shear strength could be obtained by the control of pulse waveform to perform the good joining without weld defects.

In chapter 5, the investigation of micro-welding in the high performance material of super thermal conductive (STC) aluminum-graphite composite was experimentally and numerically investigated by pulsed Nd:YAG laser with the potential of pulse waveform. Process parameters of laser power and pulse width are investigated in terms of molten zone generated in the material, and requirements for optimum conditions to obtain feasible parameter ranges of pulse waveform. In the bead-on-plate welding of STC Al-Gr composite, the process parameters had a great influence on the top surface of weld bead and the graphite was not be mixed with aluminum during welding process to prevent from the formation of aluminum carbide, which can degrade the weld joint. Porosity and bump were observed as remarkable weld defects without a control of laser pulse in the overlap welding of aluminum and STC Al-Gr composite. On the other hand, the overlap welding was successfully carried out using an appropriate controlled pulse waveform. It proved that the proper control of laser power and pulse width could perform a positive result with largely free of weld defects and a relatively small bump and consequently resulted the higher strength of weld joint. Furthermore, the controlled pulse waveform with slow cooling at the end of laser pulse was essential to relieve internal stress during solidification, since the lack of fusion was observed on the joining zone due to the rapid cooling.

In overall, the primary goal of this thesis was to provide a systematic approach to understand the laser micro-welding in engineering materials. As described above, a new phenomenon, originalities and advantages of the micro-welding by high brightness lasers were represented in this thesis. The author hopes this thesis will be a strong motivation to diffuse and widespread the laser micro-welding into the industrial application and stimulate scientific researchers of the related fields.

Acknowledgements

In the name of Allah SWT, the Merciful, the Passionate.

I would like to express my grateful thanks and appreciation to the Almighty God for giving me the determination and ability to complete this thesis. All praises are due to Allah, the Creator of humankind.

The present work was carried out at the Nontraditional Machining (NTM) Laboratory, the Graduate School of Natural Science and Technology, Okayama University. This doctoral thesis would not possible without the guidance and the cooperation of several individuals who contributed and extended their valuable assistance in the preparation and completion of this study.

First and foremost, my utmost gratitude to former Head of NTM Laboratory, Prof. Dr. Yoshiyuki Uno, I will never forget his sincerity and encouragement. He had kind concern and consideration regarding my academic requirements.

I would like to give special thanks to Prof. Dr. Akira Okada, Prof. Dr. Shinya Tsukamoto and Prof. Dr. Masahiro Fujii for their guiding comments and revision of this thesis.

Special thanks to Dr. Yasuhiro Okamoto for his supervision, scientific guidance, valuable discussions, continued support and kind assistance during this study.

I would like to thank all past and present members of NTM Laboratory for the moral support, continuous assistance and cooperation. Sincere thanks to Mr. Kentaro Ueoka, Mr. Muhaizad Mukhtar and Mr. Satoshi Matsuoka for their assistance in the experimental works.

Special thanks to the technical and secretarial staff at the Department of Mechanical Engineering, Okayama University. Special thanks to Mr. Koji Tabuchi who helped in the fabrication of the experiment jigs at the early stages of the research. I am also very appreciative to Ms. Naoko Okamoto for her secretarial support.

I would like also to thank the Shimane Institute for Industrial Technology for supplying super thermal conductive aluminum-graphite composites.

Special thanks to the Ministry of Higher Education Malaysia and the University of Putra Malaysia for the scholarship during my doctoral course.

Finally, special and deep appreciation to my wife, Raha Abdul Gani and my kids, Muhammad Faris Shah, Muhammad Fakhri Shah, Muhammad Fadhli Shah and Raha Nadhirah Aishah for their support, patience, encouragement, never ends love and prayers during this study.

List of publications

Journal

1. M.I.S. Ismail, Y. Okamoto and Y. Uno. Numerical Simulation on Micro-welding of Thin Stainless Steel Sheet by Fiber Laser. International Journal of Electrical Machining. Vol. 16, (2011), 9-14.
2. M.I.S. Ismail, Y. Okamoto, A. Okada and Y. Uno. Experimental Investigation on Micro-welding of Thin Stainless Steel Sheet by Fiber Laser. American Journal of Engineering and Applied Sciences. Vol. 4, No. 3, (2011), 306-312.
3. M.I.S. Ismail, Y. Okamoto, A. Okada, Y. Uno and K. Ueoka. Direct Micro-joining of Flexible Printed Circuit and Metal Electrode by Pulsed Nd:YAG Laser. International Journal of Precision Engineering and Manufacturing. Vol. 13, No. 3, (2012), (Accepted).

Chapter in book

1. M.I.S. Ismail, Y. Okamoto and A. Okada. Micro-welding of Super Thermal Conductive Composite by Pulsed Nd:YAG Laser. Nd:YAG Laser, Intech., (2012), (Accepted).

Conference

1. M.I.S. Ismail, Y. Okamoto and Y. Uno. Fundamental Study on Micro-Welding of Thin Stainless Steel Sheet by Fiber Laser. Proceedings of the 16th International Symposium on Electromachining (ISEM-XVI), (2010), 431- 435.
2. M.I.S. Ismail, Y. Okamoto and Y. Uno. Direct Joining of FPC and Metal Electrode by Pulsed Nd:YAG Laser. The 73rd Conference of Japan Laser Processing Society (JLPS), (2010), 206, (Poster Presentation).
3. M.I.S. Ismail, Y. Okamoto and Y. Uno. Direct Joining of FPC and Metal Electrode by Pulsed Nd:YAG Laser. The 29th International Congress on Applications of Lasers and Electro-Optics (ICALEO 2010), Vol. 103, (2010), 864-870.
4. M.I.S. Ismail, Y. Okamoto, A. Okada, Y. Uno and M. Mukhtar. Micro-welding of High Thermal Conductive Material Aluminum- Graphite Composite by Pulsed Nd:YAG Laser. The 12th International Symposium on Laser Precision Microfabrication (LPM 2011), (2011), 84.